Study of neutral-current de-excitation gamma-rays with the T2K neutrino beam

Koh Ueno
Department of Physics, School of Science,
The University of Tokyo

February 2012

Abstract

This thesis presents a study of low energy neutrino-induced events such as nuclear de-excitation gamma-rays from neutral-current (NC) interactions using the Tokai-to-Kamioka (T2K) neutrino beam. So far, long baseline neutrino experiments analyzed neutrino events only above $\mathcal{O}(100)$ MeV. This thesis gives the first measurement of low energy events in a long baseline neutrino experiment.

We selected low energy NC candidate events at the Super-Kamiokande (SK) detector using T2K data collected from January 2010 to March 2011, which amounts to 1.43×10^{20} protons on target. After thorough background reduction, there remained 20 observed events in the reconstructed energy range of $4-30$ MeV while the expectation is 22.8 ± 6.2 beam-related events and 0.6 beam-unrelated events.

Using the NC nuclear de-excitation gamma-ray sample, we searched for the depletion of the total beam neutrino flux. Such depletion at a 295 km far detector would suggest that the three known flavors of neutrinos couple with extra light neutrinos, which are sterile to any neutrino detector. As a result, the neutrino mixing angle, θ_{34}, is constrained to be below 58° at 90% C.L. for two different models with one sterile neutrino. Also, we put a limit on the coupling between the active and sterile neutrinos by constraining $f_s \equiv P(\nu_\mu \to \nu_s)/(1 - P(\nu_\mu \to \nu_\mu))$, the fraction that a muon neutrino disappears into a sterile state. We set a upper limit of $f_s < 0.58$ at 90% C.L. for those models. Future sensitivity of the sterile neutrino search is also discussed.

We can also use the NC nuclear de-excitation gamma-ray sample to estimate atmospheric neutrino backgrounds for low energy astrophysics analyses at a water Cherenkov detector such as supernova relic neutrino (SRN) search at a gadolinium-loaded SK. Since the beam neutrino energy of T2K $\sim$0.6 GeV is similar to those of atmospheric neutrinos, a low energy T2K beam-related event enriched sample can be directly used for the estimation of the event rates of atmospheric neutrino backgrounds in such astrophysics analyses. We demonstrated as an example that we can lower the uncertainty to $\sim$10% level with the statistical goal of T2K, which enables us to discover the SRN signal at more than 3σ level with 10 year exposure times at the upgraded SK.

Acknowledgments

First of all, I would like to express my great gratitude to my adviser, Prof. M. Nakahata for giving me the opportunity of studying astrophysics, particle physics and nuclear physics. I have learned a lot of things under his excellent guidance. This thesis would never exist without his support and encouragement.

I would like to thank Prof. Y. Suzuki and Prof. T. Kobayashi, the spokespersons for the Super-Kamiokande experiment and the T2K experiment, respectively. This thesis is greatly indebted to them.

I would like to extend my gratitude to the members of the LOWE group. Special thanks go to Prof. Y. Takeuchi, Y. Koshio, A. Takeda, H. Sekiya, S. Yamada, H. Watanabe, L.M. Magro, T. Iida, M. Ikeda, B. Yang, T. Yokozawa, Prof. M. Sakuda, Prof. H. Ishino, T. Mori, Prof. Y. Fukuda, Prof. S. Tasaka, Prof. M. Vagins, Prof. M. Smy, K. Bays, A. Renshaw, Prof. K. Martens, J. Schuemann, Prof. S. Chen, and H. Zhang.

I'm also grateful to the members of the T2K-SK group, especially Prof. M. Shiozawa, Prof. Y. Hayato, Prof. K. Okumura, M. Miura, Y. Obayashi, J. Kameda, S. Nakayama, Y. Shimizu, H. Kaji, Y. Nishimura, M. Otani, K. Iyogi, Prof. K. Scholberg, Prof. C. Walter, R. Wendell, S. Mine, Prof. H.A. Tanaka, and P.de Perio.

Many thanks to the members of the Kamioka group: Prof. T. Kajita, Prof. K. Kaneyuki, Prof. Y. Kishimoto, Prof. S. Moriyama, Prof. M. Yamashita, K. Abe, H. Ogawa, K. Kobayashi, K. Hiraide, J. Liu, T. Tomura, Y. Takenaga, N. Tanimoto, A. Minamino, G. Mitsuka, H. Nishino, C. Isihara, K. Ueshima, Y. Furuse, Y. Idehara, T. Tanaka, S. Hazama, D. Motoki, Y. Nakajima, Y. Yokosawa, Y. Kozuma, H. Nishiie, A. Shinozaki, T. McLachlan, K.P. Lee, S. Hirano, Y. Nakano, D. Umemoto, O. Takachio, and K. Hieda.

There are far too many people to name here without whose help this thesis would never be completed.

I gratefully acknowledge the cooperation of Kamioka Mining and Smelting Company for hosting the Super-Kamiokande. This work was supported by the Japan Society for the Promotion of Science.

Contents

Chapter 1

Introduction

In the standard model of elementary particle physics, neutrino masses are assumed to be zero. Therefore, the finite masses of neutrinos indicate physics beyond the standard model.

Neutrinos are also important probes for astrophysics such as investigation of the solar interior and supernovae. As an example, on 23 February 1987, a supernova named SN1987A appeared in the Large Magellanic Cloud at a distance of about 50 kpc from the Earth. This was the first time neutrinos originating from an identified stellar object outside the solar system are observed.

So far, the neutrino astrophysics has been extensively studied: from low energy neutrinos from the Sun to ultra high energy neutrinos of cosmic origin. However, the neutrino astrophysics of energy region of $\mathcal{O}(10)$ MeV, relevant for supernova relic neutrinos (SRN) or monopole-induced neutrinos, has not been dedicatedly studied. In this energy region, nuclear de-excitation gamma-ray production after neutrino-nucleus neutral-current interaction plays an important role in a neutrino experiment as both signal and background.

1.1 Neutrino

1.1.1 Overview

There are three flavors of neutrinos and antineutrinos with the corresponding charged leptons: (ν_e, ν_μ, ν_τ) and ($\bar{\nu}_e$, $\bar{\nu}_\mu$, $\bar{\nu}_\tau$). Neutrinos are electrically neutral leptons and effectively interact with other particles only via the weak interaction, so that the cross section is very small. It is an experimental fact that only left-handed neutrinos and right-handed antineutrinos are observed.

Neutrinos are also known to have very tiny masses compared to other matter particles ever observed. The finite masses of neutrinos were confirmed by the observation of neutrino flavor oscillations (hereafter neutrino oscillations), which is described later. Combined with the superposition principle of quantum mechanics, oscillating neutrinos reveal the following fundamental facts: (1) neutrino masses are not degenerate; (2) the neutrino weak flavor eigenstates (hereafter flavor eigenstates) are not identical to the mass eigenstates.

1.1.2 Neutrino oscillations

The neutrino oscillation is a phenomenon where a neutrino produced with a specific flavor is later observed to have a different flavor. The neutrino flavor eigenstates $|\nu_\alpha\rangle$ are related to the mass eigenstates $|\nu_i\rangle$ as

$$|\nu_\alpha\rangle = \sum_i U_{\alpha i}|\nu_i\rangle, \tag{1.1}$$

where the unitary matrix $U_{\alpha i}$ is the mixing matrix in the neutrino sector, called Pontecorvo-Maki-Nakagawa-Sakata (PMNS) matrix [1]. Both eigenstates are assumed to satisfy the orthonormal condition: $\langle\nu_\beta|\nu_\alpha\rangle = \delta_{\alpha\beta}$, $\langle\nu_i|\nu_j\rangle = \delta_{ij}$.

Since the time evolution of each mass eigenstate is written as

$$|\nu_i(t)\rangle = \exp(-iE_i t)|\nu_i(0)\rangle \tag{1.2}$$

with neutrino energy E_i, the time evolution of each flavor eigenstate is

$$\begin{aligned} |\nu_\alpha(t)\rangle &= \sum_i U_{\alpha i}\exp(-iE_i t)|\nu_i(0)\rangle \\ &= \sum_i U_{\alpha i}(U^\dagger)_{i\beta}\exp(-iE_i t)|\nu_\beta(0)\rangle \end{aligned} \tag{1.3}$$

Hereafter, we assume neutrino oscillations in vacuum. In case a neutrino is relativistic, *i.e.*, the rest masses of the mass eigenstates, m_i, are small enough, the neutrino energy E_i is approximated as

$$E_i = \sqrt{p^2 + m_i^2} \simeq p + \frac{m_i^2}{2p} \simeq p + \frac{m_i^2}{2E}, \tag{1.4}$$

Then, the probability that a flavor eigenstate α oscillates into another flavor eigenstate β after the time of flight t is written as

$$\begin{aligned} P(\nu_\alpha \to \nu_\beta) &= |\langle\nu_\beta|\nu_\alpha(t)\rangle|^2 \\ &= \sum_{i,j} U_{\alpha i}U^*_{\beta i}U^*_{\alpha j}U_{\beta j}\exp\{-i(E_i - E_j)t\} \\ &\simeq \delta_{\alpha\beta} - 4\sum_{i>j}\mathrm{Re}(U_{\alpha i}U^*_{\beta i}U^*_{\alpha j}U_{\beta j})\sin^2\left(\frac{\Delta m^2_{ij}}{4E}t\right) \\ &+ 2\sum_{i>j}\mathrm{Im}(U_{\alpha i}U^*_{\beta i}U^*_{\alpha j}U_{\beta j})\sin\left(\frac{\Delta m^2_{ij}}{2E}t\right), \end{aligned} \tag{1.5}$$

where

$$\Delta m^2_{ij} \equiv m_i^2 - m_j^2. \tag{1.6}$$

Three-neutrino oscillations

In the case of three generations of massive neutrinos, the mixing matrix $U_{\alpha i}$ can be written using three Euler angles $\theta_{ij} \in [0, \pi/2]$ called "mixing angles", one Dirac phase $\delta \in [0, 2\pi]$ and two Majorana phases α_i $(i = 1, 2)$ called "CP-violating phases" as

$$U_{\alpha i} = R_{23}(\theta_{23}) R_{13}(\theta_{13}, \delta) R_{12}(\theta_{12}) diag(e^{i\alpha_1/2}, e^{i\alpha_2/2}, 1), \tag{1.7}$$

or, written explicitly in a matrix representation as

$$\begin{aligned} U_{\alpha i} &= \begin{pmatrix} U_{e1} & U_{e2} & U_{e3} \\ U_{\mu 1} & U_{\mu 2} & U_{\mu 3} \\ U_{\tau 1} & U_{\tau 2} & U_{\tau 3} \end{pmatrix} \\ &= \begin{pmatrix} c_{13}c_{12} & c_{13}s_{12} & s_{13}e^{-i\delta} \\ -c_{23}s_{12} - s_{13}c_{12}s_{23}e^{i\delta} & c_{23}c_{12} - s_{13}s_{12}s_{23}e^{i\delta} & c_{13}s_{23} \\ s_{23}s_{12} - s_{13}c_{12}c_{23}e^{i\delta} & -s_{23}c_{12} - s_{13}s_{12}c_{23}e^{i\delta} & c_{13}c_{23} \end{pmatrix} \begin{pmatrix} e^{i\alpha_1/2} & 0 & 0 \\ 0 & e^{i\alpha_2/2} & 0 \\ 0 & 0 & 1 \end{pmatrix}, \end{aligned} \tag{1.8}$$

with $c_{ij} \equiv \cos\theta_{ij}$, $s_{ij} \equiv \sin\theta_{ij}$. Since the oscillation probability does not differ between Dirac and Majorana neutrinos, we set both Majorana phases to 0 hereafter.

In reality, it is often allowed to assume only one mass scale is relevant for an oscillation because of the observed mass hierarchy among three generations of neutrinos[1)]:

$$\Delta m^2_{\rm sol} \ll \Delta m^2_{\rm atm}. \tag{1.9}$$

with

$$\Delta m^2_{\rm sol} \equiv \Delta m^2_{21} \tag{1.10}$$

$$\Delta m^2_{\rm atm} \equiv |\Delta m^2_{32}| \approx |\Delta m^2_{31}|. \tag{1.11}$$

In that case, one can calculate the oscillation probability with the formula of a two-generation case.

Two-neutrino oscillations

When it is allowed to approximate the mixing to that between two generations, the mixing unitary matrix $U_{\alpha i}$ can be represented as

$$U_{\alpha i} = \begin{pmatrix} \cos\theta & \sin\theta \\ -\sin\theta & \cos\theta \end{pmatrix}. \tag{1.12}$$

[1)] There still remain three possibilities of the neutrino mass spectrum: normal hierarchical (NH), $m_1 < m_2 \ll m_3 \simeq 0.05$ eV, inverted hierarchical (IH), $m_3 \ll m_1 < m_2 \simeq 0.05$ eV, and quasi-degenerate (QD), $m_1 \simeq m_2 \simeq m_3 \gtrsim 0.1$ eV.

Substituting the mixing matrix (1.12) to the oscillation formula (1.5), the probability that ν_α oscillates into $\nu_{\beta\neq\alpha}$ after traveling a distance $L \simeq t$ is,

$$\begin{aligned} P(\nu_\alpha \to \nu_{\beta\neq\alpha}) &= \sin^2 2\theta \sin^2\left(\frac{\Delta m^2 L}{4E}\right) \\ &= \sin^2 2\theta \sin^2\left(\frac{1.267\Delta m^2 L}{E}\right)\Bigg|_{\rm SI} \\ &= \sin^2 2\theta \sin^2\left(\pi\frac{L}{L_{\rm osc}}\right), \end{aligned} \tag{1.13}$$

with the oscillation length,

$$L_{\rm osc} \equiv \frac{4\pi E}{|\Delta m^2|} = \frac{2.48E}{|\Delta m^2|}\Bigg|_{\rm SI}. \tag{1.14}$$

Here $\mathrm{eV}^2/\mathrm{c}^4$, GeV and km are used for Δm^2, E and L (L_{osc}) in the SI representations[2)]. From (1.13), the oscillation to the other flavor is maximized at

$$\frac{L}{E} = \frac{2(2n-1)\pi}{|\Delta m^2|} = \frac{1.24(2n-1)}{|\Delta m^2|}\Bigg|_{\rm SI} \quad (n = 1, 2, \cdots). \tag{1.15}$$

1.2 Neutrino oscillation experiments

In this section, we briefly overview the history and current status of neutrino oscillation experiments, which are largely divided into four sectors: the solar neutrino sector ($\Delta m^2_{\rm sol}$), the atmospheric neutrino sector ($\Delta m^2_{\rm atm}$), the $\nu_e - \nu_3$ mixing (θ_{13}) sector, and the sterile neutrino sector.

1.2.1 Solar neutrino sector

In the center of the Sun, which is 1.5×10^8 km apart from the Earth, electron neutrinos are produced from thermonuclear reactions. Neutrino flux and spectrum are reliably calculated within the standard solar model (SSM) [2]. The energy range of the solar neutrinos is $0 \leq E_\nu \lesssim 20$ MeV. So far, the following experiments have measured the solar neutrino flux: the Homestake experiment [3] with a ^{37}Cl target via $\nu_e\ ^{37}\mathrm{Cl} \to e^-\ ^{37}\mathrm{Ar}$, the Kamiokande [4] and later Super-Kamiokande [7] experiments with an H_2O target via $\nu e^- \to \nu e^-$, the SAGE [5] and GALLEX [6] experiments with a ^{71}Ga target via $\nu_e\ ^{71}\mathrm{Ga} \to e^-\ ^{71}\mathrm{Ge}$ and the SNO experiment [8] with a D_2O target via $\nu_e d \to e^- pp$, $\nu d \to \nu pn$ and $\nu e^- \to \nu e^-$. All but one result indicated that the ν_e flux from the Sun is significantly lower than the SSM prediction while the neutral current interaction rate measured at the SNO detector, which is not sensitive to the ν_e flux but the total ν flux, agrees with the ν_e flux predicted by the SSM.

[2)] $\hbar c \to 197.3$ MeV·fm.

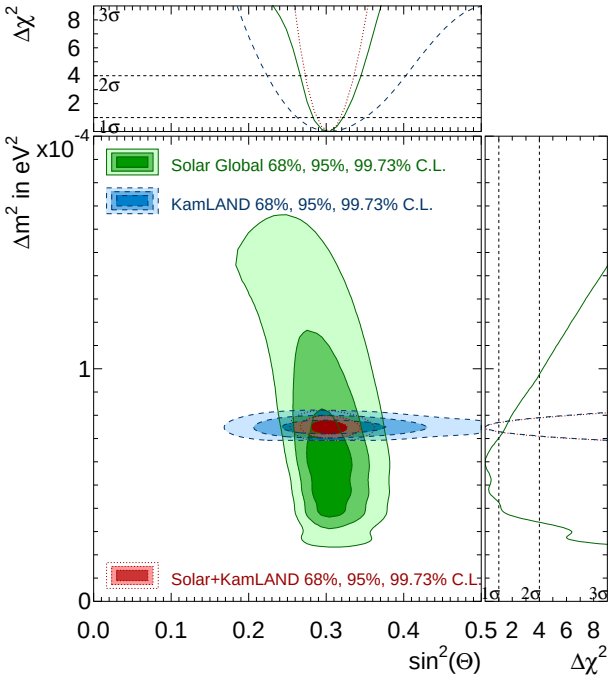

Figure 1.1: Allowed regions of oscillation parameters for the solar neutrino sector. The horizontal axis shows $\sin^2 2\theta_{12}$ and the vertical axis shows $\Delta m^2_{\rm sol}$. Shown are results from a solar global analysis [10], KamLAND [11] and solar+KamLAND [10].

These measurements favored a parameter region of neutrino oscillations called the LMA-MSW solution [9]. The result was confirmed by the KamLAND experiment [11], which uses a liquid scintillator and detects antineutrinos produced in nuclear reactions at distant nuclear reactors via $\bar{\nu}_e p \to e^+ n$ combined with the delayed coincidence of $np \to d\gamma$ (2.2 MeV). The energy of electron antineutrinos is $3-6$ MeV and the effective baseline is about 180 km. The combined analysis of the solar neutrino data and the KamLAND data leads to the oscillation parameters [12] of

$$\begin{aligned} &\Delta m^2_{\rm sol}: \ (7.32 - 7.80) \times 10^{-5} \ {\rm eV}^2, \\ &\sin^2\theta_{12}: \ 0.291 - 0.324 \ (\pm 1\sigma). \end{aligned} \tag{1.16}$$

Figure 1.1 shows the contours of allowed parameter regions obtained by these experiments.

1.2.2 Atmospheric neutrino sector

When primary cosmic rays interact with the Earth atmosphere, pions and other hadrons are produced. Charged pions which do not reach the Earth surface decay in the atmosphere, producing neutrinos called atmospheric neutrinos: $\pi^+ \to \mu^+ \nu_\mu$; $\mu^+ \to e^+ \nu_e \bar{\nu}_\mu$ and the corresponding reactions for π^-. As shown in Fig. 1.2, the energy spectra of the atmospheric neutrinos peak at

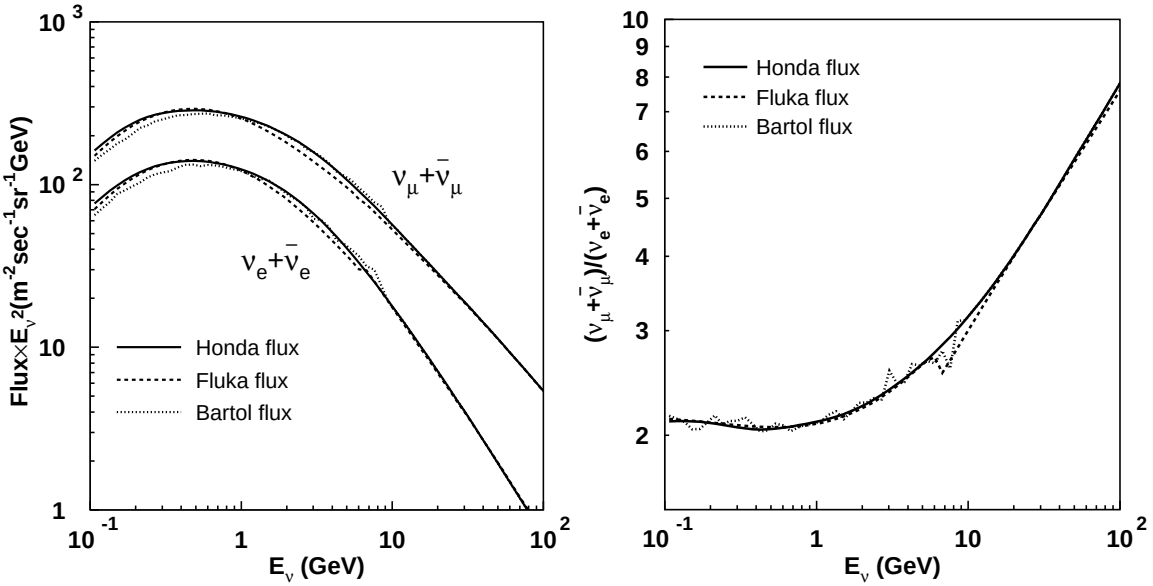

Figure 1.2: Atmospheric neutrino flux of each flavor (left) and the flavor ratio (right) expected at the Super-Kamiokande site without neutrino oscillations. Shown are three models: the Honda flux (solid) [14], the Fluka flux (dashed) [15] and the Bartol flux (dotted) [16].

around 0.6 GeV and above that energy, dN_ν/dE_ν fall with energy according to the power law of $E_\nu^{-2.7}$ to about 100 GeV. The neutrino flight length ranges from about 15 km for neutrinos produced above the detector to 13,000 km for ones produced below passing through the entire Earth. Since the primary cosmic ray flux is isotropic, the flux of atmospheric neutrinos in the absence of oscillations should be isotropic as well. In 1998, Super-Kamiokande reported that the zenith angle distribution of muon neutrinos is asymmetric while that of electron neutrinos is almost symmetric [13]. The deficit of muon neutrinos and no obvious excess of electron neutrinos indicate that there is $\nu_\mu - \nu_\tau$ oscillation.

Muon neutrino oscillations were confirmed by the K2K experiment [17]. Here the source of muon neutrinos are pion decay neutrinos of $E_\nu \sim 1.3$ GeV, where pions are produced by proton beam from the accelerator at KEK in Japan. These neutrinos are detected by Super-Kamiokande, 250 km downstream of KEK. The K2K experiment measured disappearance and spectral distortion of muon neutrinos, and the results are in good agreement with the atmospheric neutrino data. Other long-baseline experiments using the muon neutrino beam such as MINOS ($L \simeq 730$ km, $E_\nu = 1 - 5$ GeV) [18] and T2K ($L \simeq 295$ km, $E_\nu \sim 0.6$ GeV) [19] also measured the atmospheric neutrino sector and the results are consistent with the previous experiments. In

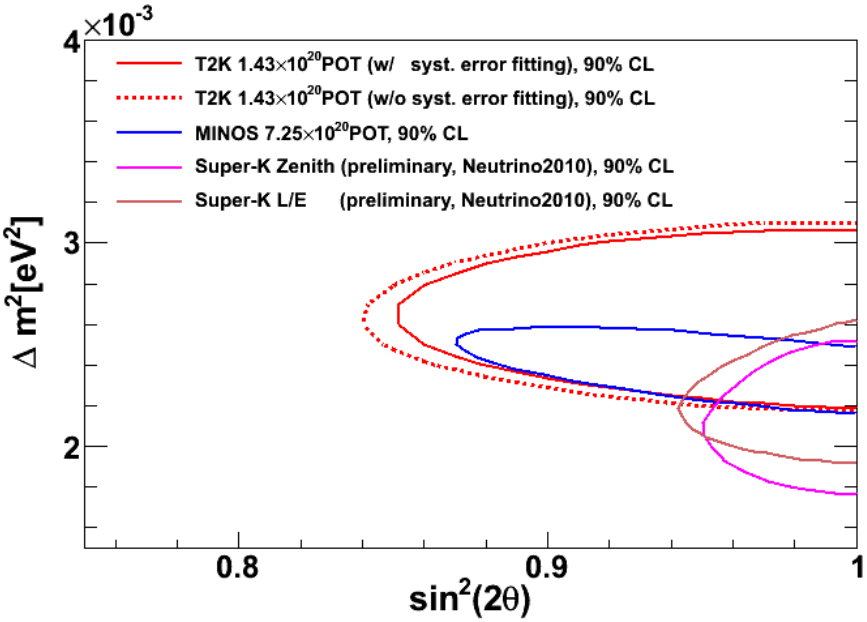

Figure 1.3: 90 % confidence level allowed regions of oscillation parameters for $\nu_\mu \leftrightarrow \nu_\tau$ oscillation. The horizontal axis shows $\sin^2 2\theta$ and the vertical axis shows $\Delta m^2_{\rm atm}$. The results are taken from Super-Kamiokande [20, 21], MINOS [18] and T2K [22].

the two-flavor mixing framework, the neutrino oscillation parameters are measured to be

$$\begin{aligned} \Delta m^2_{\rm atm} &: \ (2.26 - 2.47) \times 10^{-3} \ {\rm eV}^2, \\ \sin^2\theta_{23} &: \ 0.39 - 0.50 \ (\pm 1\sigma). \end{aligned} \tag{1.17}$$

Figure 1.3 shows the contours of 90% confidence level allowed parameter regions obtained by these experiments.

1.2.3 $\nu_e - \nu_3$ mixing sector

The third mixing angle θ_{13} is constrained by the atmospheric data in the three-flavor mixing framework and the CHOOZ experiment [23]. The CHOOZ experiment measured disappearance of electron antineutrinos from a nuclear reactor, 1 km away from the gadolinium-loaded liquid scintillation detector. Experiments with $L \sim 1$ km and $E_\nu \sim 3$ MeV are sensitive to $\Delta m_{\rm atm}$, where oscillations driven by $\Delta m_{\rm sol}$ can be neglected. The distortion of energy spectrum was not observed, and the result yields the bound at $\Delta m^2_{\rm atm} \simeq 2.4 \times 10^{-3}$ eV^{-2},

$$\sin^2 2\theta_{13} : < 0.15 \text{ at } 90\% \text{ C.L.} \tag{1.18}$$

Recently, the T2K experiment published the first result which indicates electron neutrino appearance [24]. The observed events are equivalent to 2.5 σ significance, and the constraint on

θ_{13} is:

$$\sin^2 2\theta_{13} : \ 0.03 - 0.28 \ (0.04 - 0.34) \text{ at } 90\% \text{ C.L.} \tag{1.19}$$

for $\delta_{CP} = 0$ and a normal (inverted) hierarchy, which does not conflict with the CHOOZ upper limit. In addition to T2K, experiments using reactors such as Double Chooz [25][3)], RENO [26], and Daya Bay [27] are now ongoing for the measurement of θ_{13}.

1.2.4 Sterile neutrino sector

Four experiments at LEP which measured the invisible Z-width of the Z^0 resonance [28] gave a constraint on the number of light ($m_\nu < m_Z/2 \simeq 45$ GeV) neutrinos, where the combined result is $N_\nu = 2.984 \pm 0.008$. These experiments, however, are not sensitive to the mass region above the weak scale, and there can be extra massive neutrinos. Also, the constraint above is only relevant for the active neutrinos, which are coupled to the Z^0 boson, and does not reject the possible existence of extra light massive neutrinos that are sterile, *i.e.*, insensitive to weak interactions.

LSND anomaly

Light sterile neutrinos (hereafter, also denoted as ν_s) have been postulated in order to explain the LSND anomaly. The LSND experiment [29] measured $\bar{\nu}_\mu \to \bar{\nu}_e$ oscillation. The experiment used $\bar{\nu}_\mu$ from μ^+ decay at rest ($E_\nu < 52.8$ MeV) and searched for $\bar{\nu}_\mu \to \bar{\nu}_e$ oscillations. The detector filled with dilute liquid scintillator was located about 30 meters from the neutrino source, which maximizes the sensitivity to oscillations at $\Delta m^2 \sim 1$ eV^2, and searched for a $\bar{\nu}_e$ excess via $\bar{\nu}_e p \to e^+ n$ followed by the neutron capture reaction $np \to d\gamma$ (2.2 MeV). LSND reported the positive evidence of $\bar{\nu}_e$ appearance with 3.8 σ significance, and its L/E dependence is consistent with oscillations. The parameter region that fits the data except that excluded by the KARMEN experiment [30] and some reactor experiments is:

$$\begin{aligned} &\Delta m^2 : \ 0.2 - 2.0 \text{ eV}^2 \\ &\sin^2\theta : \ (3 - 30) \times 10^{-3} \end{aligned} \tag{1.20}$$

Figure 1.4 shows the allowed parameter regions of various confidence obtained by a combined analysis of the LSND and KARMEN results. This mass squared difference is much larger than $\Delta m^2_{\rm atm}$ and $\Delta m^2_{\rm sol}$, which suggests the possibility of one or more sterile neutrinos which have a Δm^2 of $\mathcal{O}(1)$ eV^2.

Present status

Recently, the MiniBooNE experiment ($L \simeq 541$ m, $E_\nu \sim 0.5$ GeV) [32], using 800 tons of pure mineral oil (CH_2), tested the result of the LSND experiment by searching for ν_e and

[3)] The Double Chooz experiment presented the first result at LowNu11, November, 2011, which is $\sin^2 2\theta_{13} = 0.085 \pm 0.029$ (*stat.*) ± 0.042 (*sys.*).

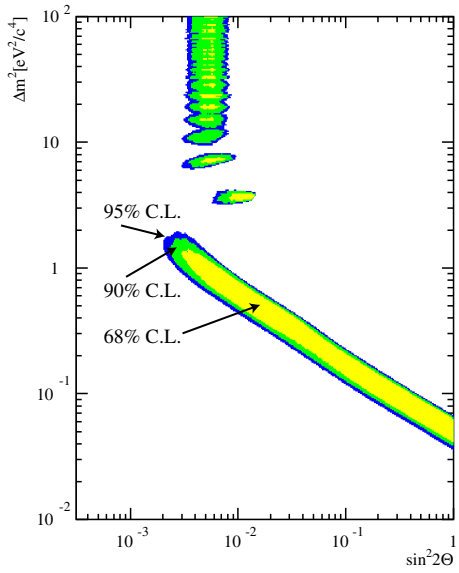

Figure 1.4: LSND regions of various confidence for oscillation parameters under a two-neutrino oscillation approximation, from Ref. [31]. The horizontal axis shows $\sin^2 2\theta$ and the vertical axis shows Δm^2.

$\bar{\nu}_e$ appearances in ν_μ and $\bar{\nu}_\mu$ beams during separate periods via a charged-current quasi-elastic interaction. The detector location is chosen so that L/E is similar to that of LSND. In the $\nu_\mu \to \nu_e$ search, MiniBooNE found no evidence for an excess of ν_e candidate events at reconstructed neutrino energy $E_\nu^{QE} > 475$ MeV [33]. A joint analysis of LSND and MiniBooNE, assuming the oscillations of neutrinos and antineutrinos are the same, excludes at 98% C.L. two-neutrino $\nu_\mu \to \nu_e$ oscillations as an explanation of the LSND anomaly. On the other hand, in the $\bar{\nu}_\mu \to \bar{\nu}_e$ search, MiniBooNE found an excess of $\bar{\nu}_e$ events at $E_\nu^{QE} > 475$ MeV and the probability with the background-only hypothesis is 0.5% [34]. The data is consistent with $\bar{\nu}_\mu \to \bar{\nu}_e$ oscillations in the Δm^2 range of $0.1 - 1.0$ eV^2 and agree with the two-neutrino $\bar{\nu}_\mu \to \bar{\nu}_e$ oscillation interpretation of LSND. To explain these results including a possible CP violation, hypotheses with two or more sterile neutrinos are discussed as well as one-sterile $(3+1)$ one [35].

1.3 Limits on neutrino mass

From precisely measured mass differences of neutrinos by neutrino oscillation experiments, one can set a lower limit on the absolute mass of the heaviest neutrino mass eigenstate:

$$\max_i m_i > \sqrt{\Delta m^2_{\rm atm}} \simeq 0.05 \text{ eV}. \tag{1.21}$$

Recent cosmological observations, including the precise observation of the cosmic microwave

background (CMB) anisotropies by the Wilkinson Microwave Anisotropy Probe (WMAP) satellite, and the results of a new generation of very deep galaxy redshift surveys, constrain the sum of the masses of the three neutrino mass eigenstates

$$\sum_i m_i < 0.17 - 2.0 \text{ eV at } 95\% \text{ C.L.} \tag{1.22}$$

depending on the data included and the assumed cosmological model [36, 37].

On the other hand, there are some experiments obtaining direct limits on absolute neutrino masses. Measuring the endpoint of the energy spectrum of electrons in tritium beta decay, Mainz [38] and Troitsk [39] set upper limits on the effective mass of the electron neutrino, where the effective mass of a flavor eigenstate neutrino is defined as

$$m^2_{\nu_\alpha} \equiv \sum_i |U_{\alpha i}|^2 m_i^2. \tag{1.23}$$

The best limit comes from the Mainz experiment [38]: $m_{\nu_e} < 2.3$ eV at 95% C.L.

As for the limits on the muon and tau neutrinos, measurements using π^+ and τ^- decays yield $m_{\nu_\mu} < 0.19$ MeV at 90% C.L. [40] and $m_{\nu_\tau} < 18.2$ MeV at 95% C.L. [41].

1.4 Astrophysics at Super-Kamiokande

In this section, two subjects of astrophysics, supernova relic neutrino search and GUT monopole search, at Super-Kamiokande (SK) and the relation of them to nuclear de-excitation gamma-rays are outlined.

1.4.1 Supernova relic neutrino search

Physics background

Core collapse supernovae emit energy of $\mathcal{O}(10^{53})$ ergs, about 99% emerging as neutrinos. All the past supernovae since the beginning of gravitational collapses should together have created supernova "relic" neutrinos (SRN) or also referred to as diffuse supernova neutrino background (DSNB). The SRN arriving at the Earth is the superposition of neutrinos from each supernova explosion. Taking into account the redshift of neutrinos by the expansion of the universe, the SRN spectrum at the Earth is

$$\frac{d\phi_\nu}{dE_\nu} = \frac{c}{H_0}\int_0^{z_{max}} R_{SN}(z)\frac{dN_\nu(E'_\nu)}{dE'_\nu}\frac{dz}{\sqrt{\Omega_m(1+z)^3+\Omega_\Lambda}} \tag{1.24}$$

where c is the speed of light in vacuum, z is the redshift parameter, and $E'_\nu = (1+z)E_\nu$ is the energy of neutrinos at z, where E_ν is the current one. $R_{SN}(z)$ represents the supernova rate (SNR) per comoving volume at z:

$$R_{SN}(z) \simeq R_{SN}(0)(1+z)^\beta \tag{1.25}$$

where $R_{SN}(0) \sim \mathcal{O}(10^{-4})$ Mpc^{-3}yr^{-1} and $\beta \simeq 3$ for $0 \leq z \lesssim 1$ [42]. The rate flattens at larger z. dN_ν/dE_ν is the neutrino spectrum per one supernova explosion. $H_0 \simeq 70$ km s^{-1}Mpc^{-1}, $\Omega_m \simeq 0.3$ and $\Omega_\lambda \simeq 0.7$ denote the Hubble constant and the current fractions of matter and dark energy in the cosmic energy density in the standard ΛCDM cosmology, respectively. $z_{max} \simeq 4.5$ means the beginning of gravitational collapses and results of Eq. (1.24) depend weakly on z_{max} for $z_{max} \gtrsim 3$ [43].

SRN search at Super-Kamiokande

SRN interacts with a water molecule via the following four interactions:

1. Inverse beta decay — $\bar{\nu}_e + p\ (\text{free}) \rightarrow n + e^+$,
2. Electron elastic scattering — $\nu + e^- \rightarrow \nu + e^-$,
3. Charged-current interaction with oxygen — $\nu_e + {}^{16}\text{O} \rightarrow e^- + {}^{16}\text{F}$, $\bar{\nu}_e + {}^{16}\text{O} \rightarrow e^+ + {}^{16}\text{N}$,
4. Neutral-current interaction with oxygen — $\nu_x + {}^{16}\text{O} \rightarrow \nu_x + \gamma + X$,

Figure 1.5 shows the cross sections of $\bar{\nu}_e p$, ν^{16}O and νe in the relevant energy region for the SRN analysis. At 10 MeV, the cross section of the inverse beta decay is two orders of magnitude larger than those of the electron elastic scattering and the charged-current interaction with an oxygen nucleus. Also, gamma-rays from the NC inelastic interaction with an oxygen nucleus are less than 10 MeV, which is below our analysis threshold. Figure 1.6 shows the expected event rate of each interaction mode for a constant supernova rate model [44]. Since the interaction modes other than inverse beta decay of $\bar{\nu}_e$ are negligibly small for the SRN search at SK, only the inverse beta decay is used for the analysis. In 2003, the Super-Kamiokande experiment provides the world's best SRN flux limit of 1.2 cm^{-2} s^{-1} $\bar{\nu}_e$ by using the inverse beta decay and the result excludes some theoretical models [45].

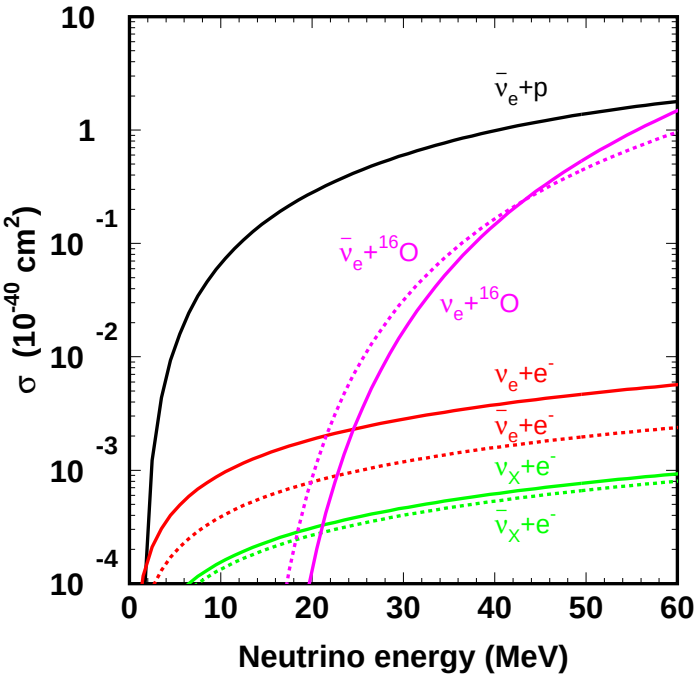

Figure 1.5: Comparison of cross section of each interaction.

Figure 1.7 shows the predicted $\bar{\nu}_e$ spectra for several theoretical SRN models with those for relevant backgrounds superimposed. Currently, the energy region below 16 MeV is not used for the SRN analysis because nuclear spallation events induced by cosmic ray muons (CRM) are dominant in this region even though we reduce the solar neutrinos using the information of neutrino directions. Also, atmospheric neutrino fluxes are much higher than SRN above several tens of MeV. Thus the search window for SRN at SK is from 16 to several tens of MeV at most.

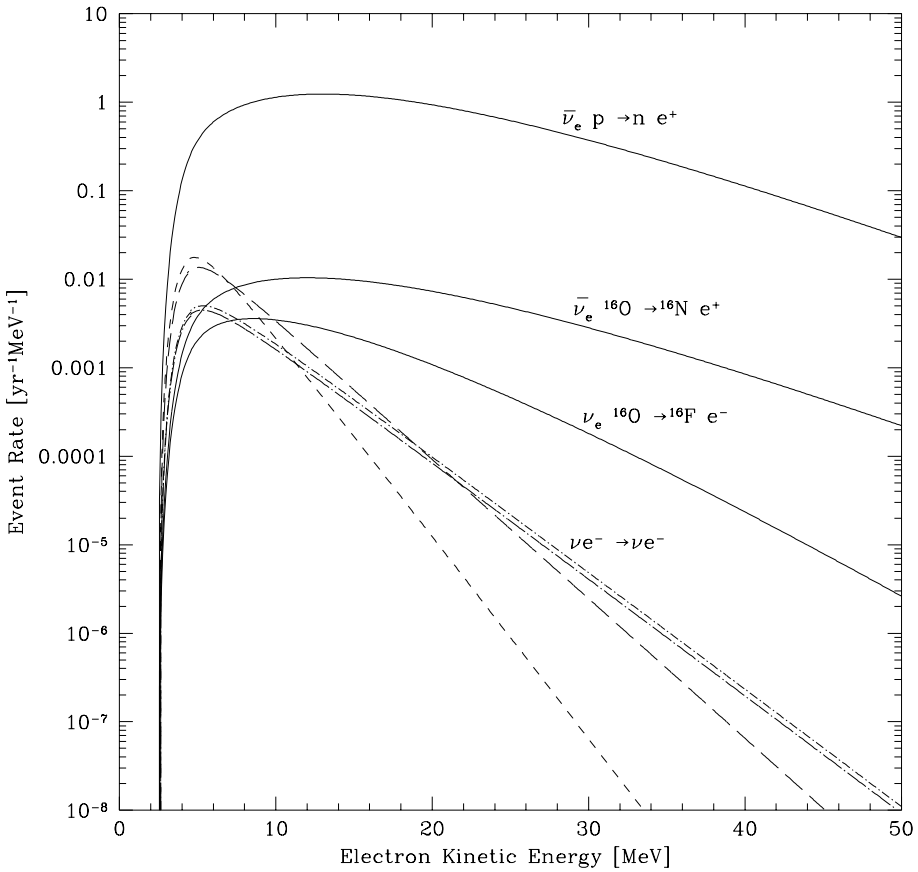

Figure 1.6: Expected event rate of each neutrino interaction mode inside the 22500 m^3 SK fiducial volume are shown for a constant supernova rate model [44]. The event rate of inverse beta decay is higher than those of other modes by two orders of magnitude.

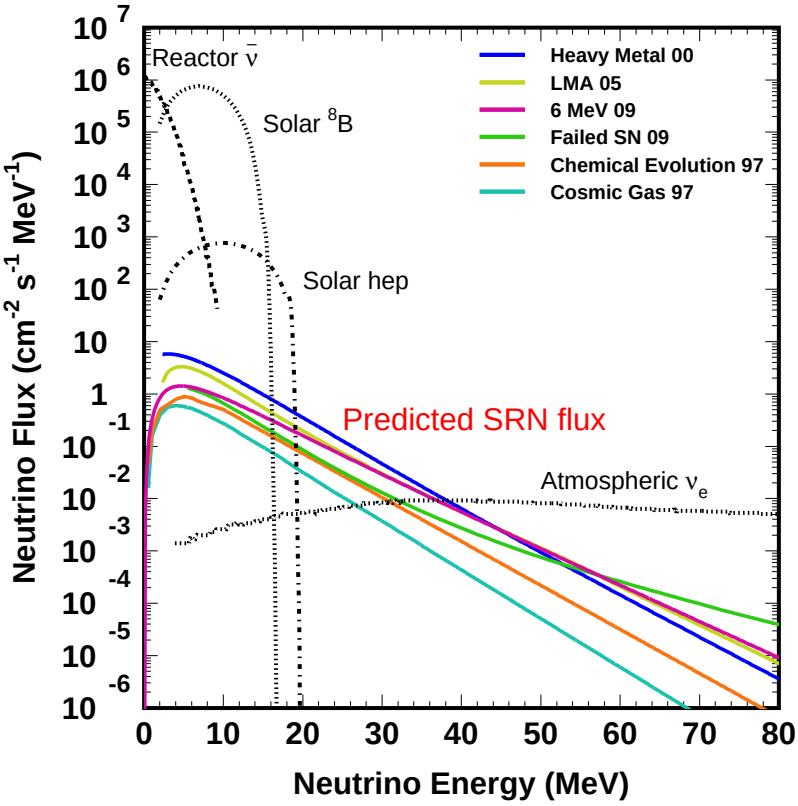

Figure 1.7: Solid lines show the predicted SRN spectra of several SRN models [46–51]. Dotted or dashed lines represent background neutrinos: the reactor $\bar{\nu}_e$, the solar ^{8}B and hep ν_e, and the atmospheric ν_e.

The SRN analysis result of SK-I data is shown in Fig. 1.8. The dots with error bars show the energy spectrum of data final sample, and the histogram shows the result of a Monte Carlo simulation of atmospheric neutrinos. The peak around 40 MeV comes from the decay electrons of muons produced by the charged-current interactions of atmospheric ν_μ and $\bar{\nu}_\mu$, which is shown by the dotted line. Here, parent muons ($\mu^\pm$) have momenta less than the Cherenkov threshold, which are not detected, and only the decay electrons ($e^\pm$) are observed. The dashed line, which extends to above the upper threshold, shows the ν_e and $\bar{\nu}_e$ components. Here the low momentum electrons ($e^\pm$) produced by the charged-current interaction of ν_e and $\bar{\nu}_e$ are directly observed. As can be seen, the shown data is almost accounted for by the atmospheric neutrino simulation. According to Fig. 1.6, most of the SRN signal exists in the low energy region of below about 20 MeV. The SRN analysis including constraining the flux limit is largely dependent on how well

we estimate the irreducible backgrounds in the low energy region and to what extent we lower the analysis threshold. Recently, the combined analysis of SK-I/II/III (2853 live days of data) was conducted, where the sensitivity was improved compared to the 2003 SK result and also the energy threshold was lowered from 18 to 16 MeV [52].

In the future, we are planning to ultimately lower the threshold to 10 MeV. There, nuclear de-excitation gamma-rays induced by neutral-current interactions of atmospheric neutrinos will be dominant background as well as CRM-induced nuclear spallation events.

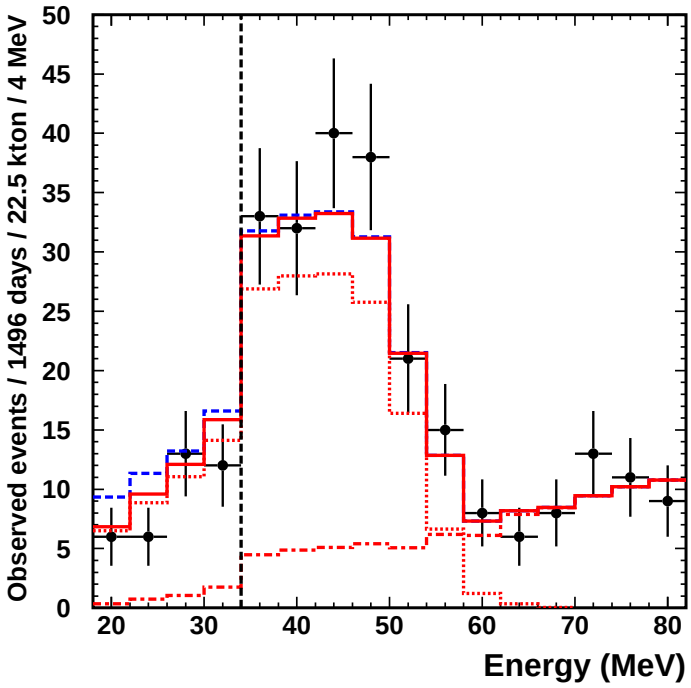

Figure 1.8: Energy spectra of SK-I data and backgrounds of atmospheric neutrinos. Dots with error bars are data and the solid histogram is best fit with an atmospheric neutrino MC. The dotted histogram which has a peak around 40 MeV is the ν_μ and $\bar{\nu}_\mu$ components of atmospheric neutrinos (electrons from the decay of invisible muons) and the dashed-dotted one, which extends to above the upper threshold, is the ν_e and $\bar{\nu}_e$ components. The dashed line shows the sum of the total background and the 90% C.L. upper limit on the SRN flux signal. The black dotted line at 34 MeV is a boundary line where the efficiency changes discontinuously due to the spallation event cut.

1.4.2 GUT monopole search

Physics background

Grand Unified Theories (GUT) predict the production of superheavy magnetic monopoles (GUT monopoles) in the very early Universe [53, 54]. GUT monopoles are predicted to have appeared as topological defects at the phase transition of vacuum, where GUT gauge group spontaneously broke to leave the U(1) of electromagnetism. Monopoles are non-relativistic at temperatures below the phase transition in which they are produced. If the monopole-antimonopole annihilation were negligible, their number density would decrease $n_M(t) \propto a^{-3}(t)$ and the monopole-entropy ratio would remain constant. If we calculated in this way the mass density of monopoles today, considering the scale 10^{16} GeV is typical for GUTs, it would exceed the critical density of the universe $\rho_c \sim 10^{-5}$ GeV cm^{-3} by many orders of magnitude. This result does not change qualitatively if we take into account the monopole-antimonopole annihilation. Even though the inflationary universe scenario [55, 56] overcomes this problem, the monopole flux in the universe depends on some parameters such as monopole mass and the reheating temperature, and therefore the large uncertainty remains. In fact, due to the wide variety of elementary particle models, several models coexist with the Parker limit ($\sim 10^{-15}$ cm^{-2} s^{-1} sr^{-1}) [57–60], and a flux in that range can be relatively easily detected by underground experiments.

Arafune *et al.* [61] pointed out copious low energy neutrinos might be emitted when monopoles accumulating inside the Sun catalyze proton decay,

$$p \to (\rho^0, \omega, \eta, K^+, \cdots) + e^+(\text{or } \mu^+) \tag{1.26}$$

along their paths with cross sections typical of strong interactions via the Callan-Rubakov process [62,63]. When decay mesons produced by the process above subsequently decay into positive pions, ($(\rho^0, \omega, \eta, K^+, \cdots) \to \pi^+$), ν_e, ν_μ and $\bar{\nu}_\mu$ are produced by the reactions,

$$\pi^+ \to \mu^+ + \nu_\mu \tag{1.27}$$

$$\mu^+ \to e^+ + \nu_e + \bar{\nu}_\mu \tag{1.28}$$

After undergoing neutrino oscillation, all neutrino species are present when they arrive at the Earth, and such low energy neutrino events can be detected by a water Cherenkov detector.

GUT monopole search at Super-Kamiokande

Monopole-induced neutrinos include all six types, and so for the monopole-induced neutrino search both electron elastic scattering, $\nu_x(\bar{\nu}_x) + e^- \to \nu_x(\bar{\nu}_x) + e^-$, and inverse beta decay, $\bar{\nu}_e + p \to e^+ + n$, were assumed to contribute. Figure 1.9 shows the expected energy spectra and solar direction distributions of recoil electrons and inverse beta positrons at SK. As in the case of SRN search, the event rate of the inverse beta decay is much higher, but since the monopole-induced neutrinos only come from the solar direction, the electron elastic scattering events, which are highly correlated with neutrino directions, can be used to search the signal neutrinos [64].

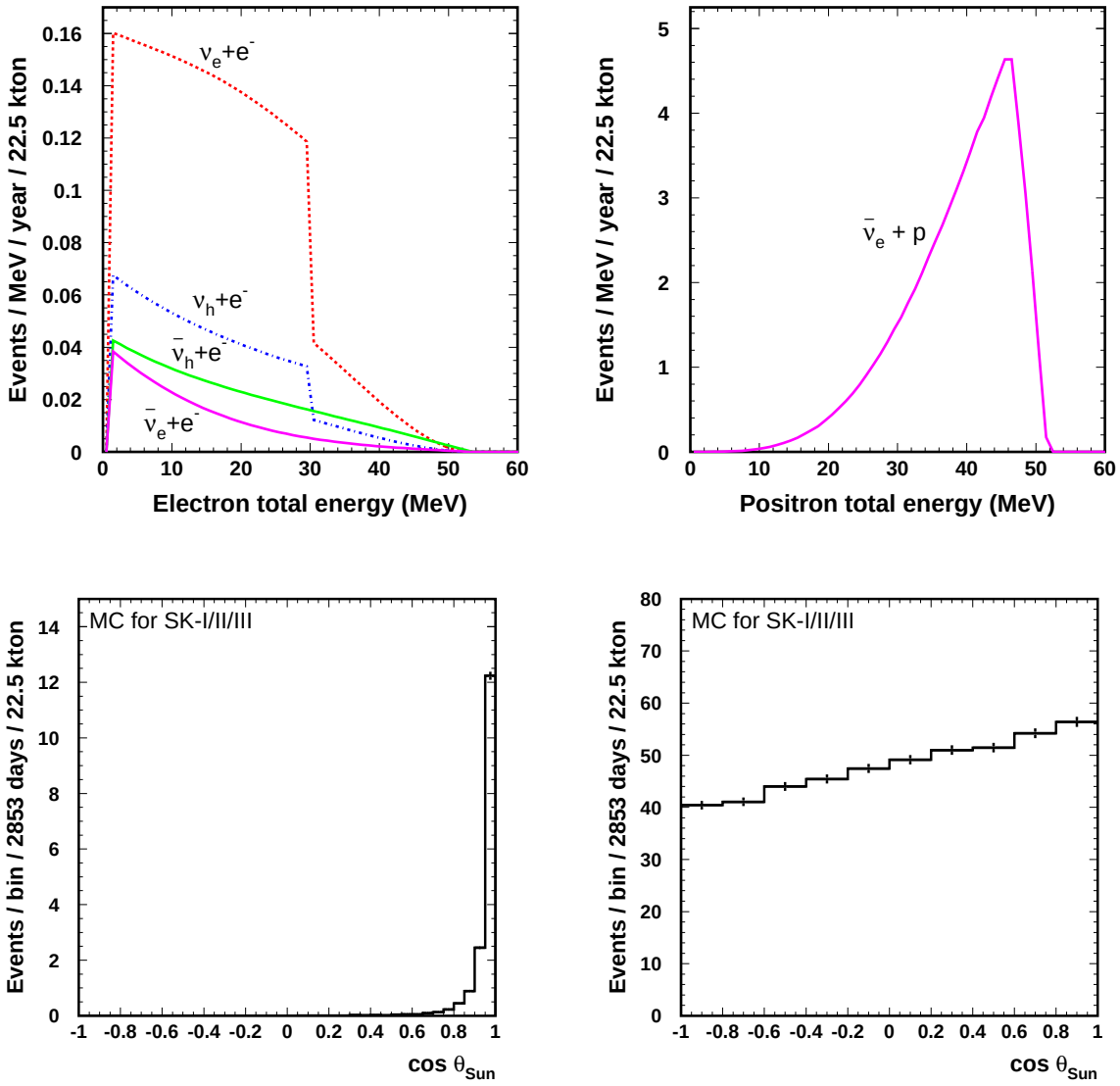

Figure 1.9: Expected energy spectra of recoil electron (upper left) and inverse beta positron (upper right) and solar direction distributions of recoil electron (lower left) and inverse beta positron (lower right) in SK assuming neutrino flux of 3.0×10^2 cm^{-2}s^{-1}. The energy spectra are described analytically without energy resolution included. The discontinuity at 29.79 MeV of some spectra of recoil electron comes from neutrinos from pion two-body decays. μ and τ components are collectively denoted as h since these two flavors of neutrinos have identical cross sections for electron scattering. The solar direction distributions include the detection efficiency of various cuts.

Figure 1.10 shows the solar direction distributions of the final data sample of SK-I/II/III (317 events) and the fitting results of the 90% C.L. limit + background and those by only background. We have not found any evidence of GUT monopoles and given a monopole flux limit of $F_M(\sigma_0/1mb) < 1 \times 10^{-23}(\beta_M/10^{-3})^2$ cm^{-2} s^{-1} sr^{-1} at 90% C.L., where β_M is the monopole velocity in units of the speed of light and σ_0 is the catalysis cross section at $\beta_M = 1$ [64]. As in the case of the SRN search, most events come from atmospheric neutrinos and a precise estimation of them leads to a great improvement of this analysis.

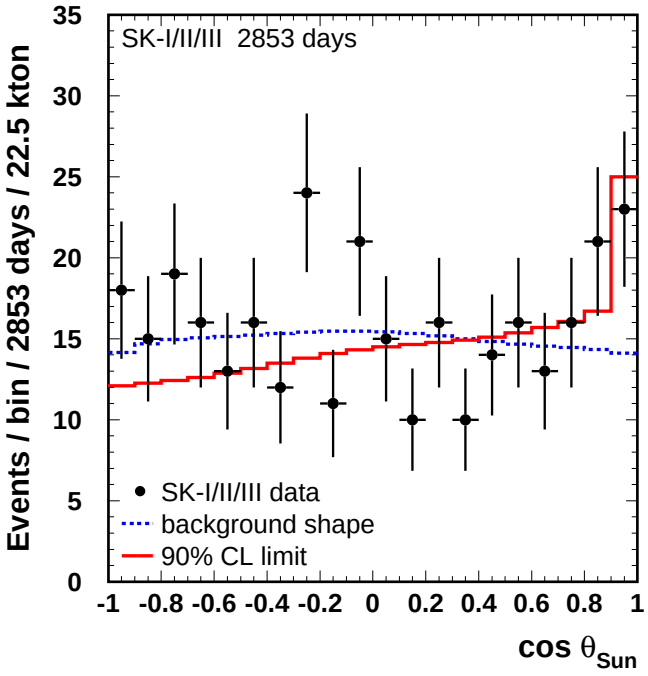

Figure 1.10: The points with error bars show the angular distribution with respect to the expected neutrino direction from the Sun for the data final sample. The solid and dashed histograms represent the fitting results of the 90% C.L. limit + background and only background, respectively.

1.5 Synopsis of thesis

This thesis aims to study the neutral-current nuclear de-excitation gamma-rays induced by the T2K beam neutrinos, whose peak energy $E_\nu \simeq 600$ MeV is similar to those of atmospheric neutrinos which are a major source of backgrounds for low energy analyses described in this chapter. Also, the study of neutral-current events at T2K would give information of a new neutrino oscillation channel, such as $\nu_\mu \rightarrow \nu_s$ oscillation. In Chapters 2 and 3, the T2K experiment and the Super-Kamiokande (SK) detector are overviewed. The event reconstruction and detector calibration at SK are described in Chapters 4 and 5. Chapter 6 details the Monte Carlo (MC) simulation of T2K beam neutrino events. Event reduction and its result are shown in Chapters 7 and 8, respectively. In Chapter 9, the data is compared to the prediction with the systematic uncertainties. Also, the experiment's sensitivities to two independent physics − sterile neutrino search and future astrophysics analyses at SK − are evaluated. The conclusion is given in Chapter 10.

Chapter 2

The T2K Experiment

2.1 T2K overview

The Tokai-to-Kamioka (T2K) experiment [19] is a long baseline neutrino oscillation experiment that began physics data-taking in January 2010, which uses a high intensity muon neutrino beam produced at Japan Proton Accelerator Research Complex (J-PARC) and directed toward Super-Kamiokande (SK), 295 km away (Fig. 2.1).

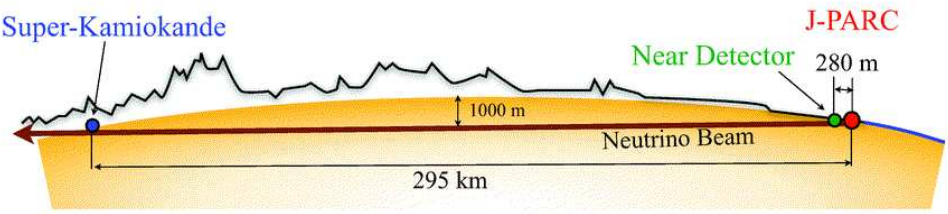

Figure 2.1: T2K overview.

The experiment has two main purposes. One is to determine the neutrino mixing angle, θ_{13}, by searching for ν_e appearance [24], and the other is to measure oscillation parameters in the atmospheric sector with a precision of $\delta(\Delta m^2_{atm}) \sim 10^{-4}$ eV^2 and $\delta(\sin^2 2\theta_{23}) \sim 0.01$ by measuring ν_μ disappearance [22].

T2K is the first long baseline neutrino experiment which adopts the off-axis method to obtain the narrow-band neutrino beam [65]. The off-axis angle is defined as the angle of the neutrino beam direction with respect to the baseline from the proton target to the far detector. The neutrino beam energy is determined by the pion energy and the off-axis angle as

$$E_\nu = \frac{m_\pi^2 - m_\mu^2}{2(E_\pi - p_\pi \cos\theta)} \tag{2.1}$$

where E_ν is the energy of the outgoing ν_μ, m_π and m_μ are the masses of π^+ and μ^+, respectively, E_π and p_π are the energy and momentum of the π^+, and θ denotes the off-axis angle.

The off-axis angle is set to 2.5° so that a peak energy corresponds to the first oscillation maximum $E_\nu = |\Delta m^2_{23}|L/1.24 \simeq 0.6$ GeV at the far detector (see Eq.(1.15)) and at the same time the background against ν_e appearance detection is minimized. Figure 2.2 shows the dependence of the neutrino energy spectrum on the off-axis angle.

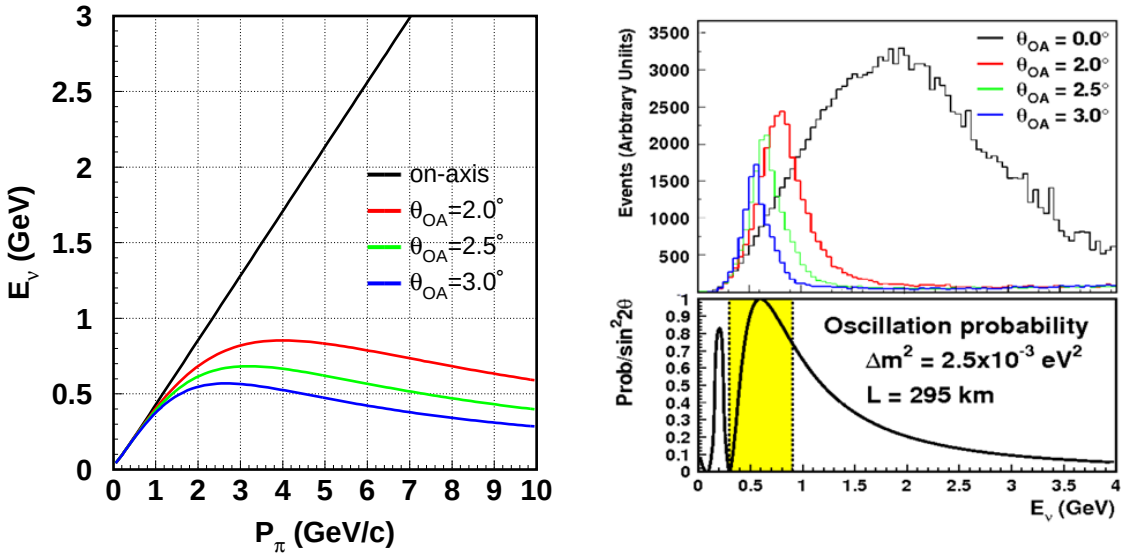

Figure 2.2: The off-axis angle dependence of the neutrino beam energy. Shown are a two-dimensional plot of neutrino beam energy versus pion energy (left) and neutrino energy spectra expected at SK with different off-axis angles, together with the probability that ν_μ oscillates into other flavor eigenstates, the value being normalized by its maximum peak (right).

In the rest of this chapter, neutrino beam line and near detectors are outlined. The far detector, SK, is detailed in Chapter 3.

2.1.1 Neutrino production

J-PARC accelerator

J-PARC (Fig. 2.3), located in Tokai, Ibaraki Prefecture, consists of a linear accelerator (LINAC), a rapid-cycling synchrotron (RCS) and the main ring (MR). The LINAC accelerates hydrogen with negative charge (H^-) up to 400 MeV (181 MeV as of March 2011) and the negative hydrogen is then converted to protons by charge-stripping foils at the RCS injection. The RCS accelerates them up to 3 GeV with a 25 Hz cycle and ultimately, the MR accelerates the proton beam injected from the RCS up to 30 − 50 GeV with an about 0.3 Hz cycle [66],

designed to produce a beam power of 0.75 MW at 3.3×10^{14} protons per pulse (ppp). In the extraction for the neutrino beamline, eight circulation proton bunches with the 581 ns interval are extracted within a single turn of 5.2 μs by a set of five kicker magnets[1)]. The time structure of the extracted proton beam is necessary to discriminate beam-unrelated background in each neutrino detector. Table 2.1 summarizes the machine parameters of the MR.

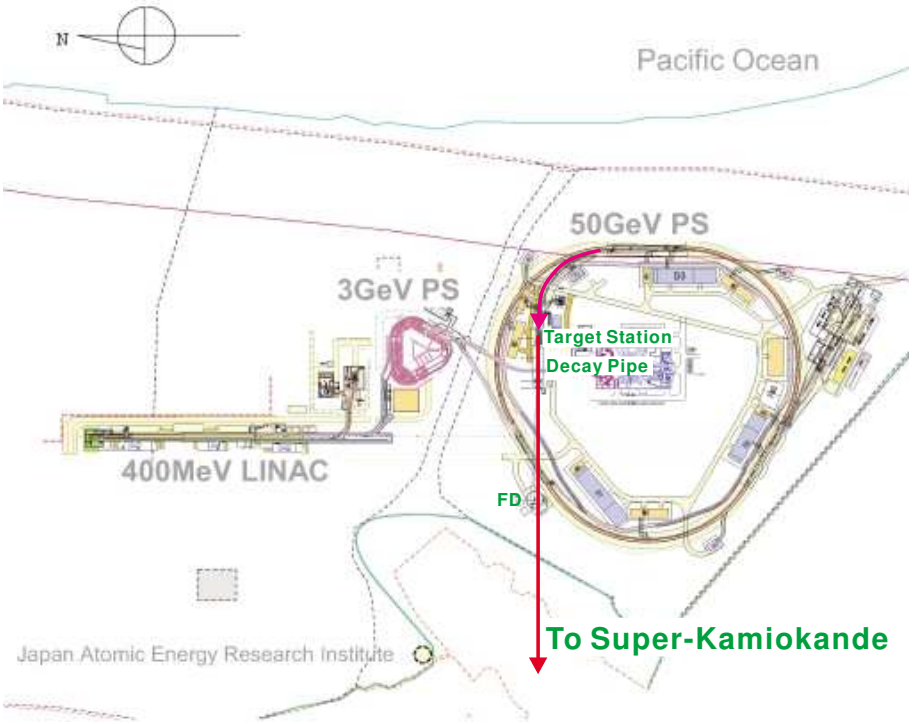

Figure 2.3: Overview of the J-PARC facility: LINAC (181 MeV at present), RCS, and MR (30 GeV PS at present). *Arrows*: The upper arrow shows the proton beam direction and the lower one shows the neutrino beam direction.

Neutrino beamline

In the neutrino beamline (Fig. 2.4), the extracted proton beam is bent toward the direction of Kamioka by 80.7°, with a 104.4 m of curvature, using superconducting combined-function magnets. Then, using normal conducting magnets the beam is guided and focused onto the graphite target while it is directed downward by 3.637° with respect to the horizontal plane.

At the graphite target, which is 2.6 cm in diameter and 90 cm long ($1.9\lambda_{\rm int}$), the beam protons generate secondary pions. These pions are collected and focused by three magnetic horns on the

[1)] Until June. 2010, six proton bunches are extracted.

Table 2.1: Machine parameters of the MR.

Circumference	1567.5 m
Beam kinetic energy	50 GeV
	(30 GeV as of March 2011)
Beam power	750 kW
	(145 kW as of March 2011)
Protons per spill	3.3×10^{14}
	(9×10^{13} as of March 2011)
Spill cycle	0.28 Hz
Spill width	5.2 μs ($= 1567.5m/c$)
Number of bunches	8/spill
	(6/spill until June 2010)
Bunch full width	10-20 ns (56 ns @ 750 kW)
Bunch interval	581 ns

beamline with operation currents of 250 kA. The focused pions then decay in flight inside a 96 m long decay tunnel, filled with 1 atm helium gas instead of air to prevent pion absorption. They mainly decay into muons and muon neutrinos. The hadrons, as well as muons below about 5 GeV/c, are stopped by the beam dump, which sits at the end of the decay tunnel. Any muons with higher momenta passing through the beam dump are monitored on a spill by spill basis to characterize the neutrino beam.

Beamline simulation for neutrino flux estimation

The neutrino flux is predicted by a Monte Carlo simulation based on experimental data. Hadron production by 30 GeV protons on the graphite target was measured by a dedicated experiment, NA61/SHINE [67], which covers most of the phase space relevant for T2K.

In the beam Monte Carlo (MC) simulation, with the detailed geometry of the beamline, protons with a kinetic energy of 30 GeV are injected into the graphite target and then secondary particles are generated and focused by the horn magnets. The secondaries and un-interacted protons are tracked until they decay into neutrinos. Pion production from the primary interaction of the 30 GeV proton with carbon is simulated based on NA61/SHINE data, typically with 5-10% uncertainties. Pions produced outside the experimentally measured phase space or other hadronic interactions such as kaon production inside the target are simulated[2)] by FLUKA [68]. The uncertainties for the pion production in FLUKA are estimated to be 50% and those for kaon production are estimated to range from 15-100% based on existing data [69]. Particle propagation

[2)] In addition to the simulation, they are also constrained with other external data.

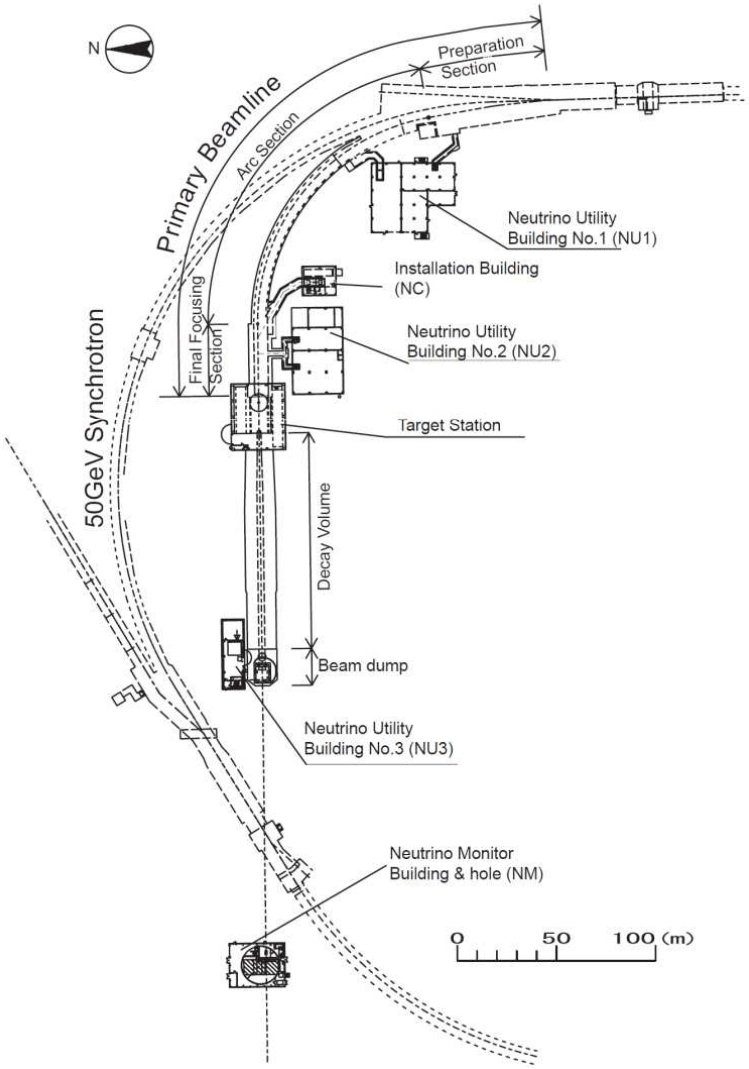

Figure 2.4: Neutrino beamline.

outside the target, *i.e.*, magnetic horns, target hall, decay volume and beam dump, are simulated using GEANT3/GCALOR [70] with the interaction cross sections tuned to experimental data.

The tracks of neutrinos in the beam MC are then extrapolated to the near and far detectors, providing the expected fluxes at both detector sites. Figure 2.5 shows the obtained predicted fluxes.

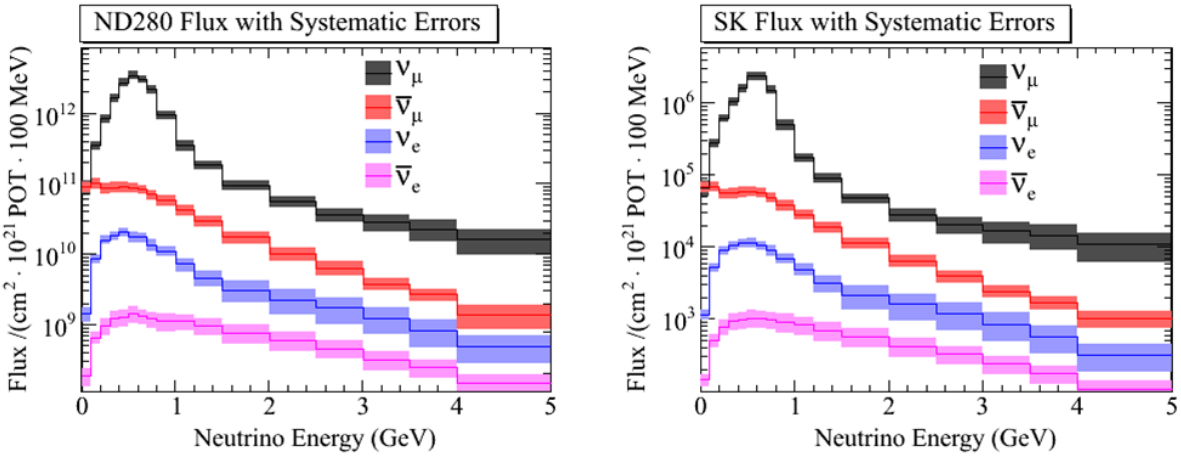

Figure 2.5: The predicted fluxes at the near detector site (left) and far detector site (right).

Time synchronization

In the T2K experiment, the Global Positioning System (GPS) provides a means for synchronization of clocks within $\mathcal{O}(100)$ ns accuracy at the near and far detector sites. At both sites, two independent GPS receivers, which are connected to antenna modules, output a one-pulse-per-second (1PPS) signal whose leading edge is aligned with the second transitions in the Coordinated Universal Time (UTC) to within $\mathcal{O}(10)$ ns.

At both sites, there is a custom electronics board called Local Time Clock (LTC) connected to GPS receivers to time stamp a beam spill trigger or an event trigger. Commercial rubidium (Rb) clocks are used as the LTC time base and one of the Rb clocks was synchronized using the 1PPS from the GPS system. In this way, timestamps between sites are synchronized within $\mathcal{O}(100)$ ns. In case of temporary loss of GPS signals, the Rb clock provides a stable time base for the system.

When the timing signal synchronized with the MR extraction is received, it is recorded to an LTC module at J-PARC. The LTC module counts the accumulated number of received signals as the spill number. This time information and the spill number are transported between sites for the consistency check.

2.1.2 Near detector complex

The energy spectrum, flavor and interaction rates of the T2K neutrino beam are measured by a set of detectors located 280 m downstream the proton target, where the spatial spread of the neutrino beam is about 5 meters at 1 σ. The information is then used to predict the neutrino interactions at SK.

As shown in Fig. 2.6, the near detector complex [19] is housed in a pit inside the ND280 hall, hosting two detectors − an on-axis detector (INGRID) and off-axis detector (ND280).

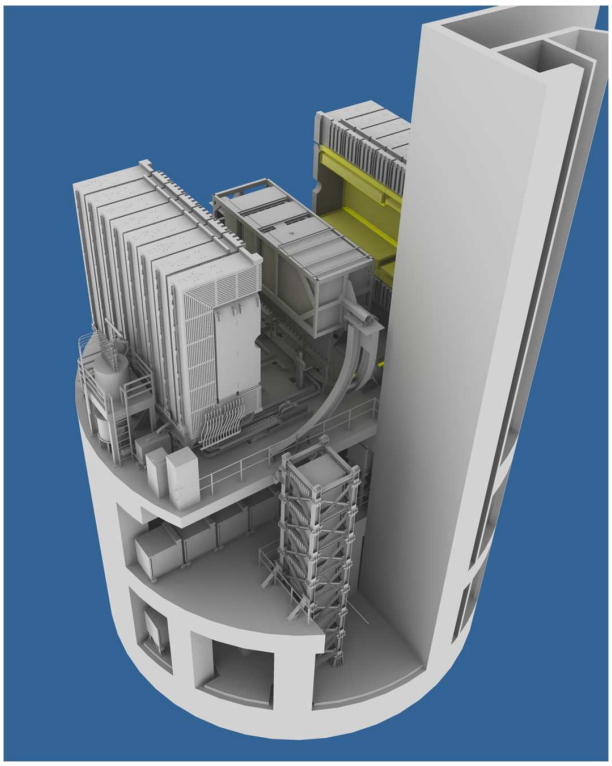

Figure 2.6: ND280 detector complex. Horizontal INGRID modules are located on the level below, and the vertical ones span the bottom two levels. The off-axis detector and the magnet are located on the upper level.

On-axis detector (INGRID)

As described above, the neutrino energy spectrum on an off-axis is sensitive to the off-axis angle. Therefore, it is necessary to monitor the beam direction precisely. Also, we need to ensure the stability of the beam neutrino production. Interactive Neutrino GRID (INGRID) was developed to directly monitor the direction and intensity of the neutrino beam.

The detector consists of 14 identical modules arranged as a cross of two identical groups along the horizontal and vertical axis in 10 meters by 10 meters, and two additional separate modules located at off-axis directions outside the main cross as shown in Fig. 2.7. The modules consist of a sandwich structure of nine iron plates 6.5 cm thick and eleven tracking scintillator planes as shown in Fig. 2.8. INGRID measures the rate of muon events from neutrino charged-current interactions in each module with high statistics and reconstructs the beam profile center within 0.4 mrad.

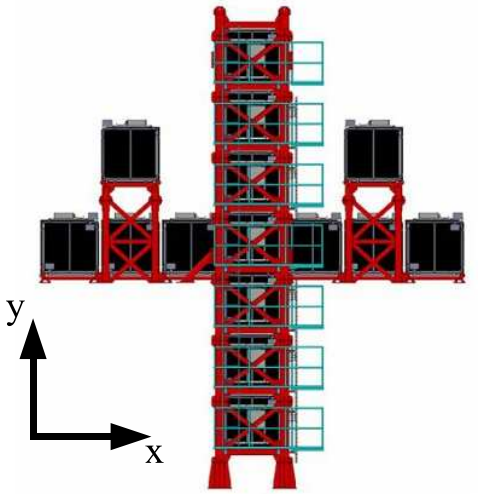

Figure 2.7: INGRID on-axis detector. Transverse cross section is 10 m $\times$ 10 m, and the center of the main cross is located at the expected neutrino beam center.

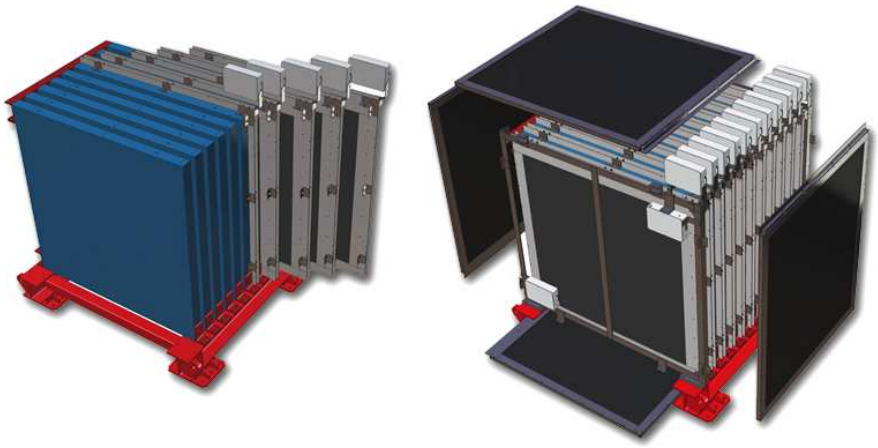

Figure 2.8: An INGRID module: the tracking planes and iron plates (left), and veto planes (right).

Off-axis detector (ND280)

A large fine grained off-axis detector (ND280) serves to measure the flux and energy spectrum of ν_μ and ν_e contamination in the direction of the far detector as well as measuring rates for exclusive neutrino reactions.

Fig. 2.9 shows an exploded view of ND280 with the beam direction. ND280 consists of the following several detectors:

- Magnet

  ND280 uses the ex-UA1 magnet, which is composed of aluminum coils and iron yoke. It generates a horizontal magnetic field of 0.2 T.

- Pi-Zero Detector (P0D)

  The P0D consists of tracking planes composed of scintillating bars alternating with lead foil, and serves as a detector for the π^0 generated by the single-pion neutral-current interaction, which is the major background for the ν_e appearance search at SK. It measures the interaction rate and the π^0 momentum distribution.

- Electromagnetic Calorimeter (ECAL)

  ECAL is arranged to surround the P0D, and measures gamma-rays from π^0 decays in ND280 which do not convert in the inner detectors.

- Tracker

  The tracker consists of three large volume Time Projection Chambers (TPCs) [71] interleaved with two Fine Grained tracking Detectors (FGDs). This tracker system measures each event rate of ν_μ and ν_e by reconstructing the sign and momentum of charged particles from the track curvature and identifying particles with the dE/dx profile.

- Side Muon Range Detector (SMRD)

  The magnet yoke is instrumented with plastic scintillators as an SMRD. It measures muons which exit the side of the ND280. SMRD can also serve as a veto for incoming events from outside the detector.

An inclusive ν_μ CC measurement in the off-axis near detector is used to constrain the expected event rate at SK.

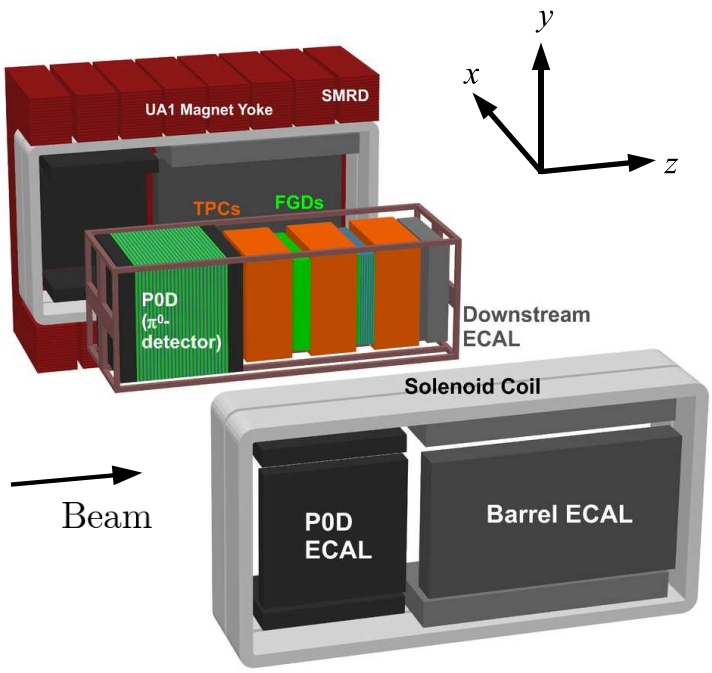

Figure 2.9: An exploded view of the off-axis near detector.

Chapter 3

Super-Kamiokande Detector

Super-Kamiokande (SK) [72] is an imaging water Cherenkov detector. The detector consists of a cylindrical stainless water tank 39.3 meters in diameter, 41.4 meters in height, filled with 50,000 m^3 of ultrapure water (Fig. 3.1). Photomultiplier tubes (PMT) are arranged equally-spaced inside the detector and detect Cherenkov light emitted by charged particles ($e^{\pm}$, $\mu^{\pm}$, $\pi^{\pm}$, p, etc) traveling through the water. This detector is located 1,000 meters, or 2,700 meter water equivalent (m.w.e) beneath the summit of Mt. Ikenoyama[1)] so that the intensity of cosmic ray muons is reduced by five orders of magnitude compared to the ground level, and the muon rate for the entire detector volume is 2 Hz.

SK started observation in April 1996, and the scientific goals include searches for nucleon decays inside the water tank and studies of neutrinos from various sources: atmosphere, the Sun and astrophysical sources (supernovae, gamma-ray bursts, dark matter, GUT monopoles, etc) as well as artificial neutrino beams (K2K, T2K).

In this chapter, the detection principle of SK, the detector components and the data acquisition system are outlined.

3.1 Detection principle

3.1.1 Cherenkov radiation

If a charged particle moves in a dielectric medium faster than the phase velocity of light in the medium, an electromagnetic shock wave known as Cherenkov radiation arises. As shown in Fig. 3.2, a coherent wavefront forms a cone with the opening angle of θ_{Ch} called Cherenkov opening angle with respect to the trajectory of the particle. θ_{Ch} is geometrically determined by the ratio of the particle speed to the phase velocity of light in the medium:

[1)] SK is on the border between Gifu and Toyama prefectures and 36°25′32.6”N, 137°18′37.1”E at geographic coordinates, which is given by a GPS survey for long-baseline neutrino oscillation experiments [73].

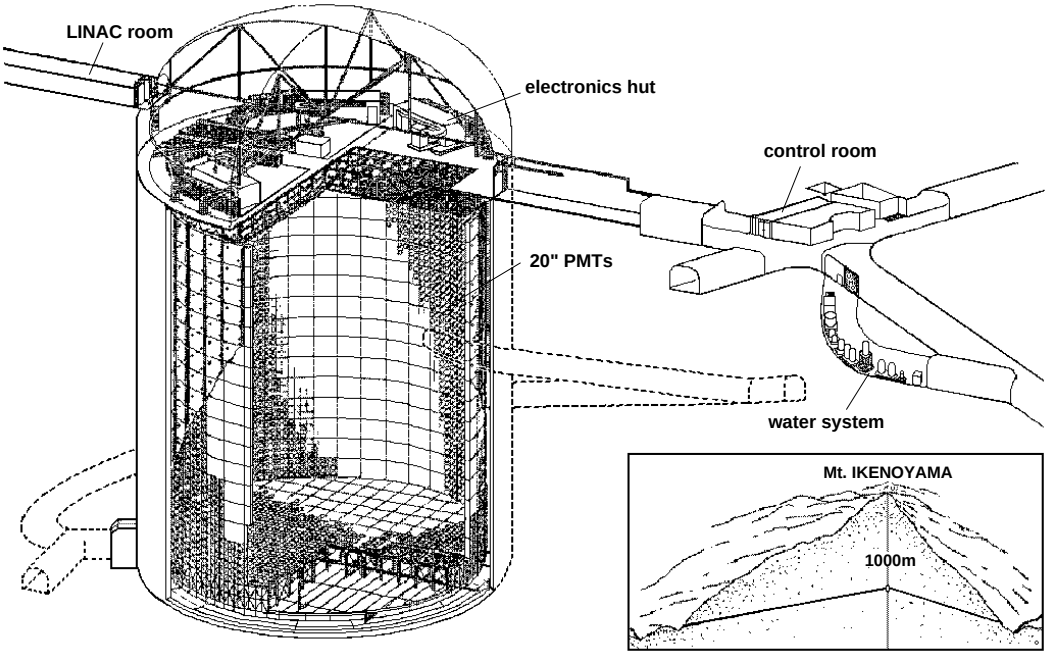

Figure 3.1: Overview of the Super-Kamiokande detector

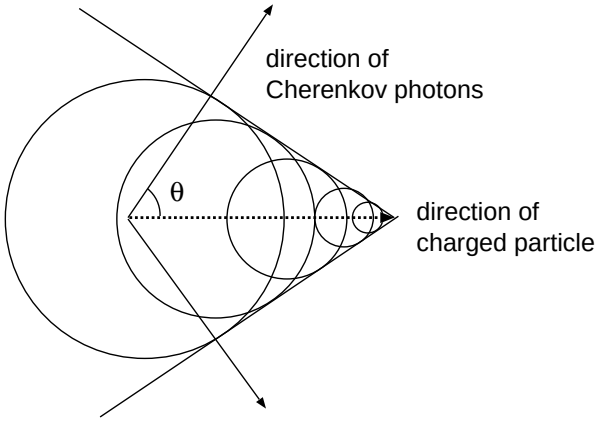

Figure 3.2: Schematic diagram of Cherenkov radiation.

$$\cos\theta_{Ch} = \frac{1}{n\beta}. \tag{3.1}$$

Here $n = n(\lambda, T, p)$ denotes the refractive index of the medium, which depends on the light wavelength λ, the temperature T and pressure p of the medium. $\beta = v/c$, the particle velocity, is written in units of the speed of light in vacuum, c.

The total energy of a charged particle moving at the phase velocity of light in a medium is

$$E_{th} = \frac{nmc^2}{\sqrt{n^2-1}} \qquad (\beta = c/n), \tag{3.2}$$

where m is the rest mass of the charged particle. This value is called "Cherenkov threshold energy".

Under the environmental condition of SK, the refractive index of the water is $1.33 - 1.34$ at the sensitive wavelength region, $300 \lesssim \lambda \lesssim 600$ nm. Thus, the maximum value of the Cherenkov opening angle, which is obtained at the relativistic limit of $\beta = 1$, is about 42°. Table 3.1 summarizes the Cherenkov thresholds of some charged particles in water at $n = 1.34$.

Table 3.1: Cherenkov thresholds of charged particles at the refractive index of $n = 1.34$. Total energy and momentum are shown.

Particle	E_{th} (MeV)	p_{th} (MeV/c)
$e^{\pm}$	0.768	0.573
$\mu^{\pm}$	158.7	118.5
$\pi^{\pm}$	209.7	156.5
$K^{\pm}$	741.6	553.5
p	1409.6	1051.9

The number of Cherenkov photons emitted per unit wavelength and unit track length of a particle with the charge of ze is given as

$$\frac{d^2\mathrm{N}_{\mathrm{photon}}}{dLd\lambda} = \frac{2\pi z^2\alpha}{\lambda^2}\left(1 - \frac{1}{n^2\beta^2}\right), \tag{3.3}$$

where $\alpha \simeq 1/137$ is the fine structure constant. For a relativistic particle with the charge of $z = \pm 1$ passing through the SK water tank, the total number of emitted Cherenkov photons at the sensitive region of SK is calculated to be $300 - 400$ per cm.

3.1.2 Event reconstruction

Super-Kamiokande detects Cherenkov photons emitted from charged particles by the surrounding PMTs arrayed inside the water tank. The vertex of a charged particle is reconstructed

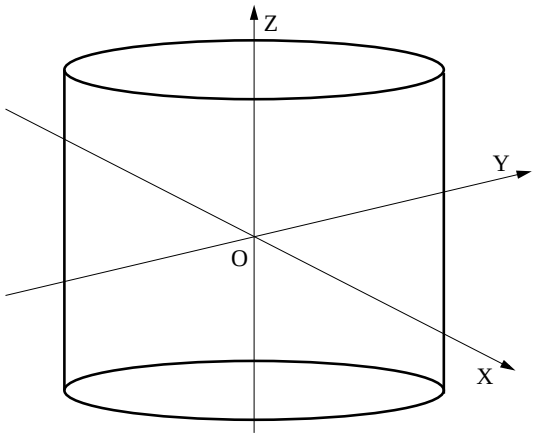

Figure 3.3: Coordinate system of the SK tank.

by timing information of each hit PMT, its direction by hit pattern, and its energy by the number of hit PMTs or the total photoelectrons (p.e.). For the particle identification (PID), the topology of the Cherenkov ring is used. The detail of the event reconstruction will be given in the next chapter.

3.2 Water tank

The Super-Kamiokande tank is optically composed of two regions − an inner detector (ID) and an outer detector (OD). Positions within the tank are described by an orthogonal coordinate system which has its origin at the center of the tank, as shown in Fig. 3.3.

3.2.1 Inner detector

The ID is a cylinder that measures 33.8 meters in diameter and 36.2 meters in height, and encloses 32,481 m^3 of ultrapure water. 11,129[2)] of inward-facing PMTs, 50 cm in diameter, are mounted on the points of a 70 cm grid. All the ID PMTs are attached to the stainless frames called super-module, each of which has twelve ID PMTs on one side and two OD PMTs on the other side. Figure 3.4 shows the schematic diagram of the super-module.

The photo-coverage of the inner detector is about 40%. To prevent light from going through between ID and OD, the ID wall is covered by black polyethylene sheets. The sheets also reduce the reflection of light to make simple the event reconstruction.

[2)] This number is for SK-III and IV. In SK-I and II, there were 11,146 and 5,182 PMTs, respectively.

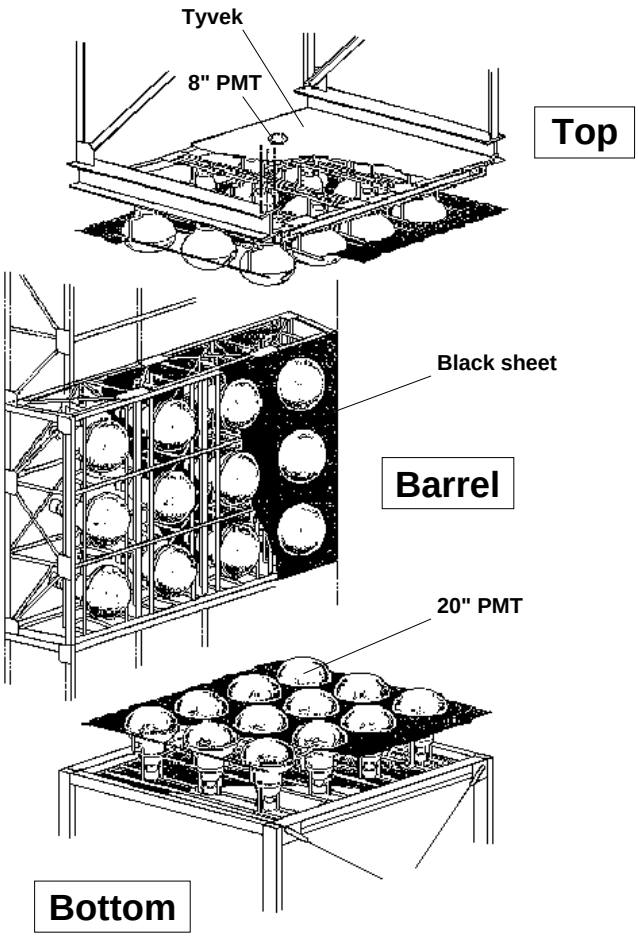

Figure 3.4: Super-module used in Super-Kamiokande.

3.2.2 Outer detector

The OD is a cylindrical shell which surrounds the ID. The thickness of the OD is 2.6 meters at top and bottom, and 2.7 meters at barrel. Also, the OD volume is viewed by 1885 outward-facing PMTs, 20 cm in diameter. Therefore, the OD serves as a passive shield for neutrons and gamma-rays emitted from the surrounding rocks as well as an active veto counter against incoming particles such as cosmic ray muons. To enhance the efficiency of photon detection as much as possible, acrylic plates are attached to the face of each OD PMT [75]. Each plate contains the wavelenth-shifting additive bis-MSB, which absorbs ultraviolet light and emits the light at blue-green wavelengths to effectively enlarge the sensitive region. In addition, the whole wall of OD is covered with white Tyvek sheets whose reflectivity is above 80%.

3.2.3 Photomultiplier tubes

The 50 cm ID PMTs (Fig. 3.5) were developed by the HAMAMATSU Photonics Company with the Kamiokande collaboration [74]. In the development, the resolution of the timing response for 1 p.e. and the pulse height distribution were greatly improved.

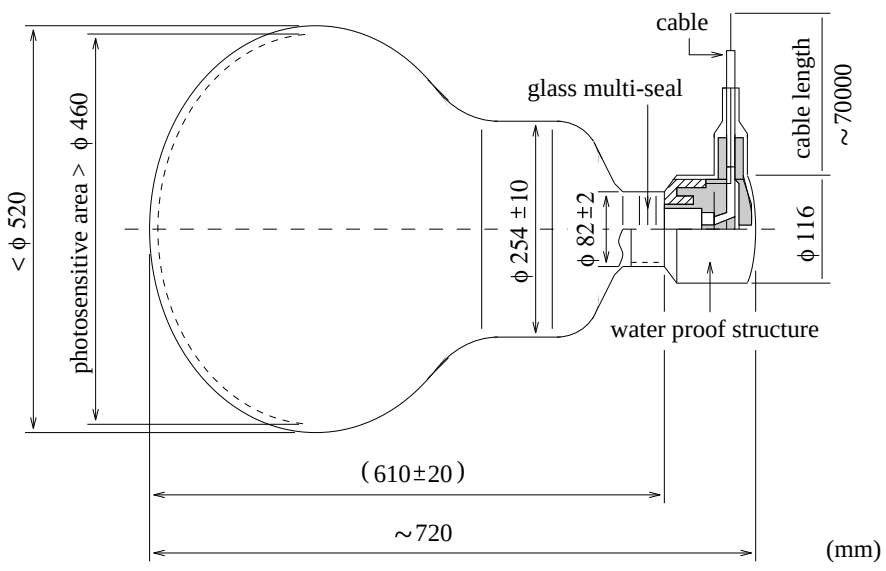

Figure 3.5: Structure of 50 cm PMT

The PMT photocathode material is made of bialkali (Sb-K-Cs), where the sensitive wavelength region is $300 \lesssim \lambda \lesssim 600$ nm and the quantum efficiency (QE) maximizes at 390 nm (about 22%),

as shown in the left panel of Fig. 3.6. This is ideal for the detection of Cherenkov light, whose wavelength peaks near the QE peak after traveling several meters through the ultrapure water of SK.

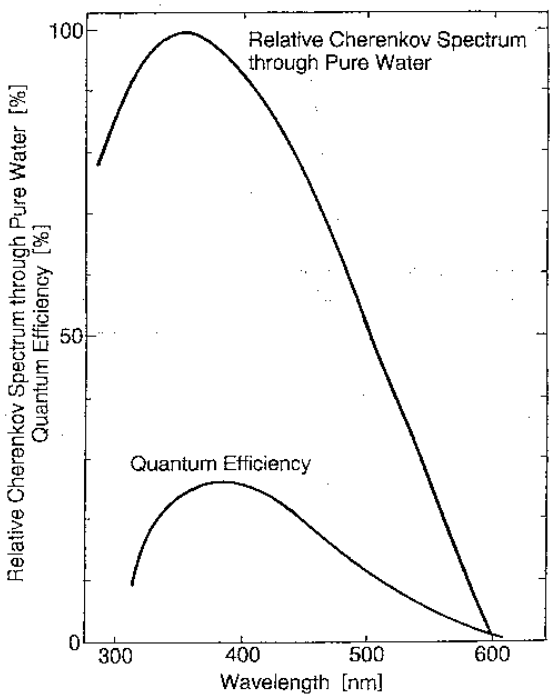

Figure 3.6: Quantum efficiency of 50 cm PMT and the wavelength distribution of Cherenkov photons after traveling several meters through the ultrapure water of SK.

As shown in Fig. 3.7, the 1 p.e. peak is clearly seen as a result of the improvement of dynode. The threshold at each frontend electronics is 0.25 p.e., which corresponds to the valley of the distribution. The dark rate which exceeds this threshold is about 5.7 kHz on average.

In reconstructing low energy events, the timing resolution of each PMT is important. There are differences in photon transit time in PMT depending on where the photon hits, especially in the case of PMTs with large diameters. To minimize this difference, the electric fields inside PMTs are improved and the timing resolution is 3 ns for 1 p.e. signals (the right panel of Fig. 3.7). Table 3.2 summarizes the specifications of the 50 cm PMTs.

3.2.4 PMT case

PMT is evacuated so as to multiply photoelectrons. Thus, if the glass tube in contact with water is broken, implosion can happen. The accident at SK in 2001 was caused by a shock wave produced by the implosion. One of the bottom PMTs broke and it generated shock wave,

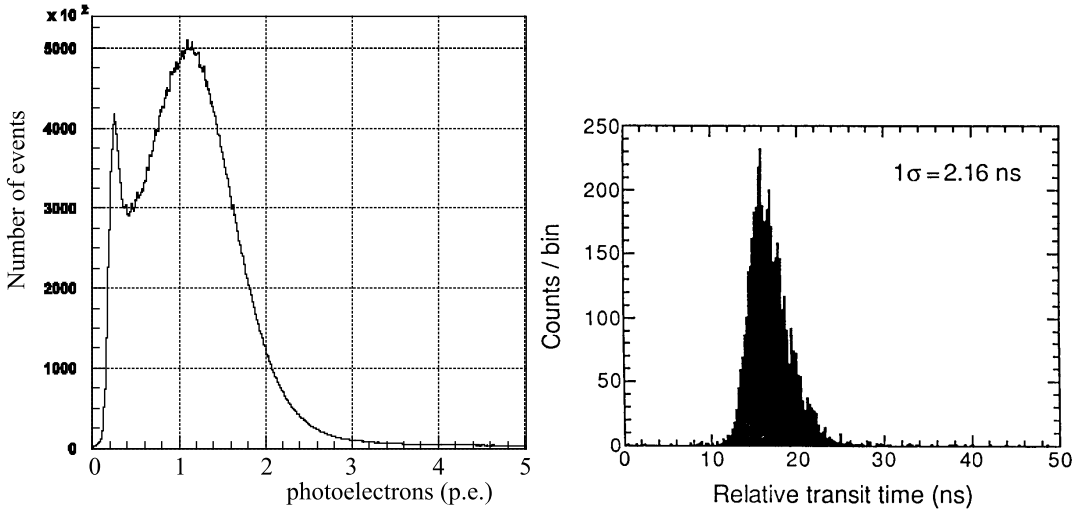

Figure 3.7: The left panel shows the single photo-electron (p.e.) peak in the ID PMTs. The peak around 0 p.e. comes from the dark noise hits. The right panel shows the transit time distribution for a typical ID PMT for intensity of 1 p.e.

Table 3.2: Specifications of the 50 cm PMTs

Shape	Hemispherical
Photocathode area	50 cm diameter
Photocathode material	Bialkali (Sb-K-Cs)
Dynode	Venetian blind type (11 stages)
Quantum efficiency	22% @ 390 nm (peak)
Gain	$\sim 10^7$ @ 2 kV
Dark current	200 nA
Dark noise rate	3.5 kHz
Transit time	100 ns
Transit time spread	3 ns @ 1 p.e.

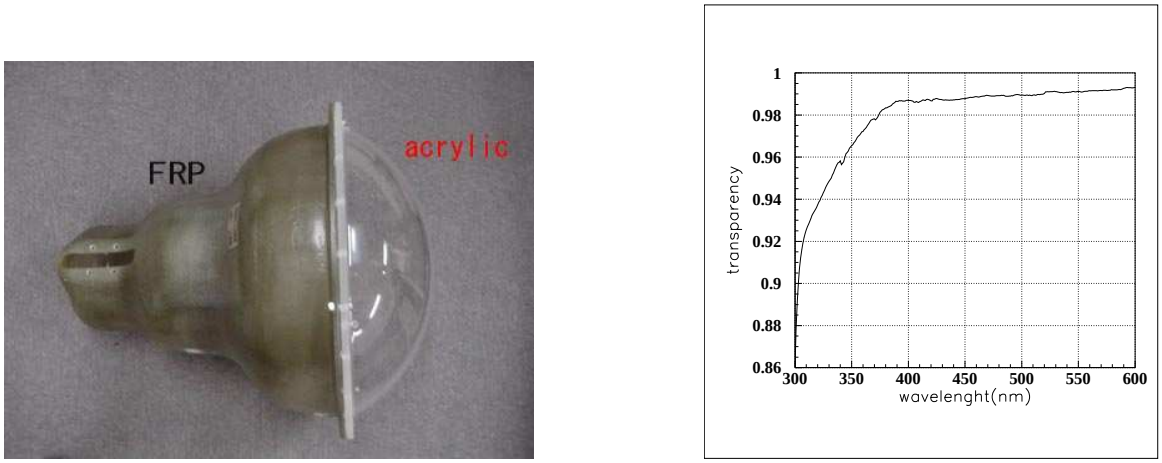

Figure 3.8: PMT case attached to the inner PMT after the accident (left) and the transparency of the acrylic case as a function of wavelength (right).

which destroyed neighboring PMTs. This way a chain reaction was triggered and ultimately destroyed more than half of the PMTs in the SK detector. From then on, all ID PMTs have been encased in a fiber reinforced plastic shell (FRP) at the base and an acrylic case over the photocathode to prevent production of a shock wave, as shown in the left panel of Fig. 3.8. The right panel of Fig. 3.8 shows the transparency of the acrylic case as a function of wavelength with the perpendicular incident angle. The photon attenuation by the case is included in our event simulation.

3.3 Water purification system

The 50,000 m^3 of ultrapure water filled in SK is made up of underground water in the Kamioka mine. Underground water includes such impurities as tiny dusts, ions, and bacteria, which absorb and scatter Cherenkov light and decrease the water transparency. Also, radioactive isotopes included in the underground water[3)] emit electrons and gamma-rays via their decays, which can be reconstructed above the energy thresholds of some low energy analyses due to the detector finite resolution. In this way, the impurities can be a source of background for various SK analyses. SK has a purification system to reject those impurities as much as possible before injecting water into the water tank.

Figure 3.9 shows a schematic diagram of the SK water purification system. This system circulates water inside the tank at $30 - 70$ m^3/hour, and the water is subjected to the following processes:

[3)] Radioactive isotopes of the uranium or thorium chains are abundantly contained in the earth crust and tend to be soluble in water. Thus, they are also included in the underground water used in SK.

1. Water Filter

   Relatively large dusts of $\mathcal{O}(1)$ μm are removed. At the same time, ^{222}Rn's attached to the dusts are also rejected.

2. Heat Exchanger

   Pump and PMT constantly heat the SK water. This temperature increase causes the increment of dark current, the convection inside the ID, and also the growth of bacteria. To reduce this effect, the supply water is cooled and kept around 13 °C.

3. UV Sterilizer

   Bacteria in water are degraded by the radiation of ultraviolet light.

4. Ion exchanger

   Metallic ions (Fe^{2+},Ni^{2+},etc) and carbonate ions can be removed[4)]. ^{218}Po, the daughter nuclei of ^{222}Rn, is also removed.

5. Rn-less-air Dissolving Tank

   Radon-less air is dissolved into the water in order to improve the radon removal capabilities of the vacuum de-gasifier.

6. Reverse Osmosis Filter

   Organic compounds down to a molecular weight of 100 are rejected with a high-performance membrane.

7. Vacuum De-gasifier System

   Dissolved gases (96% of radon, 99% of oxygen) are removed.

8. Ultra Filter

   Small contaminants down to sizes of 10 nm are removed.

9. Membrane De-gasifier

   Radon and oxygen dissolved in water are further removed.

This purification system enables us to decrease the radon concentration to the level of 10^{-3} Bq/m^3. The light attenuation length in the purified water reaches around 100 m.

[4)] Metallic ions are actually not abundant in the SK tank

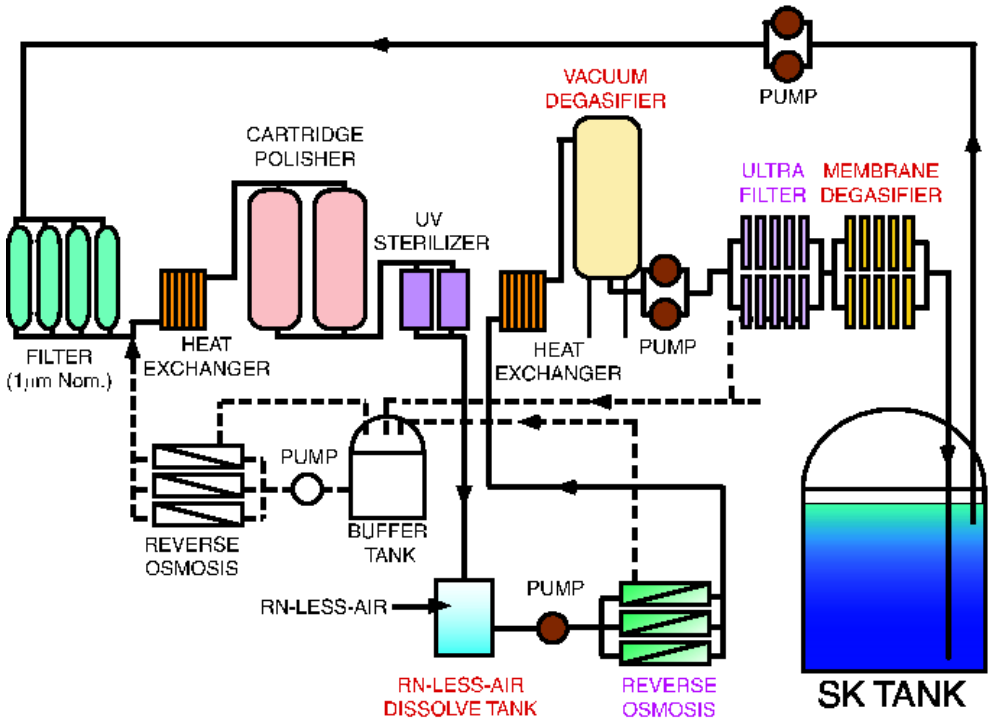

Figure 3.9: SK water purification system

3.4 Air purification system

Since SK is located inside the mine, the concentration of ^{222}Rn is very high ~ 2000 Bq/m^3 in the air. Therefore, the dome over the SK tank is covered with a mine-guard (polyurethane) not to allow the radon gas which emanates from the surrounding rock to enter the experimental site. Air-tight double-doors sit at the entrance of the experimental site. Also, radon-less air outside of the mine is sent to the site at $5 - 12$ m^3/min so that the mine air does not enter the site. The typical radon concentration in the SK dome air is $20 - 30$ Bq/m^3.

The air in the SK tank is kept low enough through the process shown in Fig. 3.10. Here, each component plays the following role:

1. Compressor

   The air is pressurized to $7 - 8.5$ atm.

2. 0.3, 0.1 and 0.01 μm Air Filters

   Dust in the air is removed.

3. Air Drier, CO_2 Extraction Equipment

   Water vapor and CO_2 are removed.

4. Carbon Column

   CO absorbs radon.

5. Cooled Charcoal

   Radon is trapped by an active charcoal cooled to -41°C.

After the process, about 99.98% of radon is rejected. The air of $2 - 3$ mBq/m^3 is then sent to the SK tank (upper 60 cm air layer in the tank) at 18 m^3/hour.

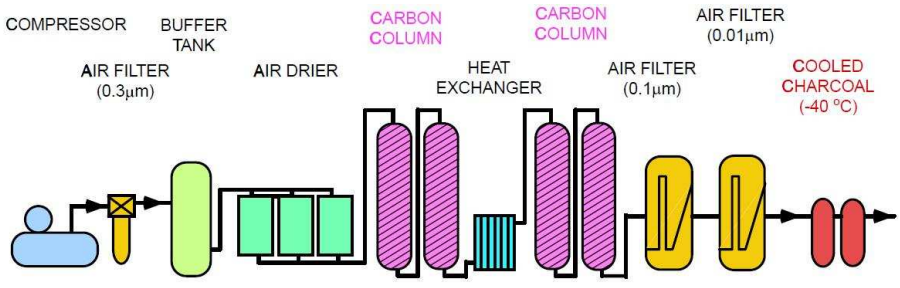

Figure 3.10: SK air purification system

3.5 Data acquisition systems

In this section, the data acquisition (DAQ) system at SK-IV and the event timing measurement at T2K are described.

3.5.1 Upgraded DAQ system

The Super-Kamiokande upgraded the detector's readout electronics [76–78] in September 2008. The data-taking period after the upgrade is called SK-IV. The new upgraded electronics includes a new front-end with a higher data processing. The triggering method is also renewed. In the old trigger system, candidate events were selected by hardware triggers and the arrival time and charge (TQ) information was available only within 1.3 μs around the trigger timing. In the new system, the TQ information of all PMT hits is sent to a cluster of PCs that organizes the hit data and searches for event candidates based on software triggers. This enables us to implement a coincidence trigger with a beam arrival time as in the case of the T2K experiment or delayed-coincidence trigger required for supernova relic neutrino searches.

The new front-end boards shown in Fig. 3.11 are called QTC-Based Electronics with Ethernet (QBEE). The QTC (Charge to Time Converter) is a custom ASIC that responds to input PMT pulses by producing a square-wave pulse as shown in Fig. 3.12. The front edge of the QTC's output coincides with the arrival time of the PMT signal and the length is proportional to the integrated charge of the PMT pulse. The output of the QTC is then fed to a TDC (Time to Digital Converter) that digitizes the time and length of each QTC pulse. The digitized data from the TDCs are then read by FPGAs (Field-Programmable Gate Array) which calculate the digitized hit timing and integrated charge, and ultimately sent to readout PCs with Ethernet which provides the high rate of data transfer. The whole circuit of the QBEE board transfers data up to at 11.8 Mbps, which corresponds to the input pulse rate of 80 kHz/channel. Each QBEE has eight QTC chips, each chip providing three channels, and the whole DAQ system employs 550 QBEE boards which together read out the 13,014 (11,129 ID and 1,885 OD) PMTs of SK and send their hit information to a cluster of online PCs.

The online PCs organize the PMT hit information from the QBEEs and produce data files of candidate events which are later subjected to offline analyses. Figure 3.13 shows the schematic diagram of online processes. The PCs are classified into three groups based on their roles: Frontend PC, Mergers and Organizer PC. There are 20 Frontend PCs, each of which collects data from 30 ID and 20 OD QBEEs, and then sorts the PMT hit information in time order. Mergers collect the hit information from all Frontend PCs into a time-ordered list of PMT hits. They also apply a set of software triggers summarized in Tab. 3.3 to select event candidates from these lists. There are 10 Merger PCs and each collects data from Frontend PCs. For each candidate event, a window including the event trigger time, whose width is defined in Tab. 3.3, is opened and all the hit information within that window are sent to a single Organizer PC. The Organizer PC collects all the candidate events eliminating overlaps and writes them onto disks

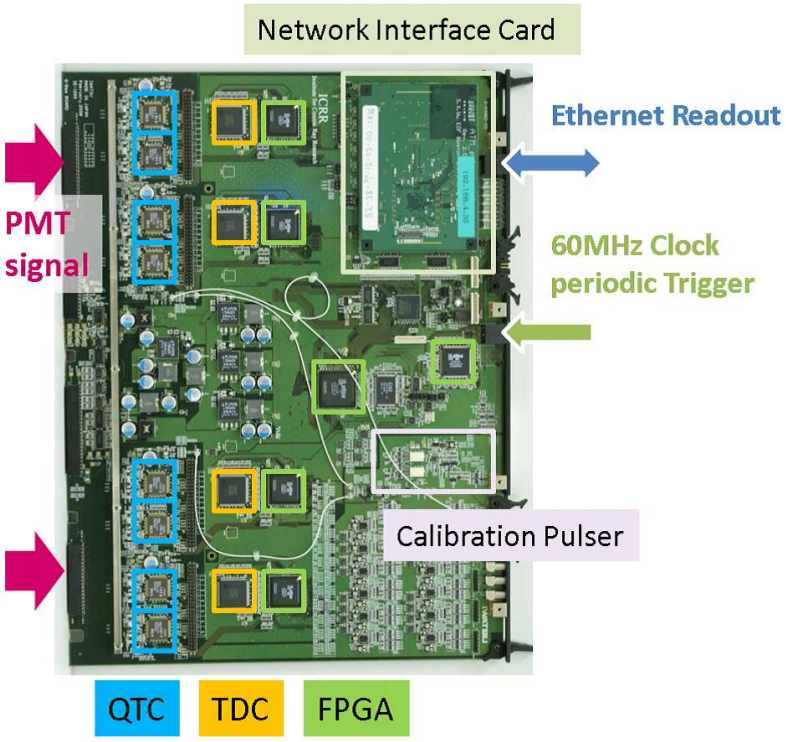

Figure 3.11: Photograph of a QBEE. There are eight QTC chips, four TDCs, six FPGAs and a network interface card. PMT signals are fed into the board from the left side while the readout data, distributed 60 MHz clock and periodic trigger are transmitted through connectors on the right side.

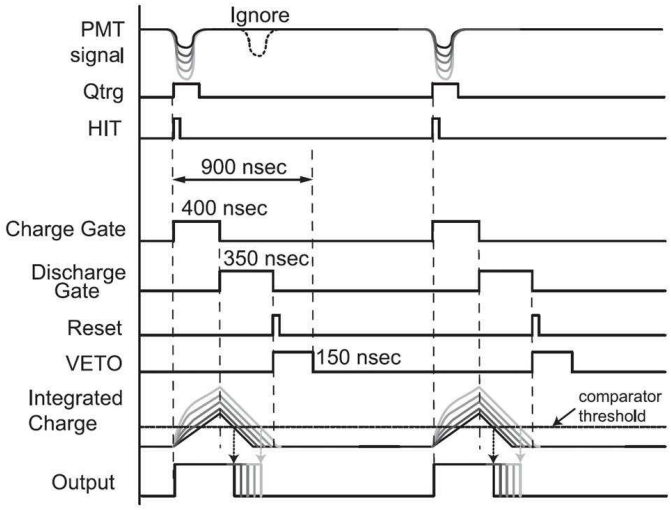

Figure 3.12: Timing chart for QTC operation [78]. The QTC integrates the charge of an input signal during the first 400 ns and discharges the integrated charge with constant current during the next $\sim$ 400 ns. The total processing time for one hit is 900 ns. In the case a signal comes during the discharging period, the signal is ignored.

for later offline analyses. During a typical period of detector operation, about 470 Mbps of data flows from the SK PMTs through to the Merger PCs. After the Merger's selection, that stream of hit information results in about 9 Mbps, which corresponds to the software trigger rate of 3 kHz.

Table 3.3: Software triggers used in SK-IV DAQ system. Trigger types, the thresholds of PMT hits within 200ns, and the time windows with respect to the trigger timing where the TQ info is extracted, are shown. Each trigger name is from the top: SLE (Super Low Energy), LE (Low Energy), HE (High Energy), SHE (Super High Energy), and OD (Outer Detector).

Trigger	Hits	Time window (μs)
SLE	34	$[-0.5, +1.0]$
LE	47	$[-5, +35]$
HE	50	$[-5, +35]$
SHE	70	$[-5, +35]$
OD	22	$[-5, +35]$

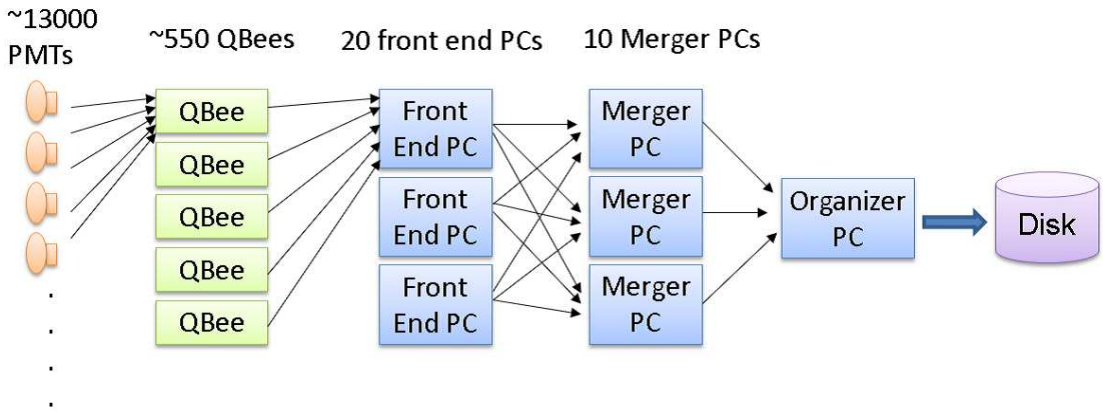

Figure 3.13: Schematic diagram of online processes.

3.5.2 Overview of T2K data acquisition system at SK

As described above, data from all hit signals[5)] is continuously collected by online PCs. Events are extracted by a software trigger program running on online PCs and recorded onto disks. This system enables us to record all the detector activities by T2K beam neutrinos.

Figure 3.14 shows a schematic view of the T2K beam DAQ at SK. Spill by spill, the SK DAQ gets information on the absolute timing of each beam spill, which is measured by using the GPS system at J-PARC. We store all PMT hit information within the window of $\pm$ 500 μs from the beam arrival time at SK (hereafter called "1 ms T2K window"). The beam arrival time at SK is predicted by adding the neutrino time-of-flight of 985.134 μs[6)] to the arrival time of the protons in the first bunch at the carbon target in J-PARC.

3.5.3 GPS-based event timing measurement

Overview of the hardwares

Figure 3.15 shows a schematic design of the SK DAQ hardware relevant for the event timing measurement using the GPS clock. Through an optical fiber of 1.8 km length, one pulse per second (1PPS) signals from the GPS reviewer are sent from the mine entrance to a local time clock (LTC) located in the mine. All the front-end electronics (QBEE) are synchronized by a 60 kHz trigger clock from a 60 MHz master clock module and the same 60 kHz trigger signal is also received by the LTC. This system enables us to calculate the time difference between the 1PPS signal from the GPS clock and the PMT signals recorded by the QBEE modules from the LTC counts.

[5)] Here "hit signals" mean those detected by a built-in discriminator in QTC chips on QBEE boards with the threshold level set to about 0.25 p.e.

[6)] The measured distance is $295,335.2 \pm 0.7$ m.

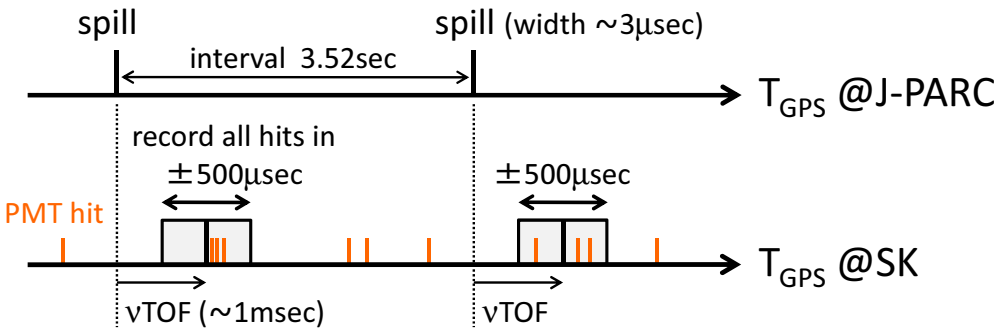

Figure 3.14: Schematic view of T2K beam data acquisition at SK.

SK is equipped with two independent GPS modules: one made by Truetime (GPS1) and the other made by Motorola (GPS2). A Rb clock is also installed as an auxiliary source of timing information in case the two GPS timings are inconsistent for some unknown reasons.

A timing chart of the SK DAQ hardware is summarized in Fig. 3.16. In the QBEE, the TDC count is set to zero when a 60 kHz trigger arrives. Therefore, the absolute time for each PMT hit, T_{abs}(PMT hit), can be calculated as follows by using the TDC count of the QBEE and the LTC count:

$$\begin{aligned} T_{abs}(\text{PMT hit}) &= T_{abs}(\text{GPS 1PPS}) \\ &+ 10008 \text{ ns} \\ &+ (\text{LTC count (60 kHz trigger)} - \text{LTC count (1PPS)}) \text{ / LTC freq.} \\ &+ \text{TDC count / TDC freq.} \\ &- 972.1 \text{ ns}, \end{aligned} \tag{3.4}$$

where we take into account timing delays, whose locations are shown in Fig. 3.16: the transit time of the 50 cm PMTs, the signal propagation time in the PMT signal cables, and the signal delays in the electronics modules and cables which connect each electronics module. The transit times of the PMTs and signal cables are measured using a laser and a diffuser ball, whose setup is detailed in Chapter 5. The relevant delays are summarized in Tab. 3.4.

Stability of GPSs and selection of GPS

The validity of the SK event time determination is tested by monitoring the difference in the time stamps from GPS1 and GPS2. It is known that the GPS1 and GPS2 almost always agree within 200 ns, but some time when the number of available satellites becomes small (~ 1) compared to the standard one ($\gtrsim 4$), deviation from that range is seen.

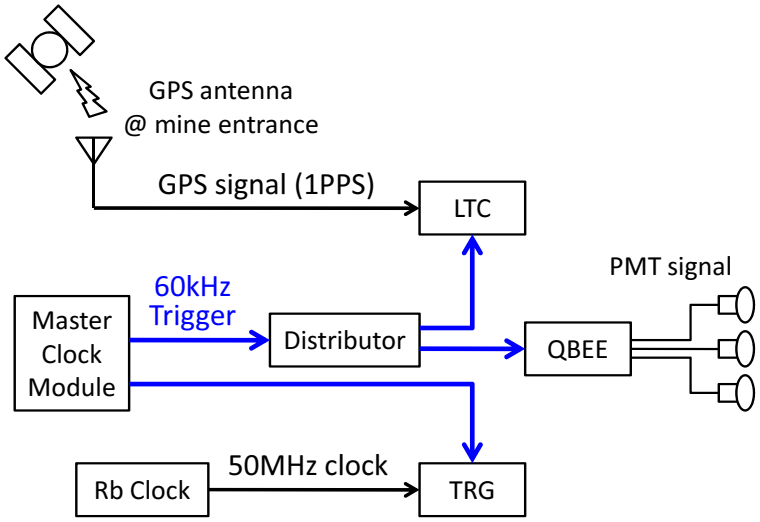

Figure 3.15: Schematic view of the Super-K DAQ hardware relevant for the event timing measurement using the GPS clock. The absolute timing of each PMT hit is obtained by comparing the 60 kHz trigger signal from the master clock with the 1PPS signal from the GPS clock.

Table 3.4: Summary of timing delays. Note that the delay from the cable for the 60 kHz trigger is added with the opposite sign.

Source	Delay time (ns)	Uncertainty (ns)
PMT and signal cables	470.0	6
LTC	633.2	4.5
Cable for the 60 kHz trigger	224.2	0.1
QBEE	93.2	-
Total	972.1	7.5

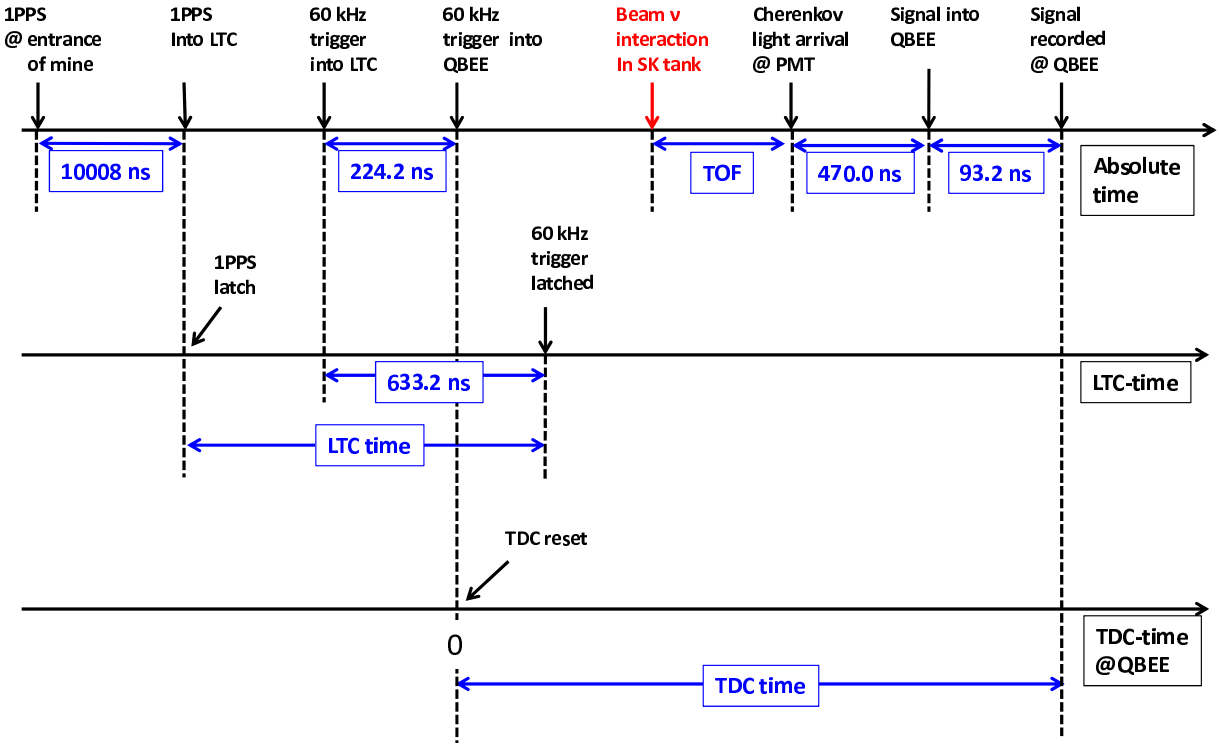

Figure 3.16: Timing chart of the Super-K DAQ hardware. The delay in each element on Table 3.4 is also shown.

From the comparison between the GPSs and the rubidium clock, we find the GPS2 is more stable than the GPS1 and determine the GPS2 as the default clock for the absolute beam spill timing at SK. In case the GPS2 is inconsistent with the GPS1 ($\geq$ 100 ns), we select a more reliable clock by the rule shown in Tab. 3.5.

Table 3.5: The clock selection rule for the absolute timing of beam spills at SK.

Condition (flow to down)	Clock
$\lvert t(GPS1) - t(GPS2) \rvert < 100$ ns	
or $\lvert t(GPS2) - t(Rb) \rvert < 100$ ns	GPS2
$\lvert t(GPS1) - t(Rb) \rvert < 100$ ns	GPS1
Otherwise	Rb clock

Chapter 4

Event Reconstruction

In the analysis of low energy ($\lesssim$ 100 MeV) events at SK, we reconstruct an event vertex using the timing information of hit PMTs, and then reconstruct an event direction using the hit PMT pattern. After that, we calculate the effective number of hit PMTs (N_{eff}), which is converted to energy by using a conversion function obtained by an absolute energy calibration using a LINAC and *etc.*, which are described in the next chapter. We also reconstruct the event absolute timing based on the GPS. The followings are technical descriptions of each reconstruction method.

4.1 Vertex reconstruction

To reconstruct an event vertex, the timing information of hit PMTs is used. A vertex is defined as the point where the track of a charged particle starts. In the low energy region, electrons do not propagate in water more than the vertex resolution for SK-IV, which is about 50 cm at 10 MeV [79]. Therefore, the track is treated as a point in our vertex reconstruction program.

The vertex fitter used in this analysis is called BONSAI [80]. BONSAI is a maximum likelihood fit to the timing residuals of the hit PMTs. The timing residual of an event, $t_{res,i}$, is defined as the hit timing of the i-th hit PMT, t_i, with the correction of the time-of-flight (TOF) of emitted Cherenkov photons:

$$t_{res,i}(\boldsymbol{v}) \equiv t_i - \frac{|\boldsymbol{v} - \boldsymbol{h}_i|}{c'}, \tag{4.1}$$

where $\boldsymbol{v}$ denotes the event vertex position, $\boldsymbol{h}_i$ the position of the i-th hit PMT, and c' the group velocity of Cherenkov light in water. Ideally, $t_{res,i}$ has the common value to all hit PMTs.

BONSAI uses all the hit PMTs within 1.3 μs and their timing residuals to determine the position of the vertex. It takes dark hits into account by calculating a likelihood which describes the shape of the timing residual distribution obtained from LINAC calibration data. Here, the

likelihood is defined with $\Delta t_i(\boldsymbol{v}) = t_{res,i}(\boldsymbol{v}) - t_0$ (t_0 is fitted to minimize all $t_{res,i}$) as :

$$\mathcal{L}(\boldsymbol{v}, t_0) \equiv \sum_{i=1}^{N_{hit}} \log(P(\Delta t_i(\boldsymbol{v}))), \tag{4.2}$$

where $P(\Delta t_i(\boldsymbol{v}))$ is the probability density function of Δt_i. Figure 4.1 shows the BONSAI likelihood obtained by LINAC calibration data.

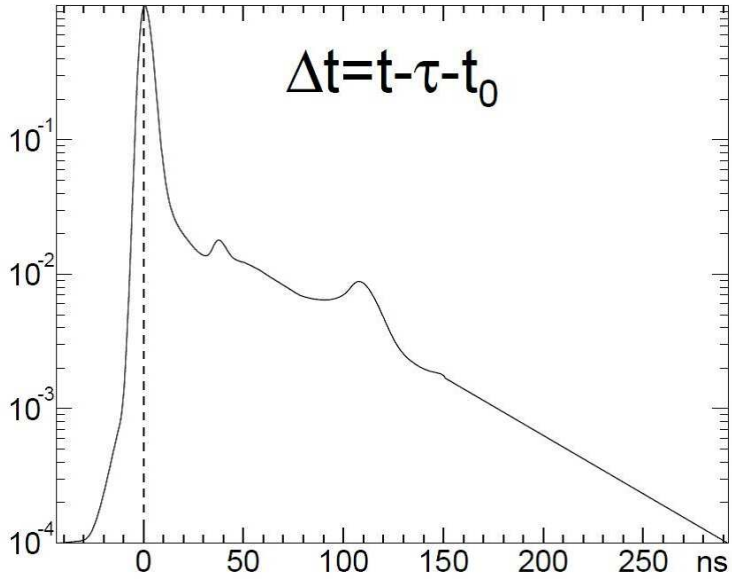

Figure 4.1: BONSAI likelihood obtained by LINAC calibration data. Horizontal axis is $\Delta t_i(\boldsymbol{v}) = t_{res,i}(\boldsymbol{v}) - t_0$ (τ denotes TOF). The peaks at 40 ns and 110 ns are after-pulses.

In selecting the vertex candidate, we first select a set of hit PMTs to be used for the calculation. We require a causality condition for any pair of the selected hit PMTs, *i.e.*, the arrival time difference of photons, $\Delta t_{ij} > 0$, must satisfy[1)]

$$\Delta t_{ij} < \frac{|\boldsymbol{h}_i - \boldsymbol{h}_j|}{c} \quad (i \neq j). \tag{4.3}$$

Also, to reject dark noise, reflection and scattering light, we do not use the hit PMTs which are more than 1250 cm or 35 ns apart from any hit PMT, and choose the set of hit PMTs so that the number of pairs included in the set which satisfy the above triangle inequality Eq. (4.3) is maximized.

[1)] This condition is derived from the triangle inequality assuming the particle track is point-like, *i.e.*, all Cherenkov photons are emitted at the same time.

Generally, when you choose a combination of four different hit PMTs, the event vertex is uniquely determined. We calculate the likelihoods for the vertices determined by various combinations of four hit PMTs. In order to find the vertex which has the maximum likelihood, we evaluate vertices around the vertex using a search grid of 200 cm in size. Similar searches are repeated by contracting the search radius, until the radius is below 1 cm and the likelihood range is below 0.01. The grid point which has the maximum likelihood value at this point is determined to be the reconstructed vertex.

In the event vertex reconstruction, the center of the 10 ns wide window, t_0, is uniquely determined. The t_0 is approximately equal to the timing of the neutrino interaction[2)]. Since we know the absolute time of each PMT hit after correcting the offset in the SK DAQ system (Eq.(3.4)), we reconstruct the absolute timing of the neutrino interaction as

$$\begin{aligned} \mathrm{T_{abs}(vertex)} &= \mathrm{T_{abs}(PMT\ hit)} \\ &+ t_0 - \mathrm{TDC\ count\ (PMT\ hit)\ /\ TDC\ freq.} \end{aligned} \tag{4.4}$$

4.2 Direction reconstruction

After determining the event vertex, the event direction is reconstructed by using the Cherenkov ring pattern of hit PMTs. Ideally, the event pattern should be a clear ring which has an opening angle of 42° with respect to the electron direction. However, since an electron is multiple-scattered in water the track is not straight. Also, Cherenkov photons are scattered in water and reflected by PMTs and black sheets. These effects make the Cherenkov ring fuzzy.

For the direction reconstruction, the hit PMTs within a 20 ns wide search window in $t_{res,i}$ which maximizes the number of hits inside are used. The event direction, $\boldsymbol{d}$, is determined by using the maximum likelihood method. The likelihood function is defined as follows:

$$\mathcal{L}(\boldsymbol{d}) = \sum_{i=1}^{N_{20}} \log(P_i(\cos\theta_{dir}(\boldsymbol{d}))) \times \frac{\cos\theta_i}{a(\theta_i)}, \tag{4.5}$$

$$\theta_i \equiv \cos^{-1}(\boldsymbol{d}_i \cdot \boldsymbol{p}_i), \tag{4.6}$$

where N_{20} is the number of hit PMTs included in the 20 ns wide window. $P_i(\cos\theta_{dir})$ is the probability density function of the emission angle of Cherenkov photons with respect to the electron momentum direction, which is estimated by a Monte Carlo (MC) simulation. θ_i is the incident angle of a Cherenkov photon to the i-th hit PMT. $\boldsymbol{p}_i$ is the unit vector which points from the i-th hit PMT to the reconstructed vertex. $\boldsymbol{d}_i$ is the unit vector which points from the i-th hit PMT to the direction it faces. $a(\theta_i)$ is the acceptance of the photo-cathode as a function of θ_i.

[2)] Major factors which can contribute to the difference between the reconstructed absolute timing and the true event timing are as follows: the vertex resolution, the relative timing resolution, and the conversion length of a gamma-ray.

The maximum value of the likelihood is obtained by a grid search. The grid interval is 20°, 9°, 4° and 1.6°. Taking into account the fact that the average value of the electron multi-scattering angle is 27° at 10 MeV, these grid intervals are small enough to reconstruct the direction of low energy electrons. The LINAC calibration in SK-III measures the direction resolution and obtains about 25° when the electron energy is 10 MeV.

4.3 Energy reconstruction

The number of Cherenkov photons emitted from a charged particle is approximately proportional to the kinetic energy of the particle. Hereafter, we assume all Cherenkov photons in an event come from a single electron, and reconstruct the total energy (not the kinetic energy) of the electron.

In SK, the sum of photo-electrons of all hit PMTs is approximately proportional to the number of emitted Cherenkov photons. To reconstruct the energy of low energy events, however, we use the number of hit PMTs instead of the number of photo-electrons. The reasons are as follows:

- In low energy events, since the number of emitted Cherenkov photons is small, *e.g.*, about 2,600 photons at 16 MeV, the average number of Cherenkov photons of each hit PMT is about 1, if the vertex is well apart from the PMT surface.
- The resolution of photo-electrons is not very good at the 1 p.e. level.
- The number of photo-electrons is dependent on the PMT gains while the number of hit PMTs with a low discrimination threshold (~ 0.25 p.e.) is not affected much by the gain change.

For the energy reconstruction, we use only the hit PMTs of N_{50}, whose definition is the same as N_{20} except for using a search window 50 ns wide instead of 20 ns wide one. This selection criterion rejects accidental hits from the dark noise in PMTs. However, N_{50} depends on several factors such as the water transparency and the acceptance of each hit PMT. Therefore, to calculate the effective number of hit PMTs, N_{eff}, we sum up as follows the number of hit PMTs included in N_{50} with a combination of various correction factors as the weight:

$$N_{eff} = \sum_{i=1}^{N_{50}} \left[(X_i - \epsilon_{\rm dark} + \epsilon_{\rm tail}) \times \frac{N_{\rm all}}{N_{\rm alive}} \times \frac{1}{S(\theta_i, \phi_i)} \times \exp\left(\frac{r_i}{\lambda}\right) \times G(i) \right] \tag{4.7}$$

The meaning of each correction factor is described below:

- X_i : Correction factor for multi-photo-electron hits

  If the event vertex is near the edge of the fiducial volume and the direction points to the nearest wall, some PMTs can have multiple photons. The number of photo-electrons of

each PMT is estimated by the occupancy of the eight surrounding PMTs. Using the ratio of the number of hit PMTs and functional PMTs surrounding the i-th PMT, n_i and N_i, the correction is written as follows:

$$X_i = \begin{cases} \log(1 - n_i/N_i)^{-N_i/n_i} & (n_i < N_i) \\ 3 & (n_i = N_i), \end{cases} \tag{4.8}$$

where the Poisson distribution for the hit of a photon and the uniformity of photons to 3×3 PMTs are assumed.

- ϵ_{dark} : Correction for dark noise hits

  This correction factor is for hits induced by the dark noise in the PMT:

$$\epsilon_{\text{dark}} = \frac{N_{\text{alive}} \times R_{\text{dark}} \times 50 \text{ ns}}{N_{50}}, \tag{4.9}$$

  where N_{alive} is the number of active PMTs in the ID and R_{dark} is the average dark rate during the period (RUN) including the event.

- ϵ_{tail} : Correction for reflected Cherenkov photons

  This correction factor is for the tail of hits after the 50 ns timing window and defined as:

$$\epsilon_{\text{tail}} = \frac{N_{100} - N_{50} - N_{\text{alive}} \times R_{\text{dark}} \times (100 - 50) \text{ ns}}{N_{50}}, \tag{4.10}$$

- $\frac{N_{\text{all}}}{N_{\text{alive}}}$: Correction for dead PMTs

  This factor corrects the time variation of the number of dead PMTs. $N_{\text{all}} = 11129$ is the total number of ID PMTs in SK-IV.

- $\frac{1}{S(\theta_i, \phi_i)}$: Correction for effective photo-coverage

  $S(\theta_i, \phi_i)$ is the effective area of photo-cathode of the i-th hit PMT seen from the direction of the incident direction of a photon[3)], (θ_i, ϕ_i).

- $\exp\left(\frac{r_i}{\lambda}\right)$: Correction for water transparency

  This factor corrects the attenuation of Cherenkov photons in water. r_i is the distance between the i-th hit PMTs and the reconstructed vertex. λ is the water transparency measured during the period (Run) including the event, which is obtained by Cherenkov photons of the decay electrons from cosmic ray muons stopping inside of the fiducial volume, as described in the next chapter.

[3)] Asymmetry exists at large θ due to shielding by surrounding PMTs.

- $G(i)$: Correction for the QE of PMTs

  This factor is to correct the relative QE of each PMT.

We make N_{eff} distributions of some fixed energies using a tuned MC, and take the average of each N_{eff} distribution. Then we fit these energies as a function of the averaged N_{eff} with a polynomial, so that the reconstructed energy is converted from N_{eff}.

Chapter 5

Detector Calibration

The precision of a measurement depends on how well the detector is calibrated. In this chapter, energy scale, timing calibration and water transparency measurement are overviewed.

5.1 Energy scale

As explained in Section 4.3, the energy reconstruction of low energy events uses the effective number of hit PMTs. We determine the conversion factor from N_{eff} to energy within about 1% by two independent calibrations: The LINAC and DT calibrations.

5.1.1 LINAC calibration

The LINAC [81] employed at SK is a Mitsubishi ML-15MIII electron linear accelerator which was originally produced for medical purposes. Using electrons from the LINAC, we determine the energy scale of low energy analyses in SK within a few percent level.

Setup of LINAC system

The LINAC accelerates electrons using microwave pulses of $1 - 2$ μs width generated by a klystron. The pulse rate is adjustable between 10 and 66 Hz. Electrons from the electron gun are accelerated when they travel with the microwave in the accelerating tube. The average beam momentum is adjusted by changing the input power and frequency of the microwave. Table 5.1 summarizes the specifications of the LINAC.

Figure 5.1 shows the setup of the LINAC calibration system. Since the LINAC itself can be a source of backgrounds such as X-rays and gamma-rays, we locate the mainframe of the LINAC far enough from the SK tank. Electrons accelerated by the LINAC are selected, narrowed and injected into the tank through a stainless beam pipe by using an arrangement of collimators, bending magnets and focusing magnets (Fig. 5.2−5.3).

Table 5.1: The specifications of the LINAC

Microwave frequency	2.856 GHz
Pulse width	$1 - 2$ μs
Pulse rate	$10 - 66$ Hz
Beam energy	$4.4 - 18$ MeV
Maximum beam intensity	10^6 electron / pulse
@ the end of the accelerating tube	
Momentum spread	$< 0.3\%$
Accelerator tube	1.69 m length and 26 mm diameter
Vacuum in the accelerating tube	10^{-4} Pa

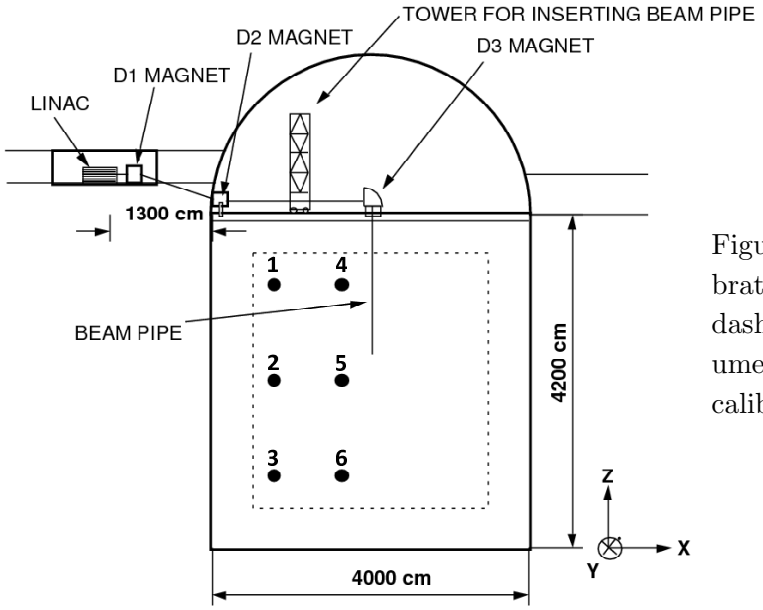

Figure 5.1: Setup of the LINAC calibration system at the SK detector. The dashed line indicates the fiducial volume. Black dots are positions where calibration data are taken.

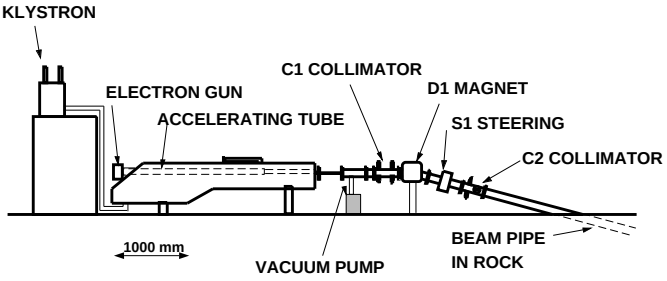

Figure 5.2: The first bending magnet (D1) and associated collimators. This magnet determines the beam momentum.

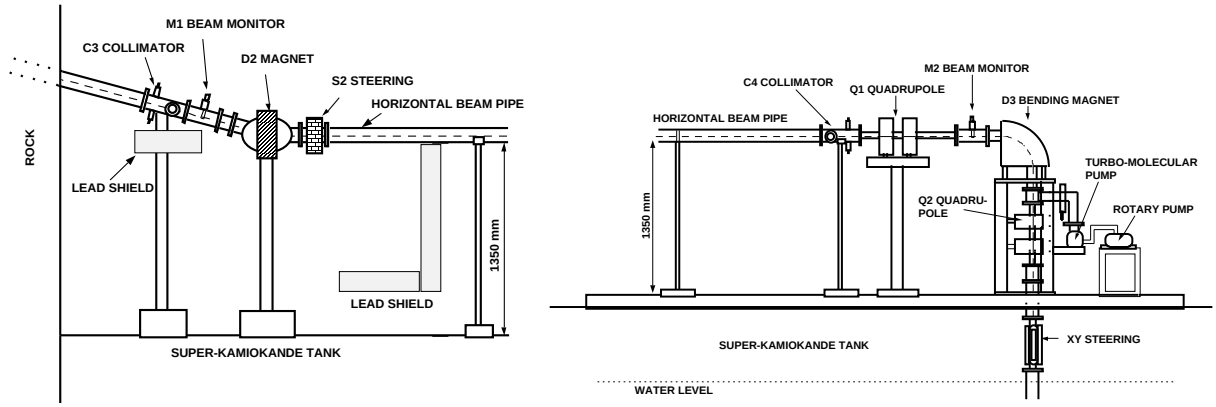

Figure 5.3: The left panel shows the second bending magnet (D2), where the beam is bent to horizontal after momentum selection. The right panel shows the quadratic magnets (Q1, Q2) and 90° bending magnet (D3).

The beam pipe can be extended to as long as 60 meters. We surround the inner surface of the beam pipe by a μ-metal to reduce the effect of external magnetic fields. Inside of the beam pipe is evacuated to 0.1 Pa so that the electron beam can reach the end of the pipe without scattering by air. The beam pipe is inserted to the tank through calibration holes on the top of the tank. The end of the pipe is capped by a titanium (Ti) cap with the thickness of 0.1 mm as shown in Fig. 5.4. A scintillator and PMT are placed at the end of the beam pipe to trigger LINAC events and also there are ones for its veto.

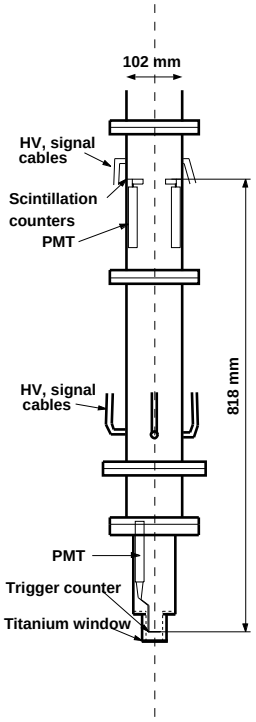

Figure 5.4: The end-cap of the LINAC beamline. A scintillation trigger counter is located above the titanium window.

Beam energy measurement

We separately measure the beam electron energy by a germanium (Ge) detector when we do the LINAC calibration. The germanium detector is a negative type semiconductor detector and we use the germanium of a cylindrical pure crystal 57.5 mm in diameter and 66.4 mm thick. After the LINAC data taking is finished for a given beam momentum, the germanium detector is placed just behind the D3 magnet (Fig. 5.3). We cover the position where the LINAC electron beam exit by a thin (30 μm thick) titanium window.

Due to small ionization energy of germanium (2.96 eV), the detector enables us to measure the beam electron energy very precisely. Also, the detector output has good linearity for input particle energy. The latter characteristic is important because we use radioactive sources for the energy calibration of the germanium detector, but available sources are only up to 9 MeV while

the beam energy ranges from 4 to above 10 MeV.

The energy determination of beam electrons is done by comparing the spectrum between data and MC. The MC of the germanium calibration is a particle gun MC prepared with the 1 keV energy interval within all the relevant energy ranges. Also, the energy losses in the beryllium window, the inactive region of the germanium detector and the titanium window are included in the MC simulation.

The left panel of Fig. 5.5 shows the gamma-ray energy of each radioactive source versus the output charge of the germanium detector with the fitting line. The deviation from the fitting line is shown in the right panel of Fig. 5.5. Except for the low energy region below 3 MeV, which is not relevant for our analysis, the deviation is below 0.1%.

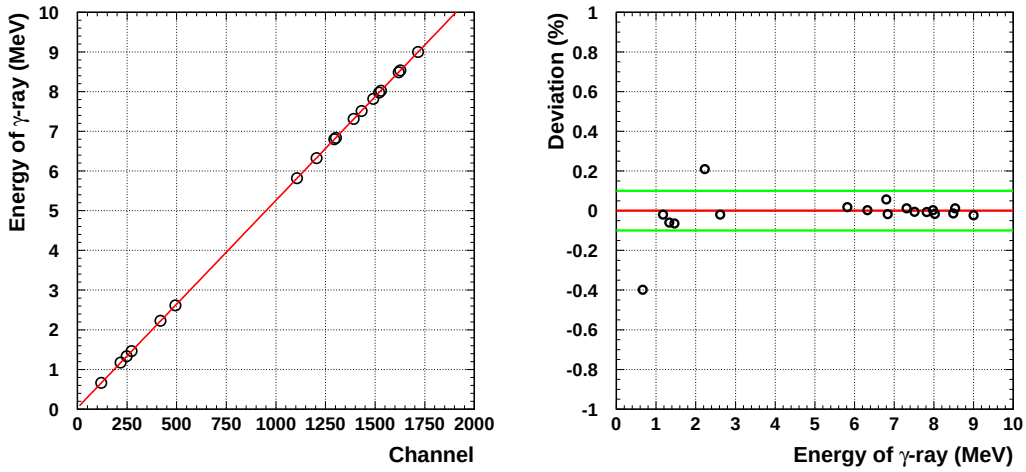

Figure 5.5: Left: Linearity of the germanium detector. The horizontal axis is the output from the germanium detector (count) and the vertical axis is the energy of a gamma-ray from each radioactive source (keV). Right: Deviation of the output of germanium detector from the fitted line. The horizontal axis is the energy of a gamma-ray from each radioactive source (keV). The vertical axis is the deviation of the data point from the fitted line (%).

Result of LINAC calibration

We take LINAC data at the six positions which are the combination of X of -12 or -4 m and Z of -12, 0, or $+12$ m, X and Z being SK coordinates. For each position, data is separately taken using two different monochromatic energies of electrons: 13.7 MeV and 7.0 MeV in total energy.

Figures 5.6 and 5.7 show the N_{eff} distributions of 13.7 MeV and 7.0 MeV data. After each N_{eff} distribution is iteratively fitted with a Gaussian, the central values of the fits are compared

between data and MC. Figure 5.8 shows the fractional difference between data and MC at six data-taking positions, where the ID numbers correspond to those of Fig. 5.1. The difference is well within 1.5%.

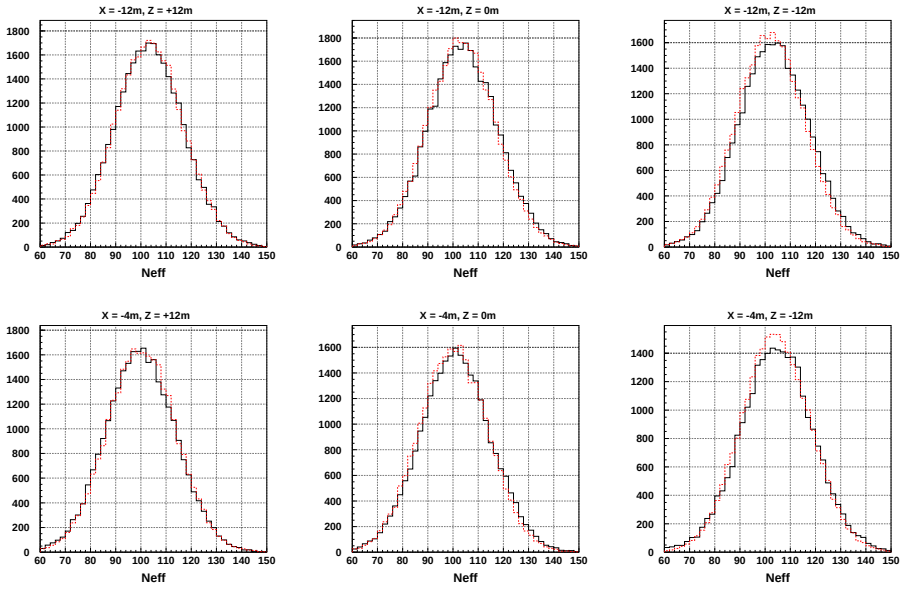

Figure 5.6: N_{eff} distribution of 13.7 MeV electrons at each six position. Solid lines show data and dashed ones show MC.

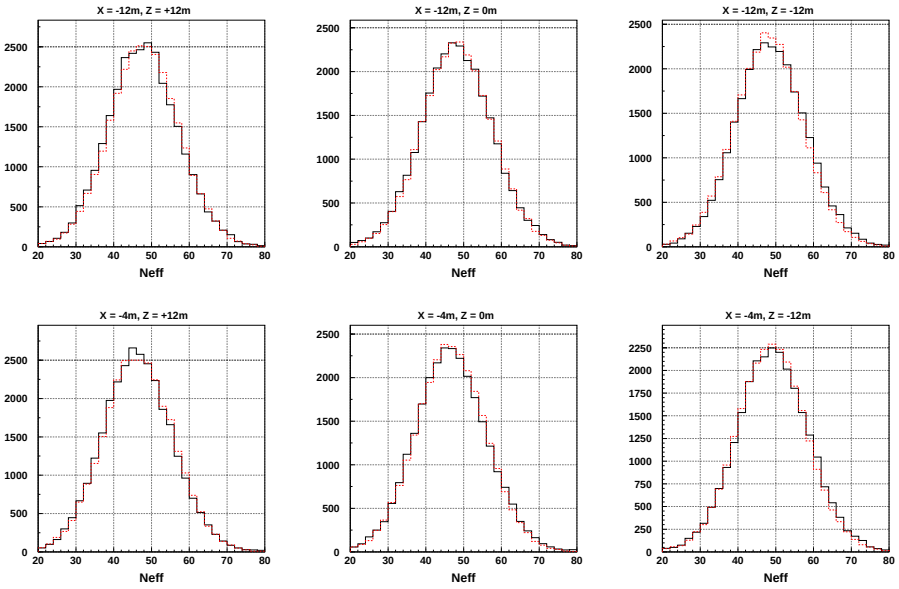

Figure 5.7: N_{eff} distribution of 7.0 MeV electrons at each six position. Solid lines show data and dashed ones show MC.

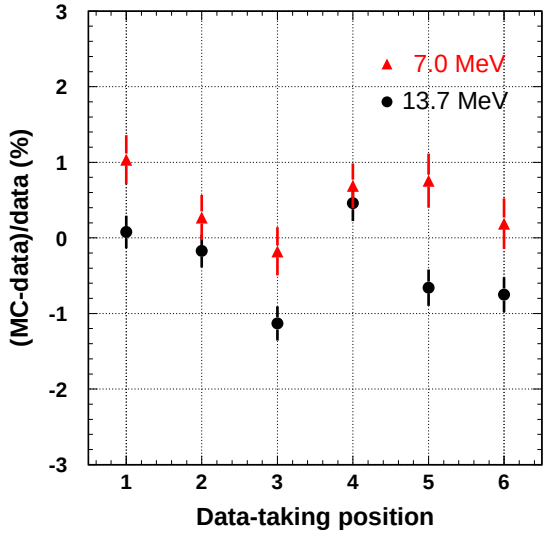

Figure 5.8: Difference of N_{eff} between data and MC at each data-taking position, where each ID number from one to six indicates the position shown in Fig. 5.1.

5.1.2 DT calibration

As well as the LINAC calibration, the decay of ^{16}N is used for the energy calibration. For that, a neutron generator of the following deuterium-tritium (DT) reaction is developed [82].

$$^{3}\mathrm{H} + {}^{2}\mathrm{H} \rightarrow {}^{4}\mathrm{He} + \mathrm{n}. \tag{5.1}$$

The neutron generator accelerates deuterium ions with a voltage of $80 - 180$ kV and collides them with a tritium target. At one pulse of collisions, approximately 10^6 neutrons are generated. The kinetic energy of this neutron is 14.1 MeV, which makes nitrogen excited states, ^{16}N*, in interacting with ^{16}O in water. The fraction of neutrons which create ^{16}N* is estimated using GEANT/CALOR [70] to be 1% and the mean distance neutrons travel in water to create ^{16}N* is about 20 cm.

The decay of ^{16}N*, which has the Q-value of 10.4 MeV and the half-life of 7.13 s, is dominated by the emission of a 4.3 MeV electron with a 6.1 MeV gamma-ray (66%) while 10.4 MeV electrons are also produced (28%). This calibration has some more advantageous points than the LINAC calibration, *e.g.*, (1) the neutron generator is easier to handle as shown in Figure 5.9, (2) we can take data in the places difficult for the LINAC calibration, and (3) ^{16}N* decay products are isotropically emitted. (2) and (3) enable us to more precisely measure the position and direction dependence of the energy scale.

Figure 5.10 and 5.11 show the position and direction dependence of the energy scale obtained by DT calibration data, which are estimated to be below 1% and 0.4%, respectively.

The comparison result of the energy scale between DT and LINAC calibration data is shown in Figure 5.12. The energy scale is consistent within 1% between the two independent calibrations.

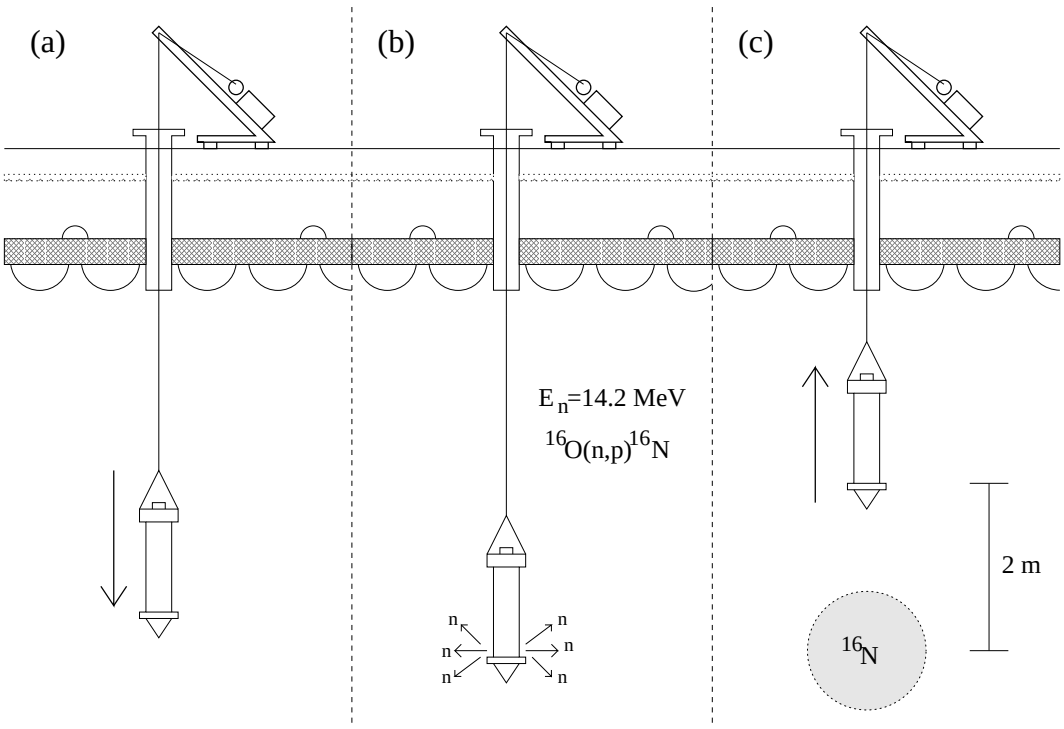

Figure 5.9: A schematic view of the setup of DT generator

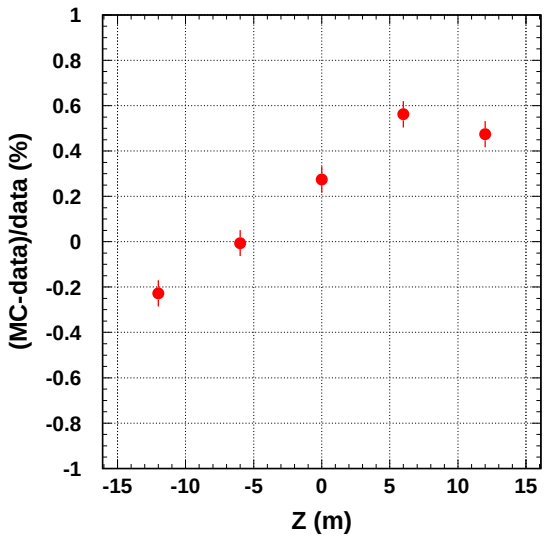

Figure 5.10: The position dependence of the energy scale obtained from DT calibration data. Z(m) is the height of the SK tank. Each data point is the position-weighted average over all data-taking positions within the fiducial volume: (X(m),Y(m))= $(-12, 7), (-4, -0.7), (0.35, -12), (-0.35, 12), (0.35, -7), (11, -0.7)$. Only statistical errors are shown.

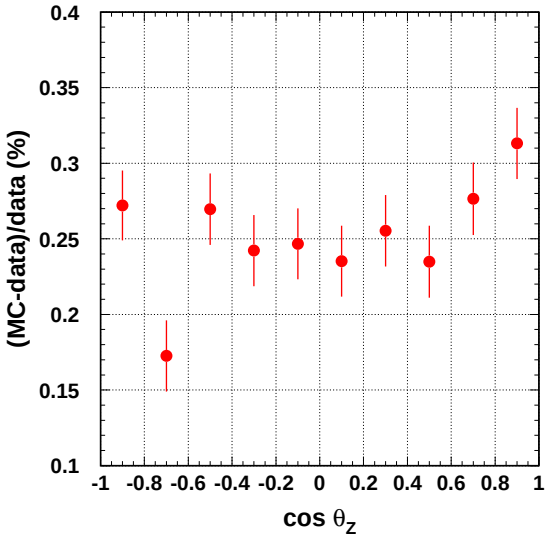

Figure 5.11: The direction dependence of the energy scale obtained from DT calibration data. Each data point is the position-weighted average over all data-taking positions within the fiducial volume. Only statistical errors are shown. The horizontal dashed line indicates the mean value for all directions.

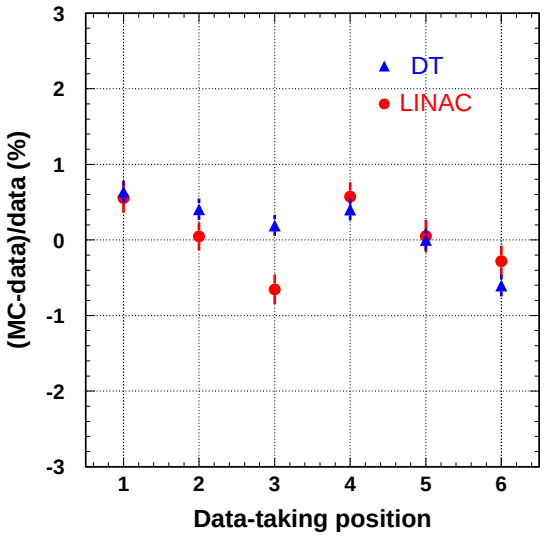

Figure 5.12: Comparison of energy scale between DT and LINAC calibration. The horizontal axis shows the positions of data taking, where each ID number from one to six indicates the position shown in Fig. 5.1. Energy scales in DT and LINAC are consistent within 1%.

5.2 Timing calibration

As explained in Section 4.1, for the reconstruction of event vertex we use the relative timing information of hit PMTs. Also, the relative timing information is necessary for the identification of T2K beam neutrino events.

The timings of PMT signals depend on the magnitude of detected charge due to the time-walk effect of discriminators. Figure 5.13 shows a two-dimensional plot called "TQ map", which shows hit timings as a function of detected charges.

A nitrogen laser generator is used for the timing calibration. This generator emits intense light with 337 nm wavelength within a time width of 3 ns. This wavelength is converted to 384 nm by a dye laser module. By using an attenuation filter, the light intensity can be changed. After passing through the filter, the laser light is injected into a diffuser ball in the tank via an optical fiber. For the uniformity of the emitted light, the injected light is diffused by MgO_2 in an acrylic ball.

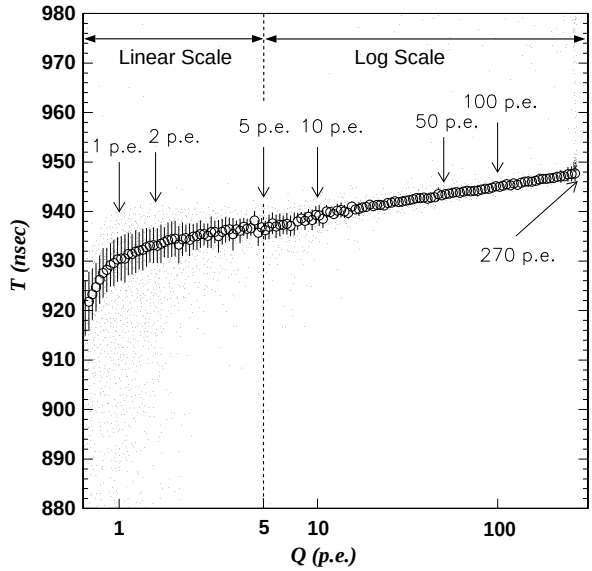

Figure 5.13: Two-dimensional plot of hit timings (T) versus detected charges (Q).

5.3 Water transparency measurement

Water transparency is defined as the light attenuation length in water,

$$L = (\alpha_{\rm abs} + \alpha_{\rm scat})^{-1}, \tag{5.2}$$

where $\alpha_{\rm abs}$ and $\alpha_{\rm scat}$ are the absorption and scattering coefficients.

The absorption coefficient $\alpha_{\rm abs}$ is known to have the z-dependence in the detector. For the analysis of this thesis, the following parameterization of the coefficient is used:

$$\alpha_{\rm abs}(\lambda) = \begin{cases} \alpha_1/\lambda^4 + \alpha_2(\lambda/500)^{\alpha_3} & (\lambda \leq \lambda_0 \text{ nm}) \\ \alpha_1/\lambda^4 + p(\lambda) & (\lambda > \lambda_0 \text{ nm}) \end{cases} \tag{5.3}$$

$$\alpha_{\rm abs}(\lambda, z) = \begin{cases} \alpha_{\rm abs}(\lambda)(1 + \beta \cdot z) & (z \geq -1200 \text{ cm}) \\ \alpha_{\rm abs}(\lambda)(1 - \beta \cdot 1200) & (z < -1200 \text{ cm}) \end{cases} \tag{5.4}$$

with $\lambda_0 = 463.918$ nm and the tuning parameter α_i and β. $p(\lambda)$ is obtained from a measurement for long wavelength water absorption [83]. As for the z-dependence, we assume there is no position dependence of the water quality below -1200 cm due to the convection of water.

The scattering in water is mainly categorized into two scattering processes. The scattering dominant for shorter wavelength, $\lambda \lesssim 450$ nm, is the Rayliegh scattering, which has a scattering angular dependence of $(1 + \cos^2\theta)$ and caused by water molecules and other tiny particles whose diameters are much smaller than the wavelength. For larger wavelength, on the other hand, the Mie scattering becomes dominant, which is caused by relatively large particles and characterized by a sharp peak in the forward direction. We parameterize the scattering coefficient as

$$\alpha_{\rm scat} = \frac{S_1}{\lambda^4}\left(1 + \frac{S_2}{\lambda^2}\right) + A_1\left(1 + \frac{A_2}{\lambda^4}(\lambda - A_3)^2\right), \tag{5.5}$$

with the tuning parameters S_i and A_i. The first term in the right hand side of Eq. (5.5) describes the symmetric scattering (the forward-backward symmetric parts of the Rayliegh and Mie scatterings), and the second term the asymmetric one (the rest of the scatterings after the subtraction of symmetric parts).

5.3.1 Measurement with lasers

One way we adopt to measure the coefficients is using lasers of various wavelengths. We use the wavelength of 337 nm from a nitrogen laser, and 375, 405 and 445 nm wavelengths from laser diodes. The laser light is injected into the detector toward the bottom via an optical fiber. Each light injector fires every six seconds during normal data taking periods.

In the analysis, the detector is divided into six regions, top and five in barrel. Figure 5.14 shows calibration data and MC simulation of PMT hit timing distributions in each region. The earlier PMT hits on the top and barrel wall are due to the photons scattered in water, and the

later hits are caused by those reflected on the surfaces of the bottom PMTs or black sheets. The absorption and scattering coefficients are tuned so that the PMT hit timing distributions of the MC agree with the calibration data.

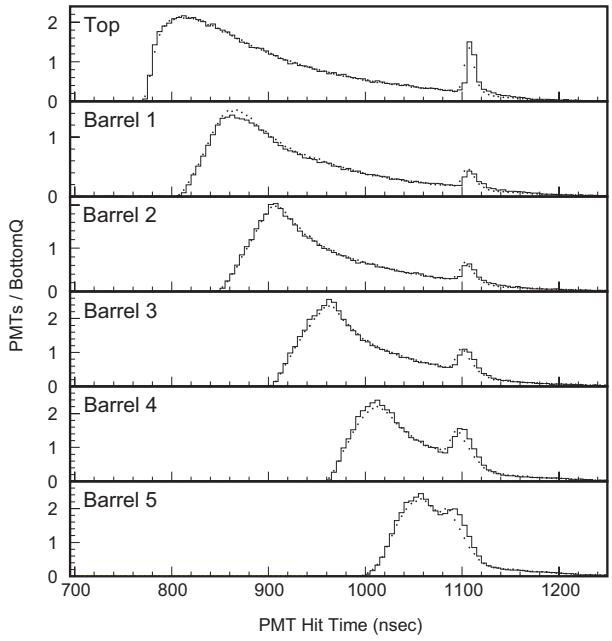

Figure 5.14: PMT hit timing distribution of 337 ns laser events in each part of the tank geometry. The dots and solid lines show the data and the MC simulated events, respectively. The earlier and later peaks correspond to the photons scattered in water and reflected on the surface of the bottom PMTs.

Figure 5.15 shows the attenuation coefficients obtained by this method. The solid line is the fitting result and the dotted lines show each component of the solid line.

5.3.2 Measurement with decay electrons from cosmic ray muons

The water transparency is independently measured by Cherenkov light of the decay electrons (positrons) from cosmic ray muons stopping inside the detector. Since the energy spectrum of the decay electron from a muon at rest is known as the Michel spectrum [84],

$$\frac{dN}{dE_e} = \frac{G_F^2}{12\pi^3} m_\mu^2 E_e^2 \left(3 - \frac{4E_e}{m_\mu}\right), \qquad E_e < \frac{m_\mu}{2}, \tag{5.6}$$

these events can be used for monitoring the water transparency. About six thousand muons stop inside the detector every day and produce decay electrons. To select decay electron events, the following selection criteria are applied: (i) the time difference between a decay electron candidate

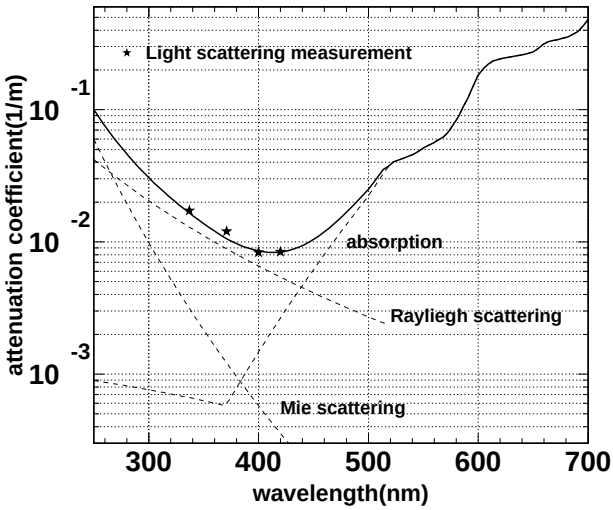

Figure 5.15: Attenuation coefficients as a function of wavelength. The data (star) and fitting results (lines) are shown.

and the preceding stopping muon is within the range of $2 - 8$ μs; (ii) the reconstructed vertex of the decay electron is within the 200 cm fiducial volume; (iii) the number of hit PMTs within 1.3 μs is above 50. By applying these criteria, about 1,500 decay electron events remain per day.

Hit PMT selection is also applied to remove the effect of scattered and reflected photons with criteria of (1) only hit PMTs in N_{50} are used, (2) all hit PMTs are required to be between 32° and 52° with respect to the reconstructed direction.

The logarithm of the charge of hit PMTs is then plotted as a function of the distance between the reconstructed vertex of the decay electron and each hit PMT. Fitting the histogram with a line, the water transparency is calculated from the slope of the line. Figure 5.16 shows the time variation of the water transparency obtained by this method.

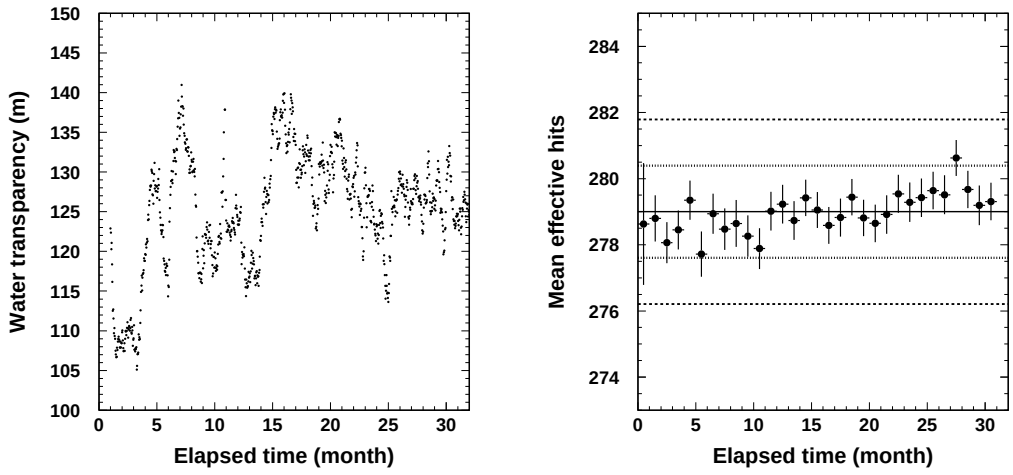

Figure 5.16: Time variation of the transparency (left) and stability of the energy scale (right) measured using decay electron events. In both panels, horizontal axis shows the elapsed months from the start of SK-IV. In the right panel, the error bars are only statistical errors and the central horizontal line shows the time-averaged hits (279.0) and the $\pm 0.5\%$ and $\pm 1\%$ deviations from the average are also shown by dashed-dotted and dashed lines, respectively.

Chapter 6

Event Simulation

6.1 T2K neutrino flux

As mentioned in Chapter 2, the expected fluxes of T2K beam neutrinos at SK are obtained by extrapolating the tracks of neutrinos in the beam Monte Carlo (MC) to the SK detector. The predicted fluxes at the near and far detector sites are shown in Fig. 2.5. Most of the beam neutrinos are in the energy range from $0.1 - 1$ GeV, and the peak energy is similar to that of atmospheric neutrinos (Fig. 1.2).

6.2 Neutrino interaction

The interaction of T2K beam neutrinos with components of water molecules in the SK detector is simulated by the NEUT neutrino interaction event generator [85,86], which is also used for the MC simulation of INGRID and ND280.

In NEUT, the following charged-current (CC) and neutral-current (NC) interactions are simulated,

1. CC/NC (quasi) elastic scattering $\quad \nu + N \rightarrow l + N'$,
2. CC/NC single meson production $\quad \nu + N \rightarrow l + N' + \text{meson} \quad (W \leq 2.0 \text{ GeV})$,
3. CC/NC deep inelastic scattering $\quad \nu + N \rightarrow l + N' + \text{hadrons} \quad (W > 1.3 \text{ GeV})$,
4. CC/NC coherent pion production $\quad \nu + {}^{16}\text{O} \rightarrow l + {}^{16}\text{O} + \pi$,

where ν denotes a neutrino or anti-neutrino, N and N' are a nucleon, l is a lepton, and W is the invariant mass of the hadronic system. Since NEUT has been developed for the simulation of the interaction of atmospheric neutrinos in a detector, it is also suitable for the simulation of the interaction of T2K beam neutrinos, where the energies of the beam neutrinos are similar to those of atmospheric neutrinos. The neutrino-electron scattering is neglected due to its much smaller cross section.

6.2.1 Charged-current quasi-elastic scattering

The differential cross section of the charged-current quasi-elastic (CCQE) scattering for free protons is given by [87, 91]

$$\frac{d\sigma^{\nu(\bar{\nu})}}{dq^2} = \frac{M^2 G_F^2 \cos^2\theta_C}{8\pi E_\nu^2}\left[A(q^2) \pm B(q^2)\frac{s-u}{M^2} + C(q^2)\frac{(s-u)^2}{M^4}\right], \tag{6.1}$$

where E_ν is the neutrino energy, $M = 0.938$ GeV is the nucleon mass , G_F is the Fermi coupling constant, θ_C is the Cabibbo angle, $q = p_\nu - p_{l^\pm}$ is the four-momentum transfer, and s and u are Mandelstam variables[1)] [87]. With $\tau = -q^2/4M^2$, the factors A, B and C are written as

$$\begin{aligned}
A(\tau) &= \left(4\tau + \frac{m^2}{M^2}\right)\left[(1+\tau)|F_A|^2 - (1-\tau)|F_V^1|^2 + \tau(1-\tau)|F_V^2|^2\right. \\
&\quad \left. +4\tau F_V^1 F_V^2 - \frac{m^2}{4M^2}\left(\left(F_V^1 + F_V^2\right)^2 + |F_A|^2 + 4F_A F_p - 4\tau|F_p|^2\right)\right], \\
B(\tau) &= 4\tau F_A(F_V^1 + F_V^2), \\
C(\tau) &= \frac{1}{4}\left(|F_A|^2 + |F_V^1|^2 + \tau|F_V^2|^2\right),
\end{aligned} \tag{6.2}$$

where m is the outgoing lepton mass. The form factors, F_V^i, F_A and F_p are experimentally determined and given by

$$\begin{aligned}
F_V^1 &= \frac{G_E^V + \tau G_M^V}{1+\tau}, \qquad F_V^2 = \frac{G_M^V - G_E^V}{1+\tau}, \\
F_A &= g_A\left(1 - \frac{q^2}{M_A^2}\right)^{-2}, \qquad F_p = \frac{2M^2 F_A}{m_\pi^2 - q^2},
\end{aligned} \tag{6.3}$$

where $M_A = 1.21$ GeV is the axial-vector mass and $g_A = -1.267$ is the axial-vector weak coupling constant, which is measured precisely from neutron beta decay [28]. For the charged pion mass $m_\pi = 0.13957$ GeV is used.

For the electric and magnetic form factors, G_E^V and G_M^V, the following two parameterizations are prepared in NEUT.

1. Dipole parameterization

   Here, we parameterize nucleon form factors as

$$\begin{aligned}
G_E^V &= (1+\xi)^{-1} G_M^{V,0} = \left(1 - \frac{q^2}{M_V^2}\right)^{-2}, \\
G_M^V &= G_M^{V,0} \times \sqrt{1 - Aq^2 e^{q^2/B}},
\end{aligned} \tag{6.4}$$

[1)] $s - u = 4ME_\nu + q^2 - m^2$

Table 6.1: Parameters used for the nucleon elastic form factors from Ref. [89]. μ_p and μ_n are set to 2.793 and -1.913, respectively.

Form factor	μ	a_0	a_1	a_2	b_1	b_2	b_3	b_4
G_E^p	1	1	-0.0578	0	11.1	13.6	33.0	0
G_M^p	μ_p	1	0.15	0	11.1	19.6	7.54	0
G_E^n	1	0	1.25	1.3	-9.86	305	-758	802
G_M^n	μ_n	1	1.81	0	14.1	20.7	68.7	0

where $M_V = 0.84$ GeV is the vector mass and $\xi \equiv \mu_p^a - \mu_n^a = 3.706$ is the difference between the proton and neutron anomalous magnetic moments in units of the nuclear magneton ($\mu_p^a = \mu_p - 1 = 1.793$, $\mu_n^a = \mu_n = -1.913$). The correction of magnetic form factors in the latter equation represents the effect of the transverse enhancement, where the parameters $A = 6.0$ and $B = 0.34$ GeV^2 are from Ref. [88].

2. BBBA05 parameterization

   This parameterization is from Ref. [89]:

$$G_E^V = G_E^p - G_E^n, \qquad G_M^V = G_M^p - G_M^n,$$

$$G_{E,M}^{p,n} = \mu \frac{\sum_{k=0}^{2} a_k \tau^k}{1 + \sum_{k=1}^{4} b_k \tau^k} \tag{6.5}$$

   with parameters μ, a_k and b_k for each $G_{E,M}^{p,n}$ are summarized in Tab. 6.1. Figure 6.1 shows the comparison results between the BBBA05 and conventional dipole form factors.

Figure 6.2 shows the resultant differential cross sections of the CCQE scattering as a function of Q^2, and the difference of the cross sections between the two parameterizations. We use the dipole form factors by default for CCQE, and the effect of the difference between the two parameterizations is included as a systematic uncertainty in the cross section.

For scattering off nucleons in ^{16}O, the Fermi motion of the nucleons and Pauli blocking effect are taken into account [92]. NEUT uses the momentum distribution of nucleons in ^{16}O estimated from the experimental data of electron ^{12}C scattering [93], and the momentum dependent nuclear potential calculated by Brieva *et al* [94]. Assuming the Fermi gas model, the momentum of the recoil nucleon is required to be greater than the Fermi surface momentum of 225 MeV/c for a quasi-elastic scattering to occur.

Figure 6.3 shows the total cross section of the CCQE interaction measured by several experiments and our simulation by NEUT using the dipole parameterization for nucleon form factors. Figure 6.4 shows the low energy region for the cross section of CCQE interactions with free nucleons and bound nucleons in oxygen nuclei, used in the NEUT simulation.

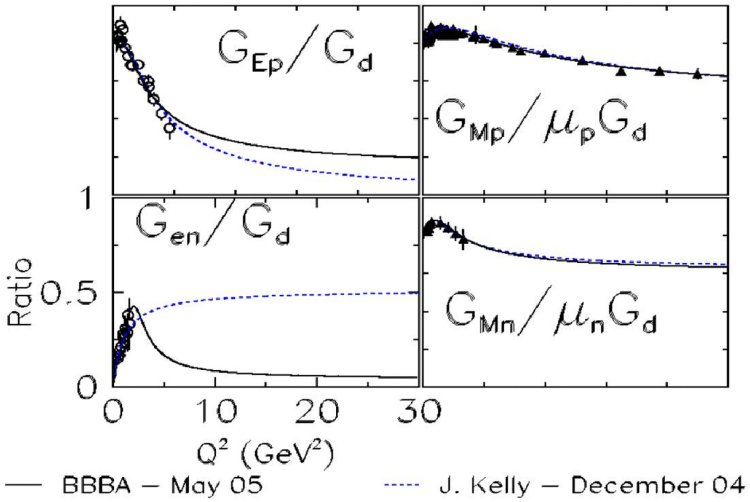

Figure 6.1: The black solid line shows the ratio of the BBBA05 form factors [89] to a dipole form factor $G_d = (1 + Q^2/M_V^2)^{-2}$, $Q^2 = -q^2$, $M_V^2 = 0.71$ GeV^2, and the blue dashed line is the ratio of the Kelly form factors [90] to G_d. In all panels, an x-axis is Q^2 ranging from 0 to 30 GeV^2 and a y-axis is the ratio ranging from 0 to 1. This plot is from Ref. [89].

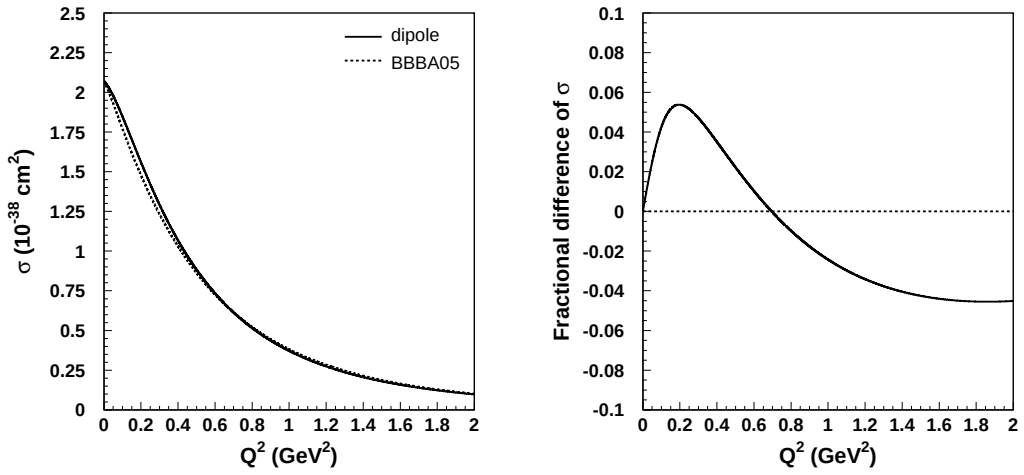

Figure 6.2: The left panel shows the differential cross sections of the CCQE scattering as a function of Q^2 at neutrino energy of 2 GeV. Solid lines show those with dipole form factors and dashed lines show those with the BBBA05 form factors. The right panel shows the fractional difference, 2× (dipole-BBBA05)/(dipole+BBBA05), of the cross sections calculated with the two different form factors.

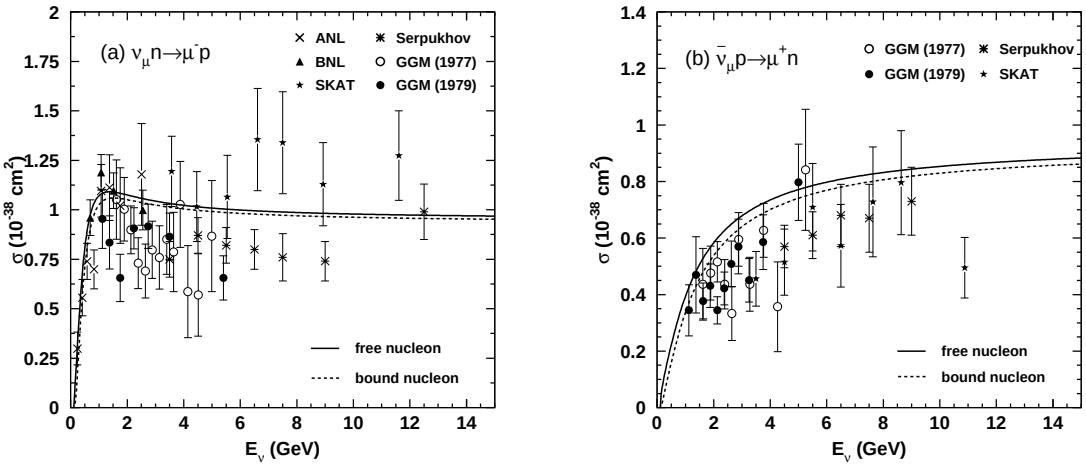

Figure 6.3: The total cross sections of (a) $\nu_\mu + n \to \mu^- + p$ and (b) $\bar{\nu}_\mu + n \to \mu^+ + p$ with experimental data from ANL [95], Gargamelle [96,97], BNL [98], Serpukhov [99] and SKAT [100].

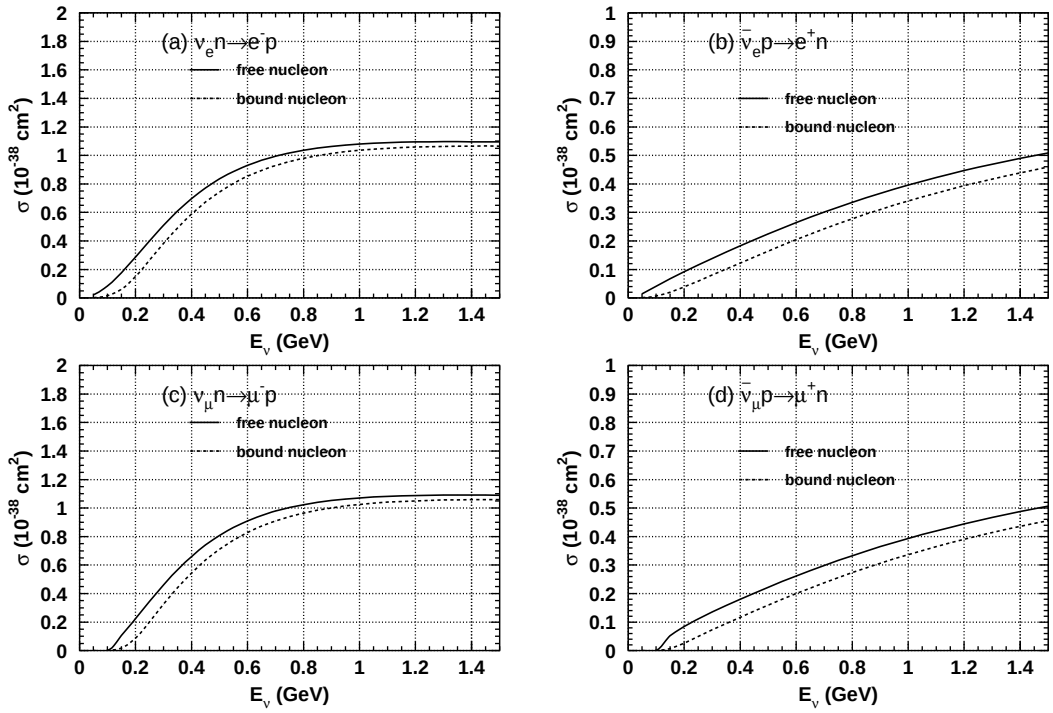

Figure 6.4: The total cross sections of CCQE interaction in the low energy region for (a) ν_e, (b) $\bar{\nu}_e$, (c) ν_μ and (d) $\bar{\nu}_\mu$. The solid (dashed) lines show the cross-sections for free (bound) nucleon.

6.2.2 Neutral-current elastic scattering

The differential cross section for NC elastic scattering has the same form as Eq. (6.1), but $\cos\theta_C$ is replaced by unity, and nucleon form factors are replaced by the corresponding NC nucleon form factors:

$$\begin{aligned}
\tilde{F}_V^{1,N} &= \pm\frac{1}{2}F_V^1 - 2\sin^2\theta_W \cdot F_N^1, \\
\tilde{F}_V^{2,N} &= \pm\frac{1}{2}F_V^2 - 2\sin^2\theta_W \cdot F_N^2,
\end{aligned}$$

$$\begin{aligned}
F_V^1 &= \frac{\tilde{G}_E^V + \tau\tilde{G}_M^V}{1+\tau}, \qquad F_V^2 = \frac{\tilde{G}_M^V - \tilde{G}_E^V}{1+\tau}, \\
F_N^1 &= \frac{\tilde{G}_E^N + \tau\tilde{G}_M^N}{1+\tau}, \qquad F_N^2 = \frac{\tilde{G}_M^N - \tilde{G}_E^N}{1+\tau}, \\
\tilde{F}_A &= \frac{1}{2}(F_A^s \pm F_A) = \frac{1}{2}(\Delta s \pm g_A)\left(1 - \frac{q^2}{M_A^2}\right)^{-2}, \\
\tilde{F}_p &= \frac{2M^2\tilde{F}_A}{m_\pi^2 - q^2},
\end{aligned} \tag{6.6}$$

where $N = p, n$ and the upper (lower) sign is for proton (neutron). In NEUT, the weak mixing angle is set to $\sin^2\theta_W = 0.23117$, and the strange quark contribution Δs is set to 0.

As in the case of the CCQE interaction, we also prepare two types of parameterizations for the NC elastic scattering. Dipole nucleon form factors need to be replaced:

$$\begin{aligned}
\tilde{G}_E^V &= \tilde{G}_E^p - \tilde{G}_E^n, \qquad \tilde{G}_M^{V,0} = \tilde{G}_M^p - \tilde{G}_M^n, \\
\tilde{G}_M^V &= \tilde{G}_M^{V,0} \times \sqrt{1 - Aq^2 e^{q^2/B}}, \\
\tilde{G}_E^p &= \frac{\tilde{G}_M^p}{\mu_p} = \frac{\tilde{G}_M^n}{\mu_n} = \left(1 - \frac{q^2}{M_V^2}\right)^{-2}, \qquad \tilde{G}_E^n = 0.
\end{aligned} \tag{6.7}$$

Figure 6.5 shows the resultant differential cross sections as a function of Q^2 for protons and neutrons, and the difference of the cross sections between the two parameterizations. We use the BBBA05 form factors by default for the NC elastic scattering, and the effect of the difference between the two parameterizations is included as a systematic uncertainty in the cross section.

6.2.3 Charged/Neutral-current single meson production

The resonant single meson production is simulated based on the Rein-Sehgal model [101]. This model assumes an intermediate baryon resonance,

$$\nu + N \to l + N^*, \tag{6.8}$$

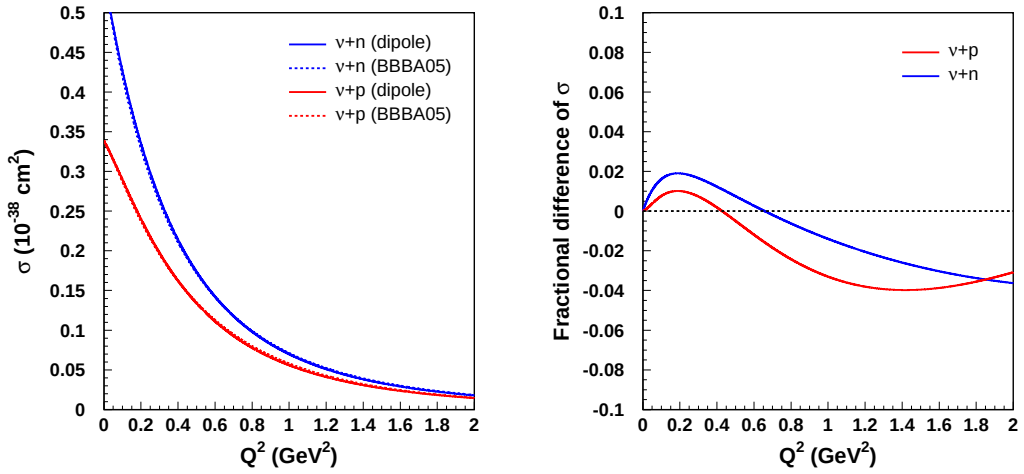

Figure 6.5: The left panel shows the differential cross sections of the NC elastic scattering as a function of Q^2 for free protons and neutrons at the neutrino energy of 2 GeV. Solid lines show those with dipole form factors and dashed lines show those with the BBBA05 form factors. The right panel shows the fractional difference, 2× (dipole-BBBA05)/(dipole+BBBA05), of the cross sections calculated with the two different form factors.

where N and N^* denote the nucleon and its resonance, and l is a lepton. The differential cross section of a single resonance production with a negligible decay width is written as,

$$\frac{d\sigma}{dq^2 dE_\nu} = \frac{1}{32\pi M E_\nu^2} \cdot \frac{1}{2} \cdot \sum_{\text{spins}} |T(\nu N \to l N^*)|^2 \delta(W^2 - M_*^2), \tag{6.9}$$

where M and M_* are the masses of the nucleon and its resonance, E_ν is neutrino energy, W is the invariant mass of the hadronic system, and $T(\nu N \to l N^*)$ is the amplitude of the resonance production, which is calculated using the Feynman-Kislinger-Ravndal (FKR) model [102]. For a baryon resonance with a finite decay width, the differential cross section is derived by replacing the δ-function in Eq. (6.9) with a Breit-Wigner factor,

$$\delta(W^2 - M_*^2) \to \frac{1}{2\pi} \cdot \frac{\Gamma}{(W - M_*)^2 + \Gamma^2/4}. \tag{6.10}$$

The cross section of a single meson production is obtained by multiplying the cross section of each resonance production by the probability of the resonance decay into the meson. In NEUT, 18 baryon resonances with the invariant mass of $W < 2.0$ GeV/c^2 are simulated. The interactions with $W > 2.0$ GeV/c^2 are simulated as deep inelastic scattering (DIS). The axial-vector mass M_A is set to the common value of 1.21 GeV as in the quasi-elastic scattering. The Pauli blocking effect is taken into account. For the pion-less delta decay, 20% of resonances are required to

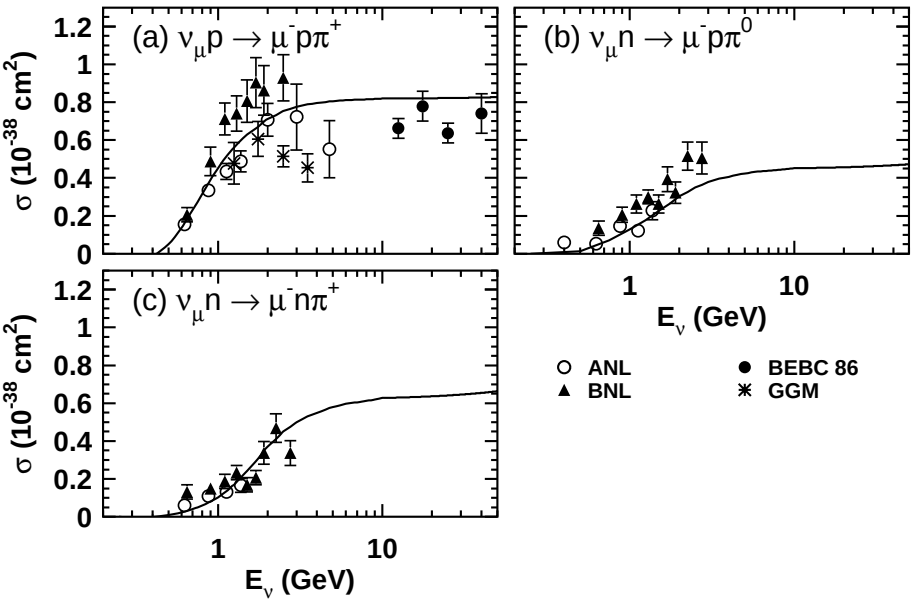

Figure 6.6: The total cross sections for ν_μ CC 1π productions. (a) $\nu_\mu p \to \mu^- p \pi^+$, (b) $\nu_\mu n \to \mu^- p \pi^0$, (c) $\nu_\mu n \to \mu^- n \pi^+$. Solid lines show our simulation. Experimental data are from ANL [103], BNL [104], BEBC [105, 106] and Gargamelle [107].

decay only to a lepton and a nucleon. In addition to the baryon resonance decay into π, decays to η and K mesons are also simulated.

Figures 6.6 and 6.7 show experimental data of the total cross sections of CC resonant single-pion productions and our simulation. Figures 6.8 shows the simulation of the total cross section of NC resonant single pion production.

6.2.4 Charged/Neutral-current deep inelastic scattering

The cross section of CC deep inelastic scattering (DIS) is calculated by integrating the following equation in the range of the invariant mass $W > 1.3$ GeV/c^2 [110],

$$\frac{d^2\sigma^{\nu,\bar{\nu}}}{dxdy} = \frac{G_F^2 M E_\nu}{\pi}\left(\left(1 - y + \frac{y^2}{2} + C_1\right) F_2(x,q^2) \pm y\left(1 - \frac{y}{2} + C_2\right) xF_3(x,q^2)\right) \tag{6.11}$$

with

$$\begin{aligned} C_1 &= \frac{ym^2}{4ME_\nu x} - \frac{xyM}{2E_\nu} - \frac{m^2}{4E_\nu^2} - \frac{m^2}{2ME_\nu x}, \\ C_2 &= -\frac{m^2}{4ME_\nu x}, \end{aligned}$$

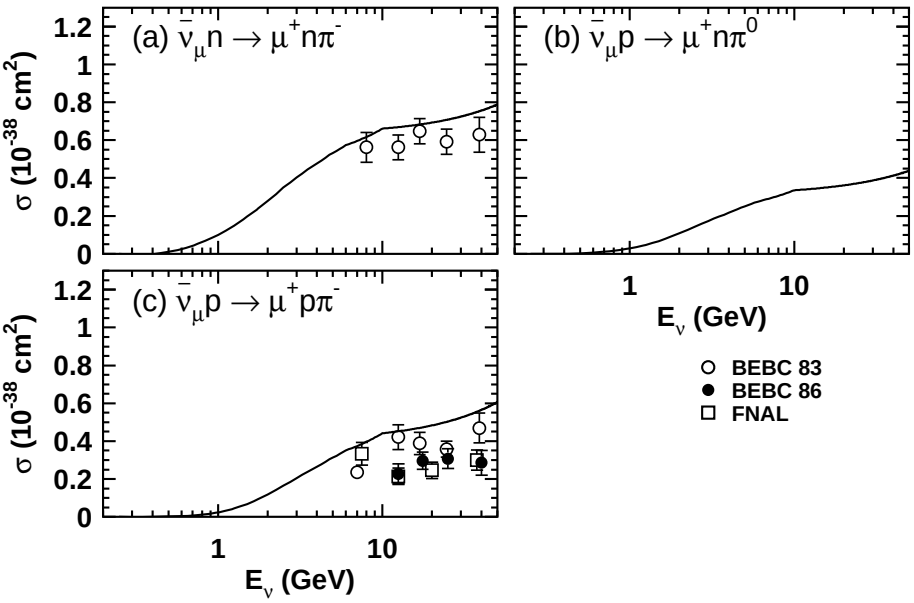

Figure 6.7: The total cross sections for $\bar{\nu}_\mu$ CC 1π productions. (a) $\bar{\nu}_\mu n \to \mu^+ n\pi^-$, (b) $\bar{\nu}_\mu p \to \mu^+ n\pi^0$, (c) $\bar{\nu}_\mu p \to \mu^+ p\pi^-$. Solid lines show the result of our simulation. Experimental data are from BEBC [108] and FNAL [109].

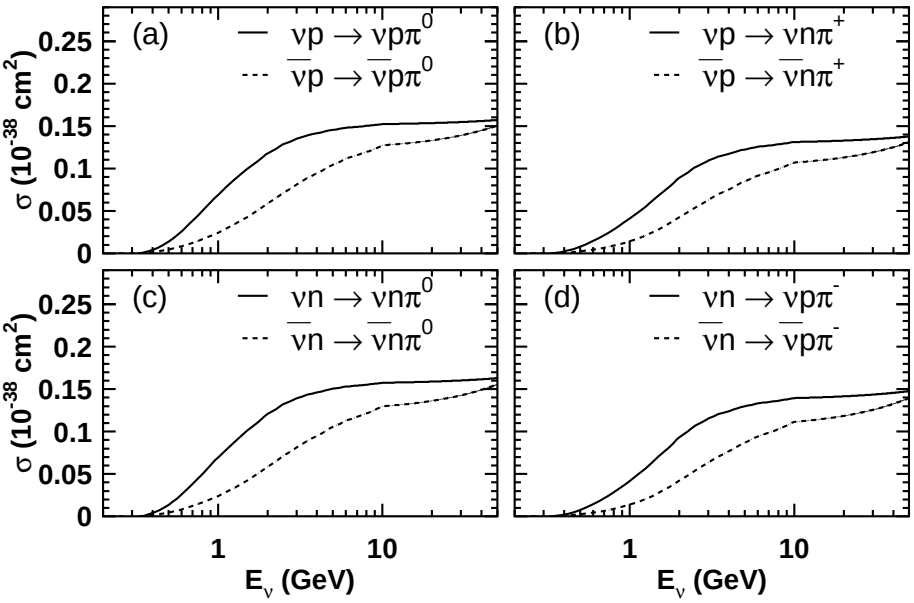

Figure 6.8: The total cross sections for ν_μ ($\bar{\nu}_\mu$) NC 1π productions. Solid (dashed) lines show the result of our simulations for ν_μ ($\bar{\nu}_\mu$) interactions.

where $x = -q^2/2M(E_\nu - E_l)$ and $y = (E_\nu - E_l)/E_\nu$ are the Bjorken scaling parameters, E_ν and E_l are the energy of the incoming neutrino and outgoing lepton in the laboratory frame, respectively. The nucleon structure functions F_2 and xF_3 are taken from GRV98 [111] with corrections proposed by Bodek and Yang [112] to improve the agreement with the experiments in the low Q^2 region.

In NEUT, the ratios of the NC DIS to CC DIS cross sections are set to

$$\frac{\sigma(\nu N \to \nu X)}{\sigma(\nu N \to \mu^- X)} = \begin{cases} 0.26 & (E_\nu < 3 \text{ GeV}) \\ 0.26 + 0.04(E_\nu/3 - 1) & (3 \leq E_\nu < 6 \text{ GeV}) \\ 0.30 & (E_\nu \geq 6 \text{ GeV}) \end{cases} \tag{6.12}$$

$$\frac{\sigma(\bar{\nu} N \to \bar{\nu} X)}{\sigma(\bar{\nu} N \to \mu^+ X)} = \begin{cases} 0.39 & (E_\nu < 3 \text{ GeV}) \\ 0.39 - 0.02(E_\nu/3 - 1) & (3 \leq E_\nu < 6 \text{ GeV}) \\ 0.37 & (E_\nu \geq 6 \text{ GeV}) \end{cases} \tag{6.13}$$

which are estimated from experimental results [113, 114].

The kinematics of the hadronic system is simulated by two different methods according to the range of the invariant mass. In the region of $1.3 < W < 2.0$ GeV/c^2, only pions are considered as outgoing mesons. The mean multiplicity of charged pions is estimated from the result of the Fermilab 15-foot hydrogen bubble chamber experiment [115],

$$\langle n_\pi \rangle = 0.09 + 1.83 \ln W^2 \tag{6.14}$$

The number of pions in each event is determined by using the Koba-Nielsen-Olsen (KNO) scaling, which reproduces well the BEBC data for the process $\nu p \to \mu^- X^{++}$ [116, 117]. To avoid double counting with the single pion production, $n_\pi \geq 2$ is required in this W region. The forward-backward asymmetry of pion multiplicity in the hadronic center of mass system is included using the results from the BEBC experiment [118],

$$\frac{n_\pi^F}{n_\pi^B} = \frac{0.35 + 0.41 \ln W^2}{0.5 + 0.09 \ln W^2} \tag{6.15}$$

In the region of $W > 2.0$ GeV/c^2, the kinematics of the hadronic system is calculated by using the PHYTIA/JETSET package [119].

6.2.5 Charged/Neutral-current coherent pion production

It is possible for a pion with the same electric charge as the incoming weak current to be produced in a coherent interaction of the neutrino with an oxygen nucleus in a water Cherenkov detector. Since little momentum is transferred to the oxygen nucleus, the angular distributions of the outgoing lepton and pion tend to peak at the forward direction. The formalism developed by Rein and Sehgal [120] is used to simulate the interaction, and the differential cross section is given by

$$\frac{d^3\sigma}{dxdyd|t|} = \frac{G_F^2 M E_\nu}{\pi^2}\frac{\beta}{2} f_\pi^2 (1-y)\frac{d\sigma(\pi^{16}\mathrm{O}\to\pi^{16}\mathrm{O})}{d|t|}\left(1-\frac{q^2}{M_A^2}\right)^{-2} \tag{6.16}$$

with

$$\frac{d\sigma(\pi^{16}\mathrm{O}\to\pi^{16}\mathrm{O})}{d|t|} = A^2 \exp\left(-\frac{R^2|t|}{3}\right) F_{\mathrm{abs}} \left.\frac{d\sigma(\pi N\to\pi N)}{d|t|}\right|_{t=0},$$
$$\left.\frac{d\sigma(\pi N\to\pi N)}{d|t|}\right|_{t=0} = \frac{1}{16\pi}(\sigma_{\mathrm{tot}}^{\pi N})^2\left\{1+\left(\frac{\mathrm{Re}f_{\pi N}(0)}{\mathrm{Im}f_{\pi N}(0)}\right)^2\right\}, \tag{6.17}$$

where t is the square of the four-momentum transfer to the nucleus, β is the axial-vector coupling constant[2)], $f_\pi = 0.93 m_\pi$ is the pion decay constant, $A = 16$ is the atomic number of oxygen, R is the oxygen's radius, $\sigma_{\mathrm{tot}}^{\pi N}$ is the average pion-nucleon cross section, and $f_{\pi N}(0)$ is the πN scattering amplitude. F_{abs} represents the effects of pion absorption in oxygen,

$$F_{\mathrm{abs}} = \exp\left(-\frac{9A}{16\pi R^2}\sigma_{\mathrm{inel}}\right), \tag{6.18}$$

where σ_{inel} is the inelastic πN cross section which is taken from the data tables [121]. The K2K experiment at an average neutrino energy $E_\nu = 1.3$ GeV set an upper bound on the coherent pion production [122], which is significantly lower than the predicted cross section by Rein and Sehgal. The cross section later calculated by Kartavtsev and Paschos [123] agree better with several experimental data. In this thesis, however, the model of Rein and Sehgal is used since the difference between two models is expected to have little effect on this analysis.

6.2.6 Nuclear effects

The hadrons resulting from the neutrino interactions with oxygen then propagate through the nuclear medium before escaping from the nucleus. The re-interaction within the nucleus prior to escape is referred to as a "final state interaction (FSI)". FSI can affect the observable final state through particle absorption, scattering and particle production[3)].

We can safely ignore FSI for leptons since they rarely interact with the nuclear medium. Also, FSI is not considered for hadrons produced off hydrogen in water.

Pion nuclear effect

In NEUT, the following pion FSI are included: quasi-elastic (QE) scattering, absorption, hadron production and charge exchange. Figure 6.9 shows the cross section of $\pi^+ + {}^{16}\mathrm{O}$ with experimental data [124] and Fig. 6.10 shows the probability of $\pi^0 + {}^{16}\mathrm{O}$ interaction.

[2)] $\beta = 1$ for neutral-current and $\beta = 2$ for charged-current.

[3)] For example, NC π interactions with the absorption of all pions would contaminate an NC elastic measurement.

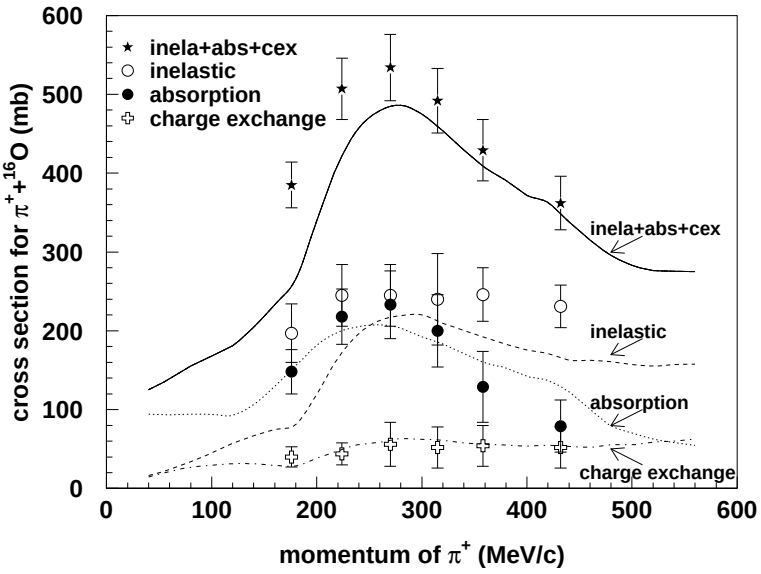

Figure 6.9: The cross section of π^+-^{16}O interaction as a function of π^+ momentum. Lines show the result of Monte Carlo simulation, and data points are taken from experimental data [124].

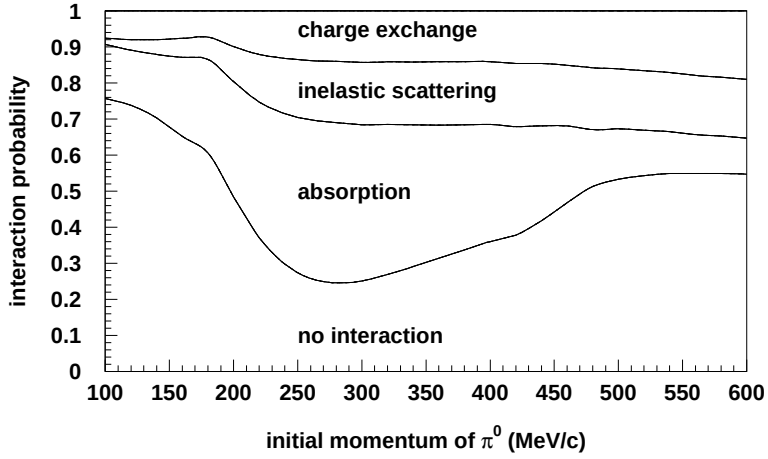

Figure 6.10: The probability of π^0+^{16}O interaction obtained from Monte Carlo simulation.

The neutrino-nucleon vertex is determined according to the Woods-Saxon type nucleon density ditribution for $N = p$ or n:

$$\rho_N(\boldsymbol{r}) = f_N \cdot \bar{\rho} \left\{ 1 + \exp\left(\frac{|\boldsymbol{r}| - c}{a} \right) \right\}^{-1}, \tag{6.19}$$

where $\boldsymbol{r}$ is the position relative to the center of the nucleus, f_p (f_n) is the number fraction of proton (neutron) in nucleus and $\bar{\rho} = 0.48 m_\pi^3$ is the average density of nucleus. Two parameters a and c are the surface thickness and nuclear radius, which are determined from electron scattering data [125]. For oxygen, the values of $f_N = 0.5$, $a = 1.80/(4 \ln 3) = 0.41$ fm and $c = 2.69$ fm are used. The interaction mode is determined by using the calculated mean free path of each interaction, where the calculation is based on the model by Salcedo *et al.* [126]. In calculating the pion scattering amplitude, the Pauli blocking effect is taken into account by requiring the nucleon momentum after interaction to be above the Fermi surface momentum at the interaction vertex position, $\boldsymbol{x}_i$, *i.e.*,

$$p_F(\boldsymbol{x}_i) = \left(\frac{3}{2} \pi^2 \rho_N(\boldsymbol{x}_i) \right)^{-\frac{1}{3}}. \tag{6.20}$$

The kinematics of the outgoing pion and nucleon after a QE scatter are determined from phase shift fits to free $\pi^{\pm} p$ data [127]. The calculation of pion interaction is tested by using existing experimental data of π^{12}C and π^{16}O scattering [124,128], and photo-π production, $^{12}\mathrm{C}(\gamma, \pi^-)$ [129, 130].

Nucleon nuclear effect

For the nucleon rescattering, the same cascade model as the pion simulation is used. The used cross section is based on nucleon-nucleon scattering experiments [131]. The pion production caused by the decay of a produced Δ-resonance is also simulated according to the Sternheimer-Lindenbaum isobar model [132]. These pions are then propagated through the cascade. Secondaries resulting from these pions undergoing hadron production are not tracked and assumed to immediately escape.

6.3 Nuclear de-excitation in NC neutrino-oxygen interaction

When neutrinos interact with ^{16}O via the neutral-current (NC) channel, the dominant interaction at $E_\nu \lesssim 200$ MeV is the inelastic process,

$$\nu + {}^{16}\mathrm{O} \rightarrow \nu + {}^{16}\mathrm{O}^*, \tag{6.21}$$

Some of the ^{16}O* then decay to $p + {}^{15}\mathrm{N}^*$, or $n + {}^{15}\mathrm{O}^*$, and the residual nuclei left in excited states quickly de-excite by emitting gamma-rays of up to 10 MeV, which we call prompt gamma-rays.

In the higher energy region $E_\nu \gtrsim 200$ MeV, however, the cross section associated with the inelastic scattering saturates, and the quasi-elastic (QE) nucleon knockout,

$$\begin{aligned} &\nu + {}^{16}\mathrm{O} \rightarrow \nu + {}^{15}\mathrm{N}^* + p, \\ &\nu + {}^{16}\mathrm{O} \rightarrow \nu + {}^{15}\mathrm{O}^* + n, \\ &\nu + {}^{16}\mathrm{O} \rightarrow \nu + {}^{14}\mathrm{N}^* + p + n, \\ &\qquad\vdots \end{aligned} \tag{6.22}$$

becomes dominant, where dots in the equation indicate the other similar reactions including more than one escape nucleon from the nucleus due to FSI. Since the neutrino energy of the T2K beam is about 600 MeV, nuclear de-excitation gamma-ray events observed at T2K are expected to be dominantly induced by the QE interaction (6.22) rather than the inelastic process (6.21). Figure 6.11 shows the multiplicity of escape nucleons from the nucleus, which is simulated by NEUT using the expected T2K beam ν_μ flux, where the dominant process is that of single nucleon escape. If the residual nucleus in (6.22) is excited to states below the particle emission threshold, then it de-excites by emitting prompt gamma-rays in the same way as the inelastic processes. On the other hand, if the residual nucleus is excited to higher states than the threshold, it emits a nucleon or heavier nuclear fragment such as a deuteron, triton, helion or alpha. Hereafter we denote the resultant system from the decay of the residual nucleus as Φ, *i.e.*, the interaction is written as $\nu + {}^{16}\mathrm{O} \rightarrow \nu + \Phi + N + N' + \ldots$, where N, N', $\cdots$ denote single or multi nucleon knock-out[4)].

The production cross section of each resultant system Φ produced in an NCQE interaction with ^{16}O, denoted as σ_Φ, is written as the sum of the product of the neutrino NC elastic cross section with a nucleon, which is one of the inner-shell orbits of ^{16}O, and the branching ratio of each Φ produced from the decay of the nucleon-hole state. Averaging the dependence of the bound nucleon cross section on nucleon state in the nucleus, the production cross section is written as

$$\begin{aligned} \sigma_\Phi &\equiv \sigma(\nu + {}^{16}\mathrm{O} \rightarrow \nu + \Phi + N + N' + \ldots) \\ &\simeq \sigma_{\nu^{16}\mathrm{O}} \sum_i \mathrm{Br}(\mathrm{X}_i^* \rightarrow \Phi), \end{aligned} \tag{6.23}$$

[4)] For example, $\Phi = {}^{14}\mathrm{N} + n$, ${}^{14}\mathrm{C} + p$, $\cdots$ in the case of $N = p$.

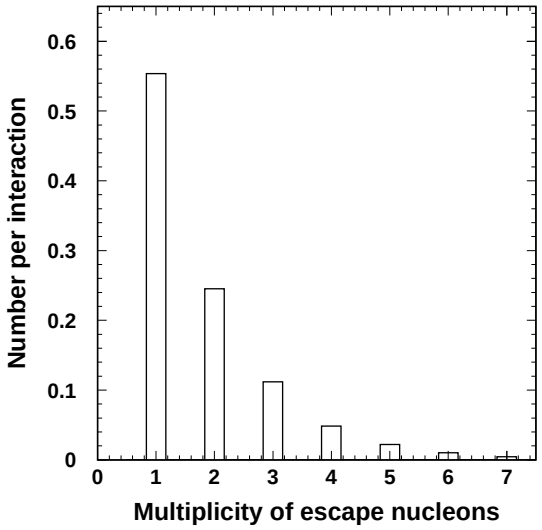

Figure 6.11: Multiplicity of escape nucleons after FSI inside the nucleus simulated by NEUT using the expected T2K beam ν_μ flux.

where X_i^* is the $1p_{1/2}$, $1p_{3/2}$, $1s_{1/2}$ and other proton hole states of ^{15}N, or the corresponding neutron hole states of ^{15}O, and i discriminates different quantum states in each shell. Since we do not have experimental data of the de-excitations from a multi-nucleon hole state appropriate for this description, we approximated those de-excitations as that from a single nucleon hole state. $\sigma_{\nu^{16}\mathrm{O}}$ is the total NCQE cross section, described as follows.

6.3.1 NCQE neutrino-nucleus scattering

The total NCQE cross section $\sigma_{\nu^{16}\mathrm{O}}$ in Eq. (6.23) is calculated using the impulse approximation and the spectral function [133] as follows:

$$\frac{d^2\sigma_{\nu^{16}\mathrm{O}}}{d\Omega dE'_\nu} = \sum_{N=p,n} \int d\boldsymbol{p} dE P_N(\boldsymbol{p}, E) \frac{M}{E_N} \frac{d^2\sigma_{\nu N}}{d\Omega dE'_\nu}, \tag{6.24}$$

with E'_ν is the energy of the outgoing neutrino, and $E_N \equiv \sqrt{M^2 + \boldsymbol{p}^2}$, $M = 0.938$ GeV being the nucleon mass. $P_N(\boldsymbol{p}, E)$ is the spectral function, which is described below. The rightmost term in the right hand side of (6.24) is the differential cross section of the NC elastic scattering with free nucleons.

Spectral fuction

According to the shell model, nuclear dynamics is described by a mean field. In the simplest implementation of this model, protons in the ^{16}O nucleus occupy three states, $1p_{1/2}$, $1p_{3/2}$ and $1s_{1/2}$, with binding energy 12.1, 18.4, and ∼42 MeV, respectively [134–136].

The spectral function $P_N(\boldsymbol{p}, E)$ is defined as the probability of removing a nucleon of momentum $\boldsymbol{p}$ from the target leaving the residual nucleus with energy $E + E_0 - M$, where E_0 and M are the target ground-state (g.s.) energy and the nucleon mass, respectively. The spectral function in the nuclear shell model is written as

$$P_N(\boldsymbol{p}, E) = \sum_i n_i |\phi_i(\boldsymbol{p})|^2 f_i(E - E_i), \tag{6.25}$$

where $\phi_i(\boldsymbol{p})$ is the wave function in the momentum space describing the i-th shell model state and E_i is the binding energy of the i-th state. The sum is taken over all occupied states belonging to the Fermi sea. The occupation probability n_i and the probability density function (PDF) $f_i(E - E_i)$ account for the effects of nucleon-nucleon (NN) correlations, which is not included in the mean field picture. In the absence of NN correlations, $n_i \to 1$ and $f_i(E - E_i) \to \delta(E - E_i)$ are obtained.

The oxygen spectral function adopted in this analysis is based on the calculation of Benhar *et al.* [133], which is obtained within the local density approximation (LDA) by combining the data of coincidence $(e, e'p)$ experiments [137] with theoretical calculations [138]. The LDA spectral function gives a nucleon momentum distribution which agrees well with the data of Ref. [139].

Figure 6.12 shows the energy spectra obtained by integrating the oxygen spectral function (6.25) over three-momentum $\boldsymbol{p}$. The $1p_{1/2}$ and $1p_{3/2}$ states have sharp peaks while the peak of $1s_{1/2}$ state is unclear and the spectrum is spread over very high energy, which is caused by the NN correlation.

From the oxygen spectral function, we estimate the probability of the residual nucleus in a specific shell state, which is called the spectroscopic factor (strength). The factors for $p_{1/2}$, $p_{3/2}$ and $s_{1/2}$ proton holes are estimated by integrating the function shown in Fig. 6.12 over the binding energy between $11.0 \leq E \leq 14.0$ MeV, $17.25 \leq E \leq 22.75$ MeV and $22.75 \leq E \leq 62.25$ MeV, respectively. The spectroscopic factors of the neutron holes are the same as the spectroscopic factors of the proton holes since the neutron levels are just more deeply bound by 3.54 MeV than those of protons as seen in Fig. 6.12. The probability of each state used in this analysis is summarized in Tab. 6.2.

6.3.2 Nuclear de-excitation

For the calculation of $\mathrm{Br}(\mathrm{X}_i^* \to \Phi)$ in Eq. (6.23), we use existing experimental data where available. We estimate the branching ratios of de-excitations of gamma-rays and particles[5)] from

[5)] In this section, "particle" is used to denote nucleons and heavier nuclear fragments emitted via the strong interaction inside the nucleus, and thus does not include gamma-rays.

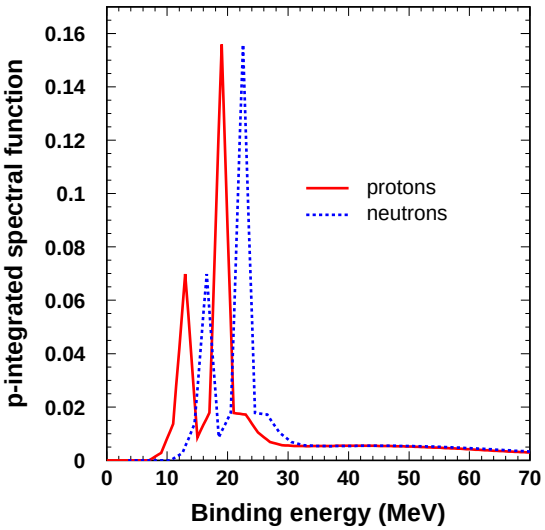

Figure 6.12: Distribution of binding energy of protons and neutrons for ^{16}O. Two peaks of each nucleon correspond to the $1p_{1/2}$-hole state (ground state) and $1p_{3/2}$-hole state. Neutron levels are more deeply bound by 3.54 MeV than those of protons.

Table 6.2: Spectroscopic factor of each hole state used in this analysis.

Residual isotope	$(1p_{1/2})^{-1}$	$(1p_{3/2})^{-1}$	$(1s_{1/2})^{-1}$	Others
^{15}N	18.8%	43.5%	18.8%	18.9%
^{15}O	18.8%	37.5%	18.8%	24.9%

Table 6.3: De-excitation modes of ^{16}O proton hole $(p_{3/2})_p^{-1}$ and neutron hole $(p_{3/2})_n^{-1}$ states. The fourth and fifth columns show the energies of de-excitation gamma-rays and protons, respectively. The sixth column shows the branching ratios of de-excitation gamma-rays from each excited state, referenced from [140].

Residual isotope	Energy level (MeV)	J^π	E_γ (MeV)	E_p (MeV)	Ratio	Br($X_i^* \to \gamma + Y$)
^{15}N	6.32	$3/2^-$	6.32	–	100%	86.2%
	9.93	$3/2^-$	5.30	–	15.3%	1.1%
			6.32	–	4.9%	0.3%
			7.30	–	2.1%	0.1%
			9.93	–	77.6%	5.4%
	10.70	$3/2^-$	–	0.5	–	6.9%
^{15}O	6.18	$3/2^-$	6.18	–	100%	100%

the $p_{1/2}$, $p_{3/2}$ and $s_{1/2}$ hole states, as described in the followings. De-excitation gamma-rays and particles are assumed to be emitted isotropically.

The $p_{1/2}$-hole states

Since $p_{1/2}$ is the ground-state, no decay occurs after the knockout. The first peaks seen in Fig. 6.12 correspond to this state.

De-excitation from the $p_{3/2}$-hole states

The second peaks seen in Fig. 6.12 correspond to the $p_{3/2}$ state protons (neutrons) with the binding energy of 18.4 (21.8) MeV. Since the binding energy of the ground-state proton (neutron) is 12.1 (15.6) MeV, the nucleus without the nucleon in these states has the excitation energy 6.32 (6.18) MeV, which mainly de-excites by emitting a single 6.32 (6.18) MeV gamma-ray. Table 6.3 summarizes the branching ratios used in this analysis in the case of the $p_{3/2}$-hole state. We assign the same branching ratio to both the 6.18 MeV $(p_{3/2})_n^{-1}$ state and the 6.32 MeV $(p_{3/2})_p^{-1}$ state. We remove the de-excitation modes from the 9.61 and 10.46 MeV levels in the $(p_{3/2})_n^{-1}$ state corresponding to the 9.93 and 10.70 MeV levels in the $(p_{3/2})_p^{-1}$ state, since these levels are higher than the proton emission threshold 7.30 MeV in the $(p_{3/2})_n^{-1}$ state.

De-excitation from the $s_{1/2}$-hole states

For the branching ratios of de-excitation gamma-rays from the $s_{1/2}$ proton hole of ^{15}N*, we use data on the quasi-free ^{16}O$(p, 2p)^{15}$N reactions measured by the E148 experiment carried out

at the Research Center for Nuclear Physics (RCNP) [141, 142]. This experiment used a 392 MeV proton beam from the cyclotron facility and H_2O (ice) for the target. The two outgoing protons of $^{16}O(p, 2p)^{15}N$ were detected in coincidence using the dual magnetic spectrometer system, consisting of Grand Raiden (GR) and the Large Acceptance Spectrometer (LAS). The de-excitation gamma-rays were measured by three arrays of NaI (Tl) detectors in coincidence with two protons. The excitation energy (E_x) was evaluated from the energies of two emerging protons measured by GR and LAS as

$$\begin{aligned} \boldsymbol{k}_{p0} &= \boldsymbol{k}_{p1} + \boldsymbol{k}_{p2} + \boldsymbol{k}_{res} \\ T_{p0} - Q &= T_{p1} + T_{p2} + (T_{res} + E_x) \end{aligned} \tag{6.26}$$

where $\boldsymbol{k}_{p0}$, $\boldsymbol{k}_{p1}$, $\boldsymbol{k}_{p2}$ and $\boldsymbol{k}_{res}$ denote the momenta of the incident proton, the emerging protons and the recoiling residual nucleus, respectively. T is the kinetic energy with subscripts of the same meanings as k. The Q-value is given by $Q = (M_p + M_{res}) - M_{targ}$, where M_{targ}, M_p and M_{res} are the masses of the target oxygen nucleus (^{16}O), proton and the residual nucleus (^{15}N), respectively. This way, de-excitation gamma-rays and particles from the $(s_{1/2})_p$-hole state in the excitation-energy region of $16 < E_x < 40$ MeV[6)] in ^{15}N, were systematically measured.

As for the $^{15}O^*$ (neutron hole) decays, there are no experiments so far which intensively measure gamma-ray yields, especially for the $(s_{1/2})_n$-hole state. Since ^{16}O is double magic and the nuclear interaction is charge symmetric, the level and de-excitation processes are similar between the proton hole in ^{15}N with $T_3 = -1/2$, where T_3 is the third component of the weak isospin, and the neutron hole in ^{15}O with $T_3 = 1/2$ [143–146]. Thus, we simply assign to the de-excitations from a neutron hole the same branching ratios as those of the corresponding proton hole.

Table 6.4 summarizes the branching ratios used in this analysis in the case of the proton $s_{1/2}$-hole state. Since the energy range of the $1s_{1/2}$-hole state is higher than the particle emission threshold, in most cases a particle emission occurs after the nucleon knockout, instead of gamma-ray de-excitation. In the simulation, we first determine the excitation energy of the $s_{1/2}$-hole state in order to later calculate the energy of the emitted particle from a two-body decay. More technically, we choose a random number following a PDF defined on the excitation energy range of the $s_{1/2}$-hole state, $10.65 \leq E_x \leq 50.15$ MeV, which corresponds to the binding energy range for a proton defined above. We adopt a uniform distribution as the PDF since after subtracting the $p_{3/2}$-state contribution in Fig. 6.12, the remaining distribution (of protons) is almost uniform between $22.75 \leq E \leq 62.25$ MeV and the effect of the deviation from uniformity on the final event energy spectrum at SK is negligible.

The decay particle is simulated only in the case of nucleon emission because heavier fragments emitted from nuclear de-excitation, such as deuteron and triton, are not expected to have any

[6)] The de-excitation in the excitation-energy above 40 MeV was not analyzed because the detection efficiencies were too low in the higher excitation-energy region due to the finite momentum acceptance of the spectrometers [141].

Table 6.4: De-excitation modes of ^{16}O proton hole $(s_{1/2})_p^{-1}$ states. The branching ratios for the gamma-rays with $E_\gamma > 3$ MeV are shown. For what each column shows, see previous figure caption.

	Energy level		E_γ		
Residual isotope	(MeV)	J^π	(MeV)	Ratio	Br(^{15}N$^* \rightarrow \gamma + $ Y)
^{13}C	3.09	$1/2^+$	3.09	100%	3.0%
	3.68	$3/2^+$	3.68	99.3%	4.2%
	3.85	$1/2^+$	3.09	1.20%	< 0.1%
			3.68	36.3%	1.7%
			3.85	62.5%	2.9%
^{12}C	4.44	2^+	4.44	100%	5.8%
^{14}N	g.s.	2^+	–	–	6.7%
	4.92	0^-	4.92	97%	5.0%
	5.11	2^-	5.11	79.9%	< 0.1%
	5.69	1^-	3.38	63.9%	2.9%
			5.69	36.1%	1.6%
	5.83	3^-	5.11	62.9%	0.3%
			5.83	21.3%	0.1%
	6.20	1^+	3.89	76.9%	< 0.1%
			6.20	23.1%	< 0.1%
	6.45	3^+	5.11	8.1%	0.2%
			6.44	70.1%	2.0%
	7.03	2^+	7.03	98.6%	(6.6%)
^{14}C	g.s.	2^+	–	–	1.1%
	6.09	1^-	6.09	100%	< 0.1%
	6.59	0^+	6.09	98.9%	< 0.1%
	6.73	3^-	6.09	3.6%	< 0.1%
			6.73	96.4%	0.4%
	6.90	0^-	6.09	100%	< 0.1%
	7.01	2^+	6.09	1.4%	< 0.1%
			7.01	98.6%	(6.6%)
	7.34	2^-	6.09	49.0%	2.8%
			6.73	34.3%	2.0%
			7.34	16.7%	1.0%

activity in water due to their low momenta. The kinetic energy of the decay particle in two-body decay is calculated as follows. The separation energies of ^{15}N to ^{14}C+p and ^{14}N+n are 10.21 and 10.83 MeV, respectively, and those of ^{15}O to ^{14}N+p and ^{14}O+n are 7.3 and 13.22 MeV, respectively. If the momentum of ^{15}N* (^{15}O*) with an excitation energy of E_x is assumed to be 0 MeV/c, the kinetic energy of the decay particle is given by

$$T_{dcy} = \frac{M^*_{res}}{m_{dcy} + M^*_{res}}(E_x - E_{sep}) \tag{6.27}$$

where m_{dcy} is the mass of the decay particle, M^*_{res} is the mass of the residual nucleus including its excitation energy, and E_{sep} is the sum of the separation energy of each corresponding nucleon from the ^{15}N (^{15}O) ground-state and the excitation energy of the residual nucleus. If a gamma-ray is emitted from the residual nucleus, the excitation energy of the residual nucleus is set equal to the energy level. This level is determined when the energy of gamma-ray is chosen, as is shown in Tab. 6.4. For the case where the residual nucleus decays to a ground state nucleus, we estimate the branching ratio from other data of the RCNP experiment [142]. Also, we estimate the branching fractions of three-body decays and sequential decays of ^{15}N (^{15}O) from data of the same reference. In the latter cases, we simply assume that the kinetic energy distribution of emitted nucleons is uniform from 0 to 5 MeV.

The $p_{1/2}$ hole state and others

De-excitations from energy states higher than $1p_{1/2}$, $1p_{3/2}$ and $1s_{1/2}$, whose binding energies extend to $E \sim 300$ MeV according to Ref. [133], are not simulated because there are no experiments that measure those states. Instead, as is discussed in Chapter 9, we include them as systematic uncertainties in this analysis assuming the kinematics and the absolute yield of gamma-rays and particles from those states are qualitatively the same as those of the $1s_{1/2}$ states, since both of the states have sufficient binding energies compared to the particle emission thresholds.

Figure 6.13 shows the resultant energy spectra of de-excitation gamma-rays from proton and neutron holes. In case more than one gamma-ray are emitted, the sum of each energy is plotted. It is clearly seen that the dominant de-excitation mode is 6.32 MeV gamma-ray for a $p_{1/2}$ proton hole and 6.18 MeV gamma-ray for a $p_{1/2}$ neutron hole, and the contributions from $s_{1/2}$ hole states are small for both nucleons.

Figure 6.14 shows the kinetic energy spectra of decay nucleons from proton and neutron holes. These plots are made by a Monte Carlo simulation for the de-excitation. The peaks below 5 MeV come from our simulation of three-body decays mentioned earlier.

6.3.3 De-excitation from π absorption

We also simulate de-excitation gamma-rays from pion absorption on oxygen nuclei. We use the data of the absorption of π^- at rest on H_2O measured by CERN [148]. As described above,

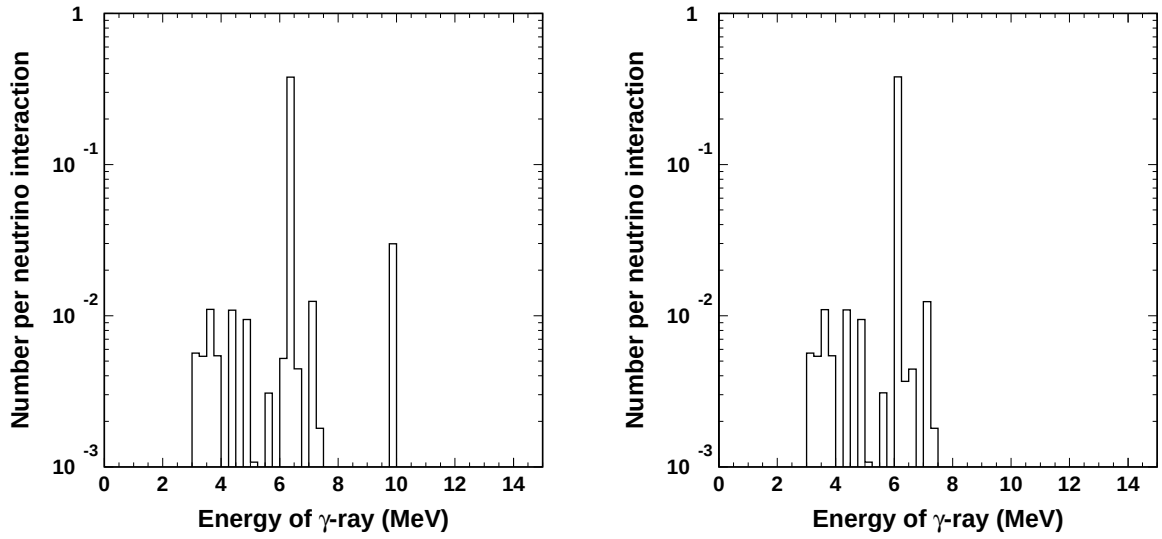

Figure 6.13: Energy spectra of de-excitation gamma-rays from proton hole (left) and neutron hole (right).

pions can be produced inside a nucleus by a neutrino primary interaction or nucleon FSI. When those pions are absorbed in the nucleus, gamma-rays are sometimes emitted. The branching ratios used in this analysis are summarized in Tab. 6.5. Figure 6.15 shows the resultant energy spectra of de-excitation gamma-rays from π absorption. In the case of more than one gamma-ray emission, the sum of all energies is plotted.

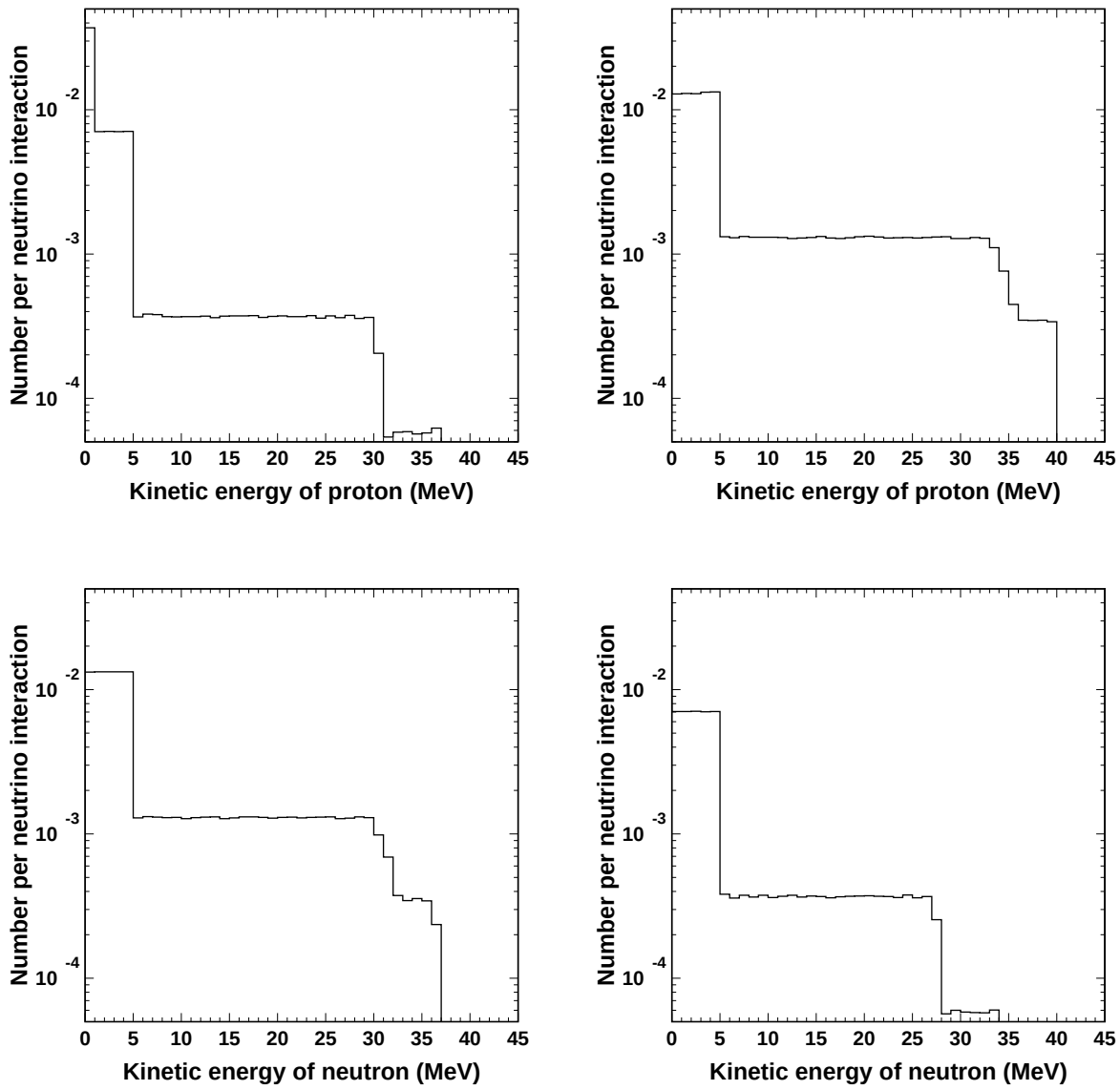

Figure 6.14: Kinetic energy spectra of decay protons from proton holes (upper left) and neutron holes (upper right), and decay neutrons from proton holes (lower left) and neutron holes (lower right). The discontinuity at 0.5 MeV in the upper left panel comes from the 0.5 MeV decay protons from the 10.70 MeV ^{15}N $(p_{3/2})_p^{-1}$ states (Tab. 6.3). The discontinuities at 5 MeV in all panels come from three-body decays mentioned earlier.

Table 6.5: Prompt gamma-ray transition yields from the absorption of π^- at rest on ^{16}O.

Residual isotope	Energy level (MeV)	J^π	E_γ (MeV)	$\mathrm{Br}(\mathrm{X}_i^* \to \gamma + \mathrm{Y})$
^{16}O	6.131	3^-	6.13	1.7%
^{15}N	5.270	$5/2^+$	5.27	0.5%
^{14}N	2.313	0^+	2.31	0.3%
	3.945	1^+	1.63 + 2.31	4.8%
	5.106	2^-	5.11	0.7%
			2.79 + 2.31	0.2%
^{14}C	6.728	3^-	6.728	-
^{13}C	3.684	$3/2^-$	3.68	1.9%
	3.854	$5/2^+$	3.85	1.0%
^{12}C	4.439	2^+	4.44	4.0%
^{10}B	0.717	3^+	0.72	1.3%

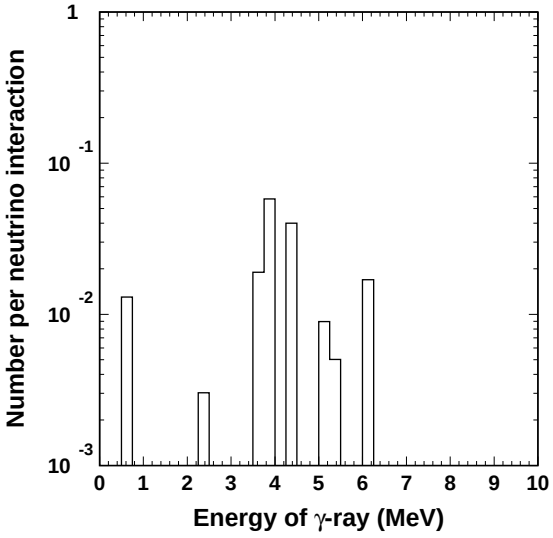

Figure 6.15: Energy spectra of de-excitation gamma-rays from π absorption.

6.4 Detector simulation

The outputs of NEUT, *i.e.*, leptons and escaped nucleons after final state interaction inside the nucleus, are then passed through a GEANT (v3.21) [149] based custom detector simulator. In Tab. 6.6 physics processes simulated by GEANT are summarized.

For hadronic interactions in water, we use the GCALOR package based on the nuclear cascade model, but for charged pions below 500 MeV/c we prepared a separate custom program based on the result of $\pi^{\pm}$ H_2O scattering experiment [150, 151].

Cherenkov light emission and propagation through water are simulated by our custom code. The group velocity of Cherenkov light in the SK water is given as

$$v_g = \frac{c}{n(\lambda, T, p) - \lambda \frac{dn(\lambda,T,p)}{d\lambda}}, \tag{6.28}$$

where the refractive index depends on the water temperature and pressure as well as the wavelength of each photon, and we adopt an existing equation with the coefficients deduced from experimental data by a least-squares fit [152] using the water temperature of 13 °C and pressure of 1 atm[7)].

Absorption and scattering of Cherenkov lights are incorporated in the simulation using the tuned water parameters obtained by the calibration described in Section 5.3. Light reflection by the black sheet and Tyvec surfaces of the detector is also taken into account.

In simulating the response of PMTs, the measured quantum efficiency and single photoelectron distributions are used. The PMTs which are not used during the DAQ for any reason are removed in the simulation. DAQ electronics and trigger systems are also simulated.

6.4.1 Secondary gamma-rays

Fig. 6.16 shows the kinetic energy distributions of nucleons just after escaping from the nucleus[8)], where discontinuities are found at around 1, 5 and 27 MeV. The first two are of the same origins as those of Fig. 6.14[9)]. The last one corresponds to the Fermi surface momentum of 225 MeV/c. These nucleons have high enough energy so that they can spall other oxygen nuclei in the water, which leads to secondary cascade nucleons and de-excitation gamma-rays. They are relevant for the analysis of this thesis because the energy spectrum of de-excitation gamma-rays from neutrino prompt interactions can be largely affected by these secondary cascade gamma-rays. In fact, even if the energy of each gamma-ray is below 10 MeV, the total number of Cherenkov photons from a cascade of all the gamma-rays in a single event is often reconstructed above the

[7)] Since the pressure dependence is much smaller than other dependences, the water pressure is effectively negligible.

[8)] The plots shown in Fig. 6.16 are after a momentum cut on the outgoing leptons in the CC case. This cut is described later.

[9)] Since nucleon FSI increases the number of nucleons in the range below 27 MeV, the ratio of nucleon fractions between the regions below and above 5 MeV is closer to 1 than that in Fig. 6.14.

Table 6.6: Physics processes simulated by GEANT

gamma	(e^+, e^-) pair production
	Compton scattering
	Photoelectric effect
$e^\pm$	Multiple scattering
	Ionization and δ-rays production
	Bremsstrahlung
	Annihilation of positron
	Generation of Cherenkov radiation
$\mu^\pm$	Decay in flight
	Multiple scattering
	Ionization and δ-rays production
	Bremsstrahlung
	Direct (e^+, e^-) pair production
	Nuclear interaction
	Generation of Cherenkov radiation
Hadrons	Decay in flight
	Multiple scattering
	Ionization and δ-rays production
	Hadronic interactions
	Generation of Cherenkov radiation

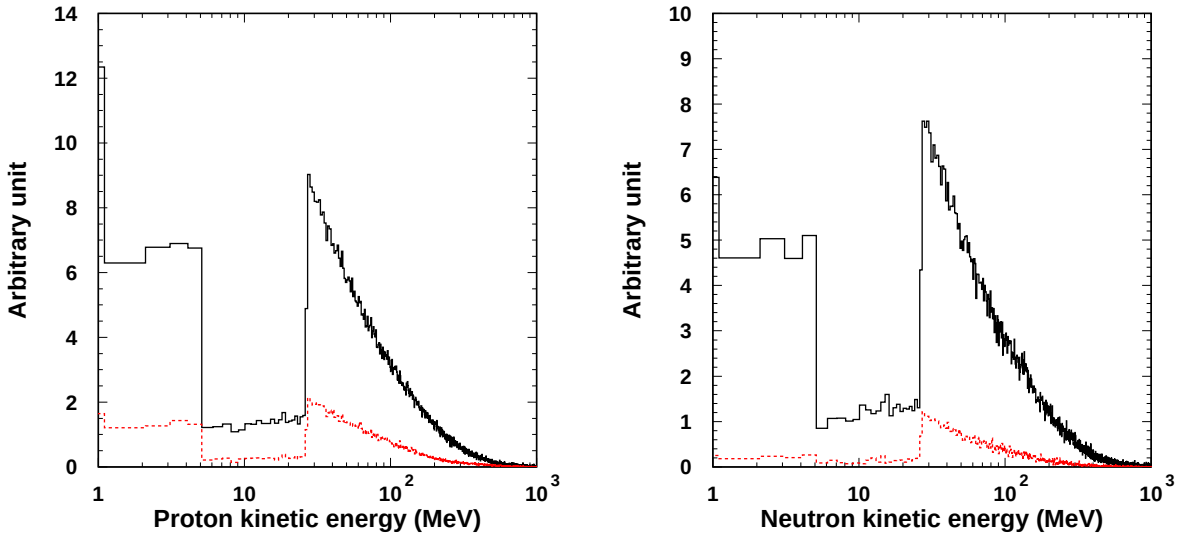

Figure 6.16: Kinetic energy distributions of protons (left) and neutrons (right) after final state interaction inside the nucleus. The T2K beam ν_μ flux is assumed. The solid lines show the total components while the dotted lines show the CC components (after a momentum cut on the outgoing leptons, described in the next section). The discontinuities at around 1 MeV and 5 MeV in both panels are of the same origins as those of Fig. 6.14, while that of 27 MeV corresponds to the Fermi surface momentum of 225 MeV/c.

analysis thresholds of low energy phenomena like supernova relic neutrinos (SRN) or the GUT monopole search at SK, and the secondary gamma-rays can be one of the most important sources of background for these analyses.

As mentioned above, hadronic interactions in water are simulated by GCALOR, and four different simulators are actually employed, as summarized in Tab. 6.7. Among them NMTC [153] and MICAP [154] are especially relevant simulators for the energy range of the analysis of this thesis. Figure 6.17 plots the energy of each de-excitation gamma-ray from GCALOR versus the kinetic energy of an incident nucleon on an oxygen nucleus. It can be seen that the absolute yield and kinematics of de-excitation gamma-rays are significantly different above and below 20 MeV only in the neutron case[10)]. Effects of these disagreements between the energy regions covered by the two simulators on this analysis are discussed in Chapter 9.

[10)] This difference should come from the different treatments of de-excitation gamma-rays between the two simulators because there is no such difference in absolute yields of the proton case despite the similarity of the kinetic energy distributions between the two nucleons (Fig. 6.16).

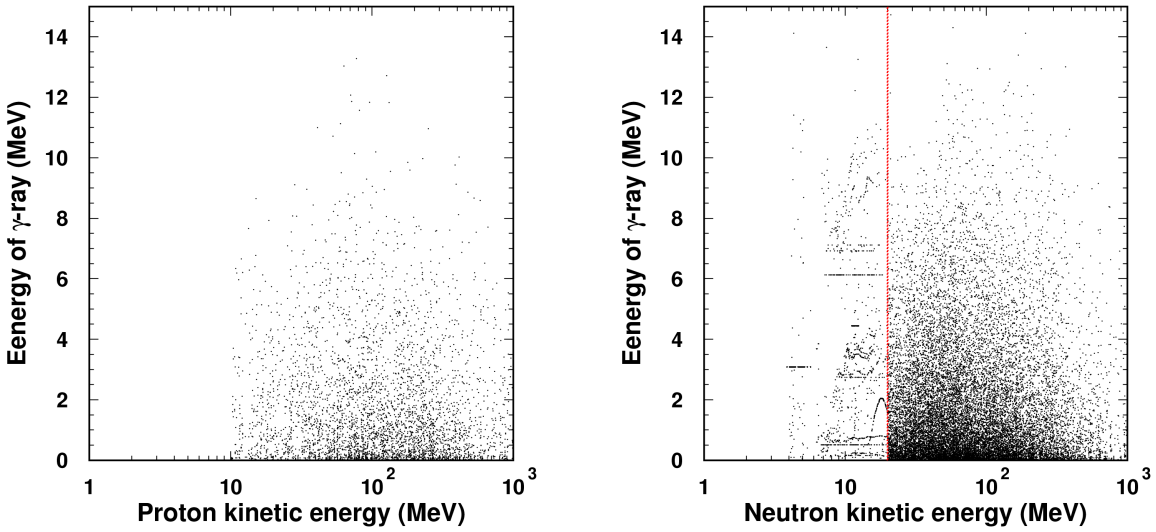

Figure 6.17: Energy of secondary gamma-ray versus kinetic energy of the incident proton (left) and neutron (right) in the GEANT detector simulation assuming the T2K beam ν_μ flux. Each dot corresponds to a single gamma-ray. The dotted vertical line in the right panel indicates the boundary of the energy ranges covered by two different simulators. It can be seen that the absolute yield and kinematics of de-excitation gamma-rays are treated differently between the two simulators.

Table 6.7: Four different simulators used in GCALOR for each kinetic energy range.

FLUKA	Nucleons and charged pions above 10 GeV
SCALE	Scaling model. 3-10 GeV for nucleons and charged pions
NMTC	Nucleons below 3.5 GeV, charged pions below 2.5 GeV
MICAP	Neutrons below 20 MeV (194.9 MeV/c)

6.5 Results of Monte Carlo simulation of T2K beam neutrino events

In this section, I present the technical procedure for producing MC simulation and the expected energy distribution of T2K beam ν_μ events in the low energy region up to 30 MeV.

6.5.1 Technical procedure of simulation

Using the beam flux normalization and spectrum, 1.4×10^{23}, 4.8×10^{24} and 6.8×10^{24} protons on target (POT) equivalent of ν_μ, $\bar{\nu}_\mu$ and ν_e are generated by NEUT, respectively. Only events whose true vertices are within 50 cm outside of the SK inner detector are produced. Before the detector simulation, charged-current (CC) events whose outgoing muon (electron) momenta are above 400 (100) MeV/c, which would be rejected by the energy selection, are rejected beforehand in order to reduce the processing time.

As can be seen in Tab. 6.3, the 6.32 MeV gamma-ray for $^{15}N^*$ and 6.18 MeV gamma-ray for $^{15}O^*$ are the strongest modes of all the de-excitations. The event trigger threshold is determined so that these 6 MeV de-excitation gamma-rays are sufficiently sampled, and ultimately set to 25 PMT hits within 200 ns. Hereafter we refer to this trigger as the HLE (Hyper Low Energy) trigger. The rate of the HLE trigger is about 43 kHz, and the efficiency in $4 - 4.5$ MeV events is above 99.5%.

Vertex, direction and energy are then reconstructed by the same tool as the real data.

6.5.2 Neutrino oscillation parameters

Throughout this thesis, the neutrinos and antineutrinos are assumed to oscillate with the same parameters of $\sin^2 2\theta_{23}$=1.0, Δm^2_{23}=2.4×10^{-3} eV^2. Except in the section of sterile neutrino search, θ_{13} is set to 0° for simplicity if not otherwise specified.

6.5.3 Predicted spectrum

Figure 6.18 shows the result of the MC simulation of T2K beam neutrino events with the reconstructed energy range between $4 - 30$ MeV and only the fiducial volume cut, which is described in the next chapter, applied. In this energy range, more than 95 % of events come from NC interactions, of which more than 85% are elastic events. T2K beam neutrino NC events are expected to peak at around 6 MeV due to the 6.18 MeV and 6.32 MeV de-excitation gamma-rays from $^{15}O^*$ and $^{15}N^*$ decays, respectively.

At this energy range, it is usually impossible to exclusively tag neutrino-induced events due to many gamma-ray background events from radioactivity in the PMT case and glass. As described in the next chapter, however, owing to the GPS-based T2K beam timing, accurate to within 100 ns, cuts on this time profile enable us to reduce this serious background to a manageable level.

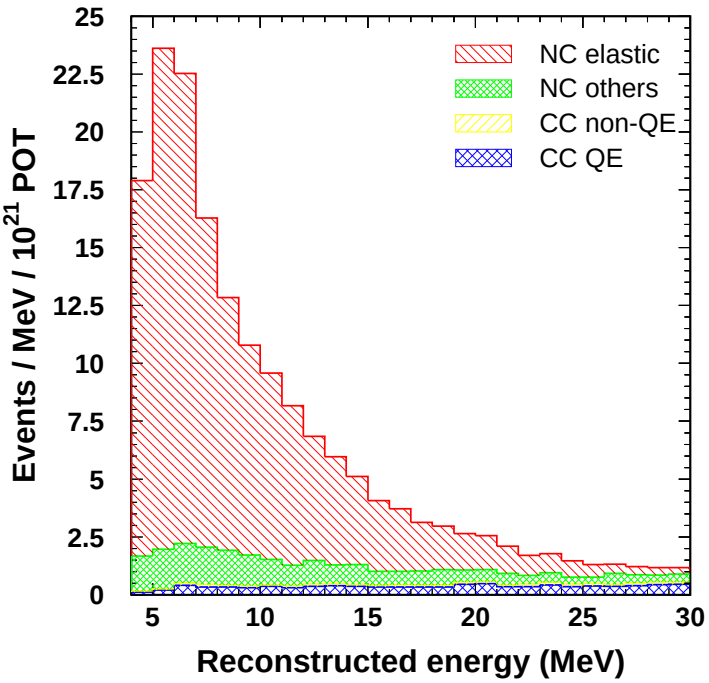

Figure 6.18: Energy distribution of T2K beam ν_μ events expected at SK assuming 1×10^{21} POT and its breakdown by neutrino interaction mode. Only the fiducial volume cut is applied.

Chapter 7

Data Reduction

7.1 First reduction

7.1.1 Good spill selection

We assign good/bad to each beam spill according to some criteria. First, judgment is done at the beam-line side by measured beam direction, horn currents, and so on. The beam spill which passes all criteria there is called "beam good spill", and then the following cuts are applied to these spills.

1. SK DAQ alive

   The SK DAQ program is running or not. The dead-time by this cut is 0.08%.

2. Bad subrun cut

   Subrun is a unit of SK data, which corresponds to about one minute of observation. Each subrun is judged to be good/bad for physics analyses depending on the detector status. Typically, a bad subrun includes flashers, i.e. PMT flashing by discharge around dynodes, DAQ trouble or necessary works which might affect the DAQ such as blasting in the mine.

3. DAQ/GPS error cut

   The numbers of ID and OD PMT hits within a 1 ms T2K window are required to be greater than 48,000 and 6,000, respectively. Since most hits come from the PMT's dark noise, these variables are almost constant. Therefore, this cut rejects the event where part of the detector is not working. The threshold values were determined by checking the data in dummy spills. In addition, if there are some problems in the GPS data, the spill is classified as a bad spill. No beam spill has been rejected by the DAQ/GPS error cut so far.

4. Special data block cut

   The SK electronics system records all PMT hit signals onto sequent 16.7 μs wide data blocks. There exist two types of special data blocks. One is a pedestal block for taking

Table 7.1: Number of spills after each cut to select the good spills for physics analyses of the T2K data observed at SK during RUN-I (Jan. 2010 - Jun. 2010) and RUN-II (Nov. 2010 - Mar. 2011) beam periods. The fifth column shows the inefficiency of each cut.

	Number of spills			Inefficiency
	RUN-I	RUN-II	Total	
Beam good spills	1,006,982	1,492,031	2,499,013	
(1) SK DAQ alive	1,006,129	1,489,826	2,495,955	0.1%
(2) Bad subrun cut	1,002,823	1,481,525	2,484,348	0.5%
(3) Incomplete data/GPS error cut	1,002,823	1,481,525	2,484,348	0%
(4) Special data block cut	1,002,011	1,480,287	2,482,298	0.08%
(5) Pre-activity cut	998,800	1,475,619	2,474,419	0.3%
Total	998,800	1,475,619	2,474,419	1%
POT (protons on target)	3.23×10^{19}	1.108×10^{20}	1.431×10^{20}	

pedestal data of all the channels on the front-end electronics modules. The other is a TDC reset block to reset some counters in the TDC chips. The TDC reset blocks (the pedestal blocks) are generated once per 4096 (65536) data blocks, which correspond to about 70 ms (1.1 s). The spill loss by this cut is 0.08%.

5. Pre-activity cut

   It is required that there is no detector activity, *i.e.*, LE or OD trigger event, within 100 μs before the leading edge of each spill. The main purpose of this cut is to remove an accidental contamination of decay electrons into the beam window, which is generated by cosmic-ray muons. The spill loss by this cut is about 0.3%.

A total of 2,474,419 spills are selected as good spills by applying all cuts. As shown in Tab. 7.1, the SK efficiency for physics analyses is about 99%. Figure 7.1 shows the accumulated number of POT as a function of elapsed days. The total POT corresponding to the T2K-SK data for this analysis is 1.43 $\times 10^{20}$.

7.2 Second reduction

The purpose of the second reduction is to reduce beam-unrelated backgrounds as much as possible. After defining the signal energy range of the analysis of this thesis as $4 - 30$ MeV, the following cuts are applied to the T2K-SK data.

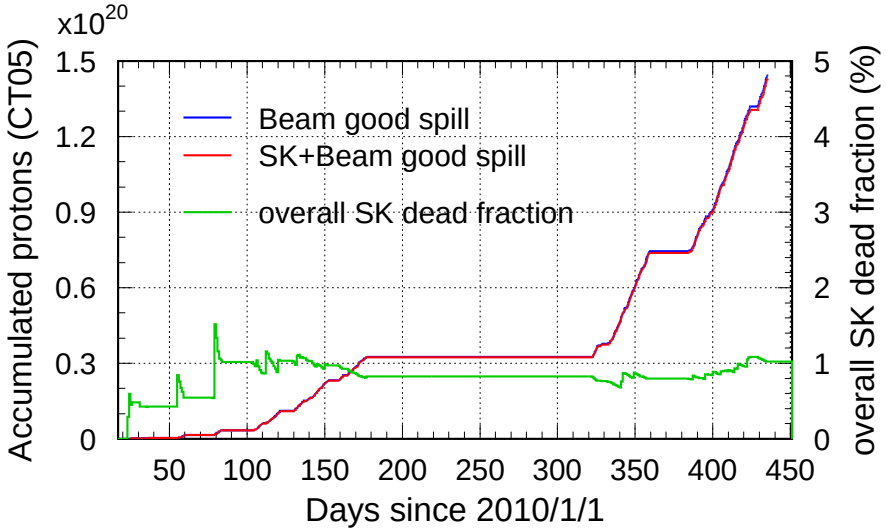

Figure 7.1: Accumulated number of POT as a function of date using the beam good spills (blue) and the SK+beam good spills (red), together with a change in the SK dead fraction (green = (blue-red)/blue).

7.2.1 Timing cut

At first, ΔT_0, which denotes the relative timing of a neutrino interaction to the spill leading edge, is calculated by combining the neutrino TOF from the proton target to the center position of SK and the hardware offsets at both sites. Then the event vertex is projected onto the direction vector from the SK origin toward the neutrino beam direction, and the time difference between the event vertex and the SK origin is calculated with the approximation that the neutrino velocity equals to the velocity of light in vacuum. This way, we know the GPS timing when the neutrino passed or would pass through the plane containing the SK origin which is perpendicular to the beam direction.

A similar estimation of the neutrino event timing is also done in a separate analysis, the fully-contained (FC) analysis [22, 24], which uses several hundred MeV neutrino events. In the FC analysis there is effectively no beam-unrelated background, and all events with $\Delta T_0 \in [-2, 10]$ μs are extracted. Figure 7.2 shows the ΔT_0 distribution of all the 121 FC events observed during the RUN-I and RUN-II. As can be seen in the right panel of the figure, more than 99% of the FC events[1)] are within 100 ns with respect to the fitted bunch center positions of $-481.5+581.0 \cdot n$ ($n = 1, 2, \cdots, 8$) ns. The RMS of the distribution is 27 ns, which means that the neutrino interaction

[1)] There is one event with $\Delta T_0 > 100$ ns. This is the T2K first FC event observed in February 2010, when the GPS time at the near detector site was found to have an offset of about 100 ns for an unknown reason.

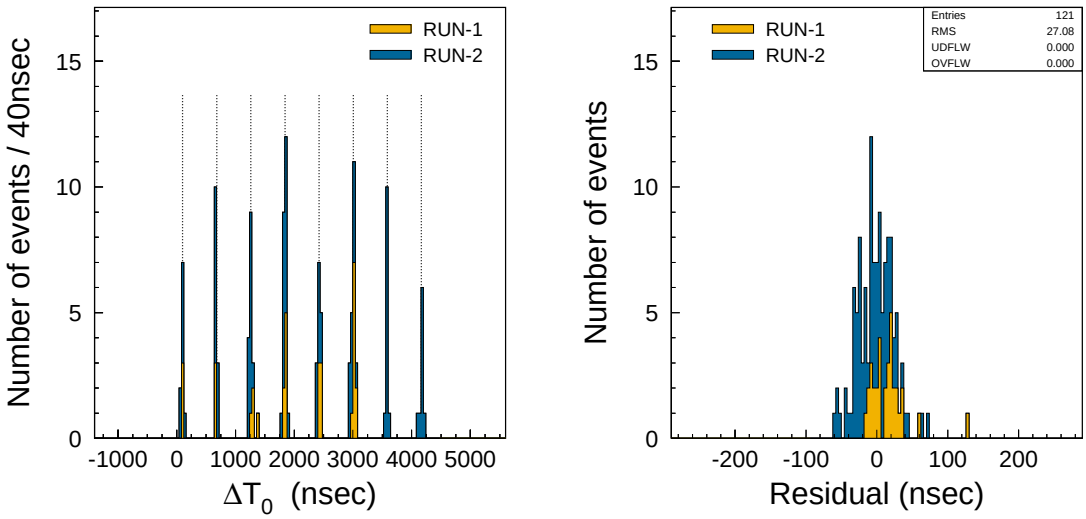

Figure 7.2: In the left panel, ΔT_0 distribution of all the 121 FC events observed during the RUN-I/II is shown. The eight dotted vertical lines indicate the 581 ns interval bunch center positions fitted to the observed FC event times. The right panel shows the timing residual of each FC event from the closest bunch center time.

timing is predicted with the accuracy of well below 100 ns in the far detector site.

In this thesis, we define an "on-timing" event as the event whose ΔT_0 is within 100 ns of the bunch center positions fitted by the FC analysis. We use the result of the FC analysis because more statistics (about five factors of magnitude) is expected in FC events than in NC de-excitation gamma-ray events for the same POT. Also, by using information of an independent analysis we can eliminate possible biases for selecting events. We use only on-timing events to select the final sample.

7.2.2 Gamma-ray cut

As mentioned in the last chapter, the main source of background for this search is gamma-rays emitted from radioactive impurities contained in the materials of the detector structure. Therefore, a higher background rate is expected near the ID walls. Also, energy resolution near the wall is much poorer. So we reject events whose *dwall*, the distance to the nearest ID wall, is less than 2 meters. This cut defines the fiducial volume (FV).

Some events originating from outside of the FV have the possibility of being reconstructed within the FV. To remove these events, the event's reconstructed direction is extrapolated backwards from the vertex position onto the ID wall, as illustrated in Fig. 7.3. This distance is called d_{eff} or *effwall*. Events with very short *effwall* are highly likely to be gamma-rays from the ID

walls and are removed by this cut. The cut criteria are determined by the optimization which is detailed later in this section.

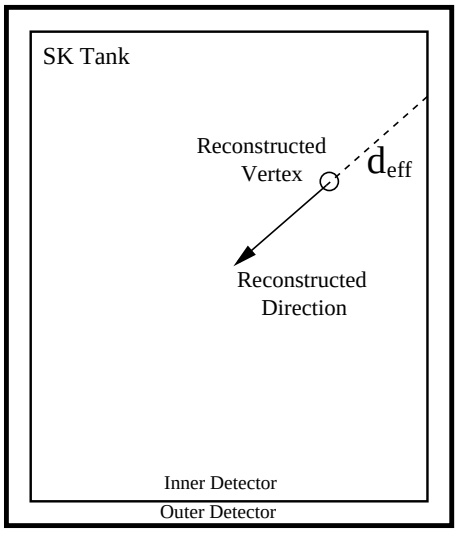

Figure 7.3: The definition of *effwall* (d_{eff}) that is used in the gamma-ray cut.

7.2.3 Fit quality cut

To further reject the remaining background, especially mis-reconstructed events, we evaluate the quality of reconstruction of the vertex (vertex goodness, G_V) and that of the direction (angular goodness, G_A).

The vertex goodness is evaluated by a fit of the PMT timing distribution and defined using hit PMT timing as,

$$G_V = \frac{\sum w_i e^{-\frac{1}{2}\left(\frac{t_{res,i}(\boldsymbol{v})-t_0}{\sigma}\right)^2}}{\sum w_i} \text{ with } w_i = e^{-\frac{1}{2}\left(\frac{t_{res,i}(\boldsymbol{v})-t_0}{\omega}\right)^2}, \tag{7.1}$$

where $\boldsymbol{v}$, $t_{res,i}(\boldsymbol{v})$ and t_0 are defined in Section 4.1. The summation is taken over all hit PMTs whose $|\Delta t| \leq 50$ ns for the numerator and those whose $|\Delta t| \leq 360$ ns for the denominator. w_i is the weight for the i-th hit PMT to reduce the dark noise hits, where ω is set to 60 ns. σ is set to 5 ns to test goodness. It follows that a sharp timing distribution defines a large goodness.

The angular goodness is evaluated using the uniformity of the spatial distribution of hit PMTs around the reconstructed direction. For the evaluation of the uniformity, the Kolmogorov-Smirnov (KS) test is applied:

$$G_A = \frac{\max_i\{\angle_{\text{uni}}(i) - \angle_{\text{data}}(i)\} - \min_i\{\angle_{\text{uni}}(i) - \angle_{\text{data}}(i)\}}{2\pi}, \tag{7.2}$$

where $\angle_{\rm data}(i)$ is the azimuthal angle of the i-th real hit PMT included in $\rm N_{50}$. $\angle_{\rm uni}(i) = 2\pi i/N_{50}$ is the azimuthal angle of the i-th virtual hit PMT assuming uniform distribution. Figure 7.4 shows typical examples of good and bad events. Clearly, the more uniform the distribution, the smaller the goodness[2)].

The correlation between ${\rm G_V}^2$ and ${\rm G_A}^2$ is shown in Fig. 7.5. The top panel shows T2K beam ν_μ MC events and the bottom shows beam-unrelated events, where in both cases only events greater than 4 MeV in the FV are used[3)]. The variable $ovaQ \equiv {\rm G_V}^2 - {\rm G_A}^2$ efficiently separates T2K beam ν_μ MC events from beam-unrelated ones.

7.2.4 Cut criteria optimization

In comparing the T2K MC prediction (signal) and beam-unrelated events (background), the signal-to-noise ratio is found to be strongly dependent on the reconstructed energy. Thus, we optimize the cut criteria of *dwall*, *effwall* and *ovaQ* simultaneously in each energy bin so as to maximize a figure-of-merit (FOM) defined as

$$\mathrm{FOM} \equiv \frac{\mathrm{N_{signal}}}{\sqrt{\mathrm{N_{signal}} + \mathrm{N_{background}}}}, \tag{7.3}$$

where $\rm N_{signal}$ and $\rm N_{background}$ are the numbers of expected signal and background in each energy bin, respectively. For the background, we calculate the number of events expected to occur within the signal timing range of $\pm$100 ns with respect to the bunch center positions. After the criteria are tuned for all bins, we fit the discrete values to a line and use it as the reduction criteria. Strictly speaking, because the T2K experiment has had different beam intensities and beam bunch structures during its runs, the relative background level has always been changing. Therefore, we prepared cut criteria for various beam intensities and bunch structures. Figure 7.6 shows the fitted cut criteria (lines) for the two parameters and Figs. 7.7, 7.8 and 7.9 show the comparison of energy spectra, signal-to-noise ratios, and reduction efficiencies before and after the second reduction in two cases of different beam intensities and bunches per beam spill[4)]. For the energy region higher than the energy at which the *effwall* cut criterion reaches 2 meters ($E \gtrsim 5-6$ MeV as can be seen from Fig. 7.6), we only apply the 2 meter fiducial volume cut.

We can see a great improvement in the background rejection ability by introducing the cuts explained above, particularly in the energy range below 6 MeV, where backgrounds are expected to be large.

In determining the cut criteria, constant beam intensities of 20 and 100 kW are assumed in RUN I and II, respectively. These values are slightly lower than the average beam intensity during each run period; the lower the beam intensity, the tighter the criteria become.

[2)] Here, the term "goodness" is used in an opposite manner.

[3)] As the sample of beam-unrelated events, off-timing events with $\Delta T_0 \in [-500, -5]$ μs in T2K beam spill data with the livetime of 1260.0 s are used for the energy range $E \leq 4.5$ MeV while for the energy range $E \geq 4.5$ MeV SLE-triggered events in an SK-IV normal run with the livetime of 22.99 hours are used.

[4)] In the case of eight (six) bunches, the livetime is $\pm$100 ns $\times$ 8 (6) = 1600 (1200) ns per beam spill.

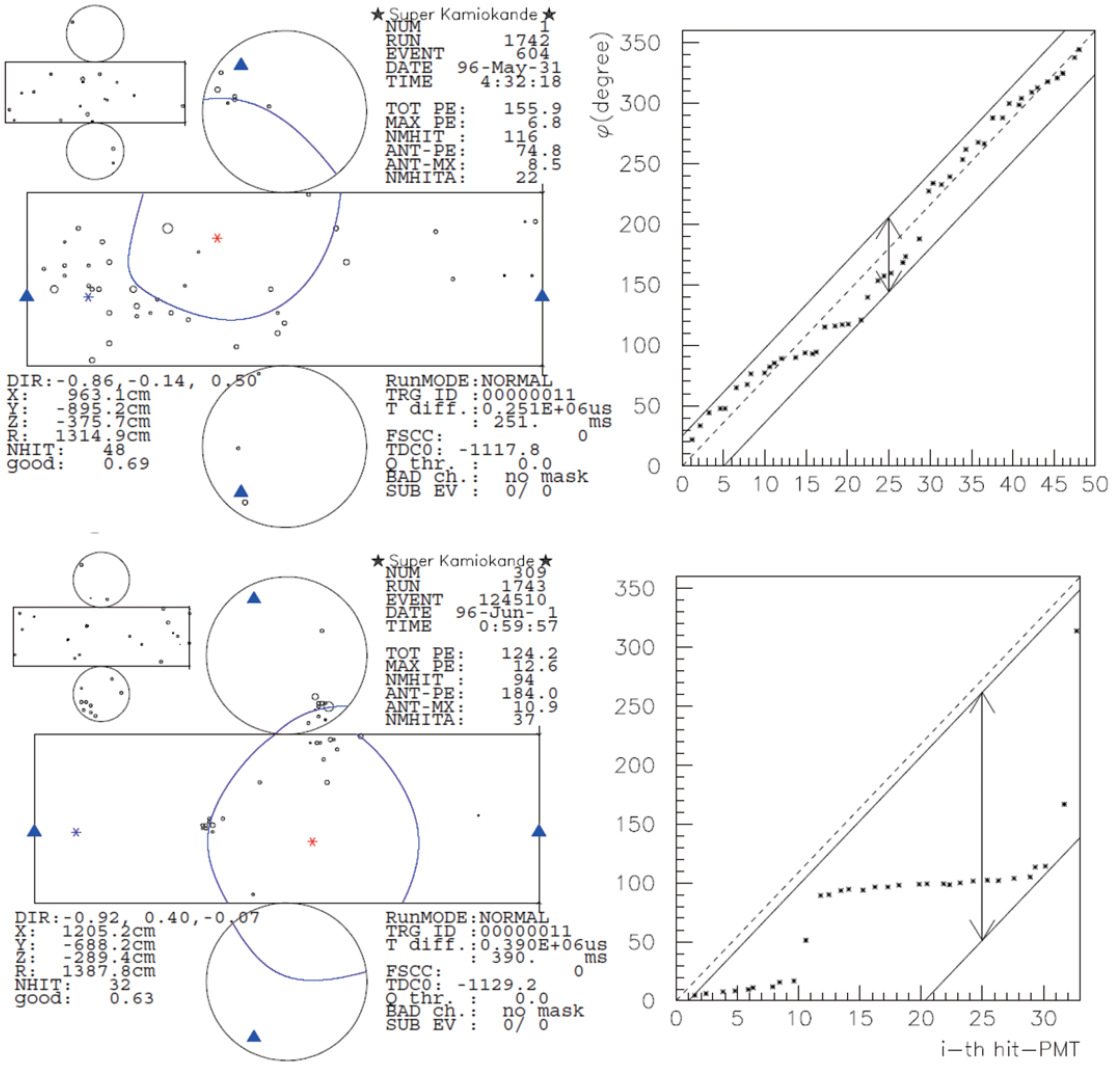

Figure 7.4: Typical examples of the Kolmogorov-Smirnov test for spatial uniformity of hit PMTs around the reconstructed direction in the case of good event (top) and bad event (bottom).

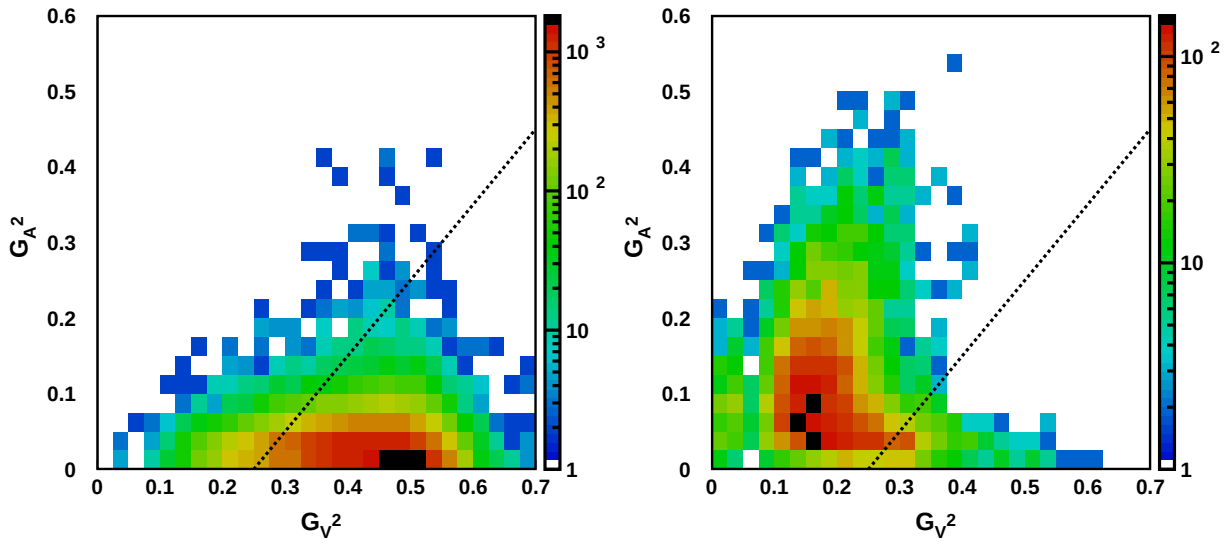

Figure 7.5: Correlation between $G_V{}^2$ and $G_A{}^2$. The left and right panels show the T2K beam ν_μ MC and beam-unrelated events, respectively. In both panels events above 4 MeV in the FV are used. The dotted straight lines correspond to the threshold of $ovaQ \equiv G_V{}^2 - G_A{}^2 = 0.25$.

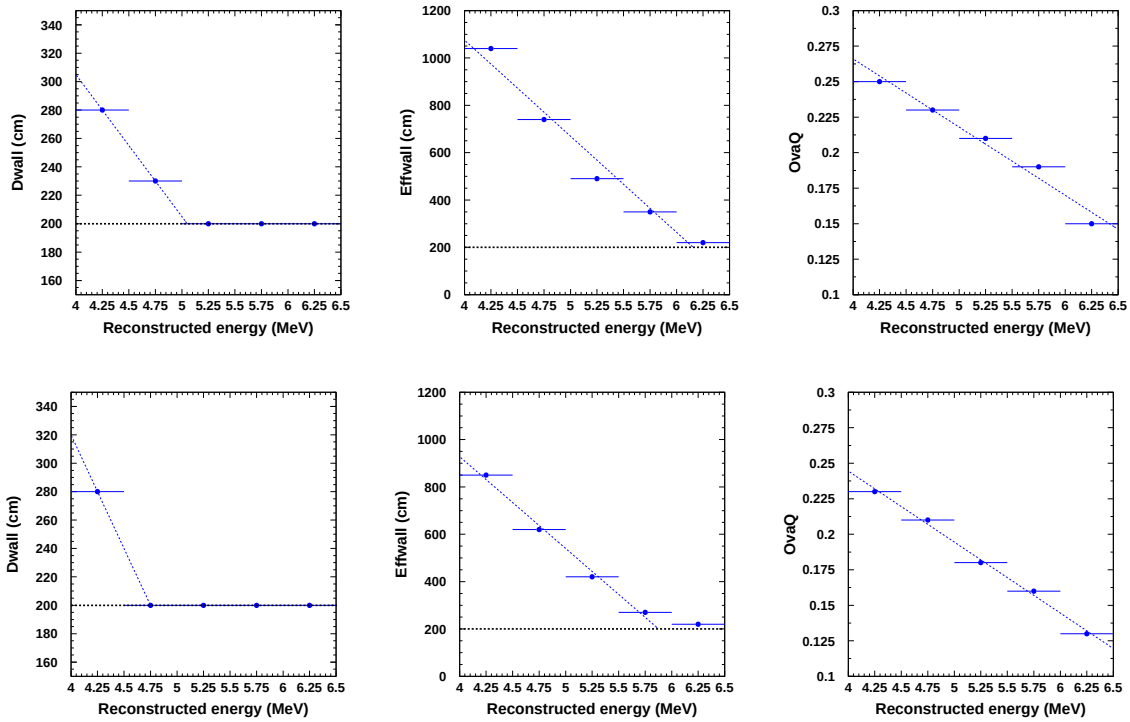

Figure 7.6: Optimized criteria of *dwall*, *effwall* and *ovaQ*. Points are the optimized criteria in each energy bin and the dotted lines are the linear fit to the points. The top panels show the results in case of the beam intensity of 20 kW and six bunches. The bottom panels show the results in case of the beam intensity of 100 kW and eight bunches. In the *dwall* and *effwall* cases, since after the fiducial cut *dwall* and *effwall* of any event are always greater than 200 cm, we use only the points far enough from 200 cm to make the linear fit.

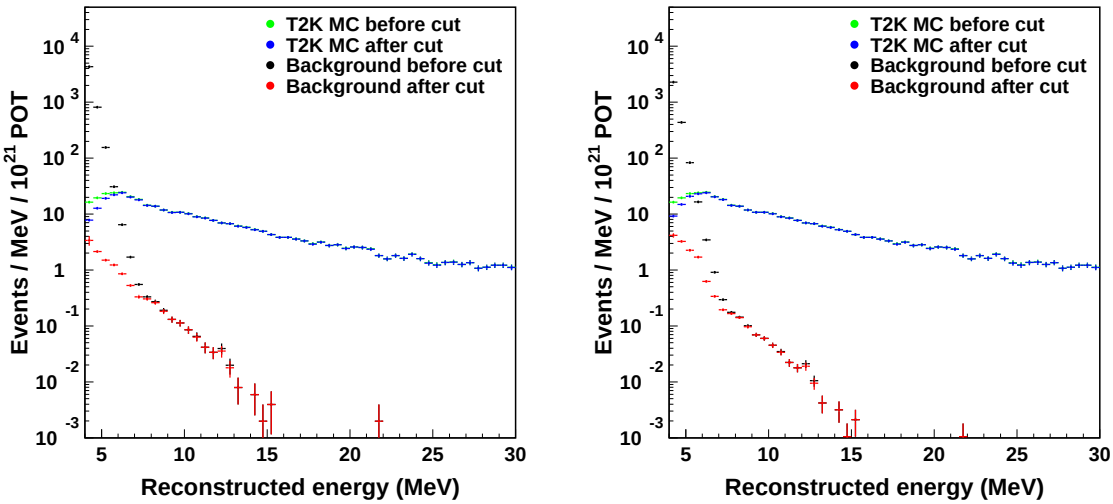

Figure 7.7: Event rates of T2K beam neutrino MC and beam-unrelated events before and after the second reduction. The left panel shows the case of a beam intensity of 20 kW and six bunches and the right panel shows the case of a beam intensity of 100 kW and eight bunches. Since the beam-unrelated events are negligibly small at the higher energy region ($\gtrsim$ 10 MeV), the cut criteria are so loose that there remain almost all the events after the reduction.

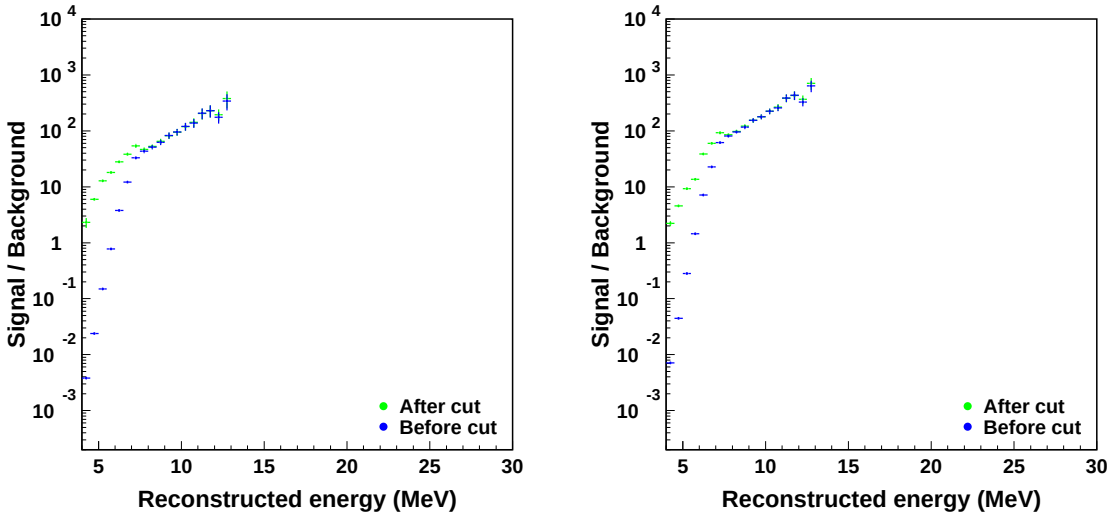

Figure 7.8: Signal-to-noise ratios before (blue) and after (green) the second reduction. The left panel shows the case of a beam intensity of 20 kW and six bunches and the right panel shows the case of a beam intensity of 100 kW and eight bunches.

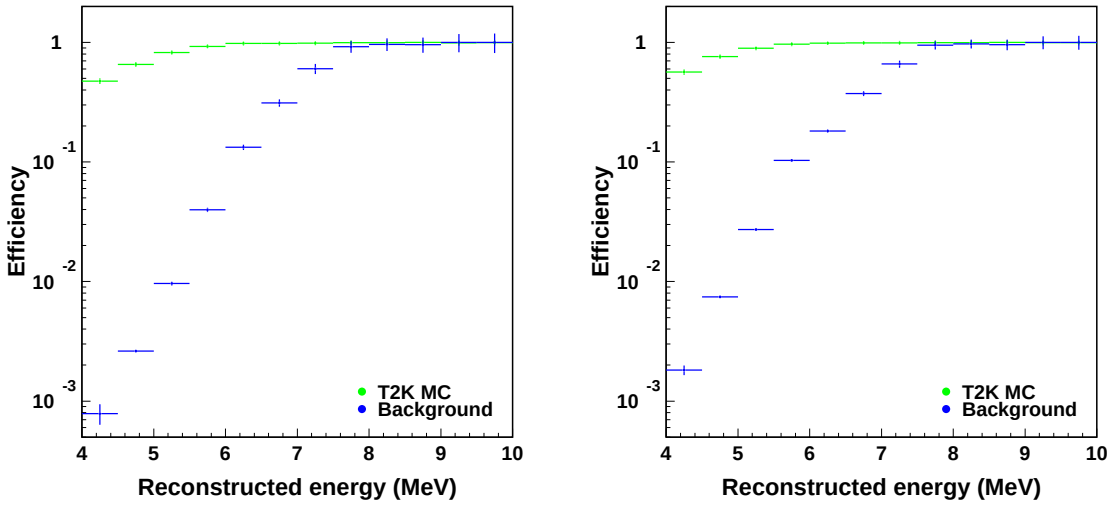

Figure 7.9: Reduction efficiency as a function of reconstructed energy for T2K beam neutrino MC (green) and beam-unrelated (blue) events. The left panel shows the case of a beam intensity of 20 kW and six bunches and the right panel shows the case of a beam intensity of 100 kW and eight bunches.

7.3 Third reduction

In contrast to the second reduction, which is applied to reject beam-unrelated events, the purpose of the third reduction is to isolate NC events among T2K beam neutrino events.

To reduce CC interaction events in the sample, we apply additional cuts: a pre-activity cut on the event's timing structure to reject decay electron events from CC events and a cut on the Cherenkov opening angle to remove muon-like events.

7.3.1 Pre-activity cut

This pre-activity cut is different from the cut with the same name applied in the first reduction in that the main purpose of this cut is to reject low energy events which are actually the decay electrons of T2K beam neutrino events themselves.

The pre-activity cut rejects events which have a pre-activity occurring $0.2 - 20$ μs before the candidate event. In order to determine the cut criterion, a T2K dummy spill data and T2K CC muon events without the momentum cut are used for the background and muon samples, respectively. We reject the candidate event if the N_{30} is greater than 22 since the timing peak is likely to be the parent muon and the candidate event is its decay electron. More than 99.9% of the decay electron events caused by T2K beam neutrinos are removed by this cut while the loss of signal NC events due to dark noise hits is less than 0.1%.

7.3.2 Cherenkov opening angle cut

The Cherenkov opening angle cut is applied as follows: the opening angle is estimated by binning all the angles defined by the possible combinations of three hit PMTs belonging to N_{15} (Fig. 7.10). The histogram is divided into 100 angle bins and peaks are located by finding the seven neighboring bins with the largest number of entries. The middle of the seven bins is taken to be the Cherenkov angle of the event.

There are three regions of Cherenkov opening angles: electron-like (e-like), muon-like (μ-like), and multi-gamma-like. These regions come from the difference in particle types and event topologies. Figure 7.11 shows the three types of event patterns.

A single electron event tends to have a Cherenkov angle of $\theta_C \sim 42^\circ$ while that of a muon is smaller than that of an electron. Figure 7.12 shows the Cherenkov opening angle of a muon in water as a function of the muon momentum. Since muons with the reconstructed (electron-equivalent) energy of 30 MeV, the upper threshold of this analysis, correspond to 250 MeV/c, those muons have Cherenkov angles well below 34°. Multi-gamma-like events are events with multiple gamma-rays of low energy and do not have a clear Cherenkov ring pattern. Figure 7.13 shows the typical histograms of three hit PMT combinations for these types of events.

Figure 7.14 shows the expected Cherenkov angle distribution and its breakdown by neutrino interaction mode. As mentioned above, the leftmost peak at the μ-like region with $\theta_C < 34^\circ$ is mostly visible muons that come from CC interactions and NC others, but remain in the signal

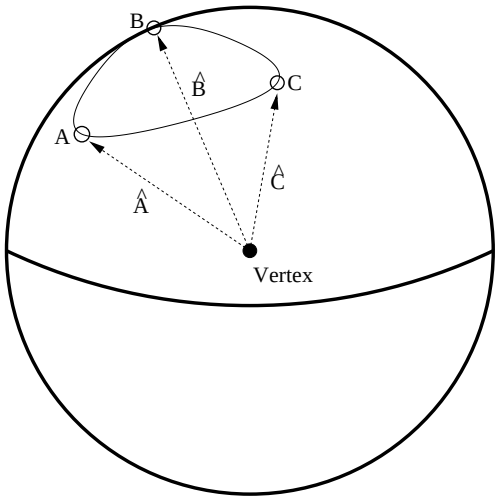

Figure 7.10: The vertex and three independent PMT vectors (A,B,C) uniquely define the Cherenkov opening angle.

energy range due to their low momenta. Single gamma-ray events typically have an opening angle in the e-like region between 38° and 50°. The large peak around 90° comes from events where an ^{16}O nucleus is excited by the knockout nucleons from the neutrino interaction and emits multiple gamma-rays.

The CC components are much larger than those of NC in the region $\theta_C < 34°$, and thus all events with $\theta_C < 34°$ are removed from the data (the threshold is shown by the dotted line).

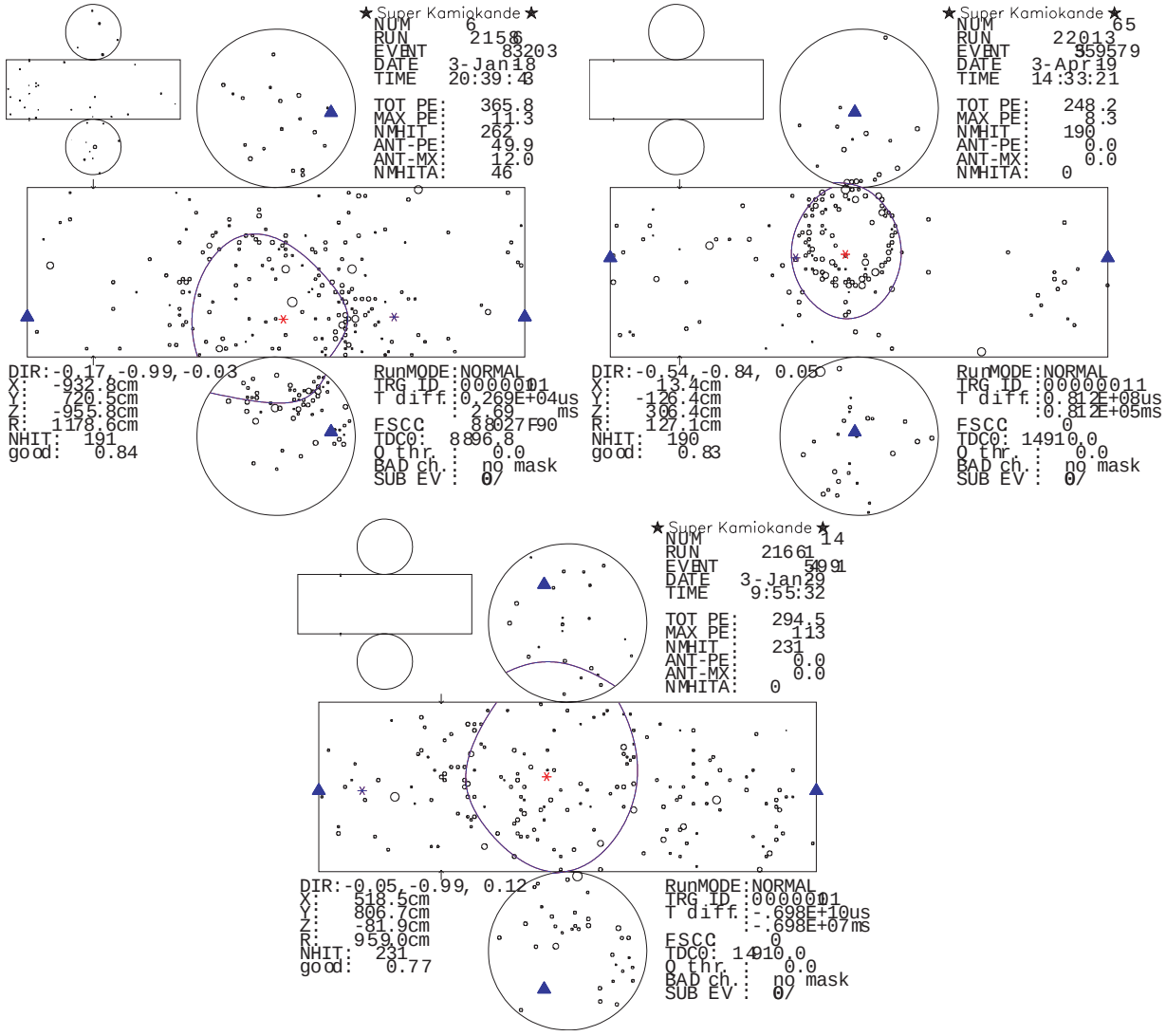

Figure 7.11: Typical event patterns of electron-like, muon-like and multi-gamma-like events. Purple circles indicate the expected Cherenkov light direction based on the reconstructed vertex and direction assuming the Cherenkov opening angle of 42°.

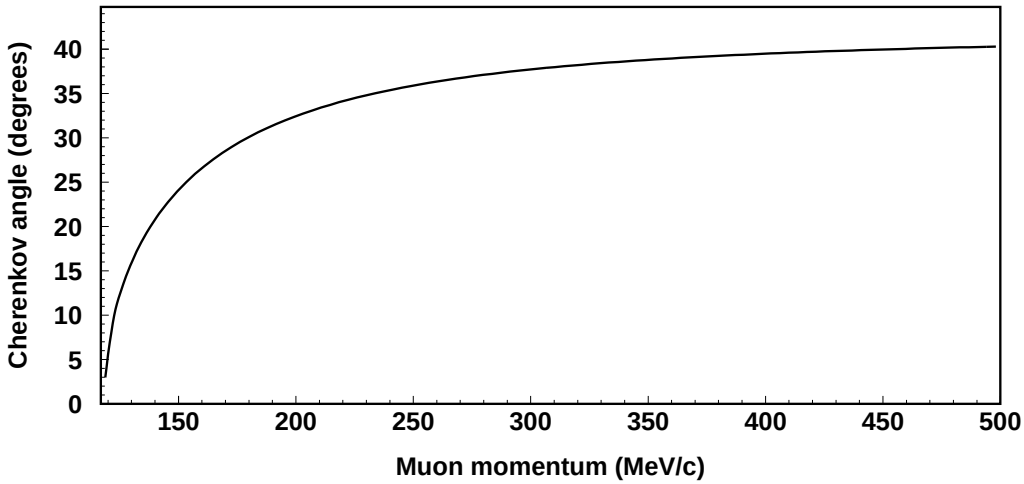

Figure 7.12: Cherenkov opening angle of a muon in water as a function of muon momentum. Since muons with the reconstructed energy of 30 MeV, the upper threshold of this analysis, correspond to 250 MeV/c, those muons have Cherenkov angles below 34°.

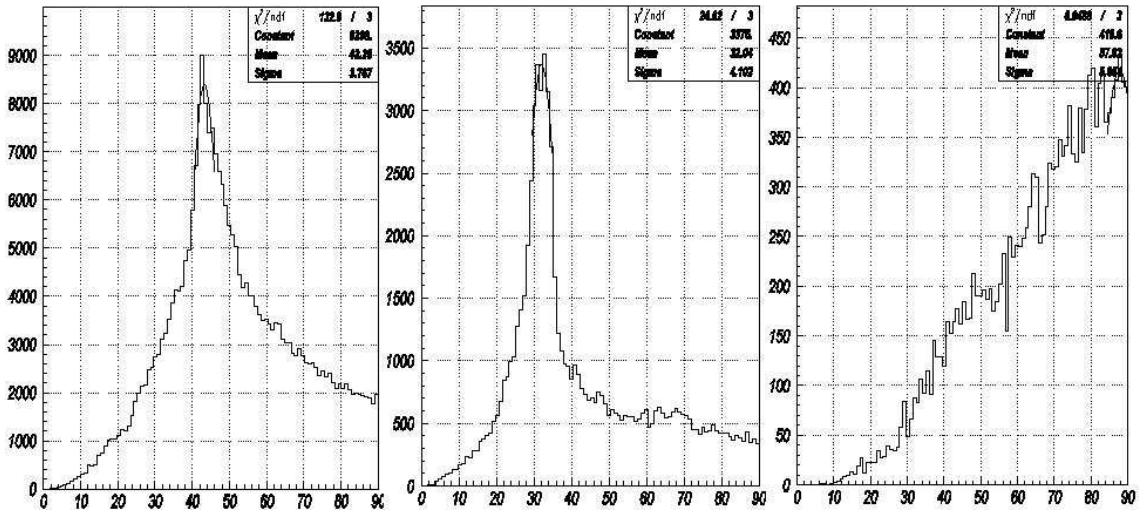

Figure 7.13: Histograms filled with all the angles defined by the possible combinations of three hit PMTs belonging to N_{15} of one event. There are three types of histograms: (from the left) electron-like, muon-like and multi-gamma-like events. The detail of each characteristic is described in the text.

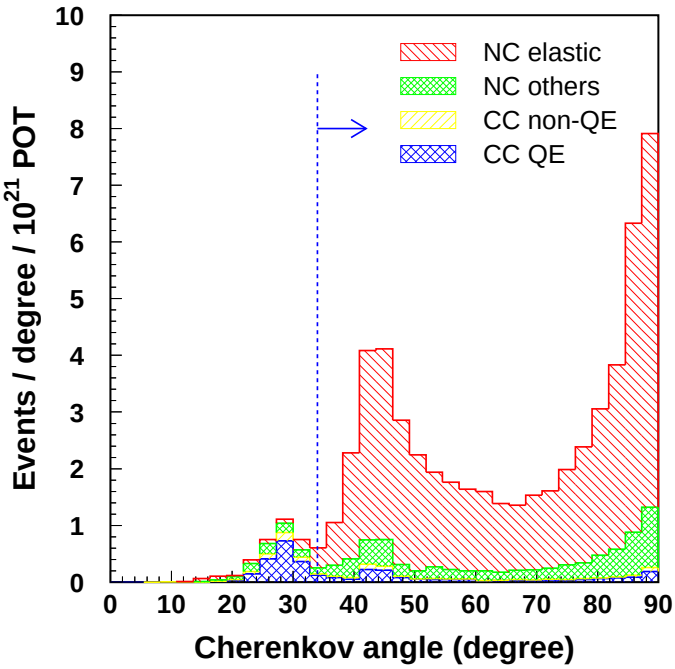

Figure 7.14: Expected Cherenkov angle distribution after the second reduction assuming 1×10^{21} POT and its breakdown by neutrino interaction mode. The dotted line shows the threshold below which events are rejected.

Chapter 8

Results

8.1 Energy and cut parameter distributions

After all cuts, 20 events remain in the data set of RUN-I/II. Figures 8.1−8.2 shows the distribution of energy and other cut parameters of the final sample.

8.2 Data quality

8.2.1 Vertex distribution

Figure 8.3 shows the two-dimensional vertex distributions of X versus Y and R^2 versus Z after each reduction and of the final data sample. Here, X, Y and Z are of the orthogonal coordinate system which has its origin at the center of the SK tank described in Fig. 3.3. $R^2(\equiv X^2+Y^2)$ is the radial distance squared of a vertex from the Z-axis of the SK tank. The one-dimensional projected vertex distributions onto the Z and R^2 axes are shown in Fig. 8.4. The vertices of the final data sample are uniformly distributed.

Also, no significant correlation is seen between the beam direction and event directions, as shown in Fig. 8.5. This is as expected since the de-excitation gamma-rays are emitted isotropically.

8.2.2 Kolmogorov-Smirnov test for the event rates

Figure 8.6 shows the Kolmogorov-Smirnov (KS) test results for the event rates in RUN-I/II. The maximum vertical difference D between observation and the ideal cumulative events was 0.52 for RUN-I and 0.173 for RUN-II after it was normalized by each final data sample, which correspond to the KS probability of 38.9% and 68.6%, respectively. These probabilities are consistent with statistical fluctuations. As mentioned in Section 7.2, the background rate as a function of POT was less in RUN-II, which is the reason we do the KS test for each run, but that effect is not apparent in these figures due to their small statistics.

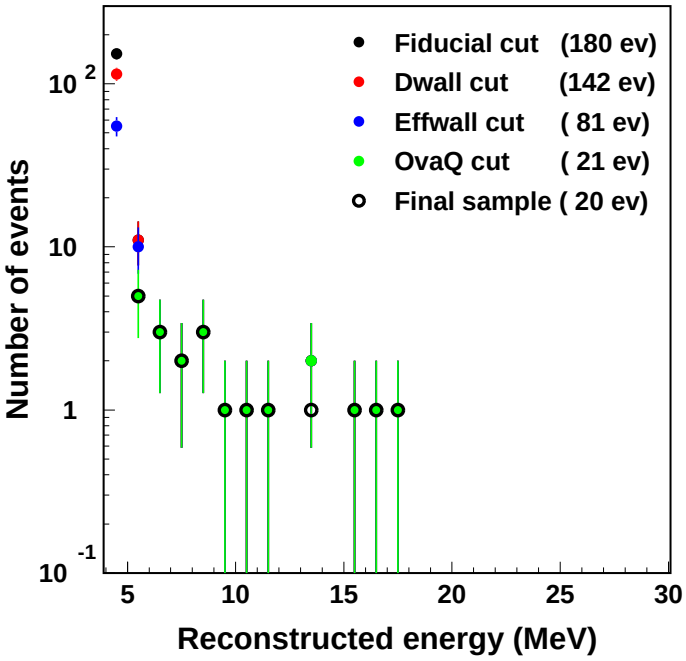

Figure 8.1: Reduction results of energy distributions. The distribution after a given cut is plotted over the previous cut. Only on-timing events are shown. Error bars show statistical errors.

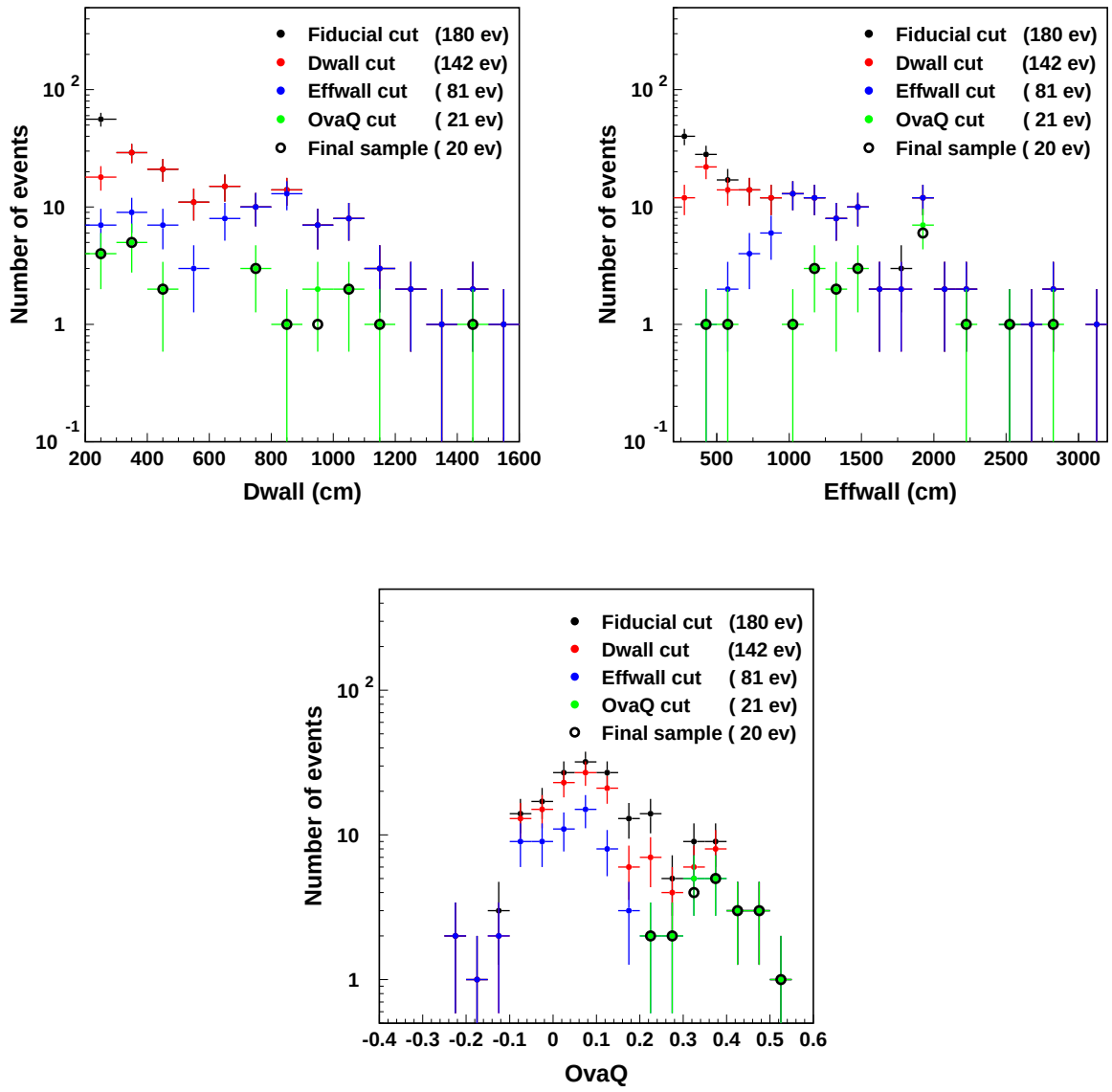

Figure 8.2: Reduction results of cut parameter distributions. The distribution after a given cut is plotted over the previous cut.

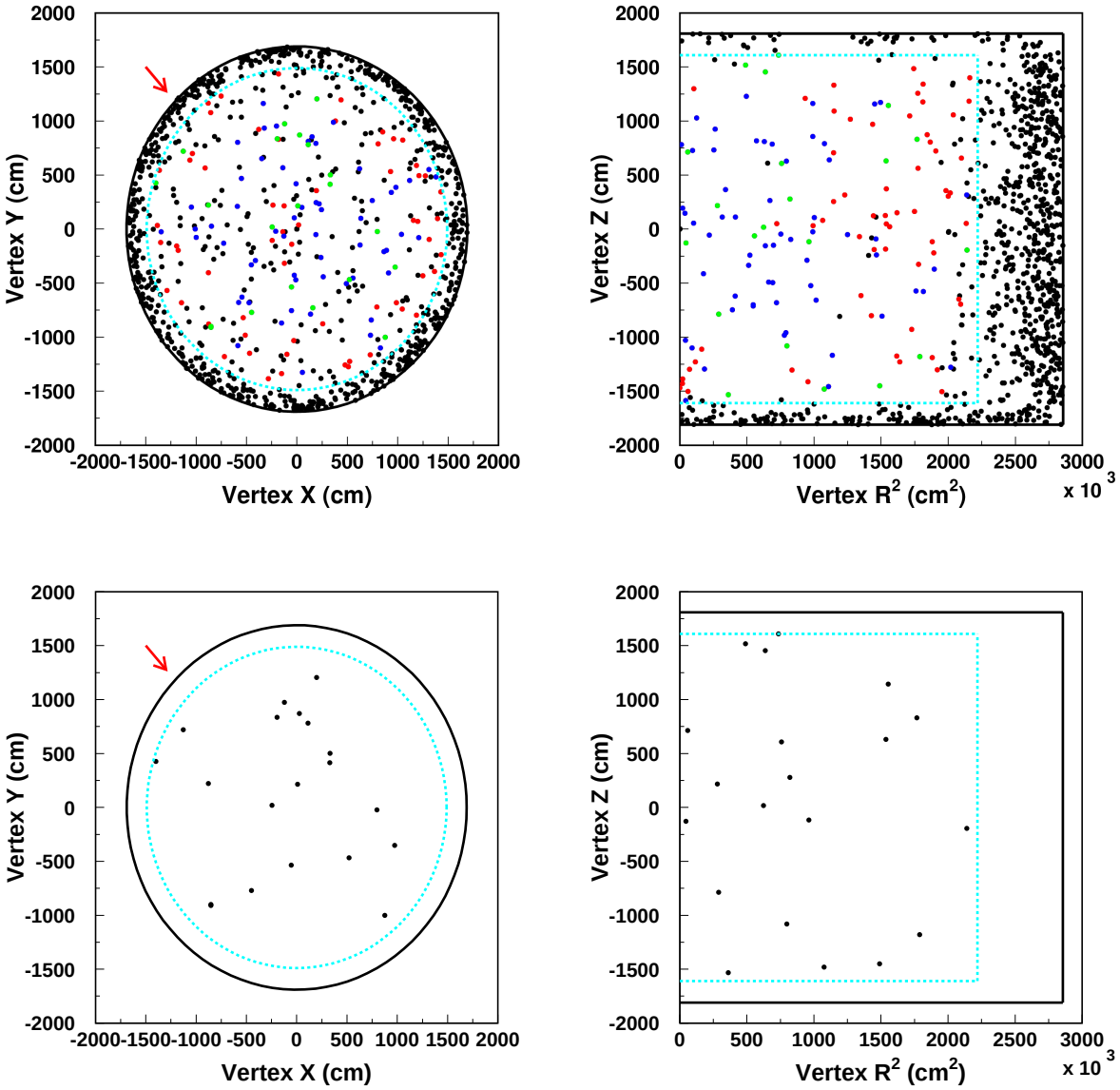

Figure 8.3: Two dimensional vertex distributions after each reduction and of the final data sample. Top: X versus Y (left) and $R^2(\equiv X^2+Y^2)$ versus Z (right) distributions after each reduction. The meanings of each color is the same as in Figs. 8.1 and 8.2 while black points show the events before the fiducial volume cut. Bottom: X versus Y (left) and R^2 versus Z (right) distributions of the final data sample. In the left two panels, the arrows show the T2K beam direction. In all panels, the solid (black) and dotted (light blue) lines show the boundaries of the inner detector and fiducial volume, respectively.

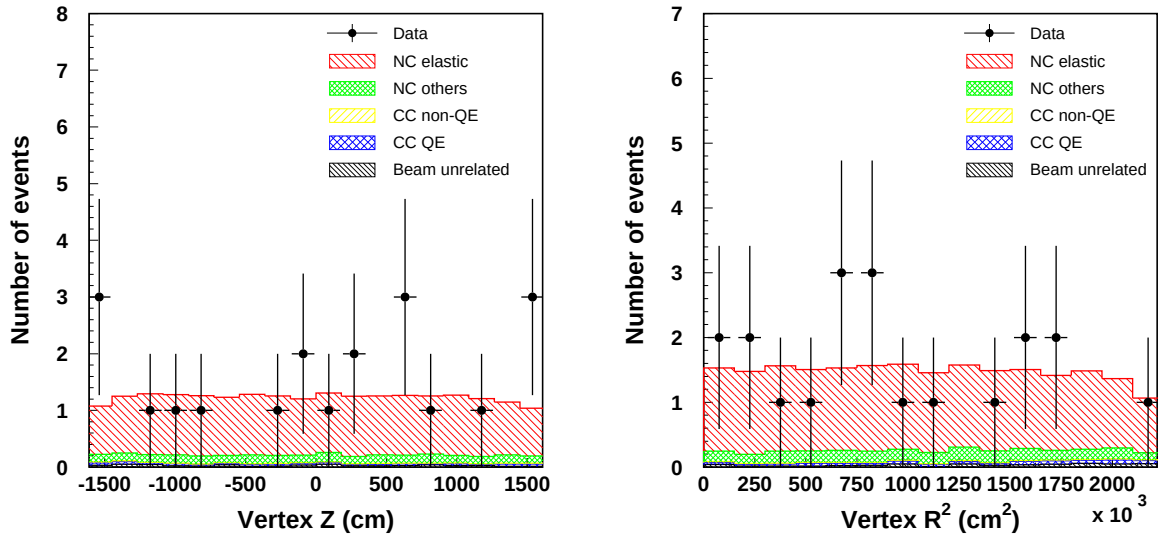

Figure 8.4: One dimensional vertex distributions of the final data sample in the Z (left) and R^2 (right).

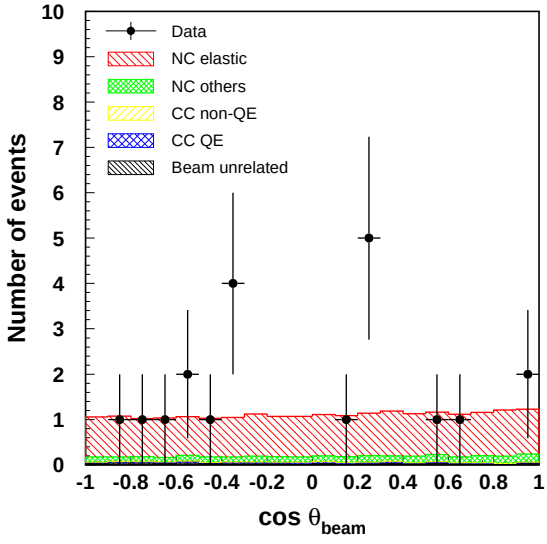

Figure 8.5: Distribution of the event direction with respect to the T2K beam direction.

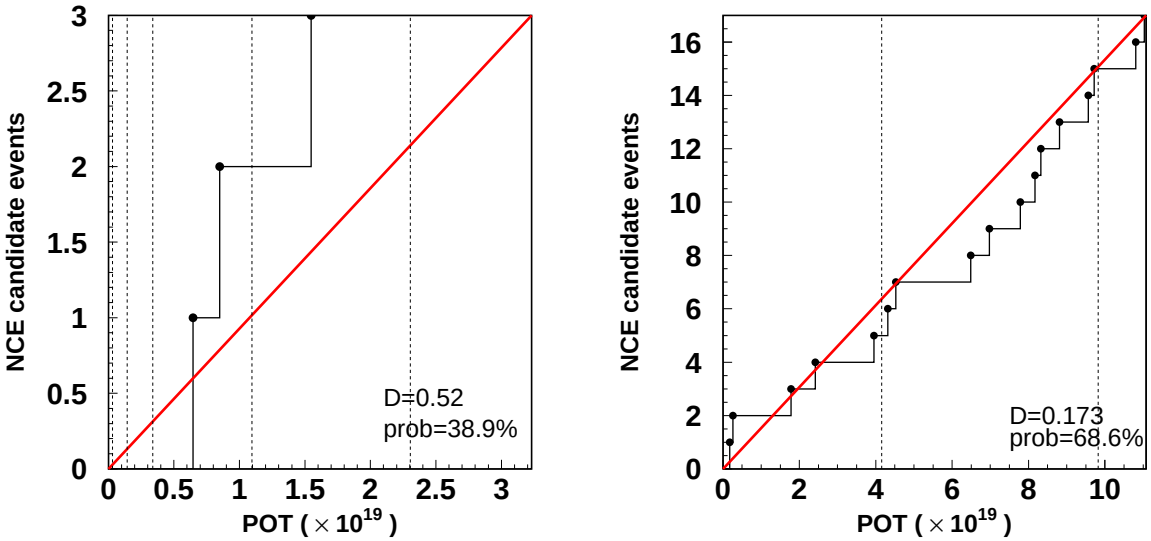

Figure 8.6: The KS test results for the event rates in RUN-I (left) and RUN-II (right).

8.3 Event timing distribution

The event timing distributions of the final sample in this analysis is shown in Fig. 8.7. In the left panel, the ΔT_0 distribution of the final sample is shown, compared to the bunch center positions fitted by those of the fully contained events. It should be noted that since the plotted events are already subjected to the timing cut, described in Section 7.2, off-timing events, if any, are not plotted in Fig. 8.7. In the right panel, the residues of the final sample ΔT_0 with respect to the bunch center positions are plotted in units of ns. All ΔT_0 agree with the bunch center positions well within 100 ns.

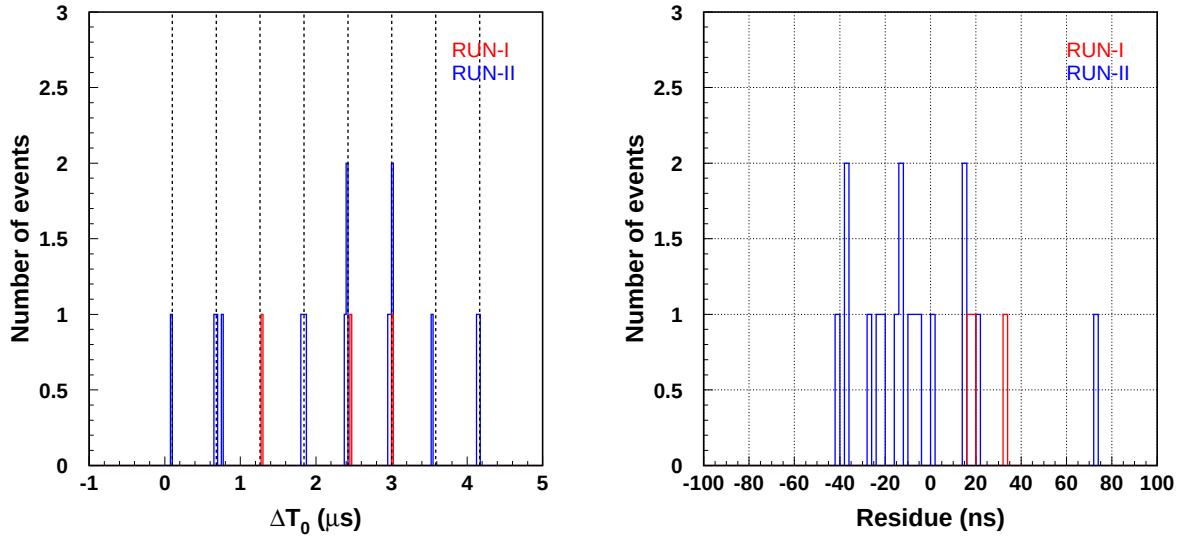

Figure 8.7: Left: ΔT_0 distribution of all the events in the final sample during the RUN-I (red) and II (blue) compared to the bunch center positions fitted by those of the fully contained events (eight dashed vertical lines). Right: The residues of the final sample ΔT_0 with respect to the bunch center positions.

Chapter 9

Discussion

9.1 Comparison with prediction

After all cuts, 20 events remain in the data set of RUN-I/II. Table 9.1 summarizes the numbers of events after each reduction. As already mentioned in previous chapters, the prediction is composed of two parts: beam-related events and beam-unrelated events. The former is normalized by the POT statistics at RUN-I/II while the latter by the livetime of this analysis, which is calculated as 9.99×10^5 spills $\times$(6 bunches $\times$ 200 ns) + 1.48×10^6 spills $\times$(8 bunches $\times$ 200 ns) = 3.57×10^9 ns, where each number of beam spills in Tab. 7.1 at RUN-I and II is used. Table. 9.2 shows the breakdown of the beam-related events. In Figs. 9.1−9.2, comparison results of distributions between data and prediction are shown. In all but Cherenkov angle distributions, data and prediction are in good agreement within statistical fluctuations. Especially, the energy distribution of observed events peaks around 6 MeV as expected. In the Cherenkov angle distribution, however, events are expected to have its maximum peak around 90° while the observed events have it around 42°. This discrepancy will be discussed later in this chapter.

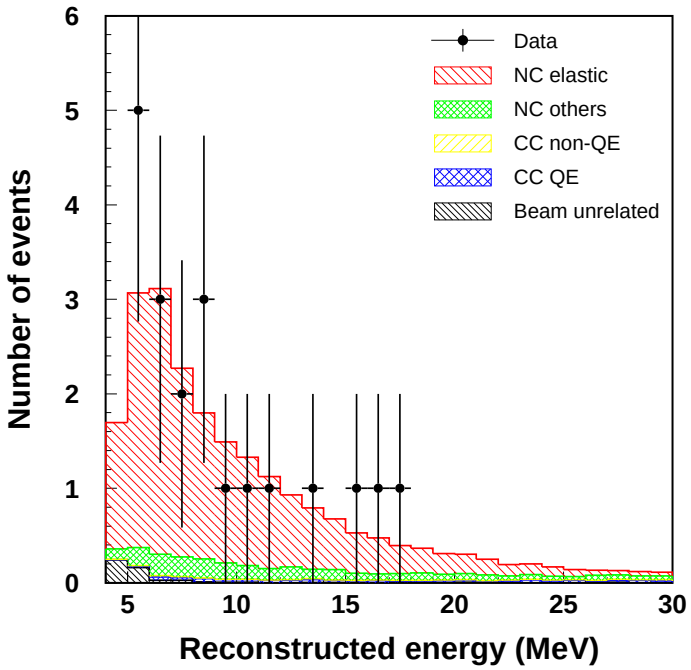

Figure 9.1: Comparison of energy distribution between the final data sample and POT-normalized MC with livetime-normalized beam-unrelated events.

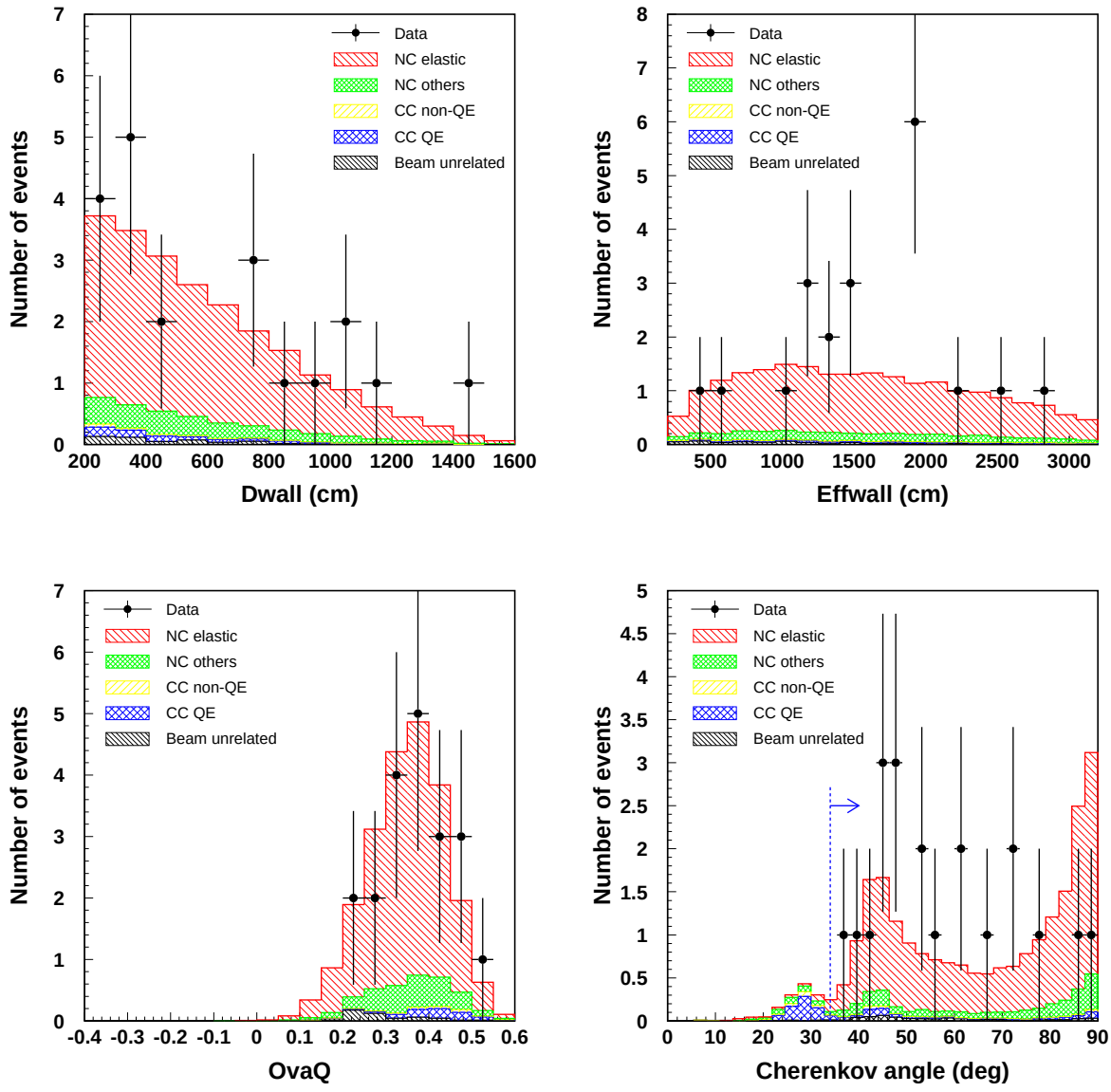

Figure 9.2: Comparison of the distributions of three cut parameters and Cherenkov angle between the final data sample and POT-normalized MC with livetime-normalized beam-unrelated events.

Table 9.1: The numbers of on-timing events which remain after each reduction are summarized with the expected numbers of beam-related and beam-unrelated events. How to normalize the prediction is detailed in the text.

	Observed events	Beam-related events	Beam-unrelated events
dwall cut	142	24.7	106
effwall cut	81	24.4	44
ovaQ cut	21	23.6	0.6
Pre-activity cut	21	23.6	0.6
Cherenkov angle cut	20	22.2	0.6

Table 9.2: Breakdown of the beam-related events.

	Events	
NC elastic	18.8	(84.7%)
NC others	2.6	(11.7%)
$\nu_\mu + \bar{\nu}_\mu$ CC QE	0.6	(2.7%)
$\nu_\mu + \bar{\nu}_\mu$ CC non-QE	0.2	(0.9%)
$\nu_e + \bar{\nu}_e$ CC	2.3×10^{-4}	(0.001%)
Total	22.2	

Table 9.3: Summary of systematic uncertainties in the prediction of the T2K beam neutrino flux.

Source	Uncertainty (%)
ν_μ	15
$\bar{\nu}_\mu$	16
ν_e	15
$\bar{\nu}_e$	30

9.2 Systematic uncertainties

In this section, the systematic uncertainty of the prediction described in the last section is discussed. Since the sterile neutrino search presented in the next section only uses the total number of events expected to remain in the final data sample, we constrain ourselves to the discussion of the uncertainty of the total number of remaining events. Also, the prediction is mostly composed of beam-related events as can be seen in the last section, and thus we focus on the uncertainty of the expected beam-related events. Possible sources of the uncertainty are roughly divided into five categories: the neutrino flux, the neutrino interaction, the production rates of prompt and secondary nuclear de-excitation gamma-rays, and the detector response.

9.2.1 Neutrino flux

The uncertainty of the neutrino flux normalization linearly affects the predicted number of beam-related events. Figure 9.3 shows fractional errors of neutrino fluxes as a function of neutrino energy. As can be seen from the parent neutrino energy spectra of the final MC sample for NC events shown in Fig. 9.4, most events come from neutrinos with $E_\nu < 2$ GeV. The flux uncertainties obtained by combining Fig. 9.3 and Fig. 9.4 are summarized in Tab. 9.3.

9.2.2 Neutrino interaction

As shown in Tab. 9.2, about 85% of beam-related events are from NC elastic interaction. Thus, the dominant source of the cross section uncertainty is that of NC elastic interaction. To estimate the systematic uncertainties of the NC elastic neutrino-nucleon cross section, we compare our simulation to existing data. Figure 9.5 shows the comparison result of NC elastic $\nu N \to \nu N$ cross section as a function of Q^2 among the measurement by the MiniBooNE experiment [155], the SciBooNE experiment [156] and our simulation. The MiniBooNE data is a flux-averaged differential cross section on CH_2, where Q^2_{QE} is defined as the $Q^2_{QE} = 2m_N \sum_i T_i$ using the nucleon mass m_N and the sum of the kinetic energies of the final state nucleons T_i. The $\nu N \to \nu N$

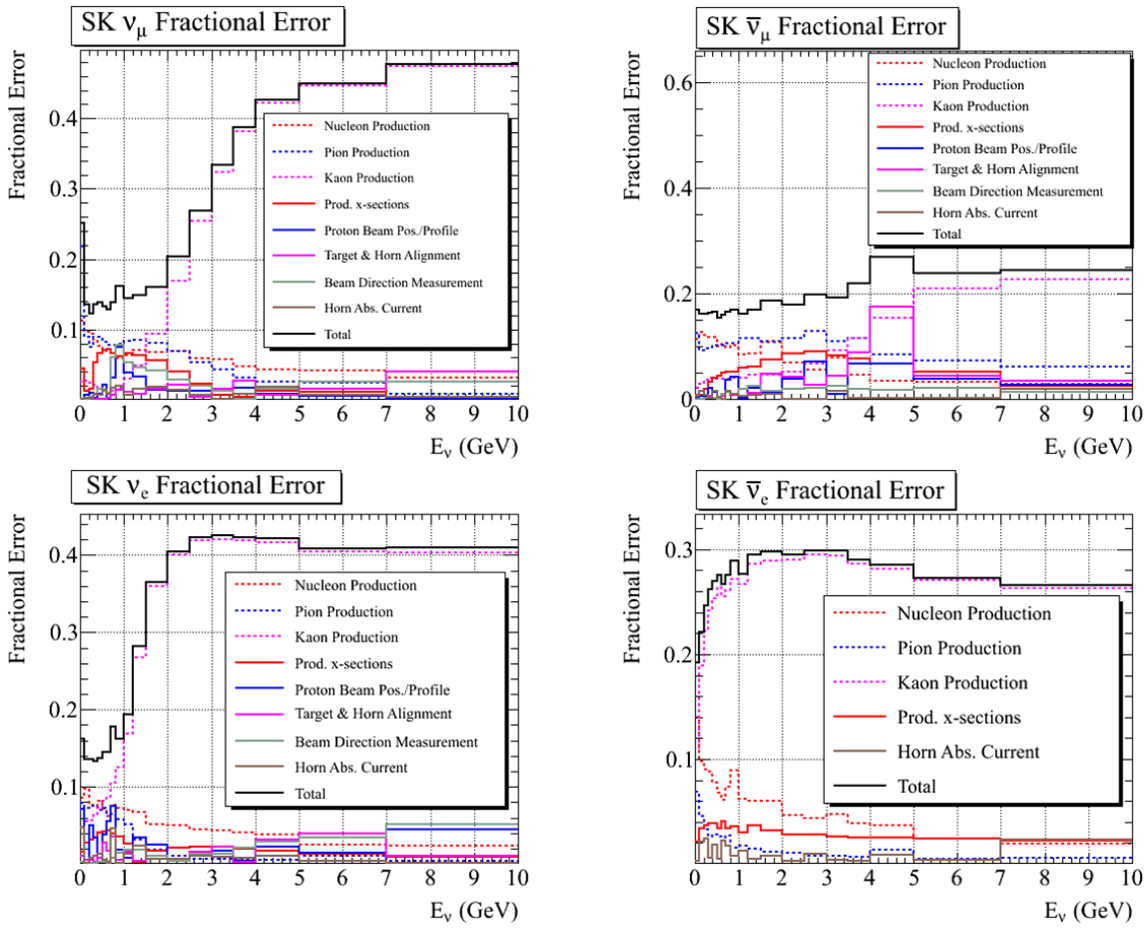

Figure 9.3: Flux fractional errors as a function of neutrino energy are shown for ν_μ (top left), $\bar{\nu}_\mu$ (top right) and ν_e (bottom). Bin-to-bin correlations are ignored.

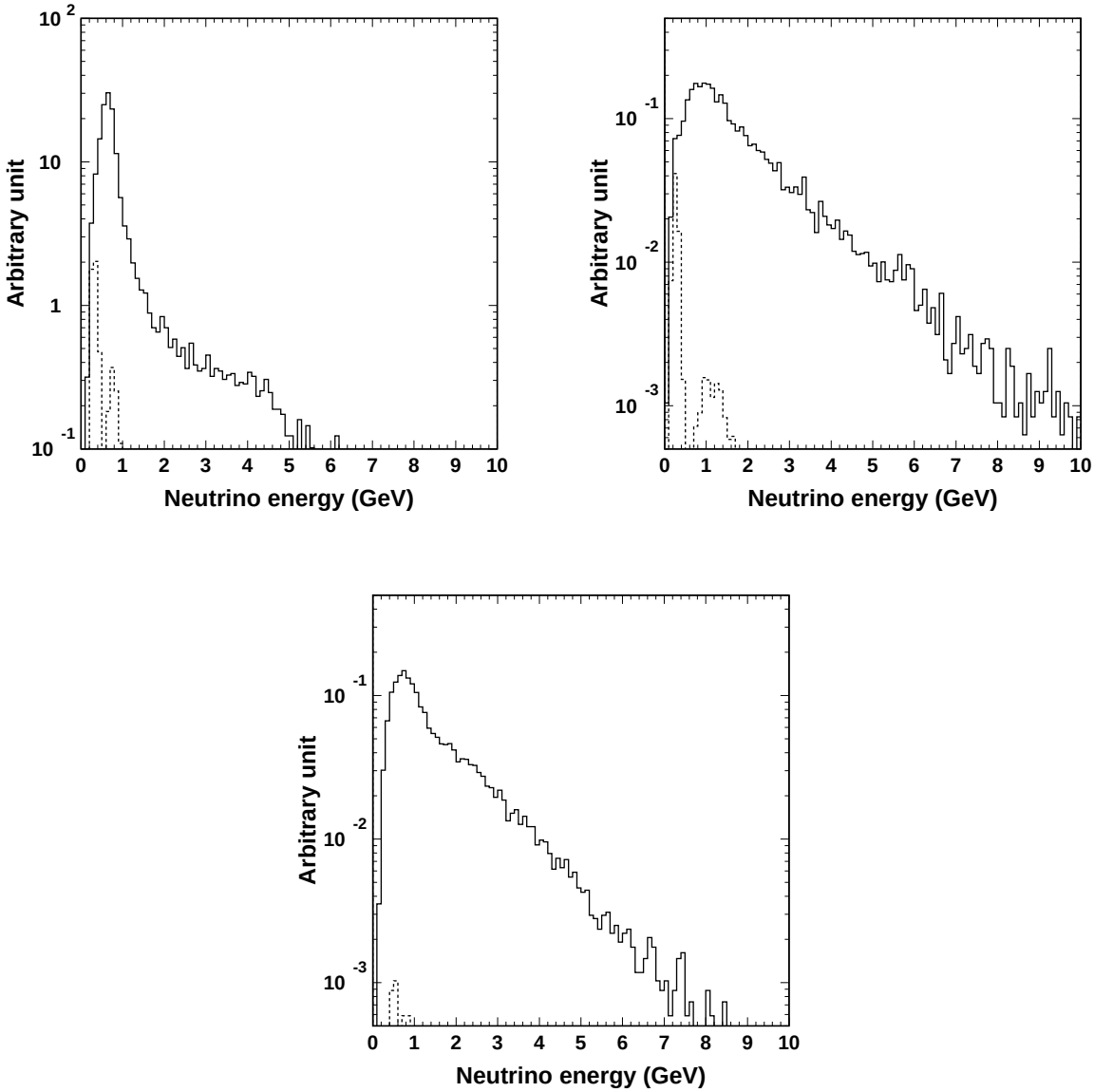

Figure 9.4: The parent neutrino energy spectra of the final MC sample selected as NC events. ν_μ (top left), $\bar{\nu}_\mu$ (top right) and ν_e (bottom) are shown. The solid lines show the total component while the dotted lines show the CC component. Each CC component in the top two panels has two peaks, where the first one comes from the low momentum but visible muons and the second one has the similar peak energy as the NC components since it comes from the invisible muons accompanied by nuclear de-excitation gamma-rays.

cross section is expressed as:

$$\frac{d\sigma_{\nu N\to\nu N}}{dQ^2} = \frac{1}{7}C_{\nu p,\mathrm{H}}(Q^2)\frac{d\sigma_{\nu p\to\nu p,\mathrm{H}}}{dQ^2} + \frac{3}{7}C_{\nu p,\mathrm{C}}(Q^2)\frac{d\sigma_{\nu p\to\nu p,\mathrm{C}}}{dQ^2} + \frac{3}{7}C_{\nu n,\mathrm{C}}(Q^2)\frac{d\sigma_{\nu n\to\nu n,\mathrm{C}}}{dQ^2} \quad (9.1)$$

where $d\sigma_{\nu p\to\nu p,\mathrm{H}}/dQ^2$ is the NC elastic cross section on free protons, $d\sigma_{\nu p\to\nu p,\mathrm{C}}/dQ^2$ is that on bound protons in carbon nucleus, and $d\sigma_{\nu n\to\nu n,\mathrm{C}}/dQ^2$ is that on bound neutrons in carbon nucleus. The efficiency correction functions $C_{\nu p,\mathrm{H}}$, $C_{\nu p,\mathrm{C}}$ and $C_{\nu n,\mathrm{C}}$ account for different selection efficiencies for each type of NC elastic scattering process, which they estimated from their MC as functions of Q^2 [155]. Our simulation assumes the neutrino flux for MiniBooNE and $M_A = 1.21$ GeV and uses the spectral function of ^{16}O instead of ^{12}C for the calculation of the last two terms of the right hand side of Eq. (9.1). This causes a slight underestimate of the cross section because larger nuclear effect is expected in oxygen nucleus. As for the SciBooNE data points, while the neutrino flux is basically the same as the MiniBooNE experiment, the different neutrino target (C_8H_8) is used, and the relatively lower density of free protons in the target leads to a several percent smaller cross section of $\nu N \to \nu N$. Also, the selection efficiency is not taken into account for the SciBooNE data points in the left panel of Fig. 9.5. As can be seen in the right panel of Fig. 9.5 which shows the simulated Q^2 distribution for the T2K beam ν_μ MC final sample, $Q^2 \lesssim 0.4$ GeV^2 is found to be the relevant Q^2 region for the analysis of this thesis. Using the Q^2 distribution as the weight for the discrepancy between data and simulation at each bin and summing them up over 23 bins from 0.101 to 1.655 GeV^2 shown in the left panel, $\pm 17\%$ is assigned to the systematic uncertainty of the cross section.

9.2.3 Prompt nuclear de-excitation gamma-rays

The uncertainty of prompt nuclear de-excitation comes from that of the spectroscopic factor of each hole state and the branching fractions of final states for each hole state.

As mentioned in Chap. 6, the region above the $1s_{1/2}$ is not simulated. We assume the kinematics and the absolute yield of gamma-rays and particles from those states are almost the same as those of the $1s_{1/2}$ state because both of the states have in common enough high binding energies compared to the particle emission thresholds. It should be noted that in this treatment of higher states the uncertainty on the spectroscopic factor of $1s_{1/2}$ state itself, which is estimated from the comparison of models to be $30 - 40\%$, can be handled in the same manner as the uncertainty stated above. We compare expected energy distributions among (1) the default, (2) the case where all states higher than the $1s_{1/2}$ state are included in the $1s_{1/2}$ state and (3) the case where the spectroscopic factor of the $1p_{3/2}$ state is increased by 8% and 17% for proton and neutron hole states, respectively, which are estimated from the difference among models [133,147]. We change the spectroscopic factor so that the increment (decrement) in the spectroscopic factor of $1s_{1/2}$ or $1p_{3/2}$ is compensated by the decrement (increment) in that of $1p_{1/2}$ or other states. It is noteworthy that since no gamma-rays are emitted in more than 70% of the $1s_{1/2}$ state, as seen in Tab. 6.4, the total number of events in the case (2) is not expected to differ so much from that of the defalt case (1). The comparison result is shown in Fig. 9.6: the increment of

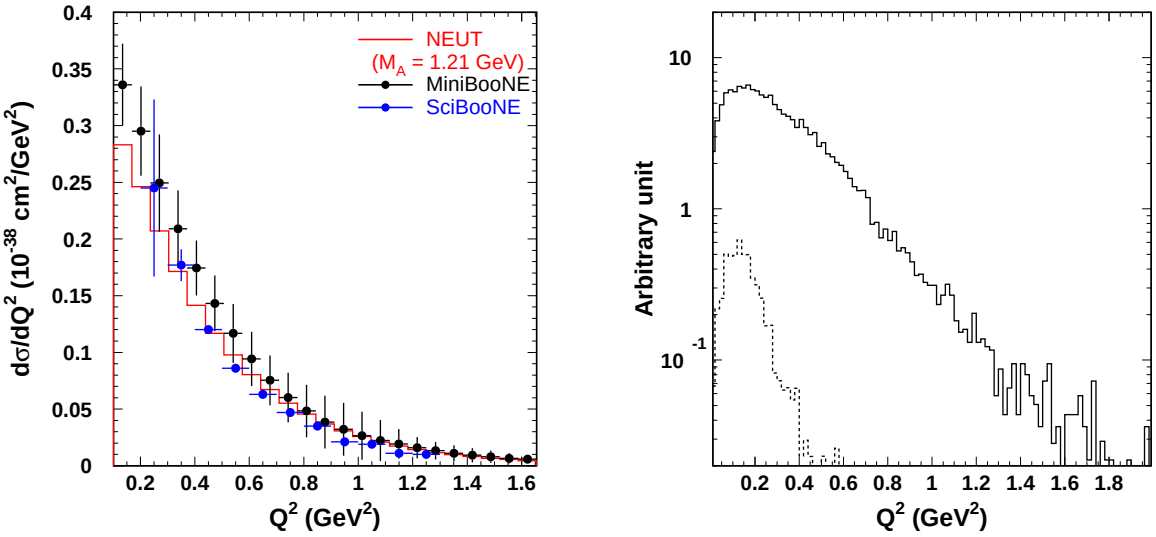

Figure 9.5: Left: Comparison result of the NC elastic cross section as a function of Q^2 among the NEUT simulation at $M_A = 1.21$ GeV^2 (red histogram), the measurement by the MiniBooNE experiment [155] (black dot) and the SciBooNE experiment [156] (blue dot). For the MiniBooNE data, the predicted NC elastic-like background is already subtracted out, and the error bar shows the total error. Right: The Q^2 distribution of the beam ν_μ MC sample selected as NC events. The solid line shows the total component while the dotted line shows the CC component.

the spectroscopic factor of each hole state leads to more events in the low reconstructed energy region, but the total numbers of events does not increase by more than 3% in both cases. We see that, compared to the extent of the increment of branching fractions, the effect on the predicted number of events is very small.

This fact can be applied to the estimation of other sources of uncertainty, such as those of the relative branching ratios of all the nuclear de-excitation modes. The authors of Ref. [141] estimate the uncertainty on the relative branching ratios (including those of ground states) for the $1s_{1/2}$ state as $+3.9/-6.4\%$ for $E_\gamma > 6$ MeV and $+12/-9.3\%$ for $3 < E_\gamma < 6$ MeV. This size of uncertainty should have a small effect on the total number of events.

Gamma-rays below 3 MeV are not simulated in the current NEUT since there are few available experimental data which provide the branching ratios of those gamma-rays. Similarly, however, we expect their contribution to the expected number of events to be very small from the fact stated above and also from the following two reasons: some models predict their yield to be below 10% of all de-excitation modes (see, *e.g.*, Fig. 5 of Ref. [157]); 3 MeV gamma-rays are hardly triggered due to their low energy, together with the fact that their Compton electrons have smaller energies than their parent gamma-rays. We assign $\pm 1\%$ uncertainty to the effect of the neglect of gamma-rays below 3 MeV.

As mentioned in Chap. 6, we assume that the de-excitations from multi-nucleon holes are basically the same as those from single-nucleon holes. Since this assumption has not been experimentally substantiated, we estimate the uncertainty conservatively as follows. According to Fig. 6.11, in more than four out of ten events, a neutrino target nucleus remains a multi-nucleon hole state after interaction. An extremely different case from our assumption is that the multi-nucleon hole states emit no gamma-rays above 3 MeV. This leads to $40 - 50\%$ smaller spectroscopic factors of the $1s_{1/2}$ and $1p_{3/2}$ states than our defalt simulation, and the effect of this decrement can be estimated through a similar study as shown above. Using the ratio between the increase (decrease) in the states and that in the total number of events, we assign $\pm 9\%$ to the uncertainty associated with the assumption.

As a total, we assign $\pm 10\%$ uncertainty to the production rate of the prompt nuclear de-excitation gamma-rays after neutrino interaction. The breakdown of the total uncertainty is shown in Tab. 9.4. Combining it with the cross section of NC elastic and other neutrino interactions, $\pm 20\%$ is assigned as a conservative value of the systematic uncertainty on the expected beam-related events caused by the uncertainties on the prompt gamma-ray production.

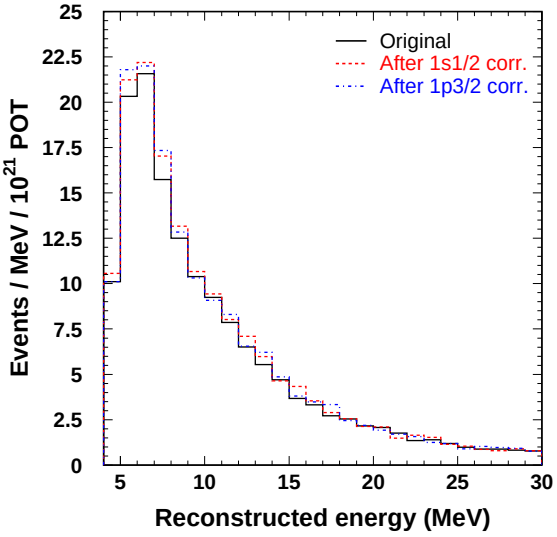

Figure 9.6: Expected energy distribution of the default (black solid), the case where all higher states than the $1s_{1/2}$ state are included in the $1s_{1/2}$ state (red dashed) and the case where the spectroscopic factor of the $1p_{3/2}$ state is increased by 8% and 17% for proton and neutron hole states, respectively (blue dashed-dotted).

Table 9.4: Summary of systematic uncertainties on prompt gamma-ray production. The second column shows the uncertainties on the expected number of events.

Source	Uncertainty (%)
$1p_{3/2}$ state	± 3
$1s_{1/2}$ state	± 1
States higher than $1s_{1/2}$ state	± 3
Gamma-rays below 3 MeV	± 1
Multi-nucleon hole state induced by FSI	± 9
Total	± 10

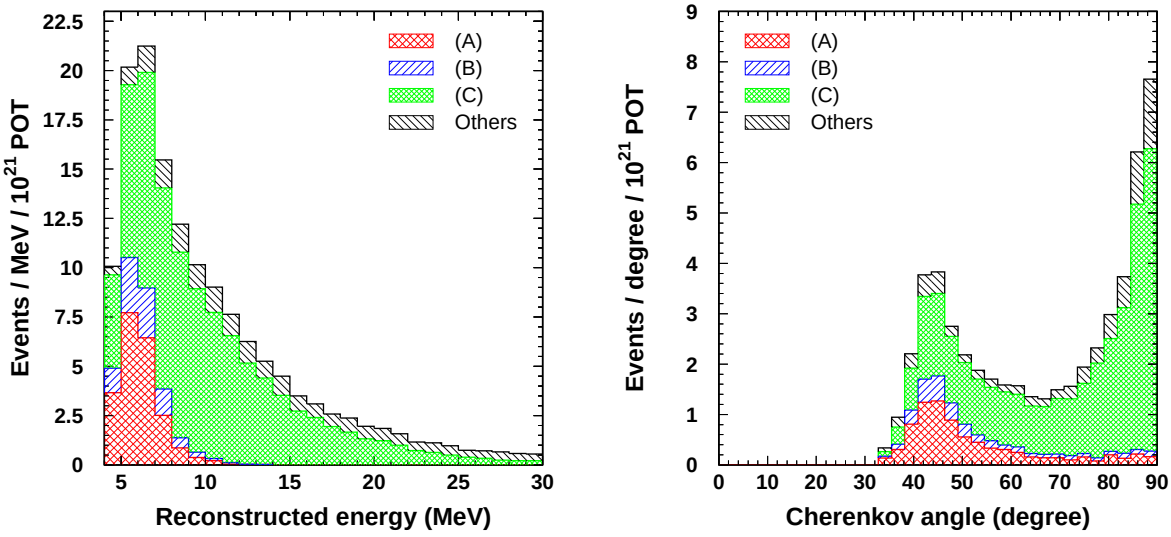

Figure 9.7: Breakdowns of predicted event energy distribution (left) and Cherenkov angle distribution (right) by sources of Cherenkov photons. Both panels show only neutral-current components. The definition of each categorized group is given in the text.

9.2.4 Secondary gamma-ray production

In order to estimate the contribution of secondary gamma-ray to the total spectrum, we decompose the spectra of beam-related events by sources of Cherenkov photons. Figure 9.7 shows breakdowns of reconstructed energy and Cherenkov angle distributions only for neutral-current components. In both panels, events are categorized by following cases,

(A) Only prompt gamma-rays

(B) Delta-rays by any proton in addition to (A)

(C) Secondary gamma-rays in addition to (B)

(D) Other sources such as prompt pions and their decay muons.

As shown in the Cherenkov angle distribution in Fig. 9.2, there is some discrepancy between data and prediction at $\theta_{Ch} \simeq 90°$, where secondary gamma-rays are dominant, which is shown in the right panel of Fig. 9.7. This discrepancy may be caused by the low statistics of observed events, but we can assume it is caused by some systematic biases included in the simulation of secondary gamma-rays when we take into account the model dependence of the production of the gamma-rays by neutrons, which is shown in the right panel of Fig. 6.17.

According to each experiment whose data is used in the simulator MICAP for the simulation of de-excitation gamma-rays [158], the systematic uncertainty on the production rate of secondary gamma-rays is $10 - 20\%$ for incident neutrons. However, we see in the right panel of Fig. 6.17 a significant (apparently greater than 20%) discrepancy of the secondary gamma-ray production rates between the two simulators below and above 20 MeV in the kinetic energy of incident nucleon for the neutron case. Since this discrepancy is not seen in the proton case (left panel) while the strong interaction process is almost the same for the two nucleons, we use as the uncertainty on the simulation the ratio of gamma-ray production rates weighted by the average energy of emitted gamma-rays between the proton and neutron cases[1)]. To estimate the effective size of the discontinuity between the two simulators, we only use gamma-rays whose parent nucleons' kinetic energies are within ± 5 MeV with respect to 20 MeV for the comparison. Also, we only use gamma-rays whose energies are above 1 MeV, since gamma-rays with lower energy are rarely detected in a water Cherenkov detector and should not affect the analysis. As a result, for the proton case, the gamma-ray production rate is only several percent lower below 20 MeV than that above 20 MeV (*i.e.*, almost smooth fuction around 20 MeV) and the average energy of emitted gamma-rays is almost the same in both energy ranges. On the other hand, for the neutron case, the production rate is more than two factors of magnitude lower below 20 MeV while the average gamma-ray energy is 20% higher there. Taking the energy-weighted ratio, we estimate about 50% as the effective magnitude of the discontinuity. Thus, we assign $\pm 50\%$ to that uncertainty.

The effect on the expected total number of events is estimated as follows. Figure 9.8 shows in the left panel the correlation between event energy and the number of Cherenkov photons. From this plot, an almost linear correlation is seen between event energy and the number of Cherenkov photons. The energy threshold of 4 MeV corresponds to about 400 in total photons in a event. The black histogram in the right panel of Fig. 9.8 is the one-dimensional projection of the number of Cherenkov photons shown in the left panel. Also shown are those after the increment (decrement) of the photons induced by secondary gamma-rays by 50%. The resultant increase (decrease) in the total number of events above 400 photons is less than 4%. The smallness of the decrease in the number of events can be understood as follows. We set the energy threshold of this analysis to 4 MeV, where the trigger efficiency is above 99.5%. The 4 MeV threshold is so low that even if one decreases the secondary interaction rate by 50%, most of the events still have enough photons to be triggered.

On the other hand, there are events below 4 MeV which originally do not have any secondary gamma-rays. The migration of such events into the signal region is not fully estimated by changing the energy scale as described above since there would be no change in the number of Chrenkov photons by the multiplication. In that case, we estimate the effect as follows. First, in the default simulation there are no secondary gamma-rays after NC interaction in about 30% cases and the

[1)] As already mentioned above, the systematic uncertainty of the simulator can only affect the analysis through the total number of Cherenkov photons in an event. Using the approximation that the number of photons is proportional to the energy of gamma-ray (strictly, that of its Compton electron), the effective systematic uncertainty for the SK is the uncertainty on "the production rate of gamma-rays $\times$ the average energy of emitted gamma-rays".

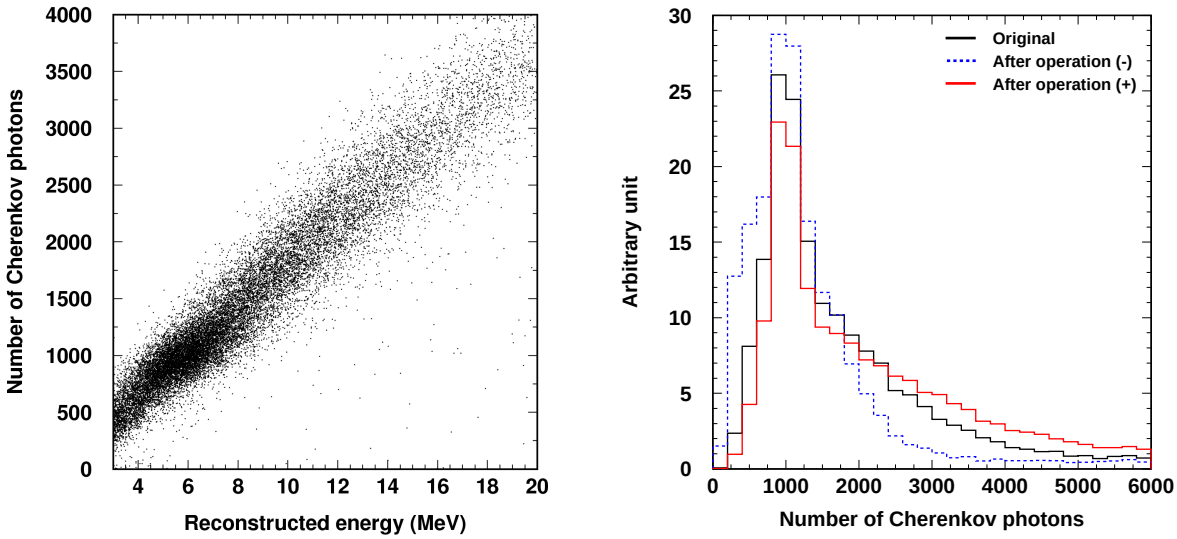

Figure 9.8: The left panel shows the correlation between event energy and the number of Cherenkov photons. The black histogram in the right pan el is one-dimensional projection of the number of Cherenkov photons shown in the left panel. Those after the increment (red solid) and decreme nt (blue dotted) of the photons induced by secondary gamma-rays by 50% are also shown.

fraction of events whose neutrino targets are protons is about 40% below 4 MeV, as shown in the panels of Fig. 9.9. For the events below 4 MeV which have no prompt gamma-rays[2)], the fraction of no nucleon-oxygen interactions which do induce secondary gamma-rays (hereafter, "secondary gamma-ray interaction") is about 80%, which is seen in Fig. 9.10. Generally, if you multiply the cross section of an interaction by r, the fraction of no interactions would be powered by r^3[3)]. So if you increase the production cross section of the secondary gamma-rays induced by neutrons by 50% (*i.e.*, $r = 1.5$), the fraction of neutrons which induce secondary gamma-rays would become 30% ($1 - 0.8^{1.5} \simeq 0.3$). Thus, if we conservatively assume any events with a finite multiplicity of secondary gamma-rays are reconstructed to be above 4 MeV, the size of the migration into the signal region is estimated as $30\% \times 40\% \times 30\% \lesssim 4\%$, where the uncertainty from the proton target is assumed to be negligibly small.

[2)] Since almost all the events which have any prompt gamma-ray are reconstructed to be above 4 MeV, only events which do not have prompt gamma-rays are considered here.

[3)] This relation is a direct consequence of the fact that the interaction probabilities can be written as $1 - \exp(-\rho\sigma x)$, where ρ denotes the medium density, σ the cross section, and x the flight distance.

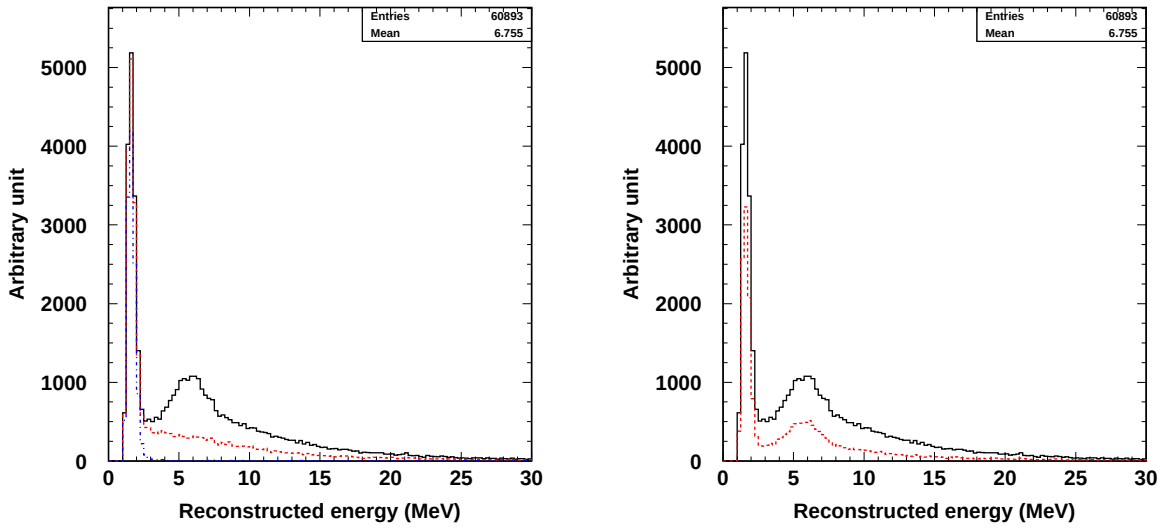

Figure 9.9: The panels show the expected event energy distribution inside of the ID full volume before the fiducial volume cut and the energy dependent cuts. In the left panel, the red histogram shows the fraction of events which are not accompanied by prompt gamma-rays while the blue one shows those which are not accompanied by prompt nor secondary gamma-rays. In the right panel, the red histogram shows the fraction of events whose neutrino targets are proton, which dominate below 4 MeV.

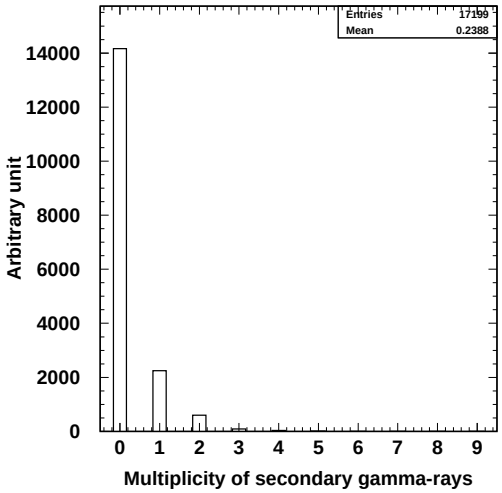

Figure 9.10: This panel shows the multiplicity of secondary gamma-rays in the events below 4 MeV which are not accompanied by prompt gamma-rays.

9.2.5 Detector response

The estimation of major uncertainties of detector response such as energy scale, vertex resolution and cut efficiency is described below. The result is summarized in Tab. 9.5, and we expect the total uncertainty to be ±2.2%.

Energy scale

As described in Chapter 5, the position and direction dependences of the energy scale in SK-IV are both within ±1%. We estimate the uncertainty on the total number of remaining events caused by the uncertainty of the energy scale by shifting the energy scale by ±1%. As a result, ±0.4% difference is obtained on the total number of events in the $4 - 30$ MeV electron total energy region.

Energy resolution

The difference of the energy resolution between LINAC data and MC is below 3%. The uncertainty caused by this difference on the total number of events is calculated by replacing the reconstructed energy of each MC event with a Gaussian whose standard deviation is the nominal value of the energy resolution scaled by the above difference (±3%) and counting the fraction of events moving out of the signal energy region of $4 - 30$ MeV. As a result the effect is estimated to be ±1%.

Trigger efficiency

As described in Chapter 6, the trigger efficiency in $4 - 4.5$ MeV events by the HLE trigger is above 99.5%. Taking into account the difference of trigger efficiency of ±2% in $4.5 - 5$ MeV between DT calibration data and MC with the SLE trigger, the uncertainty on the total number of remaining events caused by the trigger efficiency uncertainty is estimated to be ±1%.

dwall cut

The *dwall* cut defines the energy-dependent fiducial volume. It is known from a calibration at SK using a Cf-Ni gamma-ray source that the vertex of an event in the signal energy range tends to be reconstructed inward toward the detector center compared to the true vertex by $\mathcal{O}(1)$ cm [79]. The fiducial volume has some systematic uncertainty caused by this bias, which is called "vertex shift". To estimate the magnitude of the uncertainty, the reconstructed vertices of the beam-related events are shifted in the outward direction of the detector. The fraction of events which move out of the nominal fiducial volume is 1%. Thus, we estimate the systematic uncertainty on the total number of remaining events to be ±1%, conservatively.

effwall cut

The *effwall* cut uses event vertex and direction information. Therefore, to estimate the systematic uncertainty caused by this cut, the vertex shift and the angular resolution should be taken into account. Using LINAC data and MC, we estimate this effect to be ±0.5%.

ovaQ cut

For the estimation of the systematic uncertainty caused by the *ovaQ* cut, the difference of the efficiencies of the *ovaQ* cut between LINAC data and MC is used. By comparing *ovaQ* distributions of data and MC similarly to the comparison of N_{eff} described in Chapter 5, the fractional difference between data and MC is estimated to be ±2%. The fraction of the remaining events which are affected by the 2% change of the *ovaQ* cut criterion is found to be 0.5%, and we assign ±0.5% uncertainty to this cut.

Pre-activity cut

The uncertainty caused by this cut is estimated by the fractions of dark noise hits passing the cut threshold of $N_{30} > 22$ and low momentum muons below this threshold. Both of them are estimated to be below 0.1%.

Cherenkov angle cut

As for the efficiency of the Cherenkov angle cut, the uncertainty is estimated by comparing the Cherenkov angle distributions around the cut threshold of $\theta_C > 34^\circ$ between LINAC data and MC. We shift the cut threshold by the difference between the LINAC data and MC and calculate the resultant changes of remaining events. As a result, the uncertainty is estimated to be ±1%.

9.2.6 Summary of systematic uncertainties

Table 9.6 summarizes the uncertainties of the expectation in this analysis. Since these uncertainties are not correlated between each other, we obtain the total systematic uncertainty as ±25% just by adding them in quadrature.

Table 9.5: Summary of systematic uncertainties in the detector response.

Source	Uncertainty (%)
Energy scale	±0.4
Energy resolution	±1
Trigger efficiency	±1
dwall cut	±1
effwall cut	±0.5
ovaQ cut	±0.5
Pre-activity cut	±0.1
Cherenkov angle cut	±1
Total	±2.2

Table 9.6: Summary of systematic uncertainties on the expectation in this analysis.

Source	Uncertainty (%)
Neutrino flux	±15
Neutrino interaction	±17
Prompt gamma-ray	±10
Secondary gamma-ray	±4
Detector response	±2.2
Total	±25

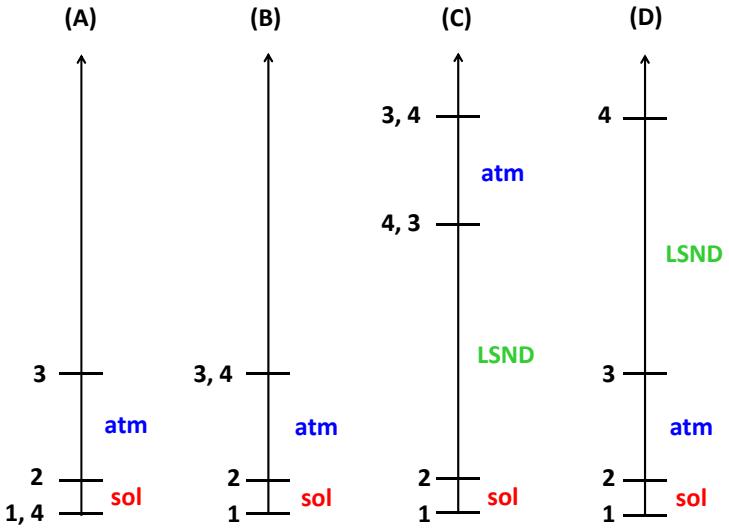

Figure 9.11: Possible mass hierarchies including just one extra neutrino. Only extensions of the normal hierarchy of three neutrinos are shown. "sol" and "atm" mean the mass differences of $\Delta m^2_{\rm sol}$ and $\Delta m^2_{\rm atm}$, respectively, while "LSND" means the mass difference of $\mathcal{O}(1)$ eV^2, as suggested by the LSND experiment or other short baseline experiments.

9.3 Search for active neutrino disappearance

In this section, the sterile neutrino search via the measurement of active neutrino disappearance using the NC de-excitation gamma-ray sample is described.

9.3.1 Possible mass hierarchies including fourth neutrinos

There are many possibilities of how to extend the observed mass hierarchies of three neutrinos by adding extra neutrinos. In this thesis, only the mass hierarchies with just one extra neutrino where the oscillation probabilities depend only on $\Delta m_{\rm atm}$ are tested. There are some cases which satisfy the above condition. One is the case where the fourth mass eigenstate is degenerate enough with one of the three mass eigenstates, which are shown by (A) and (B) in Fig. 9.11. In another case, the fourth mass eigenstate is largely, *e.g.*, by $\mathcal{O}(1)$ eV^2, separated from the other three, as suggested by LSND or other short baseline experiments. This case can be further divided into two cases: $(2+2)$ and $(3+1)$ models, as shown by (C) and (D) in Fig. 9.11, respectively. Results from solar and atmospheric neutrino data suggest that oscillations mostly take place between active neutrinos, which rule out $(2+2)$ models at a high confidence level [159]. Hereafter, we will not discuss the $(2+2)$ models ((C) in Fig. 9.11).

In the region of $L/E_\nu \simeq 500$ km/GeV, the oscillations are mostly driven by $\Delta m_{\rm atm}$ rather than $\Delta m_{\rm sol}$, and thus we can assume m_1 and m_2 are degenerate. Under this approximation, the mixing matrix can be represented in the absence of the three Majorana phases as

$$\begin{aligned} U &= R_{34}(\theta_{34})R_{24}(\theta_{24},\delta_2)R_{14}(\theta_{14})R_{23}(\theta_{23})R_{13}(\theta_{13},\delta_1)R_{12}(\theta_{12},\delta_3) \\ &\simeq R_{34}(\theta_{34})R_{24}(\theta_{24},\delta_2)R_{14}(\theta_{14})R_{23}(\theta_{23})R_{13}(\theta_{13},\delta_1) \end{aligned} \tag{9.2}$$

or, in a matrix representation,

$$U = \begin{pmatrix} U_{e1} & U_{e2} & c_{14}s_{13}e^{-i\delta_1} & s_{14} \\ U_{\mu 1} & U_{\mu 2} & -s_{14}s_{13}s_{24}e^{-i(\delta_1+\delta_2)} + c_{13}s_{23}c_{24} & c_{14}s_{24}e^{-i\delta_2} \\ U_{\tau 1} & U_{\tau 2} & -s_{14}c_{24}s_{34}s_{13}e^{-i\delta_1} - c_{13}s_{23}s_{34}s_{24}e^{i\delta_2} + c_{13}c_{23}c_{34} & c_{14}c_{24}s_{34} \\ U_{s1} & U_{s2} & -s_{14}c_{24}c_{34}s_{13}e^{-i\delta_1} - c_{13}s_{23}c_{34}s_{24}e^{i\delta_2} - c_{13}c_{23}s_{34} & c_{14}c_{24}c_{34} \end{pmatrix}, \tag{9.3}$$

where $c_{ij} \equiv \cos\theta_{ij}$ and $s_{ij} \equiv \sin\theta_{ij}$, and the elements of the matrix that are not expressed explicitly do not appear in the oscillation probabilities.

From the degeneracy of m_1 and m_2, we set $\sin(\Delta m^2_{21}L/2E) = 0$ in Eq. (1.5). This degeneracy also leads to $\sin(\Delta m^2_{42}L/2E) = \sin(\Delta m^2_{41}L/2E)$ and $\sin(\Delta m^2_{32}L/2E) = \sin(\Delta m^2_{31}L/2E)$. Thus, the probabilities become

$$\begin{aligned} P(\nu_\mu \to \nu_\mu) = 1 - 4\Bigg\{ & |U_{\mu 3}|^2(1-|U_{\mu 3}|^2-|U_{\mu 4}|^2)\sin^2\frac{\Delta m^2_{31}}{4E}L + |U_{\mu 4}|^2|U_{\mu 3}|^2\sin^2\frac{\Delta m^2_{43}}{4E}L \\ & + |U_{\mu 4}|^2(1-|U_{\mu 3}|^2-|U_{\mu 4}|^2)\sin^2\frac{\Delta m^2_{41}}{4E}L\Bigg\}, \\ P(\nu_\mu \to \nu_\alpha) = 4\cdot\mathrm{Re}\Bigg\{ & |U_{\mu 3}|^2|U_{\alpha 3}|^2\sin^2\frac{\Delta m^2_{31}}{4E}L + |U_{\mu 4}|^2|U_{\alpha 4}|^2\sin^2\frac{\Delta m^2_{41}}{4E}L \\ & + U^*_{\mu 4}U_{\alpha 4}U_{\alpha 3}U^*_{\alpha 3}\left(\sin^2\frac{\Delta m^2_{31}}{4E}L - \sin^2\frac{\Delta m^2_{43}}{4E}L + \sin^2\frac{\Delta m^2_{41}}{4E}L\right)\Bigg\} \\ & + 2\cdot\mathrm{Im}\Bigg\{U^*_{\mu 4}U_{\alpha 4}U_{\alpha 3}U^*_{\alpha 3}\left(\sin\frac{\Delta m^2_{31}}{2E}L - \sin\frac{\Delta m^2_{41}}{2E}L + \sin\frac{\Delta m^2_{43}}{2E}L\right)\Bigg\}, \end{aligned} \tag{9.4}$$

where $\alpha = e,\ \tau,$ or s.

In this thesis, a further simplification is made to reduce the number of possible parameters. First, the CP-violating phases δ_i $(i = 1, 2)$ are set to 0 because the present method in this thesis has no sensitivity to these phases combined with the assumed θ_{13}. Second, θ_{14} is also set to 0 since it does not measurably affect the above oscillation probabilities.

$m_4 = m_3$ model

In the case of $m_4 = m_3$ ((B) in Fig. 9.11), because any coupling between those neutrinos occurs only in the third and fourth mass eigenstates according to the SNO results [160], there is

no discernible mixing between the active and sterile components. Hereafter, this model will not be treated in this thesis.

$m_4 = m_1$ model

In the case of $m_4 = m_1$ ((A) in Fig. 9.11), $m_2 \sim m_4$ is derived from $m_1 \sim m_2$. Under these degeneracies, we can set $\theta_{14} = \theta_{24} = 0°$. Using this simplification, the oscillation probabilities (9.4) are simplified as:

$$\begin{aligned} P(\nu_\mu \to \nu_\mu) &= 1 - 4|U_{\mu 3}|^2(1 - |U_{\mu 3}|^2)\sin^2\frac{\Delta m^2_{31}}{4E}L \\ P(\nu_\mu \to \nu_\alpha) &= 4|U_{\mu 3}|^2|U_{\alpha 3}|^2\sin^2\frac{\Delta m^2_{31}}{4E}L \end{aligned} \tag{9.5}$$

with

$$\begin{aligned} U_{e3} &= \sin\theta_{13}, \\ U_{\mu 3} &= \cos\theta_{13}\sin\theta_{23}, \\ U_{\tau 3} &= \cos\theta_{13}\cos\theta_{23}\cos\theta_{34}, \\ U_{s3} &= -\cos\theta_{13}\cos\theta_{23}\sin\theta_{34}. \end{aligned} \tag{9.6}$$

As can be seen in Eq. (9.5) and (9.6), the introduction of the fourth mass eigenstate in this model does not affect the ν_μ survival probability. Figure 9.12 shows the oscillation probability of $\nu_\mu \to \nu_\mu$ and $\nu_\mu \to \nu_s$ at $L = 295$ km and $E = 0.6$ GeV as a function of the mixing angles in the case of $m_4 = m_1$.

$m_4 \gg m_3$ model

In the case of $m_4 \gg m_3$ ((D) in Fig. 9.11), Δm^2_{43} is assumed to be $\mathcal{O}(1)$ eV^2, so that $\sin^2(\Delta m^2_{41}L/4E)$ and $\sin^2(\Delta m^2_{43}L/4E)$ are averaged to $1/2$ and $\sin(\Delta m^2_{41}L/2E)$ and $\sin(\Delta m^2_{43}L/2E)$ are averaged to 0[4)]. Using this simplification, the oscillation probabilities (9.4) are simplified as:

$$\begin{aligned} P(\nu_\mu \to \nu_\mu) &= 1 - 4\left\{|U_{\mu 3}|^2(1 - |U_{\mu 3}|^2 - |U_{\mu 4}|^2)\sin^2\frac{\Delta m^2_{31}}{4E}L + \frac{|U_{\mu 4}|^2}{2}(1 - |U_{\mu 4}|^2)\right\}, \\ P(\nu_\mu \to \nu_\alpha) &= 4\left\{\left(|U_{\mu 3}|^2|U_{\alpha 3}|^2 + U_{\mu 4}U_{\alpha 4}U_{\mu 3}U_{\alpha 3}\right)\sin^2\frac{\Delta m^2_{31}}{4E}L + \frac{|U_{\mu 4}|^2|U_{\alpha 4}|^2}{2}\right\} \end{aligned} \tag{9.7}$$

with

$$\begin{aligned} U_{\mu 3} &= \cos\theta_{13}\sin\theta_{23}\cos\theta_{24}, \\ U_{\mu 4} &= \cos\theta_{14}\sin\theta_{24}. \end{aligned} \tag{9.8}$$

[4)] The change of the $\Delta m^2_{41}L/4E$ by unity costs the shift of energy by $\delta E = 4E^2/(\Delta m^2_{41}L) \lesssim 1$ MeV or that of flight length by $\delta L = 4E/\Delta m^2_{41} \lesssim 500$ m. It follows that the averaging stated above mainly occurs due to the broadening of the beam neutrino flux energy spectrum.

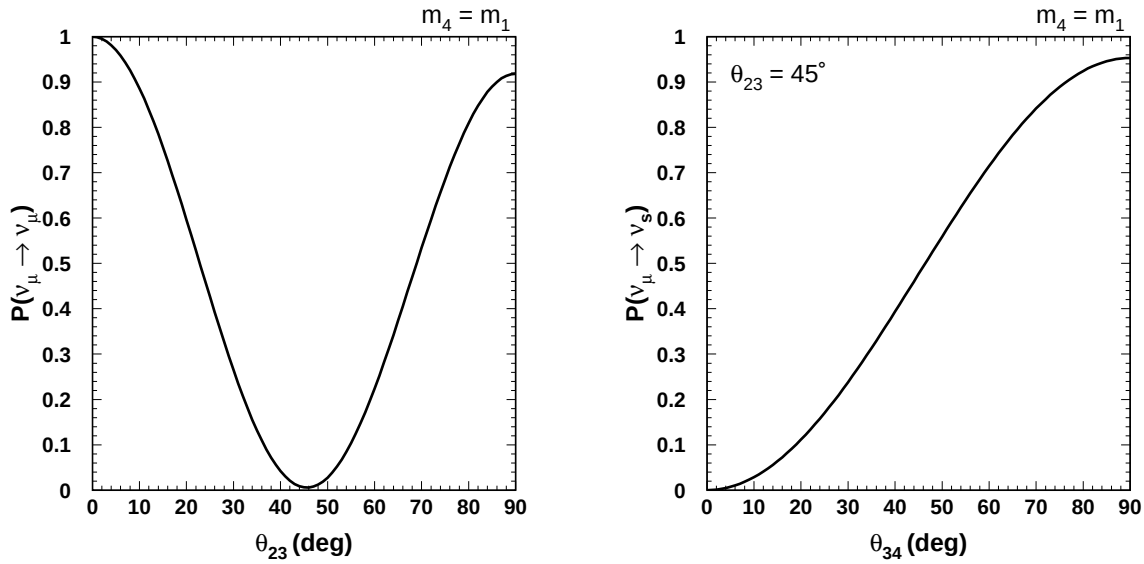

Figure 9.12: Oscillation probability of $\nu_\mu \to \nu_\mu$ (left) and $\nu_\mu \to \nu_s$ (right) at $L = 295$ km and $E = 0.6$ GeV as a function of the mixing angles in the case of $m_4 = m_1$. As described in the text, the probabilities are common to both $\mathrm{m_4 = m_1}$ and $\mathrm{m_4 \gg m_3}$ models under the assumption of $\theta_{24} = 0$.

In atmospheric L/E ν_μ disappearance experiments, ν_μ oscillations can be well fitted in terms of oscillations between three active flavors, and they put a stringent bound on the mixing angle θ_{24}. For this reason, we set $\theta_{24} = 0^\circ$ hereafter. As directly seen from Eq. (9.5)$-$(9.8), under the assumption of $\theta_{24} = 0^\circ$ both the probabilities $P(\nu_\mu \to \nu_\mu)$ and $P(\nu_\mu \to \nu_s)$ of this model are equivalent to those of the $m_4 = m_1$ model.

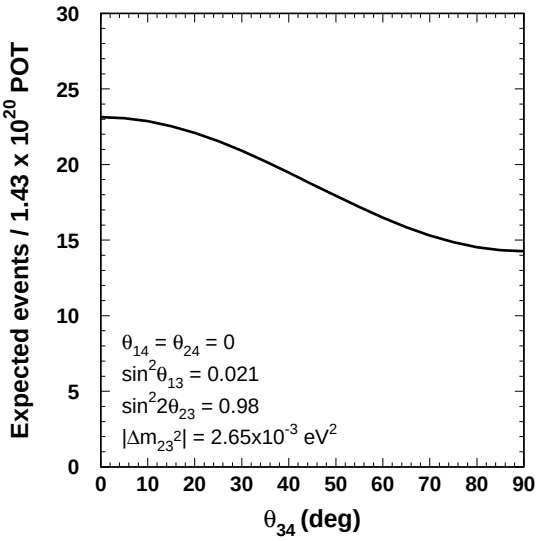

Figure 9.13: Expected number of events at RUN-I/II as a function of θ_{34}.

9.3.2 Data analysis using NC de-excitation gamma-ray sample

Figure 9.13 shows the expected number of events at RUN-I/II as a function of θ_{34}. As for other oscillation parameters, the current T2K best-fit values $\sin^2 2\theta_{23} = 0.98$ and $|\Delta m^2_{23}| = 2.65 \times 10^{-3}$ eV^2 and the current global best-fit value $\sin^2 2\theta_{13} = 0.084$ are assumed.

To evaluate the sensitivity of this analysis to constrain the mixing angle, the following $\chi^2_{\rm NC}$ is defined using the observed and expected numbers of NC de-excitation gamma-ray events,

$$\chi^2_{\rm NC} \equiv 2\left[N_{\rm exp} - N_{\rm obs} + N_{\rm obs}\ln\left(\frac{N_{\rm obs}}{N_{\rm exp}}\right)\right] + \sum_i \left(\frac{\epsilon_i}{\sigma_{sys,i}}\right)^2 \tag{9.9}$$

with

$$N_{\rm exp} = \left(1 + \sum_i f_i \cdot \epsilon_i\right) N_{\rm sig} + N_{\rm bkg}, \tag{9.10}$$

where $N_{\rm obs}$ is the number of observed events and $N_{\rm exp}$ is the expected number of events, which is calculated based on the oscillation probabilities, Eq. (9.5). $N_{\rm exp}$ is decomposed into the expected numbers of beam-related events $N_{\rm sig}$ as a function of assumed oscillation parameters and beam-unrelated events $N_{\rm bkg}$. The nuisance parameter ϵ_i is the shift from the nominal fit value for the i-th source of systematic uncertainty and $\sigma_{sys,i}$ is the uncertainty associated with that source. f_i is a factor which converts the change of the i-th source of systematic uncertainty to that of the expected number of events.

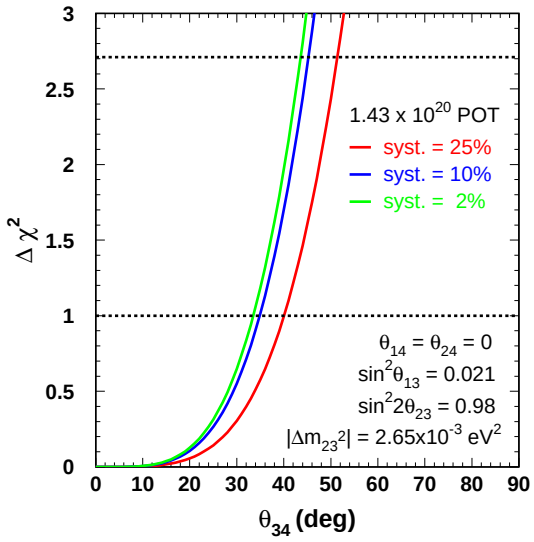

Figure 9.14: Sensitivities to the mixing angle θ_{34} of the analysis using the NC de-excitation gamma-ray sample with the statistics of RUN-I/II and different systematic uncertainties, common to both $m_4 = m_1$ and $m_4 \gg m_3$ models. The horizontal dashed lines show the values corresponding to 68% and 90% C.L.

To find the set of ϵ_i's which minimizes the $\chi^2_{\rm NC}$ in Eq. (9.9), we first calculate $\partial\chi^2_{\rm NC}/\partial\epsilon_i = 0$ for every ϵ_i:

$$\frac{\partial\chi^2_{\rm NC}}{\partial\epsilon_i} = 0 \iff \epsilon_i = f_i(\sigma_{sys,i})^2 N_{\rm sig}\left(\frac{N_{\rm obs}}{N_{\rm exp}} - 1\right). \tag{9.11}$$

Since every ϵ_i is uniquely[5)] determined for Eq. (9.11), we use the obtained ϵ_i as the best-fit values.

9.3.3 Sensitivity for RUN-I/II

Figure 9.14 depicts the sensitivities to the mixing angle θ_{34} of the analysis using the NC de-excitation gamma-ray sample with the statistics of RUN-I/II (1.43×10^{20} POT) and different systematic uncertainties of $\pm 25\%$, $\pm 10\%$ and $\pm 2\%$. In this plot, the true θ_{34} is assumed to be 0 and the number of observed events are just set equal to the expected number of events in no sterile case, *i.e.*, $N_{\rm obs} = N_{\rm exp}(\theta_{34} = 0)$. Since θ_{24} is set to zero, this sensitivity is common to both $m_4 = m_1$ and $m_4 \gg m_3$ models.

[5)] How to solve Eq. (9.11) is described in Chapter A.

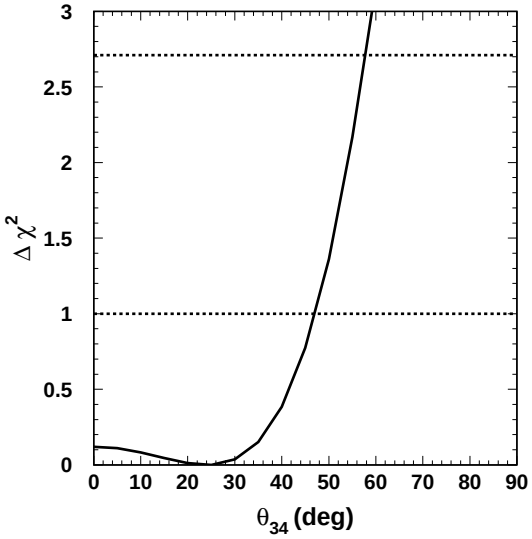

Figure 9.15: $\Delta\chi^2_{\rm NC}$ as a function of the mixing angle θ_{34}, common to both $m_4 = m_1$ and $m_4 \gg m_3$ models. The horizontal dashed lines show the values corresponding to 68% and 90% C.L.

9.3.4 Results of data analysis

Figure 9.15 shows the result when we use the actual number for the observed events, *i.e.*, $N_{\rm obs} = 20$. The resultant $\Delta\chi^2_{\rm NC}$ is slightly different from the sensitivity with the same systematic uncertainty, which reflects the fact that the number of observed events is less than the expectation. However, due to the current low statistics, the difference is not significant. The obtained upper limit on θ_{34} is 58° at 90% C.L.

We also measure the coupling between the active and sterile neutrinos by determining the fraction of the transition of $\nu_\mu \to \nu_s$, *i.e.*,

$$f_s \equiv \frac{P_{\nu_\mu\to\nu_s}}{1 - P_{\nu_\mu\to\nu_\mu}} = \frac{|U_{s3}|^2}{1 - |U_{\mu 3}|^2}, \tag{9.12}$$

where the second equality is directly derived from Eq. (9.5). Since f_s is independent of neutrino energy, we set the 90% C.L. limit on f_s simply by selecting enough numbers of test values of θ_{34} from the likelihood distribution, which is proportional to $\exp(-\Delta\chi^2_{\rm NC}/2)$, with the obtained $\Delta\chi^2_{\rm NC}$ distribution for the mixing angle (Fig. 9.15). We define the 90% C.L. limit as the value of f_s which is larger than 90% cases of the test cases. The obtained value is $f_s < 0.58$ at 90% C.L.

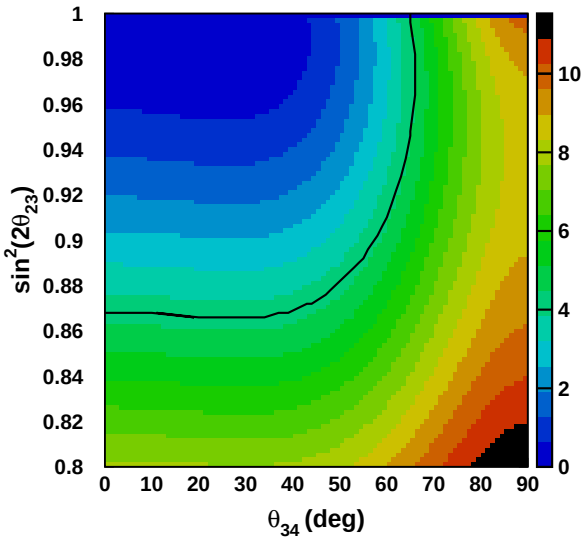

Figure 9.16: $\Delta\chi^2$ as a function of $\sin^2 2\theta_{23}$ and θ_{34} for both $m_4 = m_1$ and $m_4 \gg m_3$ models. The black contour represents 90% C.L..

9.3.5 Extended χ^2

As we saw in the above discussion, under the assumption of $\theta_{24} = 0$, the oscillation parameters associated with the fourth mass eigenstate does not affect the analysis results of the T2K ν_μ disappearance analysis, which assumes only oscillations among active flavor neutrinos [22]. Also, virtually all the systematic uncertainties of the disappearance analysis can be treated independently of those of NC de-excitation gamma-ray analysis[6)], the latter uncertainties being discussed in Section 9.2. Thus, we define an extended χ^2 function as the direct sum of the χ^2 for the NC de-excitation gamma-ray analysis, $\chi^2_{\rm NC}$, and that for the ν_μ disappearance analysis, which are obtained only with the active neutrinos, $\chi^2_{\rm CC}$,

$$\chi^2 \equiv \chi^2_{\rm NC} + \chi^2_{\rm CC}. \tag{9.13}$$

The resultant contour representing 90% C.L. for the two models is shown in Fig. 9.16.

[6)] Strictly speaking, the two analyses are not independent since the expected number of CC events in the NC de-excitation gamma-ray sample or that of NC elastic events in the other sample is dependent on the nuisance parameters related to neutrino flux and cross sections in each sample. However, the effects on the total χ^2 are negligible due to the small fraction of those events in both samples.

9.3.6 Discussion on this sterile neutrino search

Comparison with the sensitivity using the on-axis beam

As shown in Fig. 2.2, the neutrino flux and spectral shape at the far detector largely depend on its off-axis angle. As the detector is nearer the on-axis, the beam spectrum gets wider and the higher statistics is expected while the peak energy gets higher. If you take into account the oscillation parts driven by Δm^2_{41} or Δm^2_{43} in an oscillation probability such as Eq. (9.7), you can expect a higher sensitivity with the detector on the on-axis. However, as mentioned earlier, a severe upper bound is already given on the mixing angle θ_{24} by atmospheric L/E analyses, and in the limit of $\theta_{24} = 0$ both the probabilities $P(\nu_\mu \to \nu_\mu)$ and $P(\nu_\mu \to \nu_s)$ of the $m_4 = m_1$ and $\mathrm{m_4} \gg \mathrm{m_3}$ models are the same as Eq. (9.5), *i.e.*, the parts related with Δm^2_{41} or Δm^2_{43} disappear in both the probabilities. Thus, the oscillations are driven only by Δm^2_{31}, where the probability is not maximized until the beam neutrino energy gets down to $E \simeq 0.6$ GeV when the detector is located 295 km away, as shown in the right bottom panel in Fig. 2.2. On the other hand, in the search for NC de-excitation gamma-ray events, the event energy is assumed to only weakly dependent on the parent neutrino energy, and thus beam-related events whose $\sin^2(\Delta m^2_{31} L/4E)$ is not large cannot be rejected in principle. Those neutrino events cannot be used to measure the flux depletion associated with the sterile neutrinos, and instead, remain a source of background. For this reason, the search for sterile neutrinos in those models with a T2K far detector is most sensitive on a 2.5° off-axis, where narrow band neutrino beam with the peak energy of 0.6 GeV is obtained.

Comparison with the sensitivity using other NC enriched sample

There are possibilities to use other NC enriched samples at the far detector than that of NC de-excitation gamma-ray events for the search for sterile neutrinos. The most probable choice is to use NC π^0 events since the contamination from CC events is expected to be small. For the estimation of the sensitivity, we apply the following cut criteria to the T2K beam neutrino MC events in order to select NC π^0 candidate events: (1) the reconstructed vertices are within the fiducial volume (200 cm from the ID wall); (2) no decay electron is accompanied; (3) the number of Cherenkov rings is two; (4) both rings are of showering type (electron-like) and (5) the invariant mass of the two rings is in between $85 - 185$ MeV/c^2. Under this selection, the expected number of NC π^0 events at RUN-I/II is 4.8 (4.9) at $\sin^2 2\theta_{13} = 0$ (0.1). Compared to NC de-excitation gamma-ray sample, the expected number of NC π^0 events is about a factor of four smaller. Therefore, when the statistics is the dominant factor of the sensitivity, the search using de-excitation gamma-ray sample is expected to give a more stringent limit.

Comparison with limits of other experiments

There can be other ways to give constraints on the possible existence of sterile neutrinos other than observing NC events. The authors of Ref. [161] determine the individual elements of the

leptonic mixing matrix of the three active neutrinos $M_{\alpha i}$ ($\alpha = e, \mu, \tau;\ i = 1, 2, 3$) by combining analyses of CC events done by several experiments. So far, reactor experiments such as CHOOZ or KamLAND give constraints on the e-row of the matrix while the μ-row is constrained by accelerator experiments such as K2K or MINOS. Additional constraints are imposed on the e-row from the measurement of oscillations in matter at SK and SNO and also on the μ-row from near detectors at KARMEN, NOMAD, MINOS and Bugey. The resultant 90% C.L. constraints on the elements of $MM^\dagger$ are [161]

$$|MM^\dagger| \approx \begin{pmatrix} 1.00 \pm 0.04 & < 0.05 & < 0.09 \\ < 0.05 & 1.00 \pm 0.05 & < 0.013 \\ < 0.09 & < 0.013 & ? \end{pmatrix}. \tag{9.14}$$

Notice that not all matrix elements can be determined from oscillation data in the absence of ν_τ oscillations signals. A constraint of this size does not give a stringent bound on θ_{34} in both $\mathrm{m}_4 = \mathrm{m}_1$ and $\mathrm{m}_4 \gg \mathrm{m}_3$ models. Thus, so far the observation of CC events has not been a complementary constraint on the non-unitarity of the leptonic mixing matrix to those by using NC events.

The current most stringent bound on θ_{34} is the latest MINOS 90% C.L. upper limit of 17 (25) degrees at $\theta_{13} = 0$ (11.5) degrees [162], which was obtained by measuring NC events at the far detector. Figure 9.17 shows the sensitivities with the statistical goal of T2K (8×10^{21} POT) and different systematic uncertainties of $\pm 25\%$, $\pm 10\%$ and $\pm 2\%$. Neglecting the dependence of θ_{13} on this analysis since it is small compared to that for the MINOS experiment, the above two limits from MINOS roughly correspond to the systematic uncertainties of this analysis of $\pm 10\%$ and $\pm 2\%$, respectively.

One possibility to lower the uncertainty to competitive levels is to put a water Cherenkov detector at the near detector site. If the detector would be large enough to detect NC de-excitation gamma-ray events, most of the systematic uncertainties from neutrino flux, neutrino interaction and the production rates of prompt and secondary gamma-rays after neutrino interactions are expected to cancel between near and far detectors, and thus the total systematic uncertainty can be lowered to a few percent level.

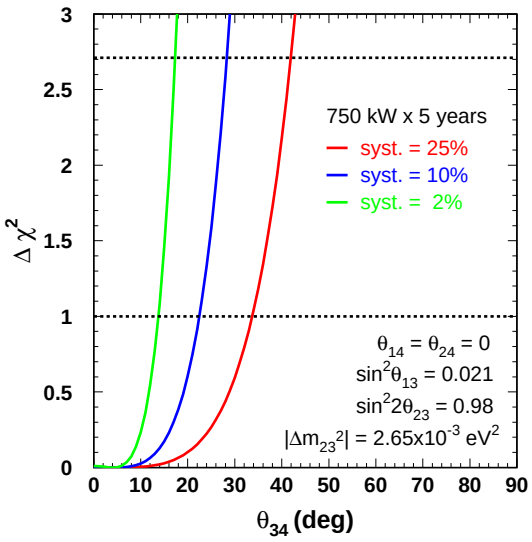

Figure 9.17: Sensitivities to the mixing angle θ_{34} of the analysis using the NC de-excitation gamma-ray sample with the statistics of 8×10^{21} POT and different systematic uncertainties, common to both $m_4 = m_1$ and $m_4 \gg m_3$ models. The horizontal dashed lines show the values corresponding to 68% and 90% C.L.

9.4 Sensitivity to astrophysics at Super-Kamiokande

As described in Section 1.4.1, the SRN flux is predicted to be very small $\mathcal{O}(1)$ cm^{-2} s^{-1}, and no evidence of SRN signals has yet been obtained in any experiment. However, since the expected event rate of inverse beta decay ($\bar{\nu}_e + p \rightarrow n + e^+$) at Super-Kamiokande is $0.8 - 5$ events/year above 10 MeV, if we reduce background events enough, it is possible to tag the signals in principle. Dominant sources of background events are nuclear spallation events induced by cosmic ray muons (CRM) and low energy atmospheric neutrino-induced events. The former background events can be reduced below the level of SRN signal by tagging neutrons, as described later. As for the latter background events, possible sources are nuclear de-excitation gamma-rays produced by the NC interaction of all flavors of atmospheric neutrinos and decay electrons from muons below the Cherenkov threshold produced by the CC interaction of atmospheric muon neutrinos.

In 2004, an idea to add a few amounts of gadolinium (Gd) to the SK tank (the GADZOOKS! project) was proposed for the improvement of the SK sensitivity to antineutrino astrophysics [163]. Currently an R&D work for the project is ongoing [164]. In this scenario, you tag the neutron which is knocked out in the inverse beta decay by Gd after it is thermalized in water. Gd has a very large (49,700 b in natural composition) capture cross section to thermal neutrons. With addition of 0.1% mass of Gd to the water, neutrons are captured on Gd within $\sim$20 μs with about 90% efficiency. Once Gd captures a neutron, it promptly de-excites by emitting cascades of gamma-rays whose energy is about 8 MeV in total.

In order to remove CRM-induced nuclear spallation background events, it is necessary to apply some selection criteria for the delayed signal events such as: (1) the reconstructed vertex position is within 200 cm from the prompt event; (2) the reconstructed energy is above 3 MeV; (3) the time after the prompt event is below 60 μs. After the ring pattern cuts, the efficiency of this selection is estimated to be $\sim$74% while the chance coincidence probability is $\sim 2 \times 10^{-4}$, where the spallation background events are reduced by many orders of magnitude and also invisible muon background are reduced by about a factor of five.

Figure 9.18 shows expected energy spectrum of the SRN signal at GADZOOKS! assuming the LMA model [47] for the SRN flux, together with those of the expected backgrounds: NC de-excitation gamma-ray events and decay electron events from CC muons, both induced by atmospheric neutrinos. In Fig. 9.18, the exposure time is assumed to be 10 years, and the signal is normalized by the tagging efficiency estimated above ($0.90 \times 0.74 = 67\%$). Since the nuclear de-excitation gamma-rays are induced by atmospheric neutrinos of typical energy 1 GeV, more than one neutron can be emitted. We estimate by a GEANT simulation the multiplicity of the secondary neutrons which are ultimately thermalized and captured by Gd. As a result, the chance coincidence that only one of the emitted neutrons is tagged is estimated to be 37%, which is multiplied for the NC background events in Fig. 9.18. As for the CRM-induced spallation background events, the current knowledge is that they are mainly from ^{9}Li nucleus and thus tend to peak below 10 MeV and negligible above 12 MeV. Though the event rate of this background strongly depends on additional selection criteria under development, we assume the background

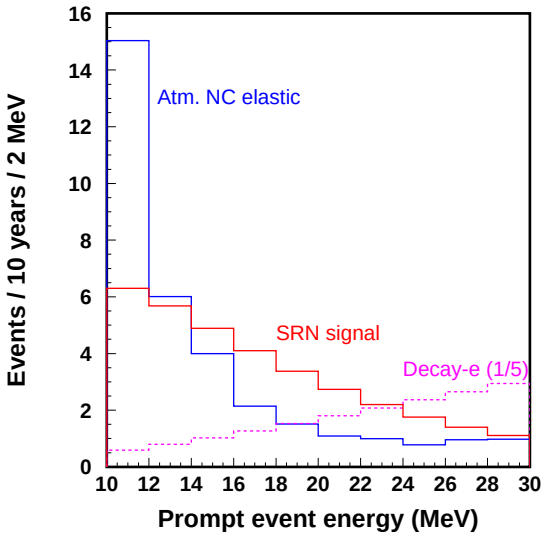

Figure 9.18: Expected energy spectrum of the SRN signal at GADZOOKS! with the exposure time of 10 years, together with those of the expected backgrounds: NC elastic and CC decay electron events induced by atmospheric neutrinos. Decay electron events are assumed to be reduced by a factor of five.

events are negligibly small hereafter.

As can be seen from Fig. 9.18, the extent of how we can precisely estimate the magnitude of the NC elastic background determines the discovery potential of the SRN signal by GADZOOKS!. For the estimation of the discovery potential, we define the following χ^2 using the total number of events in the signal energy range of $10 - 30$ MeV:

$$\chi^2(N_{\rm sig}) = \frac{(N_{\rm obs} - N_{\rm bkg} - N_{\rm sig})^2}{\sigma_{stat}^2 + \sigma_{sys}^2}, \tag{9.15}$$

where $N_{\rm sig}, N_{\rm obs}$ and $N_{\rm bkg}$ denote the numbers of signal events, observed events, and background events, respectively. $N_{\rm bkg}$ is the sum of the NC elastic events and invisible muon events, which are both estimated from the atmospheric MC simulation. For the test value of $N_{\rm obs}$, we use the sum of expected background and signal. $\sigma_{stat} = \sqrt{N_{\rm obs}}$ and $\sigma_{sys} \simeq N_{\rm NC} \cdot \varepsilon_{sys}$ denote the statistic and systematic uncertainties, respectively, where $N_{\rm NC}$ is the expected number of NC elastic background events and ε_{sys} is the uncertainty on the expectation of the NC elastic background. Currently, we estimate ε_{sys} as 50% mainly from the uncertainty on the production rate of secondary gamma-rays, as described in Section 9.2[7]. However, when T2K accumulates

[7] Actually, we can estimate the systematic uncertainty of total number of events at the range $10 - 30$ MeV from

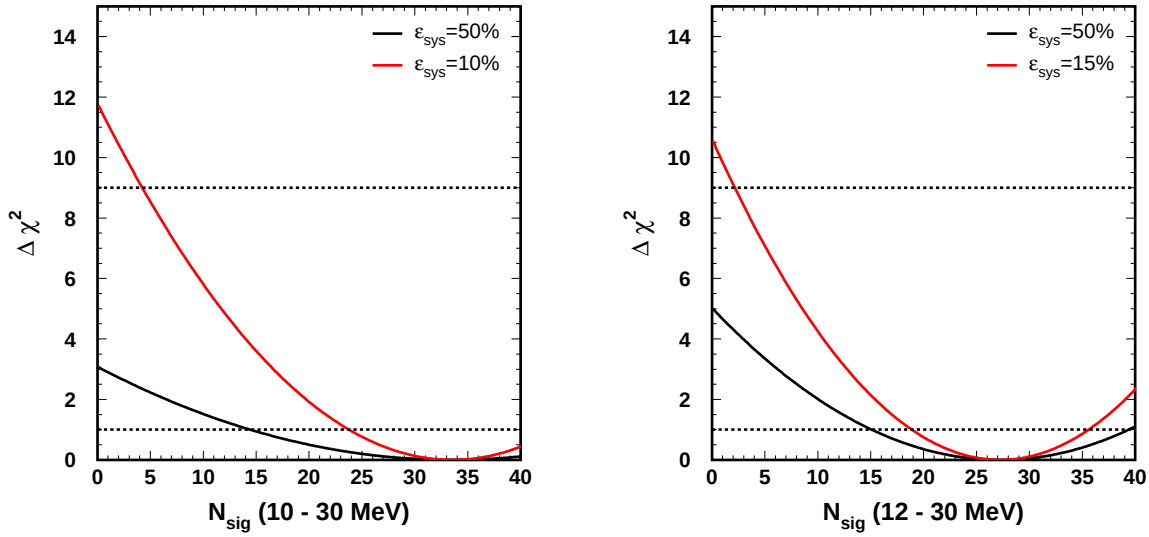

Figure 9.19: Discovery potential of GADZOOKS! with different systematic uncertainty of the expected number of atmospheric neutrino NC elastic background events at both the thresholds of 10 MeV (left) and 12 MeV (right). The horizontal dotted lines indicate 1σ and 3σ levels.

8×10^{21} POT, which corresponds to five years of running with the design power of 0.75 MW, about 100 NC events are expected at SK in the energy region of $10 - 30$ MeV after basically the same selection cut as that for the SRN prompt signal. These NC events can be directly used to give a stringent constraint on the systematic uncertainty on the event rate of atmospheric NC elastic events. In other words, we can lower ε_{sys} from 50% to ∼10% in the future by the analysis presented in this thesis. Figure 9.19 shows the discovery potential of GADZOOKS! with the two systematic uncertainties of the expected number of atmospheric neutrino NC elastic background events. As a reference, the tested result for the sample of the threshold 12 MeV is also put together with that of 10 MeV, where the uncertainty is slightly increased from 10% to 15% since the statistics of the expected T2K events should halve. In both threshold cases, SRN signals can be discovered at more than 3σ levels due to the constraint on the uncertainty of the event rate of the atmospheric NC elastic background by the analysis of this thesis.

Furthermore, there is a room for improvement of the selection efficiency of the SRN signal. For example, in the above estimate the secondary neutrons are assumed to have the same kinematical behavior as those of the SRN signal events. However, the former neutrons are induced by atmospheric neutrinos of typical energy 1 GeV, and they generally have by more than one order

Fig. 9.8 in the same way that we estimate the uncertainty for $4 - 30$ MeV, only the threshold of 400 photons being replaced with 1500 photons.

of magnitude larger kinetic energies $\mathcal{O}(100)$ MeV than those from signal inverse beta decay, which are $\lesssim 10$ MeV in the case of SRN or monopole-induced neutrinos. This leads to more spatially spread distribution of captured neutrons around the vertex of the primary interaction as they can travel longer when they are thermalized. With the knowledge of these features, it may be possible to cut more background events by optimizing the vertex correlation length.

We've already started to study neutron tagging without Gd added by using the neutron capture by free protons of water molecule: $n + p \rightarrow d + \gamma$ (2.2 MeV). Though both the capture cross section (0.33 b) and energy of gamma-rays are much lower than those of Gd, the reduction technique developed for this purpose [165] enables us to tag those neutron signals with about 20% efficiency, the background probability being 1%. For the NC de-excitation gamma-ray sample for RUN-I and II, we searched for the coincidence neutrons by the same reduction and no neutrons are detected so far. With more statistics of the T2K events, this study will give us the precise knowledge about the kinematic properties and absolute yield of neutrons, also those expected in the case of the Gd-loaded SK.

Chapter 10

Conclusion

In this thesis, nuclear de-excitation gamma-ray induced by neutrino-oxygen NC interactions was studied using a sub-GeV neutrino beam whose flux and spectrum are well understood. We selected low energy NC candidate events at SK using data of the T2K long baseline neutrino oscillation experiment collected from January 2010 to March 2011, which amounts to 1.43×10^{20} POT. After thorough background reduction, there remained 20 observed events in the reconstructed energy range of $4 - 30$ MeV while the expectation is 22.8 ± 6.2 beam-related events and 0.6 beam-unrelated events.

The result of the measurement was applied to a sterile neutrino search, which searches the depletion of the total neutrino flux at the far detector via the NC channel. As a result, the neutrino mixing angle, θ_{34}, was constrained to be below 58° at 90% C.L. for two different models with one sterile neutrino. We also put a limit on the coupling between the active and sterile neutrinos by constraining the fraction that a muon neutrino disappears into a sterile state. We set an upper limit on the fraction of $f_s < 0.58$ at 90% C.L. for those models. Future sensitivity of the sterile neutrino search was discussed.

Also, the experiment's future sensitivity to astrophysics analyses at SK was estimated. Since the beam neutrino energy of T2K is similar to those of atmospheric neutrinos, the accumulated data would give precise information on NC nuclear de-excitation backgrounds for those analyses and could lead to a great enhancement of the discovery potential of neutrinos from astrophysical sources. T2K plans to accumulate 8×10^{21} POT, which corresponds to five years of running with the design power of 0.75 MW. According to our simulation, it is expected that about 100 NC events will be accumulated in the supernova relic neutrino (SRN) signal region above 10 MeV with the full statistics. Such statistics greatly reduces the current uncertainty of the expected event rate of de-excitation gamma-ray backgrounds induced by NC interactions of atmospheric neutrinos at a gadolinium-loaded SK. Lowering the uncertainty to such level ultimately enhances the discovery potential of the SRN signals to more than 3σ level with the 10 year exposure time at the upgraded SK.

Appendix A

Solution to Eq. (9.11)

We need to obtain the set of χ^2-minimizing $\{\epsilon_i\}$ from the following equation (Eq. (9.11)),

$$\forall i,\ \epsilon_i = f_i(\sigma_{sys,i})^2 N_{\rm sig}\left(\frac{N_{\rm obs}}{N_{\rm sig}\left(1+\sum_i f_i\cdot\epsilon_i\right)+N_{\rm bkg}}-1\right). \tag{A.1}$$

We first multiply f_i to both sides of the equation for each i and then sum up for all i,

$$\sum_i f_i\cdot\epsilon_i = \sum_i f_i^2(\sigma_{sys,i})^2 N_{\rm sig}\left(\frac{N_{\rm obs}}{N_{\rm sig}\left(1+\sum_i f_i\cdot\epsilon_i\right)+N_{\rm bkg}}-1\right). \tag{A.2}$$

This equation is equivalent to a quadratic polynomial of $\sum_i f_i\cdot\epsilon_i$, and after solving the equation for $\sum_i f_i\cdot\epsilon_i$ we obtain

$$\begin{aligned}\sum_i f_i\cdot\epsilon_i &= \frac{-\left(1+N_{\rm sig}\sum_i f_i^2(\sigma_{sys,i})^2+N_{\rm bkg}/N_{\rm sig}\right)}{2} \\ &+ \frac{\sqrt{\left(1+N_{\rm sig}\sum_i f_i^2(\sigma_{sys,i})^2+N_{\rm bkg}/N_{\rm sig}\right)^2-4\sum_i f_i^2(\sigma_{sys,i})^2(N_{\rm sig}-N_{\rm obs}+N_{\rm bkg})}}{2}.\end{aligned} \tag{A.3}$$

Substituting this to the original equation (Eq. (9.11)), we ultimately obtain the set of χ^2-minimizing $\{\epsilon_i\}$.

Bibliography

[1] B. Pontecorvo, Zh. Eksp. Teor. Fiz. **33** (1957) 549 [Sov. Phys. JETP 6 (1958) 429];
Z. Maki, M. Nakagawa, and S. Sakada, Prog. Theor. Phys. **28** (1962) 870.

[2] J. N. Bahcall and M.H. Pinsonneault, Rev. Mod. Phys. **64** (1992) 885.

[3] Davis Jr., D. S. Harmer, and K.C. Hoffman, Phys. Rev. Lett. **20** (1968) 1205.

[4] K. S. Hirata *et al.*, Phys. Rev. Lett. **63** (1989) 16;
K. S. Hirata *et al.*, Phys. Rev. D **44** (1991) 2241, Erratum-ibid. D **45** (1992) 2170.

[5] A. I. Abazov *et al.*, Phys. Rev. Lett. **67** (1991) 3332;
J. N. Abdurashitov *et al.*, JETP **95** (2002) 181.

[6] P. Anselmann *et al.*, Phys. Lett. B **285** (1992) 376;
W. Hampel *et al.*, Phys. Lett. B **447** (1999) 127.

[7] S. Fukuda *et al.*, Phys. Lett. B **539** (2002) 179;
M. B. Smy *et al.*, Phys. Rev. D **69** (2004) 011104.

[8] Q. R. Ahmad *et al.*, Phys. Rev. Lett. **87** (2001) 071301;
Q. R. Ahmad *et al.*, Phys. Rev. Lett. **89** (2002) 011301;
S. N. Ahmed *et al.*, Phys. Rev. Lett. **92** (2002) 181301.

[9] J. Hosaka *et al.*, Phys. Rev. D **73** (2006) 112001.

[10] The latest analysis by the Super-Kamiokande Collaboration.

[11] A. Gando *et al.*(KamLAND Collaboration), Phys. Rev. D **83** (2011) 052002.

[12] G. L. Fogli *et al.*, arXiv:1106.6028v2 (2011).

[13] Y. Fukuda *et al.*, Phys. Lett. **81**, (1998) 1562.

[14] M. Honda *et al.*, Phys. Rev. D **70**, (2004) 043008.

[15] G.Battistoni *et al.*, Astropart. Phys. **19** (2003) 269 [Erratum-ibid. **19** (2003) 291].

[16] G. Barr *et al.*, Phys. Rev. D **70**, (2004) 0423006.

[17] E. Aliu *et al.*, Phys. Rev. Lett. **94** (2005) 081802.

[18] P. Adamson *et al.*(MINOS Collaboration), Phys. Rev. Lett. **106** (2011) 181801.

[19] K. Abe *et al.*(T2K Collaboration), Nucl. Instr. Meth. A **659** (2011) 106.

[20] Y. Takeuchi *et al.*(Super-Kamiokande Collaboration), to be published in Proceedings of Neutrino 2010.

[21] Y. Ashie *et al.*(Super-Kamiokande Collaboration), Phys. Rev. Lett. **93** (2004) 101801.

[22] K. Abe *et al.*(T2K Collaboration), arXiv:1201.1386, to be published in Phys. Rev. D.

[23] M. Apollonio *et al.*, Eur. Phys. J. C **27** (2003) 331.

[24] K. Abe *et al.*(T2K Collaboration), Phys. Rev. Lett. **107** (2011) 041801.

[25] F. Ardellier *et al.*(Double Chooz Collaboration), arXiv:hep-ex/0606025 (2006).

[26] S. B. Kim *et al.*(RENO Collaboration), AIP Conf. Proc. **981** (2008) 205.

[27] X. Guo *et al.*(Daya Bay Collaboration), arXiv:hep-ex/0701029 (2007).

[28] K. Nakamura *et al.*(Particle Data Group), J. Phys. G **37** (2010) 075021.

[29] C. Athanassopoulos *et al.*(LSND Collaboration), Phys. Rev. Lett. **77** (1996) 3082.

[30] B. Armbruster *et al.*(KARMEN Collaboration), Phys. Rev. D **65** (2002) 112001.

[31] E. D. Church, K. Eitel, G. B. Mills and M. Steidl, Phys. Rev. D **66** (2002) 013001.

[32] A. A. Aguilar-Arevalo *et al.*(MiniBooNE Collaboration), Nucl. Instr. Meth. A **599** (2009) 28.

[33] A. A. Aguilar-Arevalo *et al.*(MiniBooNE Collaboration), Phys. Rev. Lett. **98** (2007) 231801.

[34] A. A. Aguilar-Arevalo *et al.*(MiniBooNE Collaboration), Phys. Rev. Lett. **105** (2010) 181801.

[35] M. Maltoni and T. Schwetz, Phys. Rev. D **76** (2007) 093005.

[36] U. Seljak *et al.*, JCAP **0610** (2006) 014.

[37] J. Lesgourgues and S. Pastor, Phys. Rep. **429** (2006) 307.

[38] Ch. Kraus *et al.*, Euro. Phys. J. C **40** (2005) 447.

[39] V. M. Lobashev, P. E, Spivac, Nucl. Instr. Meth. A **240** (1985) 305;
A. I. Belesev *et al.*, Phys. Lett. B **350** (1995) 263.

[40] K. A. Assamagan *et al.*, Phys. Rev. D **53** (1996) 6065.

[41] R. Barate *et al.*, Euro. Phys. J. C **2** (1998) 395.

[42] A. M. Hopkins and J. F. Beacom, Astrophys. J. **651** (2006) 142.

[43] S. Ando and K. Sato, New J. Phys. **6** (2004) 170.

[44] T. Totani and K. Sato, Astropart. Phys. **3** (1995) 367.

[45] M. Malek *et al.*(Super-Kamiokande Collaboration), Phys. Rev. Lett. **90** (2003) 061101.

[46] M. Kaplinghat, G. Steigman, and T. P. Walker, Phys. Rev. D **62** (2000) 043001;
L. E. Strigari, M. Kaplinghat, G. Steigman, and T. P. Walker, J. Cosm. and Astropart. Phys. **03** (2004) 007.

[47] S. Ando, K. Sato, and T. Totani, Astropart. Phys. **18** (2003) 307;
The flux of the LMA model is increased by a factor of 2.56 from the paper,
a revision introduced at NNN05 conference in Aussois, France (2005).

[48] S. Horiuchi, J.F. Beacom and E. Dwek, Phys. Rev. D **79** (2009) 083013.

[49] C. Lunardini, Phys. Rev. Lett. **102** (2009) 231101; Assumed parameters are:
Failed SN rate = 22%, EoS = Lattimer-Swesty, and survival probability = 68%.

[50] D. H. Hartmann and S. E. Woosley, Astropart. Phys. **7** (1997) 137.

[51] R. A. Malaney, Astropart. Phys. **7** (1997) 125.

[52] K. Bays *et al.*(Super-Kamiokande Collaboration), arXiv:1111.5031 (2011).

[53] G. 't Hooft, Nucl. Phys. B **79** (1974) 276.

[54] A. Polyakov, Pis'ma Zh. Eksp. Theor. Fiz. **20** (1974) 430; [JETP Lett. **20** (1974) 194].

[55] A. H. Guth, Phys. Rev. D **23** (1981) 347.

[56] K. Sato, Phys. Lett. B **99** (1981) 66.

[57] E. N. Parker, Astrophys. J. **160** (1970) 383.

[58] M. S. Turner *et al.*, Phys. Rev. D **26** (1982) 1296.

[59] G. Lazarides, C. Panagiotakopoulos, and Q. Shafi, Phys. Rev. Lett. **58** (1987) 1707.

[60] S. Dar, Q. Shafi, and A. Sil, Phys. Rev. D **74** (2006) 035013.

[61] J. Arafune and M. Fukugita, Phys. Lett. B **133** (1983) 380.

[62] V. A. Rubakov, Pis'ma Zh. Eksp. Theor. Fiz. **33** (1981) 658 [JETP Lett. **33** (1981) 644]; Nucl. Phys. B **203** (1982) 311;
V. A. Rubakov and M. S. Serbryakov, Nucl. Phys. **B218** (1983) 240.

[63] C. G. Callan, Phys. Rev. **D25** (1982) 2141; **D26** (1982) 2058.

[64] K. Ueno *et al.*, Proc. ICRC **31** (2009);
http://icrc2009.uni.lodz.pl/proc/pdf/icrc0670.pdf

[65] D. Beavis *et al.*, Phys. Des. Rep. (1995) 52459.

[66] Y. Yamazaki *et al.*,
KEK Report No.13 (2002), JAERI-Tech 44 (2003), and J-PARC-03-01 (2003).

[67] N. Abgrall *et al.*, CERN-SPSC (2010) 025, CERN-PH-EP (2011) 005.

[68] G. Battistoni *et al.*, AIP Conf. Proc. **896** (2007) 31;
FLUKA version 2008.3c http://www.fluka.org.fluka.php (2008).

[69] T. Eichten *et al.*, Nucl. Phys. B **44** (1972) 333.

[70] GEANT3, A detector description and simulation tool (1993).

[71] N. Abgrall *et al.*, Nucl. Instr. Meth. A **637** (2011) 25.

[72] S. Fukuda *et al.*(Super-Kamiokande Collaboration), Nucl. Instr. Meth. A **501** (2003) 418.

[73] H. Nuomi *et al.*, Nucl. Instr. Meth. A **398** (1997) 399.

[74] A. Suzuki *et al.*, Nucl. Instr. Meth. A **329** (1993) 299.

[75] Becker-Szendy *et al.*, Nucl. Instr. Meth. A **324** (1993) 363.

[76] H. Nishino *et al.*, NSS'07 IEEE **1** (2008) 127.

[77] S. Yamada *et al.*, Proc. IEEE-NPSS **16** (2009) 201.

[78] H. Nishino *et al.*, Nucl. Instr. Meth. A **610** (2009) 710.

[79] K. Abe *et al.*(Super-Kamiokande Collaboration), Phys. Rev. D **83** (2011) 052010.

[80] M. Smy, Proc. ICRC **30** (2007) 1279.

[81] M. Nakahata *et al.*, Nucl. Instr. Meth. A **421** (1999) 113.

[82] E. Blausfuss *et al.*, Nucl. Instr. Meth. A **458** (2001) 636.

[83] R. M. Pope and E. S. Fry, Applied Optics **36** 33 (1997) 8710.

[84] L. Michel, Rev. Mod. Phys. **29** (1957) 223.

[85] M. Nakahata *et al.*, J. Phys. Soc. **55** (1986) 3786.

[86] Y. Hayato, Nucl. Phys. Proc. **112** (2002) 171.

[87] C. H. Llewellyn Smith, Phys. Rep. **3** (1972) 261.

[88] A. Bodek *et al.*, Eur. Phys. J. C **71** (2011) 1726.

[89] R. Bradford *et al.*, Nucl. Phys. B **159** (2006) 127.

[90] J. J. Kelly *et al.*, Phys. Rep. C **70** (2004) 068202.

[91] S. K. Singh and E. Oset, Phys. Rev. C **48** (1993) 1246.

[92] R. A. Smith and E. J. Moniz, Nucl. Phys. B **43** (1972) 605;
Erratum-ibid. B **101** (1975) 547.

[93] S. Hiramatsu *et al.*, Proc. Int. Conf. on Nucl. Str. E.S.P. (1972) 429.

[94] F. A. Brieva and A. Dellafiore, Nucl. Phys. A **292** (1977) 445.

[95] S. Barish *et al.*, Phys. Rev. D **16** (1977) 3103.

[96] S. Bonetti *et al.*, Nouvo Cimento **38** (1977) 260.

[97] M. Pohl *et al.*, Nuovo Cimento **26** (1979) 332;
N. Arimenise *et al.*, Nucl. Phys. B **152** (1979) 365.

[98] A. S. Vovenko *et al.*, Yad. Fiz. **30** (1979) 1014.

[99] S. Belikov *et al.*, Z. Phys. **320** (1985) 625.

[100] J. Brunner *et al.*, Z. Phys. C **45** (1990) 551.

[101] D. Rein and L. M. Sehgal, Ann. of Phys. **133** (1981) 1780.

[102] R. Feynman *et al.*, Phys. Rev. D **3** (1971) 2706.

[103] G. Radecky *et al.*, Phys. Rev. D **25** (1982) 116.

[104] T. Kitagaki *et al.*, Phys. Rev. D **34** (1986) 2554.

[105] P. Allen *et al.*, Nucl. Phys. B **176** (1980) 269.

[106] P. Allen *et al.*, Nucl. Phys. B **264** (1986) 221.

[107] W. Lerche *et al.*, Phys. Lett. **4** (1978) 510.

[108] D. Allisia *et al.*, Z. Phys. C **24** (1984) 119.

[109] S.J. Barish *et al.*, Phys. Lett. B **91** (1980) 161.

[110] C. H. Albright and C. Jarlskog, Nucl. Phys. B **84** (1975) 467.

[111] M. Glück, E. Reya and A. Vogt, Eur. Phys. J. C **5** (1998) 461.

[112] A. Bodek and U. K. Yang, arXiv:hep-ex/0308007 (2003).

[113] P. Musset and J. P. Vialle, Phys. Rep. C **39** (1978) 1.

[114] J. E. Kim *et al.*, Rev. Mod. Phys. **53** (1981) 211.

[115] S. J. Barish *et al.*, Phys. Rev. D **17** (1978) 1.

[116] Z. Koba, H. B. Nielsen and P. Olesen, Nucl. Phys. B **40** (1972) 317.

[117] H. Saarikko, Neutrino 1979, **2** (1979) 507.

[118] S. Barlag *et al.*, Z. Phys. C **11** (1982) 283.

[119] T. Sjöstrand *et al.*, CERN-TH-7112 (1994) 93.

[120] D. Rein and L. M. Sehgal, Nucl. Phys. B **223** (1983) 29.

[121] Compilation of cross sections $I - \pi^-$ and π^+ induced reactions, CERN-HERA **79** (1979) 01.

[122] M. Hasegawa *et al.*, Phys. Rev. Lett. **95** (2005) 252301.

[123] A. Kartavtsev, E. A. Paschos and G. J. Gounaris, Phys. Rev. D **74** (2006) 054007.

[124] C. H. Q. Ingram *et al.*, Phys. Rev. C **27** (1983) 1578.

[125] C. W. de Jager *et al.*, Atomic Data and Nuclear Data Tables **14** (1974) 479.

[126] L. L. Salcedo *et al.*, Nucl. Phys. A **484** (1988) 557.

[127] G. Rowe *et al.*, Phys. Rev. C **18** (1978) 584.

[128] D. Ashery *et al.*, Phys. Rev. C **23** (1981) 2173.

[129] T. A. Gabriel *et al.*, IEEE Trans. Nucl. Sci. **36** (1989) 14.

[130] J. Arends *et al.*, Nucl. Phys. A **526** (1991) 479.

[131] H. W. Bertini, Phys. Rev. C **6** (1972) 631.

[132] S. J. Lindenbaum and R. M. Sternheimer, Phys. Rev. **105** (1957) 1874.

[133] O. Benhar *et al.*, Phys. Rev. D **72** (2005) 053005.
A. M. Ankowski *et al.*, Phys. Rev. Lett. **108** (2012) 052505.

[134] M. Bernheim *et al.*, Nucl. Phys. A **375** (1982) 381.

[135] M. Leuschner *et al.*, Phys. Rev. C **49** (1994) 955.

[136] K. G. Fissum *et al.*, Phys. Rev. C **70** (2004) 034606.

[137] B. Frois and I. Sick, *Modern Topics in Electron scattering* (1991).

[138] O. Benhar *et al.*, Nucl. Phys. A **579** (1994) 493.

[139] D. Rohe *et al.*(JLAB E97-006 collaboration), Phys. Rev. Lett. **93** (2004) 182501.

[140] R. B. Firestone *et al.*, *Table of Isotopes* (1996).

[141] K. Kobayashi *et al.*, arXiv:nucl-ex/0604006 (2006).

[142] M. Yosoi, Ph.D thesis, Univ. of Kyoto (2003);
M. Yosoi *et al.*, Nucl. Phys. A **738** (2004) 451;
M. Yosoi *et al.*, Phys. Atom. Nucl. **67** (2004) 1810.

[143] G. Mairle and G. J. Wagner, Z. Phys. **258** (1973) 321.

[144] H. Tyrén *et al.*, Nucl. Phys. **79** (1966) 321.

[145] P. G. Roos *et al.*, Nucl. Phys. A **255** (1975) 187.

[146] J. C. Hiebert, E. Newman, and R. H. Bassel, Phys. Rev. **154** (1967) 898.

[147] K. Ejiri, Phys. Rev. C **48** (1993) 1442.

[148] H. D. Engelhardt, C. W. Lewis and H. Ullrich, Nucl. Phys. A **258** (1976) 480.

[149] GEANT, CERN Program Library Long Writeup W5013 (1994).

[150] E. Bracci, CERN/HERA **72** (1972) 1.

[151] A. S. Carroll *et al.*, Phys. Rev. C **14** (1976) 635.

[152] I. Thormählen *et al.*, J. Phys. Chem. Ref. Data, **14** No. 4 (1985) 933.

[153] H. W. Bertini, Phys. Rev. **188** (1969) 1711;
H. W. Bertini, Phys. Rev. C **6** (1972) 631.

[154] J. O. Johnson, T. A. Gabriel, ORNL/TM-10196 (1987);
J. O. Johnson, T. A. Gabriel, ORNL/TM-10340 (1988).

[155] A. A. Aguilar-Arevalo *et al.*, Phys. Rev. D **82** (2010) 092005.

[156] H. Takei, Ph.D thesis, Univ. of Tokyo Institute of Technology (2009).

[157] Y. Kamyshkov and E. Kolbe, Phys. Rev. D **67** (2003) 076007.

[158] P. G. Young *et al.*, ENDF/B Summary Documentation for ^{16}O (1979) 8-16-1, and Ref. therein.

[159] M. Maltoni, T. Schwetz, M. A. Tórtola, and J. W. F. Valle, Phys. Rev. D **67** (2003) 013011.

[160] B. Aharmim *et al.*, Phys. Rev. C **81** (2010) 055504;
B. Aharmim *et al.*, arXiv:1109.0763 (2011).

[161] S. Antusch *et al.*, JHEP **0610** (2006) 084.

[162] P. Adamson *et al.*(MINOS Collaboration), Phys. Rev. Lett. **107** (2011) 011802.

[163] J. F. Beacom and M. R. Vagins, Phys. Rev. Lett. **93** (2004) 171101.

[164] H. Watanabe and H. Zhang *et al.*, Astropart. Phys. **31** (2009) 320.

[165] H. Zhang *et al.*, Proc. ICRC 2011, Vol. **4** (2011) 70.